

Department of Physics and Astronomy
Remote Sensing and Satellite Research Group

**Satellite Remote Sensing Algorithm Development to Estimate
Total Suspended Sediment Concentration for Highly Turbid
Waters of Western Australia**

Passang Dorji

**This thesis is presented for the Degree of
Doctor of Philosophy
of
Curtin University**

April 2017

Declaration

To the best of my knowledge and belief this thesis contains no material previously published by any other person except where due acknowledgment has been made.

This thesis contains no material which has been accepted for the award of any other degree or diploma in any university.

Signature:

Date:

Abstract

In the last decade, the quality of coastal waters of northern Western Australia have been impacted by the increased activities in development of offshore oil and gas infrastructure. Regular extensive *in situ* monitoring of water quality in the region has been challenging due to the requirement of huge resources needed to monitor the large spatial extent. The total suspended sediment (TSS) concentration, which serves as a proxy for water quality, has been successfully mapped at high spatiotemporal resolution in the coastal waters via satellite remote sensing. However, the accuracy and utility of such TSS measurements is directly related to the accuracy of the TSS algorithm and satellite sensors used in mapping TSS concentration. Most previous TSS algorithms have been developed for specific regions and have been based on empirical approaches and for particular satellite sensors. Such TSS algorithms lack general applicability, and the use of a single satellite sensor with specific radiometric, spectral, temporal and spatial characteristics also limit the general application of remote sensing to study highly dynamic TSS variation across differing coastal regimes. Therefore, this research focuses on development of multi-sensor TSS model for highly turbid coastal waters of northern Western Australia, which is physically based on the principle of radiative transfer, but locally tuned using *in situ* optical properties of regional coastal waters of northern Western Australia.

In this study, a generic multi-sensor red band semi-analytic sediment model (SASM) was developed for regional waters of northern Western Australia. The SASM was used in mapping TSS concentration of the region using different satellite sensors; high spatial resolution WorldView-2 (WV2) at 2 m and Landsat-8 Operational Land Imager (OLI) at 30 m, medium spatial resolution MODerate resolution Imaging Spectroradiometer (MODIS)-Aqua at 250 m and low spatial resolution Advanced Himawari Imager (AHI) on-board Himawari-8 at 500 m – 2000 m. It was found that the satellite sensors with spatial resolution of at least 250 m were adequate in spatially discerning sediment plumes from the

background waters. Further, it was observed the temporal resolution of 1 image per day from MODIS-Aqua was sufficient to segregate TSS variation as a result of dredging and natural processes. However, diurnal TSS variation caused by the tidal currents in the study regions were only discernible from high temporal resolution geostationary satellite—Himawari-8. A feasibility study of Himawari-8 in mapping TSS concentration was conducted for the first time and the validation of AHI derived TSS concentration with MODIS-Aqua and Landsat-8 OLI showed good correlation, with correlation coefficients $r = 0.71$ and $r = 0.91$ respectively. The results from the feasibility study of Himawari-8 showed that it can be a valuable resource in monitoring the TSS dynamics of coastal regions in Western Australia at high temporal resolution which can effectively fill the temporal gaps of other satellite sensors.

The implications of using readily available TSS algorithms and different satellite sensors were also quantified using rigorous statistical tests and simulated optical datasets. It was found that few previously published TSS algorithms from the last decade were robust enough to be used in mapping TSS concentration of optically unknown water types, with Mean Absolute Relative Errors (MARE) ranging from 69.96% to 481.82%. Also, the application of an untested TSS algorithm without first testing and selecting an appropriate TSS algorithm, was shown to potentially result in errors in excess of three orders of magnitude. In highly turbid waters, the discrepancies between peak TSS levels obtained from satellite sensors with different spatial resolutions was demonstrated, with TSS concentration as high as 160 mg/L observed from WV2 at 2 m spatial resolution and only 23.6 mg/L from MODIS-Aqua at 250 m. The implications of such discrepancies in TSS estimation via satellite remote sensing are extremely important to environmental resource managers for effective implementation of monitoring policies.

Acknowledgements

This thesis would not have been possible without the guidance of my supervisor Dr. Peter Fearn. I would like to thank Dr. Fearn for introducing me to the world of satellite remote sensing in early 2011 when I was pursuing my Master's degree. Dr. Fearn's constant guidance and support has enabled me to complete my research on time and without any major hurdle. I am also deeply thankful to Dr. Mark Broomhall from the Bureau of Meteorology, who as my unofficial supervisor has provided me with much needed scientific direction and support during the last three years.

The Remote Sensing and Satellite Research Group members, Emeritus Professor Merv Lynch, Professor David Antione, Dr. Rogrigo Garcia and rest of the members are also acknowledged for providing moral encouragement and helping hand when much needed.

Dr. Brendon McGann, my thesis chairperson is also thanked for providing me with much needed advice and guidance during my PhD candidature. And, encouraging me to apply for many scholarships Curtin University had to offer.

Thank you, Dr. John Hedley, for taking the time to check my work on the atmospheric correction of Himawari-8 despite your hectic schedule.

To my wife, Pema Deki and son Ugyen, whom I love more than anything else in this world! Thank you for providing me with constant love and support, and tolerating my absence and late night habitual work on the research projects. Thank you my parents and rest of the family members for understanding my constant absence from family commitments during the last three years.

Publications presented as part of this Thesis

Chapter 3

Dorji, P., Fearn, P., & Broomhall, M. (2016). A Semi-Analytic Model for Estimating Total Suspended Sediment Concentration in Turbid Coastal Waters of Northern Western Australia Using MODIS-Aqua 250 m Data. *Remote Sensing*, 8(7), 556.

Chapter 4

Dorji, P., & Fearn, P. (2016). A Quantitative Comparison of Total Suspended Sediment Algorithms: A Case Study of the Last Decade for MODIS and Landsat-Based Sensors. *Remote Sensing*, 8(10), 810.

Chapter 5

Dorji, P., & Fearn, P. (2017). Impact of the Spatial Resolution of Satellite Remote Sensing Sensors in the Quantification of Total Suspended Sediment Concentration: A Case Study in Turbid Waters of northern Western Australia, *PLoS One*, 12(4), ep0175042.

Chapter 6

Dorji, P., & Fearn, P. (2017). Mapping Total Suspended Sediment in Near Real Time: A Preliminary Assessment of Geostationary Satellite (Himawari-8) in Coastal Waters of Western Australia. *Remote Sensing of Environment*, (Submitted).

The statements of contributions from co-authors of the publications are presented in Appendices. All publications appear in open-access journals where materials can be freely accessed and distributed under a Creative Commons Attribution (CC BY) 4.0 license <http://creativecommons.org/licenses/by/4.0/>.

Reports written during Ph.D. Candidature

Fearns, P; **Dorji, P.**; Broomhall, M.; Symonds, G.; Shimizu, K.; Contardo, S.; Mortimer, N.; Sun, C. Plume Characterization, Project 2/3.2-Dredge Node Report, Western Australian Marine Science Institute, 2016.

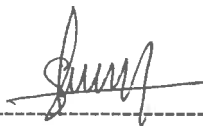
Fearns, P., **Dorji, P.**, Broomhall M., Branson, P. Mortimer, N. Plume characterisation – Laboratory studies Final Report of Project 3.2.2 of the Western Australian Marine Science Institution (WAMSI) Dredging Science Node. Perth, Western Australia, 2017.

Statement of contribution of others

Passang Dorji's contribution to this study and publications presented as chapters in this thesis included the conception and design of study, acquisition and analysis of field and satellite remote sensing data, drafting of the manuscript and all the associated works related to the publications. Co-authors made some contribution significant enough to warrant a co-authorship of the resulting articles. The details of the contributions of the co-authors are specified below:

Dr. Peter Fearn provided overall project supervision, manuscript editing and critical feedbacks on the revision of all manuscripts.

Dr. Mark Broomhall assisted in field data collection and manuscript editing for Chapter 3.



Passang Dorji



Dr. Peter Fearn

List of common symbols

Symbols	Units	Definition
λ	nm	Wavelength
θ_s	degrees	Solar zenith angle
θ_v	degrees	Sensor zenith angle
φ_s	degrees	Solar azimuth angle
φ_v	degrees	Sensor azimuth angle
$\Delta\varphi$	degrees	Relative azimuth angle between sensor and sun
$a(\lambda)$	m^{-1}	Total absorption coefficient
$a_w(\lambda)$	m^{-1}	Pure water absorption coefficient
$a_\varphi(\lambda)$	m^{-1}	Phytoplankton absorption coefficient
$a_p(\lambda)$	m^{-1}	Particulate absorption coefficient
$a_{\text{cdom}}(\lambda)$	m^{-1}	Coloured dissolved organic matter absorption coefficient
$a_p^*(\lambda)$	$\text{m}^2 \text{g}^{-1}$	Particulate mass-specific absorption coefficient
$b(\lambda)$	m^{-1}	Total scattering coefficient
$b_{\text{bw}}(\lambda)$	m^{-1}	Backscattering coefficient of pure water
$b_b(\lambda)$	m^{-1}	Total backscattering coefficient
$b_{\text{bp}}(\lambda)$	m^{-1}	Backscattering coefficient of particulate matter
$b_{\text{b}\varphi}(\lambda)$	m^{-1}	Backscattering coefficient of phytoplankton
$b_{\text{bp}}^*(\lambda)$	$\text{m}^2 \text{g}^{-1}$	Particulate mass-specific backscattering coefficient
$E_d(\lambda)$	$\text{W m}^{-2} \text{nm}^{-1}$	Downwelling plane irradiance
$F_o(\lambda)$	$\text{mW m}^{-2} \text{nm}^{-1}$	Spectral solar irradiance
$L_u(\lambda)$	$\text{N m}^{-2} \text{sr}^{-1} \text{nm}^{-1}$	Upwelling radiance
$L_{\text{sky}}(\lambda)$	$\text{N m}^{-2} \text{sr}^{-1} \text{nm}^{-1}$	Sky radiance

$L_w(\lambda)$	$\text{N m}^{-2} \text{sr}^{-1} \text{nm}^{-1}$	Water leaving radiance
$L_{\text{toa}}(\lambda)$	$\text{N m}^{-2} \text{sr}^{-1} \text{nm}^{-1}$	Top of the atmosphere radiance
$\rho_w(\lambda)$	dimensionless	Water leaving reflectance
$\rho_{\text{toa}}(\lambda)$	dimensionless	Top of the atmosphere reflectance
$R_{\text{rs}}(\lambda)$	sr^{-1}	Remote sensing reflectance
$r_{\text{rs}}(\lambda)$	sr^{-1}	Sub-surface remote sensing reflectance

List of Abbreviations

Acronym	Definitions
AHI	Advanced Himawari Imager
ARE	Absolute Relative Error
AOP	Apparent Optical Properties
AOT	Aerosol Optical Thickness
CA	Clean Area
CDOM	Coloured Dissolved Organic Matter
CHL	CHLorophyll (Phytoplankton)
DA	Dredge Area
EMS	Electromagnetic Spectrum
EUMETSAT	European Union's METeorological SATellite
GOCI	Geostationary Ocean Colour Imager
IRS	Indian Remote Sensing
IOCCG	International Ocean-Colour Coordinating Group
LISS	Linear Imaging Self Scanner
LRE	Largest Relative Error
MARE	Mean Absolute Relative Error
MODIS	MODerate resolution Imaging Spectrometer
MTA	Moderate Turbid Area
MSS	Multi-Spectral Scanner
NE_p	Noise Equivalent Reflectance
NE_L	Noise Equivalent Radiance
NE_{TSS}	Noise Equivalent Total Suspended Sediment
NIR	Near InfraRed
OLI	Operational Land Imager
RMSE	Root Mean Square Error
RP	River Plume
SASM	Semi-Analytic Sediment Model
SeaDAS	SeaWiFS Data Analysis System
SeaWiFS	Sea-viewing Wide Field-of-view Sensor

SG	Spoil Ground
SNR	Signal-to-Noise Ratio
SPOT	Système Pour l'Observation de la Terre
SRE	Smallest Relative Error
SWIR	Short Wave InfraRed
THEOS	THailand Earth Observation System
TOA	Top of Atmosphere
TSS	Total Suspended Sediment
WV2	WorldView-2

Definition of key terms

The key terms used in this thesis are operationally defined as follows:

1. "TSS Concentration" refers to the dry weight of suspended matter per volume of water (mg/L) that are retained after filtering through a 0.7 μm Whatman glass-fiber filter (GF/F).
2. "Model(s)" or "Algorithm(s)" in the context of TSS model(s)/Algorithm(s) have the same implied meaning.
3. "Open, deep or offshore" waters have the same meaning as "Case-1" waters, which are defined as those waters whose optical properties co-vary primarily with phytoplankton concentration (Gordon & Morel, 1983).
4. "Coastal" waters have same the meaning as "Case-2" waters, which are defined as those waters whose optical properties are more complex than Case-1 waters and the optical properties do not covary with phytoplankton concentration, but depend on other optically active water constituents, such as Coloured Dissolved Organic Matter and TSS (Gordon & Morel, 1983).

Table of Contents

Declaration	i
Abstract	ii
Acknowledgements	iv
Publications presented as part of this Thesis	v
Reports written during Ph.D. Candidature	vi
Statement of contribution of others	vii
List of common symbols	viii
List of Abbreviations	x
Definition of key terms	xii
List of Figures	xviii
List of Tables	xxv
Chapter 1	1
1.1 Overview	1
1.2 Background	1
1.3 Research objectives and significance	7
1.4 Thesis outline	8
Chapter 2	10
2.1 Overview.....	10
2.2 Radiative Transfer Theory and optical properties of the water column.....	10
2.2.1 Radiometric quantities in remote sensing.....	10
2.2.2 IOP and AOP	13

2.2.3 Linking IOPs and AOPs through a Radiative Transfer Equation	14
2.3 Water quality and optically active water constituents	15
2.4 Satellite Sensors used in TSS Mapping	18
2.5 TSS Algorithms.....	23
2.5.1 Empirical models	23
2.5.2 Bio-optical and semi-analytical models	25
2.6 Challenges and future direction.....	27
2.6.1 Satellite sensor requirements and limitations.....	27
2.6.2 Limitations of TSS models	29
Chapter 3.....	32
3.1 Abstract	32
3.2 Introduction.....	33
3.3 Materials and Methods	36
3.3.1 Study Site	36
3.3.2 In situ and Remote Sensing Data	37
3.3.3. SASM Model Formulations	42
3.3.4 Conversion of DALEC Remote Sensing Reflectance to Sub-Surface Remote Sensing Reflectance	45
3.3.5. Regional Empirical Model	46
3.3.6. Model Calibration and Model Uncertainty Estimates	46
3.3.7. Accuracy Assessment for Model Performance	47
3.4 Results and Discussion	48
3.4.1. Spectral Characterization of Field Spectral Measurements ..	48
3.4.2. SASM Calibration and Validation	49
3.4.3. SASM Comparison with Empirical Models.....	51
3.4.4. Application to MODIS Imagery.....	55

3.5 Conclusions	62
Chapter 4	64
4.1 Abstract	64
4.2 Introduction.....	65
4.3. Materials and Methods	68
4.3.1. Dataset.....	68
4.3.2. TSS Models.....	75
4.3.3. Statistical Tests and Scoring System	76
4.4 Results	82
4.4.1. TSS Model Comparisons	82
4.4.2. Evaluation of Models	85
4.5 Discussion	88
4.5.1. Data and Methodological Limitation	88
4.5.2. TSS Model Selection Guidelines.....	90
4.6. Conclusions	92
Chapter 5.....	93
5.1 Abstract	93
5.2 Introduction.....	94
5.3 Materials and Methods	98
5.3.1 Study Site and Context	98
5.3.2 Field Remote Sensing Reflectance and TSS Measurements	99
5.3.3 Mapping of TSS Concentration	107
5.3.4 Accuracy Assessment.....	108
5.4 Results	109
5.4.1 Validation of TSS Algorithms	109
5.4.2 Multi-Sensor Atmospheric Correction Validations.....	110
5.4.3 Sediment Plume Features Examination	113

5.4.4 Quantification of TSS in Sediment Plumes	116
5.5 Discussion	120
5.5.1 Data and Methodological Limitations	120
5.5.2 General Observation and Recommendations	122
5.6 Conclusion	124
Chapter 6	126
6.1 Abstract	126
6.2 Introduction	127
6.3. Materials and Methods	130
6.3.1. Study area	130
6.3.2 Himawari-8 (AHI) overview	132
6.3.3. Satellite sensor dataset acquisition and atmospheric correction	133
6.3.4 AHI sensor noise estimation	140
6.3.5 In situ validation dataset.....	141
6.3.6. Single red band TSS algorithm	142
6.3.7. Accuracy assessment	143
6.4 Results	144
6.4.1. Quantitative comparison of water leaving reflectance derived from the SWIR and NIR-SWIR aerosol estimation methods	144
6.4.2. In situ validation of water leaving reflectance derived from SWIR and NIR-SWIR aerosol estimation methods	147
6.4.3 Uncertainty of AHI sensor noise and comparison with the sensor noise of MODIS-Aqua and Landsat-8 OLI sensors	150
6.4.4 Cross-validation of AHI derived TSS concentration with MODIS-Aqua and Landsat-8 Sensors.....	154
6.4.5 TSS Concentration Mapping and Temporal Dynamics	156
6.5 Discussion	160

6.6 Conclusion.....	162
Chapter 7	164
7.1 Conclusion.....	164
7.2 Limitations	167
7.3 Future work and recommendations.....	168
7.4 Concluding remark	170
Appendix A.....	172
A1. Comparison of Reflectance Models for Nechad et al. (2010) and SASM	172
A1.1. NRP Reflectance Model:	172
A1.2. SASM Reflectance Model:.....	173
A2. HydroLight Simulation.....	173
A3. Reflectance Model Evaluation	174
Appendix B.....	178
Appendix C.....	179
Appendix D.....	188
Appendix E.....	191
Appendix F	192
Appendix G	207
Appendix H.....	210
Appendix I	212
Appendix J	213
References	219

List of Figures

- Figure 2.1: Geometry used to define radiance (note: image reproduced from Figure 1 of Mobley (2001)) 11
- Figure 3.1: True colour 15 m pan sharpened Landsat OLI (Operational Land Imager) imagery showing study site and the locations of sampling stations. Red squares represent the locations of dredge area (DA), spoil ground (SG), and clean area (CA) used in the temporal analysis. Red, purple and green filled circles are the locations of water sampling stations in 2013, 2014 and 2015 respectively 36
- Figure 3.2: *In situ* DALEC spectral reflectance plots for different ranges of TSS concentration. 49
- Figure 3.3: The SASM curve for $r_{rs}(B1)$ (Equation (3.18)) is shown by the solid line. The *in situ* data points are shown by open circles. The 65% confidence limits obtained through the bootstrap method are shown by dashed lines. The greyed region represents the upper and lower bound for 1000 bootstrap runs. 51
- Figure 3.4: Validation results using the LOOCV method for the three models. The box at the bottom right is a blow out of the TSS < 10 mg/L and the dashed line is 1:1 line. 52
- Figure 3.5: The empirical model curve for $r_{rs}(B1)$ is shown by the solid line, *in situ* data points shown by open circles for both (a) the linear model and (b) the exponential model. In both the figures the 65% confidence limit obtained through the bootstrap method are shown by dashed lines. The greyed region represents the upper and lower bound for 1000 bootstrap runs. The upper and lower bound for exponential model has been limited to 95% CI because few high values of TSS were in excess of several thousand mg/L. The box at the bottom right in (a) and middle left (b) is a blow out of the TSS < 10 mg/L and $r_{rs}(B1) < 0.025 \text{ sr}^{-1}$. 53
- Figure 3.6: $R_{rs}(B1)$ from the standard atmospheric correction method in SeaDAS SWIR and the MUMM atmospheric correction method in comparison with DALEC measurements for 6th July 2015. 56
- Figure 3.7: Validation between the SASM-derived TSS from MODIS-Aqua band 1 reflectance for (a) AVD30; (b) AVD60; and (c) AVD90. The error bar indicates the minimum and maximum TSS computed in 3×3 and 5×5 -pixel window widths. 59
- Figure 3.8: (a) Daily and (b) monthly averaged TSS derived from the SASM for 2013 MODIS-Aqua data. 60
- Figure 3.9: 2013 monthly averaged TSS images derived from MODIS-Aqua 250 m band 1 (January to December 2013). Rectangles represent locations for CA, DA, and SG. 62

- Figure 4.1:(a) Mineral mass-specific absorption and (b) scattering coefficients. 71
- Figure 4.2: Point classification for Landsat algorithms using the Root Mean Square Error (RMSE) Test. The upper and lower dashed lines indicate the mean \pm 95% confidence limits and the solid horizontal line is the mean RMSE of all the TSS algorithms. Unfilled circles are RMSE of each TSS algorithm with respective \pm 95% confidence limits shown by error bars. 78
- Figure 4.3: Flow diagram showing the methodology of the point scoring system described in Section 4.3.3. 82
- Figure 4.4: Final scores of MODerate resolution Imaging Spectroradiometer (MODIS) TSS models. 84
- Figure 4.5: Final scores of Landsat TSS models. 84
- Figure 5.1: Study Site. True colour imagery Landsat OLI showing the locations of field sites in the waters off the coast of Onslow, Western Australia. True colours image of the study site is reprinted from Figure 1 in Dorji et al., (2016) under a Creative Commons Attribution (CC-BY) license (<http://creativecommons.org/licenses/by/4.0/>). The black polygon added in Figure 5.1 represents the area where WorldView 2 data were captured on June 13th 2014. The coloured dots represent locations of *in situ* data with colours indicating the year of data acquisition. 99
- Figure 5.2: The atmospherically corrected R_{rs} (red band) product. (a) and (b) WV2 and MODIS-Aqua on 13th June 2014; (c)-(e) Landsat-8 OLI and (f)-(h) MODIS-Aqua on 23rd May, 10th July and 26th July 2014 respectively. The white cross mark on (a), (c)-(e) are the locations of the central pixel of 2.5 km square used in R_{rs} product validation. The black cross mark are locations corresponding to Dredged Areas (DA and DA2), Spoil Ground (SG), Clean Area (CA), River Plume (RP) and Moderate Turbid Area (MTA) in each image. 105
- Figure 5.3: The TSS model curves for MODIS-Aqua (blue), Landsat-8 OLI (green) and WV2 (red). The *in situ* data points are shown by filled circles with the same colour profile as respective TSS model curves. The data for TSS < 10 mg/L and r_{rs} < 0.025 sr⁻¹ are also shown in the blow out version of the plot. 110
- Figure 5.4: *In situ* validation of DALEC-measured R_{rs} and MODIS-Aqua derived R_{rs} for match-up data within \pm 90 min from the satellite overpass. The error bars indicate the maximum and minimum MODIS R_{rs} values in 3 \times 3 and 5 \times 5 pixel extents. The R_{rs} band were Red band of the respective sensor. 111
- Figure 5.5: Inter-satellite R_{rs} product validation results. (a) MODIS-Aqua vs Landsat-8 OLI R_{rs} product validation from May 23rd, July 10th and July 26th 2014; (b) MODIS-Aqua vs WV2 R_{rs} product validation for R_{rs} from June 13th 2014. The error bars indicate

the 17.5 percentile (lower limit) and 82.5 percentile (upper limit) of pixel values from a 2.5 km width box for each respective satellite sensors derived R_{rs} . Dashed lines indicate the 1: 1 relationship. The R_{rs} band were Red band of the respective sensor. 113

Figure 5.6: Spatially degraded images of the dredge area (DA) and river plume (RP): Extracted from images in Figures 5.2a, d, and i corresponding to (a) WV2, (b) Landsat-8 OLI and (c) MODIS-Aqua. 115

Figure 5.7. (a) MODIS-Aqua and (b) WV2 at their respective native and degraded spatial resolutions, averaged over the areas: dredge plume (DA and DA2), Spoil Ground (SG), River Plume (RP), Moderate Turbid Area (MTA) and Clean Area (CA). The error bars indicate the minimum and maximum TSS concentrations in each spatial grid. 117

Figure 5.8: Average TSS concentration. (a)—(c) Landsat-8 OLI and (d)—(f) MODIS-Aqua at their respective native and degraded spatial resolutions in the dredge plume (DA), Spoil Ground (SG), River Plume (RP), Moderate Turbid Area (MTA) and Clean Area (CA). The error bars indicate the minimum and maximum TSS concentrations in each spatial grid. 119

Figure 6.1: True colour image of the study site (RGB = AHI Band 3, 2, 1). Black filled circles are the *in situ* validation points collected during the field campaign on July 4th – July 10th 2015 (shown in blow-out version on the right for greater details). Box A corresponds to homogenous clear water area; Box B corresponds to homogenous region within the Exmouth Gulf; Box C corresponds to turbid waters near the coast. 131

Figure 6.2: Full disk view of earth as seen from Himawari-8 with different target areas (green rectangles (top) North-Eastern Japan Area and (bottom) South-Western Japan Area, red square flexible target area and white rectangles are flexible Landmark areas). The satellite view angle is show for the whole disk with satellite zenith at 140.7°E. 133

Figure 6.3: Histogram of aerosol reflectance ratio derived from clear water pixels of AHI data on July 9th 2015 at 2:00 UTC (A) $\epsilon^{(5,6)}$ and (B) $\epsilon^{(4,5)}$ from rayleigh corrected reflectance (N is the total number of pixels). 137

Figure 6.4: *In situ* DALEC measured R_{rs} used in validation of AHI derived R_{rs} 142

Figure 6.5: Scatter plot of ρ_w computed using a SWIR and NIR-SWIR atmospheric correction method. Solid line is line of best fit and broken line is 1:1 line. 145

- Figure 6.6: *In situ* validation of ρ_w for all available match-up data points for **(A)** SWIR and **(B)** NIR-SWIR atmospheric correction method. 149
- Figure 6.7: Spectral plot of atmospherically corrected ρ_w in AHI Band 1-4 using SWIR and NIR-SWIR methods and *in situ* data at **(A)** pixel close to the coast and **(B)** farther away from the coast. 150
- Figure 6.8: Plot of a **(A)** L_{typical} , **(B)** NE_L , and **(C)** SNR calculated from a clear water pixel location (Box A in Figure 6.1) for AHI Band 1-6 at different θ_0 . Note that the SNR were calculated at L_{typical} values. 151
- Figure 6.9: NE_{TSS} at different solar zenith angle, θ_0 , for MODIS-Aqua Band 1 (250 m) and Band 13 (1000 m), Landsat-8 OLI Band 4 (30 m) and AHI Band 3 (2000 m). 154
- Figure 6.10: Spatial maps of TSS concentration derived from **(A)** AHI Band 3 on July 9th 2015 at 02:40 pm, **(B)** MODIS-Aqua Band 01 on July 9th 2015 at 02:35 pm, **(C)** AHI Band 03 on July 29th 2015 at 10:20 am and **(D)** Landsat-8 OLI Band 4 on July 29th at 10:20 am. 155
- Figure 6.11: A linear regression between **(A)** AHI and Landsat-8 OLI derived TSS concentration on July 29th 2015 and **(B)** AHI and MODIS-Aqua derived TSS concentration on July 4th-6th and 8th-10th, 2015. 156
- Figure 6.12: Every 30 min TSS concentration derived by AHI on July 5th 2015 from 10:00 – 15:30 hrs. TSS was derived using SWIR atmospheric correction method described in Section 6.4.1. 158
- Figure 6.13: Daily TSS concentration from 10:00 hrs – 15:00 hrs at Boxes A, B and C (see Figure 6.12) derived using the SWIR atmospheric correction method for **(A)** July 4th 2015, **(B)** July 8th 2015, and **(C)** July 10th 2015. NE_L (TSS) and $\Delta\rho_a$ (TSS) are errors derived from AHI sensor noise and aerosol estimation. 159
- Figure A.1: **(a)** Scatter plot for modelled and HydroLight $\omega'_b(650\text{nm})$; **(b)** $\omega'_b(650\text{nm})$ as a function of TSS. 177
- Figure A.2: **(a)** Scatter plot for modelled and $\omega'_b(790\text{nm})$; **(b)** $\omega'_b(790\text{nm})$ as a function of TSS 177
- Figure F.1: Total scores for different sediments and the average scores across all five sediments in CLASS-I. 192
- Figure F.2: Total scores for different sediments and the average scores across all five sediments in CLASS-II water. 192
- Figure F.3: Total scores for different sediments and the average scores across all five sediments in CLASS-III water. 193

Figure F.4: Total scores for different sediments and the average scores across all five sediments in CLASS-IV water.	193
Figure F.5: Total scores for different sediments and the average scores across all five sediments in CLASS-V water.	194
Figure F.6: Total scores for different backscattering ratios and the average scores across all backscattering ratios in CLASS-I water for Calcareous sand.	194
Figure F.7: Total scores for different backscattering ratios and the average scores across all backscattering ratios in CLASS-II water for Calcareous sand.	195
Figure F.8: Total scores for different backscattering ratios and the average scores across all backscattering ratios in CLASS-III water for Calcareous sand.	195
Figure F.9: Total scores for different backscattering ratios and the average scores across all backscattering ratios in CLASS-IV water for Calcareous sand.	196
Figure F.10: Total scores for different backscattering ratios and the average scores across all backscattering ratios in CLASS-V water for Calcareous sand.	196
Figure F.11: Total scores for different solar zenith angles and the average scores across all solar zenith angles in CLASS-I water for Calcareous sand.	197
Figure F.12: Total scores for different solar zenith angles and the average scores across all solar zenith angles in CLASS-II water for Calcareous sand.	197
Figure F.13: Total scores for different solar zenith angles and the average scores across all solar zenith angles in CLASS-III water for Calcareous sand.	198
Figure F.14: Total scores for different solar zenith angles and the average scores across all solar zenith angles in CLASS-IV water for Calcareous sand.	198
Figure F.15: Total scores for different solar zenith angles and the average scores across all solar zenith angles in CLASS-V water for Calcareous sand.	199
Figure F.16: Total scores for different sediments and the average scores across all five sediments in CLASS-I water.	199
Figure F.17: Total scores for different sediments and the average scores across all five sediments in CLASS-II water.	200
Figure F.18: Total scores for different sediments and the average scores across all five sediments in CLASS-III water.	200
Figure F.19: Total scores for different sediments and the average scores across all five sediments in CLASS-IV water.	201

- Figure F.20: Total scores for different sediments and the average scores across all five sediments in CLASS-V water. 201
- Figure F.21: Total scores for different backscattering ratios and the average scores across all backscattering ratios in CLASS-I water for Calcareous sand. 202
- Figure F.22: Total scores for different backscattering ratios and the average scores across all backscattering ratios in CLASS-II water for Calcareous sand. 202
- Figure F.23: Total scores for different backscattering ratios and the average scores across all backscattering ratios in CLASS-III water for Calcareous sand. 203
- Figure F.24: Total scores for different backscattering ratios and the average scores across all backscattering ratios in CLASS-IV water for Calcareous sand. 203
- Figure F.25: Total scores for different backscattering ratios and the average scores across all backscattering ratios in CLASS-V water for Calcareous sand. 204
- Figure F.26: Total scores for different solar zenith angles and the average scores across all solar zenith angles in CLASS-I water for Calcareous sand. 204
- Figure F.27: Total scores for different solar zenith angles and the average scores across all solar zenith angles in CLASS-II water for Calcareous sand. 205
- Figure F.28: Total scores for different solar zenith angles and the average scores across all solar zenith angles in CLASS-III water for Calcareous sand. 205
- Figure F.29: Total scores for different solar zenith angles and the average scores across all solar zenith angles in CLASS-IV water for Calcareous sand. 206
- Figure F.30: Total scores for different solar zenith angles and the average scores across all solar zenith angles in CLASS-V water for Calcareous sand. 206
- Figure G.1: TSS concentration variability at different spatial resolutions derived from MODIS-Aqua, WV2 and Landsat-8 OLI for Moderate Turbid Area (MTA). 207
- Figure G.2: TSS concentration variability at different spatial resolutions derived from MODIS-Aqua, WV2 and Landsat-8 OLI for Moderate Turbid Area (MTA). 208
- Figure G.3: TSS concentration variability at different spatial resolutions derived from MODIS-Aqua, WV2 and Landsat-8 OLI for Clean Area (CA). 208
- Figure H.1: Daily TSS concentration variability from 10:00 hrs – 15:00 hrs at location, Box A, B and C derived using SWIR atmospheric correction method (Left) July 5th 2015, (Middle) July 7th 2015,

and (Right) July 9th 2015. NE_L (TSS) and $\Delta\rho_a$ (TSS) are error derived from AHI sensor noise and aerosol estimation. 210

Figure H.2: Daily TSS concentration variability from 10:00 hrs – 15:00 hrs at location, Box A, B and C derived using NIR-SWIR atmospheric correction method (Top Left) July 4th 2015, (Top Middle) July 5th 2015, and (Top Right) July 6th 2015, (Bottom Left) July 8th 2015, (Bottom Middle) July 9th 2015 and (Bottom Right) July 10th 2015. NE_L (TSS) and $\Delta\rho_a$ (TSS) are error derived from AHI sensor noise and aerosol estimation. 211

Figure I: Spectral plot of *in situ* ρ_w of validation data points (Plot from the top-left is the every 10th random validation data point)

List of Tables

Table 1.1: Summary of thesis chapters	9
Table 2.1: List of satellite sensors currently operational with the potential to map TSS concentration	22
Table 3.1: Validation results from the LOOCV results for the SASM for MODIS-Aqua band 1, band 2 and their combinations.	50
Table 3.2: Results for the SASM, linear and exponential models for MODIS-Aqua band 1.	52
Table 3.3: Absolute relative error for the SASM, linear and exponential models derived from the bootstrap distribution of the TSS results.	54
Table 4.1: Concentration of coloured dissolved organic matter (CDOM), chlorophyll (CHL), and total suspended solids (TSS) used in HydroLight modelling. The pure water component in all the HydroLight runs remains unchanged.	70
Table 4.2: Five different water classes.	74
Table 4.3: Relative Error and ΔR_{rs} Uncertainty Tolerance results for the highest and lowest scoring models' evaluation using HydroLight Data. The highest scoring models are in bold text and the lowest scoring models are in regular italic text. The results provided in parenthesis represent the $+\Delta R_{rs}$ and '-' indicates the model failed to provide TSS estimation within acceptable bounds. SRE: Smallest Relative Error. LRE: Largest Relative Error. MARE: Mean Absolute Relative Error. ARE: Absolute Relative Error.	87
Table 4.4: The MARE for high and low scoring models for <i>in situ</i> data. The high scoring models are in bold text and the low scoring models are in italics.	88
Table 5.1: Validation results for MODIS-Aqua, Landsat-8 OLI, and WV2 TSS algorithms.	110
Table 6.1: Data Acquisition dates for Himawari-8, Landsat and MODIS-Aqua	133
Table 6.2: Parameters and values used in generating LUT using 6SV	136
Table 6.3: Water leaving reflectance (ρ_w) of AHI sensor in Band 1, 2, 3 and 4 computed for different atmospheric correction methods (NIR-SWIR and SWIR aerosol correction methods). The mean and STD ρ_w results are determined from all pixels within Box A, B and C for all available AHI data. The ARE are determined as the absolute relative error between NIR-SWIR and SWIR results.	146
Table 6.4: Aerosol reflectance (ρ_a) of AHI sensor in Band 1, 2, 3 and 4 computed for different atmospheric correction methods (NIR-SWIR and SWIR aerosol correction methods). The mean and	

STD ρ_a results are determined from all pixels within Box A, B and C for all available AHI data. The ARE are determined as the absolute relative error between NIR-SWIR and SWIR results. 147

Table 6.5: *In situ* validation of water leaving reflectance (ρ_w) derived from AHI in Band 1, 2, 3 and 4 using SWIR and NIR-SWIR atmospheric correction method. LRE = Largest Relative Error and SRE = Smallest Relative Error are the extreme points within the Absolute Relative Error (ARE) generated from whole of AHI dataset. 148

Table 6.6: Mean (1 STD) values of SNR, L_{typical} and NE_L derived from the clear water pixels of AHI sensor for all the dates provided in Table 6.1. 152

Table 6.7: Parameters used in the computations of NE_ρ and NE_{TSS} . 154

Table A.1: Six different water types grouped based on CHL concentration and CDOM absorption. 174

Table A.2: Comparative $\omega'_b(494\text{nm})$ results for the NRP and SASM models (all $p < 0.005$). 175

Table A.3: Comparative $\omega'_b(566\text{nm})$ results for the NRP and SASM models (all $p < 0.005$). 176

Table A.4: Comparative $\omega'_b(650\text{nm})$ results for the NRP and SASM models (all $p < 0.005$). 176

Table A.5: Comparative $\omega'_b(790\text{nm})$ results for the NRP and SASM models (all $p < 0.005$). 176

Table C.1: The summary of TSS algorithms mentioned in Section 4.3.2 179

Table D.1: Mean of Total Point and Final Scores of MODIS TSS models across different water classes as derived from different sediment types, backscattering ratios and Solar Zenith Angles. The top five and bottom five scores from each water types and the final scores are in bold (top) and bold italics (bottom) 188

Table D.2: Mean of Total Point and Final Scores of Landsat TSS models across different water classes as derived from different sediment types, backscattering ratios and Solar Zenith Angles. The top five and bottom five scores from each water types and the final scores are in bold and bold italics. 190

Chapter 1

General Introduction

1.1 Overview

In addition to the development of satellite based Total Suspended Sediment (TSS) algorithms to map the TSS concentration in the turbid waters of northern Western Australia, this thesis also examines the limitations, advantages, and potential of using polar orbiting and geostationary satellite sensor based TSS algorithms in the coastal environment monitoring endeavour. The quality of coastal waters, which may be ascertained from the TSS concentration, can be remotely mapped using satellite remote sensing. However, the remote sensing of TSS concentration from satellite is not without the limitations that are inherent in the satellite sensors and TSS algorithms themselves. Thus, the outcomes from this study may lead to a better understanding of the implications of using different satellite sensors in monitoring the water quality in the coastal waters and the need for improved TSS algorithms. This chapter provides the general background of remote sensing in water quality management and the impetus for improved TSS algorithms for a range of different satellite sensors in monitoring the dynamic coastal water system.

1.2 Background

The monitoring of earth resources up until the middle of the 20th century was based predominantly on traditional ground based observations which were slow but compatible with the pace of environmental change of the time. Presently, the rapid pace of development at large spatial scales makes environmental impacts and their assessment more complex. This calls for faster data generation and dissemination processes for scientific studies which are currently benefited by the advancement in remote sensing technologies (Durrieu & Nelson, 2013). Remote sensing is the act of collecting information of objects from a distance and it is based on the basic principle that everything in nature emits, absorbs or reflects radiation in the electromagnetic spectrum (EMS). Every object has a unique radiation

signature in different regions of the EMS and it is this spectrum that may be perceived by remote sensing sensors. It is this unique spectrum of a particular object that can be exploited to distinguish between different objects (Lee, Carder, Mobley, Steward, & Patch, 1999), or changes in the spectrum exploited to measure change in the environment.

Remote sensing has seen a rapid advancement from early photography using a still camera in a single spectral band to modern hyperspectral sensors that can gather spectral signatures across hundreds of bands. The earliest of remote sensing methods from space can be traced back to an oblique photograph of a small village near Paris by Gaspard Tournachon in 1859 (Aggarwal, 2004). Space borne remote sensing, in particular the satellite based remote sensing focused on monitoring the earth's resources for scientific studies, has gained momentum from the launch of the first Earth Resource Technology Satellite in the early 1970's, to numerous earth resource monitoring satellites launched thereafter in the following decades (Xie, Sha, & Yu, 2008). The applicability of the satellite-based remote sensing of water was demonstrated as early as 1972 by McKim, Marlar, and Anderson (1972) by mapping water bodies larger than 0.02 km² using the Multispectral Scanner (MSS) on board Landsat-1. Since then, remote sensing technology has been extensively used in mapping not only the spatial extent of the water bodies, but also the water quality (turbidity) in deep and coastal waters (Blondeau-Patissier, Gower, Dekker, Phinn, & Brando, 2014). The study of water quality includes, but is not limited to, the study of concentration of Chlorophyll-a (Chl-a) for biomass and primary production (Acker, Harding, Leptoukh, Zhu, & Shen, 2005; Arrigo & McClain, 1994; Jutla, Akanda, & Islam, 2012; Sullivan, Arrigo, McClain, Comiso, & Firestone, 1993), coloured dissolved organic matter (CDOM) (Kutser et al., 2005; Loisel, Vantrepotte, Dessailly, & MÈriaux, 2014b; Tiwari & Shanmugam, 2011), and TSS (Constantin, Doxaran, & Constantinescu, 2016; Lim, MatJafri, Abdullah, & Asadpour, 2013; Ody et al., 2016; Tang, Larouche, Niemi, & Michel, 2013; Wang & Lu, 2010) which all serve as proxies for water quality.

The monitoring of coastal water systems is important because more than half the human population is settled in coastal cities and the majority of sea-food is sourced from coastal waters (Bukata, 2005). However, monitoring of coastal waters is challenging because coastal waters are affected by both natural and anthropogenic processes which contribute to the optical complexities in remote sensing. Optically, the coastal or Case-2 waters are characterized by the variation of optical properties of water being influenced by phytoplankton, TSS, and CDOM concentrations, but the clear oceanic or Case-1 waters are primarily characterized by variations of their optical properties associated with just the phytoplankton concentration (Gordon & Morel, 1983; Prieur & Sathyendranath, 1981). In sediment laden coastal waters, since the dependence of water quality is purported to be dominated by the TSS concentration (Alashloo, Lim, Asadpour, & Safarpour, 2013; Guan, Li, & Booty, 2011), the monitoring of TSS concentration can serve as a proxy for the water quality for effective coastal management programs.

Traditionally, TSS concentration monitoring is performed using point based measurements at discrete sample locations and this method, though very accurate, limits the capability to address global needs to monitor water quality at high spatiotemporal resolution (Lim, Mat Jafri, Abdullah, & Abu Bakar, 2010). Satellite based remote sensing has shown the potential of effectively mapping TSS concentration over large spatial extents and at high temporal resolution (Brando & Dekker, 2003; Chen, Cui, Qiu, & Lin, 2014a; Härmä et al., 2001; Jutla et al., 2012; Kratzer, Brockmann, & Moore, 2008; Moses, Ackleson, Hair, Hostetler, & Miller; Tiwari & Shanmugam, 2011; Tzortziou et al., 2006). However, remote sensing of TSS concentration has to be supplemented by *in situ* data for algorithm development and validation. Thus, satellite based remote sensing coupled with *in situ* measurements provides an effective method in mapping the TSS concentration for a large spatial extent of coastal waters for water quality assessment.

The quantification of TSS concentration from satellite based remote sensing involves correlating *in situ* TSS concentration measurements with the remotely sensed information. The remotely sensed information includes

radiance (L) and irradiance (E), which may be combined to derive reflectance (ρ). These measurements may in turn be related to derive parameters such as the quasi - inherent optical property (IOP) diffuse attenuation coefficient (K_d). Remote sensing scientists have explored the use of L (Onderka & Pekárová, 2008), ρ (Nechad, Ruddick, & Park, 2010; Teodoro, Veloso-Gomes, & Gonçalves, 2008) and K_d (Shi, Zhang, Liu, Wang, & Qin, 2014) to directly relate to the concentration of TSS through empirical or semi-empirical methods by applying statistical regression analysis. However, to accurately quantify the TSS concentration, information about the IOP of the water masses is needed, and potentially combined with radiative transfer theory to produce a more robust understanding of the relationships between TSS and the remotely sensed measurements (Mobley, 1994).

The ease of establishing the direct empirical relationship between the remotely sensed surface reflectance, usually the water-leaving reflectance (ρ_w) or remote sensing reflectance (R_{rs}) (both defined explicitly in Ch. 2), and TSS concentration has led to numerous studies performed in estimating TSS concentration using a wide array of satellite sensors, including: Sea-viewing Wide Field-of-view Sensor (SeaWiFS) (Doxaran, Froidefond, & Castaing, 2003; Vos, Hakvoort, Jordans, & Ibelings, 2003), Landsat series (Kallio et al., 2008b; Vanhellemont & Ruddick, 2014; Wu et al., 2015; Wu, De Leeuw, Skidmore, Prins, & Liu, 2008; Zhang, Dong, Cui, Xue, & Zhang, 2014; Zhou, Wang, Zhou, & Troy, 2006), Medium Resolution Imaging Spectrometer (MERIS) (Chen, Han, & Feng, 2015b; Kratzer et al., 2008; Odermatt, Heege, Nieke, Kneubuhler, & Itten, 2008; Qing, Zhang, Cui, & Bao, 2014; Raag, Uiboupin, & Sipelgas, 2013; Tarrant, Amacher, & Neuer, 2010), MODerate resolution Imaging Spectroradiometer (MODIS) (Ayana, Worqlul, & Steenhuis, 2015; Chen et al., 2015a; Chen, Hu, & Muller-Karger, 2007; Hudson et al., 2014; Miller & McKee, 2004; Petus et al., 2014; Raag et al., 2013), “Système Pour l’Observation de la Terre” (SPOT) (Doxaran, Froidefond, Lavender, & Castaing, 2002), and the high resolution sensor IKONOS (Ekercin, 2007). However, the use of simple direct empirical relationships to estimate TSS concentration in coastal waters are not always valid. For example, the validity of a simple linear empirical approximation

becomes invalid as the remotely sensed reflectance becomes saturated at high TSS concentrations (Doxaran et al., 2003; Petus et al., 2010). This calls for better and improved TSS algorithms in coastal waters that are not simply empirically based on the particular coastal region in which they were developed, but also physically grounded in the principle of radiative transfer theory where the relationship between the TSS concentration and reflectance are physically sensible.

Easy access to satellite datasets in the last decade has prompted a rapid growth in scientific studies in satellite remote sensing of TSS (Wulder, Masek, Cohen, Loveland, & Woodcock, 2012). Even by conservative estimates, around 49 MODIS and 27 Landsat based TSS algorithms were developed in the last decade for water quality monitoring (Dorji & Fearn, 2016). Since the TSS models developed in the studies collectively cover most geographical locations including America (Miller & McKee, 2004; Park & Latrubesse, 2014; Son & Wang, 2012), Africa (Ayana et al., 2015; Kutser, Metsamaa, Vahtmae, & Aps, 2007), Asia (Chen et al., 2015b; Choi et al., 2014; Islam, Yamaguchi, & Ogawa, 2001), Australia (Evans et al., 2012; Islam et al., 2007), and Europe (Hudson et al., 2014; Petus et al., 2014; Raag et al., 2013; Sipelgas, Raudsepp, & Kõuts, 2006) one is begged to ask if we can use 'off the shelf' TSS models in mapping the coastal waters of different geographical regions without having the need to invest in expensive field campaigns to develop a regional TSS model. Confidence in the applicability of already developed TSS models to different regions would considerably help in cutting the costs for coastal water quality management.

From the perspective of coastal water quality monitoring by environmental protection agencies via satellite remote sensing, the availability of numerous satellites does present an unparalleled capability in mapping TSS concentration at high spatiotemporal resolution, but the use of varied satellite sensors also presents the complexities of using different satellite sensors with different spatial, spectral and radiometric characterization (Ody et al., 2016). It has been observed in previous studies (Miller, Liu, Buonassissi, & Wu, 2011; Ody et al., 2016) that use of different satellite sensors in mapping the TSS concentration of coastal waters

produces different TSS results for the same region which is partly due to the different spatial resolution of the respective satellite sensors and the turbidity gradient of the water itself. Thus, a study of the variability of the TSS concentration produced by different satellite sensors with different spatial resolutions and radiometric characteristics in very turbid waters (e.g. dredge and river plumes in coastal waters) for effective compliance monitoring of coastal water quality is warranted.

The potential of low earth orbiting satellite sensors, such as the Landsat series, MODIS-Aqua and MODIS-Terra among other sensors has proved their significance in monitoring the quality of global waters at spatial and temporal resolutions that are adequate to discern the seasonal or daily temporal dynamics in water quality. However, in coastal environments where temporal dynamics of water quality changes within an hour or less depending on the tidal and locally wind driven currents (Thompson et al., 2011), the potential of low earth orbiting satellite sensors with low temporal resolution to effectively monitor the temporal dynamics of coastal waters is limited. Previous studies using the European Union's meteorological satellite (EUMETSAT) (Neukermans, Ruddick, & Greenwood, 2012; Salama & Shen, 2010) and the South Korean geostationary ocean colour imager (GOCI) satellite (Choi et al., 2014; Doxaran et al., 2014; Huang et al., 2015) have shown the potential of using a high temporal resolution sensor (numerous images per day) in discerning the diurnal variability of water quality in coastal waters from daily or seasonal variations. The availability of a high temporal resolution (10 mins for a full disk) sensor, the Advanced Himawari Imager (AHI), on board the Japanese Meteorological satellite, Himawari-8, over the Australian waters with spectral bands in the visible, NIR and SWIR regions provides the potential for mapping the daily temporal dynamics of Australian coastal water quality. Thus, the development of TSS algorithms for Himawari-8 and studying the feasibility of mapping the TSS concentrations in coastal waters in Western Australia is also needed to take advantage of this new geostationary satellite in the region.

1.3 Research objectives and significance

The main objective of this thesis is to develop a satellite based remote sensing TSS algorithm for the highly turbid coastal waters of Western Australia and to demonstrate its application to coastal water quality monitoring. Further, quantitatively and qualitatively assess existing TSS algorithms for their applicability in coastal water quality monitoring of the northern Western Australian coastal waters. In specifics, the objectives of this study are to:

- Develop a regional TSS model that is physically based on radiative transfer theory to map TSS concentration in the turbid waters of northern Western Australia;
- Quantitatively assess and identify robust TSS algorithms that have been developed in the last decade for MODIS and Landsat based sensors to study the cross-applicability of the TSS algorithms in optically unknown water types;
- Study the impact of spatial resolution of different satellite sensors in quantification of TSS concentration in turbid waters and the implications for coastal water quality monitoring, and;
- Study the feasibility of the new generation geo-stationary Himawari-8 satellite in monitoring TSS concentration in coastal waters of northern Western Australia.

The significance of the research outcomes lies in the development of a semi-analytical TSS algorithm for any satellite sensor with either a red or NIR band to estimate TSS concentration. In particular, to estimate TSS concentration for the turbid coastal waters of northern Western Australia where large dredging activities have been carried out recently and the need for high spatiotemporal water quality monitoring is needed to study the impact of such dredging activities. Further, the identification of the best performing TSS algorithms from existing Landsat and MODIS sensors in the last decade provides coastal managers and remote sensing scientists the ability to select appropriate algorithms for use in determining water quality with some level of confidence for optically unexplored waters. In addition, the

results on the effect of different spatial resolutions of different satellite sensors in the quantification of TSS concentration can also aid in informing coastal managers on the possible implication of using different satellite sensors for coastal water quality monitoring. Finally, the significance of this research also lies in showing that the Himawari-8 satellite sensor, AHI, can be used in monitoring the TSS concentration over Western Australian waters at high temporal scales to discern diurnal TSS dynamics with daily or seasonal TSS variations.

1.4 Thesis outline

This thesis comprises seven chapters, with Chapters 3 to 6 structured as self-contained scientific journal papers. The articles reproduced in Chapters 3, 4 and 5 are already published in peer-reviewed remote sensing journals (Dorji & Fearn, 2016, 2017; Dorji, Fearn, & Broomhall, 2016) while the article reproduced in Chapter 6 is submitted and in review in a peer reviewed journal (see Table 1.1 for a summary of the publications). This chapter, Chapter 1, provides a general introduction and background, including the objectives and significance of this study. Chapter 2 presents a general overview of radiative transfer principles relevant to the remote sensing of ocean colour with a particular emphasis on TSS estimation. In addition, Chapter 2 also provides a current state-of-the-field in estimation of TSS concentration via satellite remote sensing in coastal waters. The main focus of Chapter 3 is the development of a TSS algorithm for the coastal waters of Western Australia using the MODIS-Aqua sensor with the aim to use the developed TSS algorithm in a study of the spatiotemporal pattern of TSS concentration in coastal waters of northern Western Australia. Chapter 4 quantifies the existing TSS algorithms from the last decade for MODIS and Landsat based sensors with the objective to identify the most robust TSS model(s) with respect to being used in mapping TSS concentration in optically unknown water types. The advantages and limitations of using multiple satellite sensors with different spatial resolutions in estimation of TSS concentration in coastal waters are presented in Chapter 5. Chapter 6 investigates the feasibility of the geo-stationary sensor AHI on board the

Himawari-8 satellite in estimation of TSS concentration of coastal waters of northern Western Australia. Finally, Chapter 7 presents the conclusions and general implications of this study in water quality monitoring of coastal waters of Western Australia and future directions of TSS estimation via satellite remote sensing as perceived from this study.

Table 1.1: Summary of thesis chapters

Chapter	Title	Summary
1	Introduction	General background on remote sensing of TSS concentration, and objectives and significance of this research study.
2	Literature Review	Literature review of TSS estimation using different satellite sensors
3	A semi-analytic model for estimating total suspended sediment concentration in coastal waters: a case study in coastal waters of Western Australia using MODIS 250 m data (Dorji et al., 2016).	Discusses the development of a semi-analytic TSS model for the MODIS-Aqua sensor and the application of the TSS model in regional waters of northern Western Australia. <i>Published in Remote Sensing 2016, 8, 556.</i>
4	A Quantitative Comparison of Total Suspended Sediment Algorithms: A Case Study of the Last Decade for MODIS and Landsat-based Sensors (Dorji & Fearn, 2016).	Identifies robust TSS model(s) from TSS models published in the last ten years for MODIS and Landsat sensors using comprehensive statistical tests and simulations. <i>Published in Remote Sensing 2016, 8(10), 810.</i>
5	Impact of the Spatial Resolution of Satellite Remote Sensing Sensors in Quantification of Total Suspended Sediment Concentration: A Case Study in the Sediment Plume of the Waters in northern Western Australia (Dorji & Fearn, 2017).	Studies the impact of different spatial resolutions of satellite sensors in TSS estimation and discusses possible implications for coastal water quality monitoring. <i>Published in PLoS One 2017, 12(4), e0175042.</i>
6	Mapping Total Suspended Sediment in Near Real Time: A preliminary Assessment of the AHI sensor on board the geostationary Himawari-8 satellite for Coastal Waters of Western Australia (Dorji & Fearn, 2017 [unpublished]).	Explores the possibility of using Himawari-8, a meteorological geostationary satellite sensor, in TSS estimation for coastal waters of Western Australia. <i>Submitted to Remote Sensing of Environment 2017.</i>
7	Conclusion and Future Perspectives	Summary of findings from this study and perspectives on the further work.

Chapter 2

Literature Review

2.1 Overview

The literature review in this chapter is supplemented by the respective introductory sections of the papers reproduced in Chapters 3-6. Therefore, this literature review will be brief and focus on the details that are not explicit in the contents of Chapters 3-6. In particular, this chapter reviews the past and current work carried out in mapping TSS concentration in coastal waters, with greater emphasis paid to the limitations and challenges of the current state of satellite based TSS remote sensing. In addition, this chapter also describes in brief the propagation of light in water and how it is affected by different constituents present in water and the water surface itself. Specifically, Section 2.2 discusses the general radiative transfer theory used in quantification of different water constituents from a water column while the Section 2.3 discusses the major water constituents that affect the water quality and their implication on the remote sensing of TSS. The various satellite sensors used in mapping of TSS concentration are presented in Section 2.4 with Section 2.5 focusing on the past and the current TSS models used in estimation of TSS concentration via satellite based remote sensing. Finally, Section 2.6 presents the current gaps and limitations in the field of TSS mapping via satellite remote sensing.

2.2 Radiative Transfer Theory and optical properties of the water column

This section presents the theoretical framework, the fundamentals and the radiometric and geometric units used in radiative transfer theory related to the understanding of light propagation in the water column. The various optical properties of a water body that relate to the remote sensing of ocean colour are also described in this section.

2.2.1 Radiometric quantities in remote sensing

Figure 2.1 shows the configuration of the geometry used in the definition of the radiometric quantities in this chapter. The spectral radiance (L), a fundamental radiometric quantity, is operationally defined in Mobley (2001) as the amount of incident radiant energy (ΔQ) produced by photons in a wavelength range ($\Delta\lambda$) centred at λ that is incident on a surface of area (ΔA) located at point (x, y, z) in space at time (t) within the time interval (Δt) at a solid angle ($\Delta\Omega$) through direction (θ, φ) :

$$L(x, y, z, t, \theta, \varphi, \lambda) \equiv \frac{\Delta Q}{\Delta t \Delta A \Delta \Omega \Delta \lambda} \quad [\text{Js}^{-1}\text{m}^{-2}\text{sr}^{-1}\text{nm}^{-1}] \quad (2.1)$$

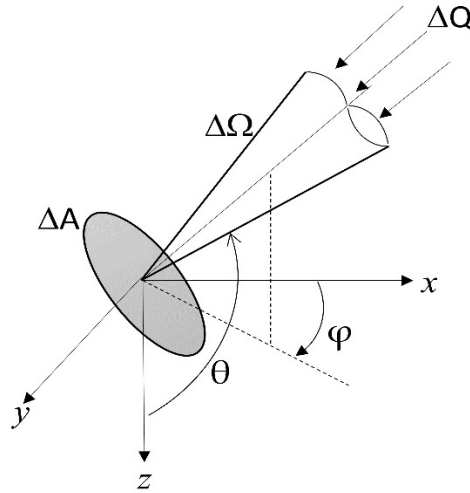


Figure 2.1: Geometry used to define radiance (note: image reproduced from Figure 1 of Mobley (2001))

Form an infinitesimal L , Equation (2.1) can be rewritten as:

$$L(x, y, z, t, \theta, \varphi, \lambda) \equiv \frac{\partial^4 Q}{\partial t \partial A \partial \Omega \partial \lambda} \quad [\text{Js}^{-1}\text{m}^{-2}\text{sr}^{-1}\text{nm}^{-1}] \quad (2.2)$$

For the oceanographic application, we can assume the optical properties of water and L are homogenous in the lateral direction and independent of t . This allows the multi-dimensional L in Equation (2.2) to be reformulated as a 1-dimensional $L(z, \theta, \varphi, \lambda)$. Even though L defined by Equation (2.2) can completely describe the light field, L at all angles are typically not measured due to the practicalities of instrumental limitations. Thus, the commonly measured radiometric quantities are various irradiances (E), such as spectral

upwelling scalar irradiance (E_o), upwelling vector irradiance (E_u), downwelling scalar irradiance (E_{od}) and downwelling vector irradiance (E_d).

An upward facing hemispherical detector sensitive to photons of wavelength λ from any direction (θ, φ) and located at depth z can collect all the photons travelling downward. The output of such a detector is the spectral downwelling scalar irradiance ($E_{od}(z, \lambda)$) at depth z . The $E_{od}(z, \lambda)$ can be related to $L(z, \theta, \varphi, \lambda)$ by:

$$E_{od}(z, \lambda) = \int_{2\pi_d} L(z, \theta, \varphi, \lambda) d\Omega \quad [\text{Wm}^{-2}\text{nm}^{-1}] \quad (2.3)$$

Here $2\pi_d$ denotes the hemisphere of the downward direction for the set of directions (θ, φ) such that $0 \leq \theta \leq \pi/2$ and $0 \leq \varphi \leq 2\pi$, if θ is measured from $+z$ or the nadir direction. Consequently, the output from the same instrument facing downward is the spectral upwelling scalar irradiance ($E_{ou}(z, \lambda)$) which measures the upwelling photons towards the ocean surface. Then the total spectral scalar irradiance ($E_o(z, \lambda)$) is sum of $E_{od}(z, \lambda)$ and $E_{ou}(z, \lambda)$ as defined by Equation (2.4).

$$E_o(z, \lambda) \equiv E_{od}(z, \lambda) + E_{ou}(z, \lambda) = \int_{4\pi} L(z, \theta, \varphi, \lambda) d\Omega \quad [\text{Wm}^{-2}\text{nm}^{-1}] \quad (2.4)$$

There are also planar detectors that are designed such that the sensitivity of the detector is proportional to $|\cos \theta|$, where θ is angle between the normal of the surface collector of area ΔA and direction of the incident photons. If such a detector is placed at depth z , collecting downward travelling photons, then the output of such a detector is directly proportional to the spectral downwelling plane, or vector, irradiance $E_d(z, \lambda)$. Such an instrument would be collecting downwelling L weighted by $|\cos \theta|$:

$$E_d(z, \lambda) = \int_{2\pi_d} L(z, \theta, \varphi, \lambda) |\cos \theta| d\Omega \quad [\text{Wm}^{-2}\text{nm}^{-1}] \quad (2.5)$$

Positioning this cosine dependent detector in the downward facing direction would then collect the upwelling photons and its output would give spectral upwelling plane, or vector, irradiance $E_u(z, \lambda)$. Such radiometric quantities are useful in remote sensing because they give energy flux per unit area in a horizontal surface at any depth.

2.2.2 IOP and AOP

The bulk or the large scale optical properties of water are classified into AOPs and IOPs. The AOPs are those optical properties of water which depend both on the medium and geometrical structure of the ambient light field while the IOPs only depend on the medium (Mobley, 1994).

Common IOPs used in radiative transfer theory are total absorption ($a(\lambda)$) and total scattering ($b(\lambda)$) coefficients as defined by Equations (2.6) and (2.7) respectively:

$$a(\lambda) = \lim_{\Delta r \rightarrow 0} \frac{1}{\Phi_i(\lambda)} \frac{\Phi_a(\lambda)}{\Delta r} \quad [\text{m}^{-1}] \quad (2.6)$$

where $\Phi_i(\lambda)$ (W nm^{-1}) is the spectral radiant power from monochromatic light of wavelength λ and $\Phi_a(\lambda)$ is amount of $\Phi_i(\lambda)$ absorbed by the volume of water column with thickness Δr .

$$b(\lambda) = \int_{4\pi} \beta(\psi, \lambda) d\Omega = 2\pi \int_0^\pi \beta(\psi, \lambda) \sin \psi d\psi \quad [\text{m}^{-1}] \quad (2.7)$$

where $\beta(\psi, \lambda)$ ($\text{m}^{-1} \text{sr}^{-1}$) is the volume scattering function which is a measure of the fraction of incident power $\Phi_i(\lambda)$ scattered at an angle ψ into a solid angle $\Delta\Omega$. The total attenuation coefficient ($c(\lambda)$) of light by a volume of water column is $a(\lambda) + b(\lambda)$. The $b(\lambda)$ in Equation (2.7) is divided into two parts: the forward scattering coefficient ($b_f(\lambda)$) is scattered at an angle $0 \leq \psi \leq \pi/2$ and the backward scattering coefficient ($b_b(\lambda)$) is scattered at an angle $\pi/2 \leq \psi \leq \pi$. Thus, $b_b(\lambda)$ is defined as:

$$b_b(\lambda) = 2\pi \int_{\pi/2}^\pi \beta(\psi, \lambda) \sin \psi d\psi \quad [\text{m}^{-1}] \quad (2.8)$$

The water column consists of pure water molecules (W) and other water constituents such as, organic and inorganic particulate matter, algal and non-algal matter, detrital matter and phytoplankton pigments (Prieur & Sathyendranath, 1981). Thus, the IOPs of the water column are a cumulative sum of absorption and scattering from all the water constituents. However, for simplicity and the general application in remote sensing, the IOPs are attributed to only optically active water constituents, such as CDOM, particulate matter (P) and CHL(ϕ). Equations (2.9) - (2.11) list the

contribution of active water constituents that are significant contributors to $a(\lambda)$, $b(\lambda)$ and $b_b(\lambda)$:

$$a(\lambda) = a_w(\lambda) + a_p(\lambda) + a_{\text{CDOM}}(\lambda) + a_\varphi \quad (2.9)$$

$$b(\lambda) = b_w(\lambda) + b_p(\lambda) + b_\varphi(\lambda) \quad (2.10)$$

$$b_b(\lambda) = b_{bw}(\lambda) + b_{bp}(\lambda) + b_{b\varphi}(\lambda) \quad (2.11)$$

Commonly used AOPs in remote sensing are irradiance reflectance ($R(z, \lambda)$), remote-sensing reflectance ($R_{rs}(\theta, \varphi, \lambda)$) and the diffuse attenuation coefficient for downwelling light ($K_d(z, \lambda)$) as defined in Equations (2.12) - (2.14) respectively.

$$R(z, \lambda) = \frac{E_u(z, \lambda)}{E_d(z, \lambda)} \quad [\text{unit-less}] \quad (2.12)$$

$$R_{rs}(\theta, \varphi, \lambda) = \frac{L_w(0^+, \theta, \varphi, \lambda)}{E_d(0^+, \lambda)} \quad [\text{sr}^{-1}] \quad (2.13)$$

$$K_d(z, \lambda) = \frac{1}{E_d(z, \lambda)} \frac{dE_d(z, \lambda)}{dz} \quad [\text{m}^{-1}] \quad (2.14)$$

The $L_w(0^+, \theta, \varphi, \lambda)$ is water leaving radiance just above the water surface. The $R_{rs}(\theta, \varphi, \lambda)$ essentially just describes the irradiance reflectance just above the water surface per unit solid angles, more commonly known as remote sensing reflectance. The $K_d(z, \lambda)$ is the decrease in the ambient downwelling irradiance as a function of depth (z).

The evaluation of $R(z, \lambda)$ and $R_{rs}(\theta, \varphi, \lambda)$ just beneath the water surface are also important in remote sensing because these AOPs can be related to the IOPs of the water column to study the bio-geochemical properties of the water column (Gordon et al., 1988; Mobley, 2001). The $R_{rs}(\theta, \varphi, \lambda)$ evaluated just beneath the water surface is called the sub-surface remote-sensing reflectance $r_{rs}(\theta, \varphi, \lambda)$ as defined in Equation (2.15):

$$r_{rs}(\theta, \varphi, \lambda) = \frac{L_w(0^-, \theta, \varphi, \lambda)}{E_d(0^-, \lambda)} \quad [\text{sr}^{-1}] \quad (2.15)$$

The $r_{rs}(\theta, \varphi, \lambda)$ is proportional to the first order approximation of the IOPs term ($b_b(\lambda) / (a(\lambda) + b_b(\lambda))$) of the water column (Gordon et al., 1988; Lee, Carder, & Arnone, 2002).

2.2.3 Linking IOPs and AOPs through a Radiative Transfer Equation

The equation that relates the IOPs and radiance (L) is termed a radiative transfer equation (RTE). Even in the simplest case, ignoring the t dependency and the horizontal gradient of the water body, the RTE is a complex integro-differential equation (Mobley, 2001):

$$\cos\theta \frac{dL(z,\theta,\varphi,\lambda)}{dz} = -c(z,\lambda)L(z,\theta,\varphi,\lambda) + \int_{4\pi} L(z,\theta',\varphi',\lambda) \times \beta(z;\theta',\varphi' \rightarrow \theta,\varphi;\lambda) d\Omega' + S(z,\theta,\varphi,\lambda) \quad (2.16)$$

where ψ in $\beta(\psi,\lambda)$ is an angle between the incident (θ', φ') and the scattered (θ, φ) direction of photons with wavelength λ . The $S(z, \theta, \varphi, \lambda)$ term accounts for the bioluminescence and inelastic scattering from photons with other wavelengths. Due to the complexity of solving the RTE analytically even in its simplest form, accurate solutions of the RTE are acquired using numerical approaches such as Monte Carlo, or Invariant Imbedding methods used by HydroLight simulations (Mobley et al., 1993). Approximate solutions are obtained using approximate analytical solutions such as single-scattering approximations or quasi-single-scattering approximations (Gordon & Wang, 1994b).

The semi-analytic relationship by Gordon et al. (1988) which relates $R(\lambda)$ to the IOPs of water at different solar zenith angles (θ_s) forms the basis in this thesis for remote sensing of TSS from satellite sensors, discussed in detail in Chapter 3. From Gordon et al. (1988) and Lee et al. (2002), $a(\lambda)$ and $b_b(\lambda)$ are directly related to $R(\lambda)$, and $R(\lambda)$ is approximately equivalent to $r_{rs}(\lambda)$ as follows:

$$r_{rs}(\lambda) \approx \frac{R(\lambda)}{Q(\lambda)} = \sum_{i=1}^2 g_i \left(\frac{b_b(\lambda)}{a(\lambda) + b_b(\lambda)} \right)^i \quad (2.17)$$

where $Q(\lambda)$ equals π for a totally diffuse radiance distribution and in the range of 4 to 5 for L distributions observed in nature. The coefficient $g_1 = 0.0949$ and $g_2 = 0.0794$ for Case-1 waters, generally open ocean waters (Gordon et al., 1988) and $g_1 = 0.084$ and $g_2 = 0.17$ (Lee et al., 2002) for Case-2 water, coastal and inland waters.

2.3 Water quality and optically active water constituents

Technically, there is no one single definition for the term “water quality”, the water quality is a relative term used to express the suitability of

water for particular purpose or processes (Bartram & Ballance, 1996). The water quality can be assessed through the measurement of change in the concentration of water constituents before and after the impact of anthropogenic or natural processes. In marine remote sensing, the water quality is synonymous with the measure of 'water clarity' or 'transparency' which can be directly related to the water constituents present in the water bodies (Gholizadeh, Melesse, & Reddi, 2016). From the perspective of coastal water quality monitoring via satellite remote sensing, the optically active water quality parameters measured include CHL concentration (Brando & Dekker, 2003; Giardino et al., 2014; Hu et al., 2004; Jutla et al., 2012; Koponen et al., 2007; Koponen, Pulliainen, Kallio, & Hallikainen, 2002; Östlund, Flink, Strömbeck, Pierson, & Lindell, 2001; Teodoro et al., 2008; Tilstone et al., 2013; Tzortziou et al., 2006; Wu, Zhang, Wang, & Luo, 2009), CDOM concentration (Brezonik, Menken, & Bauer, 2005; Keith, Lunetta, & Schaeffer, 2016; Kutser et al., 2005; Loisel et al., 2014b; Slonecker, Jones, & Pellerin, 2016; Tiwari & Shanmugam, 2011) and TSS concentration (Chen et al., 2014a; Lim et al., 2013; Miller & McKee, 2004; Ody et al., 2016; Ondrusek et al., 2012; Wang, Zhou, Xu, Song, & Wang, 2009a; Wang & Lu, 2010; Zhou et al., 2006). There are also other parameters, such as total nitrogen, ammonium nitrogen, and dissolved phosphorus, among others, which affect the water quality besides the aforementioned optically active water constituents (Gholizadeh et al., 2016). However, due to the low variation in the optical signature (low signal to noise ratio) of non-optically active water constituents they are not used as often as the optically active water constituents in water quality monitoring via satellite remote sensing.

CHL or (Chl-a) is a photosynthetic pigment common to all phytoplankton species (Bissett, Patch, Carder, & Lee, 1997) which is used as a water quality indicator in Case-1 waters because phytoplankton are the predominant water constituents compared to other optically active water constituents, such as CDOM and TSS (Gurlin, Gitelson, & Moses, 2011; Matthews, 2011). In Case-1 waters, the optical properties of water co-vary with the phytoplankton concentration, predominantly with Chl-a concentration, which absorbs light in all regions of the EMS, but strongly

reflects light in the green wavelengths (Gurlin et al., 2011). However Case-2 waters are more optically complex than Case-1 waters because of the presence of other optically active water constituents such as CDOM and TSS as well as CHL (Gordon & Morel, 1983). Further, in Case-2 waters the spectral reflectance is influenced by the absorption and scattering from all active water constituents and the optical properties of Case-2 waters do not necessarily co-vary with CHL concentration, thereby making Case 2 waters more complex than Case-1 waters.

CDOM, commonly referred as a gelbstoff or yellow substance, comprises dissolved matter, such as marine phytoplankton (humic) and land based organic matter (fulvic) acids (Loisel, Vantrepotte, Dessailly, & Mérieux, 2014a; Nebbioso & Piccolo, 2013). The CDOM in Case-1 waters usually originates from the degradation of dead phytoplankton and zooplankton while in Case-2 waters the major contributor is degraded terrestrial organic matter from river and land runoff (Boss, Pegau, Zaneveld, & Barnard, 2001; Vantrepotte et al., 2007). In coastal waters, CDOM is a major contributor to the absorption of light in the blue region of the EMS which has significant impact on the ocean colour remote sensing (Boss et al., 2001; Bricaud, Morel, & Prieur, 1981). Further, the increasing absorption of CDOM in the blue region of the EMS has impact on the estimation of CHL concentration from remote sensing because CHL algorithms are depended on the blue and green regions of the EMS (Carder et al., 1991). It has been shown by (Carder et al., 1991) that CDOM can positively bias the estimation of CHL concentration using ocean colour remote sensing by as much as 113% in a region dominated by CDOM (Hubert, Lubac, Dessailly, Duforet-Gaurier, & Vantrepotte, 2010).

The water constituent of interest in this literature review is TSS. Suspended sediments are of two types: organic (detritus and phytoplankton) and inorganic (minerals) matter (Kjelland, Woodley, Swannack, & Smith, 2015). TSS by definition is the mass of the suspended particulate matter that is left after a sample of water is filtered, then the filter has been dried and weighed. For the operational distinction between dissolved matter and TSS, the particles that are smaller than 0.2 μm are considered as dissolved matter

while particle greater than 0.2 μm are considered particulate fractions (Steven, Pantus, Brooks, & Trott, 1998). However, for the practical purpose, depending on the particle loading, any TSS is quantitatively measured in unit weight of dry weight of suspended solids in per volume of water (mg/L) that are retained after filtering through a 0.7 μm Whatman glass-fiber filter (GF/F) (Chavez et al., 1995). TSS consists of pigments and cell matter, dead organic matter, and minerals and it is synonymous with Suspended Sediment Concentration (SSC) and Suspended Particulate Matter (SPM) (Binding, Bowers, & Mitchelson-Jacob, 2005; Ouillon et al., 2008). The TSS absorbs or scatters light depending on the amount of organic and inorganic particles present in its total mass, but generally the organic components (pigments and dead organic matter) all strongly absorb light while minerals strongly scatter light (Matthews, 2011).

2.4 Satellite Sensors used in TSS Mapping

Space-borne or satellite-based remote sensing occurs from outside of earth's atmosphere using either a geosynchronous, sun-synchronous or polar orbit at heights ranging from several hundred (low earth orbit) to thousands of kilometres (high earth orbit). The launch of the first satellite (Earth Resources Technology Satellite 1 (Landsat 1)) for environmental monitoring of earth resources by the U.S Geological Survey and NASA on July 23, 1972 has led to interest in mapping TSS from space (Kim, 1980). The earliest of the studies by Klemas, Borchardt, and Treasure (1973) and Bowker, Fleischer, Gosink, Hanna, and Ludwich (1973) of the space-borne sensors used in mapping TSS includes the use of radiance (L) of multispectral channels from Landsat-1 to correlate to TSS concentration. Since then numerous studies from across the globe have been carried out using different satellite sensors based on the needs and the general requirement of the study.

The most common low earth orbiting satellite sensors used in mapping TSS concentration and currently operational are Landsat-7 and 8 (Kallio et al., 2008a; Wu et al., 2008; Zhou et al., 2006), MODIS-Aqua and MODIS-Terra (Chen et al., 2007; Doxaran, Froidefond, Castaing, & Babin,

2009; Miller & McKee, 2004) and MERIS (Kratzer et al., 2008; Odermatt et al., 2008). The historical Landsat satellite sensors, despite the low signal-to-noise ratios (SNR) and radiometric properties not suitable for ocean colour application, were still used in ocean colour applications because of the availability of long time series data to study the historical trends in TSS. The Landsat-8 OLI sensor in use today consists of improved SNR and radiometric characteristics with spatial resolution of 30 m in all visible bands except the panchromatic band (15 m) and spectral bands suitable for regional mapping of TSS (Olmanson, Bauer, & Brezonik, 2008; Onderka & Pekárová, 2008). However, the repeat cycle of 16 days and high probability of cloud coverage makes Landsat-8 OLI data not suitable for rapid change detection applications (Chen et al., 2007). The MODIS sensors on board Terra (EOS AM) and Aqua (EOS PM) satellites cover most parts of earth every 1 to 2 days and offers a near real time coverage. The MODIS band 1 (620-670 nm) and band 2 (841-876 nm) are more commonly used to map TSS in coastal waters because of their spatial resolution of 250 m compared to the remaining visible bands which have lower spatial resolution (1 km) (Chen et al., 2007; Miller & McKee, 2004). In addition, the free accessibility of MODIS and Landsat data makes them more appealing to researchers to develop regional algorithms to estimate TSS.

Other low earth orbiting satellite sensors used in mapping TSS in coastal water bodies include SPOT (Doxaran et al., 2002), MERIS (Kratzer et al., 2008), IKONOS (Ekercin, 2007), EO-1 Hyperion (Giardino, Brando, Dekker, Strömbeck, & Candiani, 2007), Indian Remote Sensing (IRS) (Mabwoga, Chawla, & Thukral, 2010), Huan Jing (HJ)-1A/B (Chen et al., 2014a) and Thailand Earth Observation System (THEOS) (Lim et al., 2013). The SPOT High Resolution Visible (HRV) data, available in three wave bands, 500-590 nm, 610-680 nm, and 790-890 nm, was found to correlate well with TSS. However, caution must be exercised while using SPOT data due to its coarse 70 nm spectral resolution (Dekker, Vos, & Peters, 2002). The availability of data in visible and NIR channels with a spatial resolution of 5.8 m and repeat cycle of 5 days makes the IRS Linear Imaging Self Scanner (LISS) IV sensor suitable to study water clarity of coastal waters.

Observation by Mabwoga et al. (2010) showed strong correlation between data from the NIR band and TSS in wetlands in India using the IRS LISS IV satellite. The Chinese disaster monitoring and forecasting satellite (HJ-1A/B) has a revisit time of 2 days with similar spectral bands (430-520nm, 520-600nm, 630-690nm, and 760-900nm) and spatial resolution (30 m) to Landsat TM which makes it more appealing in the study of TSS. Chen et al. (2014a) showed that HJ-1A data can be used to derive TSS from turbid coastal water with reasonable uncertainty (< 29%) provided that an appropriate atmospheric correction method is available. THEOS has the required spectral bands (450-520 nm, 530-600 nm, 620-690 nm, and 770-900 nm) with spatial resolutions of 15 m for the first three bands and 2 m for the last band. Lim et al. (2013) and Asadpour, Lim, Alashoo, and Mousavi (2012) have demonstrated the applicability of THEOS imagery in estimating TSS from coastal waters. The hyperspectral sensors, Hyperion, and very high spatial resolution sensors, WorldView 2-4 also have the capability to map TSS with greater accuracy and move away from localized algorithms Giardino et al. (2007). The capability of hyperspectral imagery to shift beyond empirical based algorithms to map water quality is demonstrated by Giardino et al. (2007) using Hyperion imagery, however, the limited accessibility of such data restricts its wider applicability. From the aforementioned TSS studies, the general consensus is that the selection of an appropriate satellite sensor for the water quality monitoring is generally dictated by the specific requirements of the task and the availability of the specific bands at the required spectral, temporal and spatial resolutions.

High earth orbiting geostationary satellites are designed particularly for meteorological purposes, but in the last decade, the geostationary satellites with visible and NIR bands have been found feasible in the study of water quality (Ruddick, Neukermans, Vanhellemont, & Jolivet, 2014). The geostationary satellite sensors that are currently used in the study of TSS are SEVIRI on the METEOSAT second generation platform and Geostationary Ocean Colour Imager (GOCI) on board the South Korean communication, ocean and meteorological satellite (COMS). The sensors on board the geostationary satellites do not have the high spectral resolutions of the low

earth orbiting satellite sensors but, the studies (Choi et al., 2014; He et al., 2013; Huang et al., 2015; Neukermans et al., 2009; Salama & Shen, 2010; Vanhellemont, Neukermans, & Ruddick, 2014) have shown that the geostationary satellite sensors are capable of quantitatively mapping TSS concentration in coastal waters at high temporal resolution. The GOCI, which is the first geostationary satellite sensor with designated ocean colour bands in the visible and NIR region with spatial resolution of 500 m and capable of collecting 8 images per day, has been used to study TSS concentrations in Korean and neighbouring waters (Choi et al., 2014; Doxaran et al., 2014; Huang et al., 2015). Choi et al. (2014) found that R_{rs} derived from GOCI band 5, centred at 660 nm, had a high regression coefficient ($R^2 = 0.93$) with TSS concentrations and *in situ* validation of their results also produced a high correlation coefficient ($R^2 = 0.85$). Since the feasibility study by Neukermans et al. (2009) on using the Meteosat's SERIVI sensor in estimating TSS concentration, further studies (Neukermans et al., 2012; Vanhellemont et al., 2014) have been conducted thereafter. Neukermans et al. (2009) showed that SERIVI, with a temporal resolution of 15 minutes, was able to retrieve TSS in the Southern North Sea and SERIVI- derived TSS correlated strongly ($R^2 = 0.83$) with MODIS-Aqua derived TSS in highly turbid waters but displayed high uncertainty (relative error ~ 39-100%) in clearer waters. The satellite sensors that are currently operational and that have the potential to map TSS concentration are listed in Table 2.1 with their spatial resolution, spectral bands and bandwidths, and temporal characteristics.

Table 2.1: List of satellite sensors currently operational with the potential to map TSS concentration

Satellite (Sensor)	Launch Year – Life span	Spectral Bands (range (in nm))	Spatial Resolution	Temporal Resolution
Resourcesat-2A (LISS IV)	2016 – 5 years	3 (520 – 860)	5.8	5 days
Digital Globe (WV-4) **	2016 – 12 years	5 (450 – 920)	0.31 – 3.51 m	1 – 4.5 days
Sentinel-3A & B (OCLI) ***	2016 (17) – 7 years	21 (400 – 1020)	300 m	2 days
Sentinel-2A & B (MSI) ***	2015 (17) – 7.25 years	13 (433 – 2280)	10 – 60 m	5 days with 2 satellites
TH-01 (MSI)	2015 – 3 years	5 (430 – 900)	2 – 10 m	5 days
Meteosat-11 (SEVIRI) *	2015 – 7 years	12 (3.9 – 13400)	1000 – 3000 m	Every 15 minutes for full disk
Himawari-8 & 9 (AHI) *	2014 (16) – 8 years	16 (430 – 13400)	500 – 2000 m	Every 10 minutes for full disk
ALOS-2 (AVNIR-2) **	2014 – 7 years	5 (420 – 890)	2.5 – 10 m	14 days
SPOT-7 (MSI)**	2014 – 10 years	5 (455 – 890)	1.5 – 6 m	1 day
NOAA (WV3) **	2014 – 7.25 years	17 (400 – 2365)	0.31 – 3.7 m	1 – 4.5 days
Landsat-8 (OLI) ***	2013 – 5 years	8 (433 – 2300)	15 – 30 m	16 days
SPOT-6 (MSI) **	2012 – 10 years	5 (455 – 890)	1.5 – 6 m	1 day
Resourcesat-2 (LISS-IV)	2011 – 5 years	3 (520 – 860)	5.8 m	5 days
COMS (GOCI)*	2010 – 7.7 years	8 (402 – 885)	500 m	10 acquisition / day
Digital Globe (WV-2) **	2009 – 13 years	9 (450 – 1040)	0.46 – 1.85 m	1.1 days
GeoEye (Geoeye-1)	2008 – 7+ years	5 (450 – 920)	0.41 – 1.65	< 3 days
Digital Globe (WV-1) **	2007 – 13 years	9 (400 – 1040)	0.5 m	1.7 days
Terra-EOS-PM (MODIS) ***	2002 – 6 years	36 (405 – 11650)	250 – 1000 m	1 – 2 days
EO-1 (Hyperion) ***	2000 – 1 year	242 (350 2570)	30	16 days
EO-1 (ALI) ***	2000 – 1 year	10 (433 – 2350)	10-30 m	16 days
Landsat-7 (ETM+) ***	1999 – 5 years	8 (450 – 2350)	15 – 30 m	16 days
Terra (ASTER) ***	1999 – 6 years	14 (520 – 11650)	15 – 90 m	16 days
Terra-EOS-AM (MODIS) ***	1999- 6 years	36 (405 – 14385)	250 – 1000 m	1 – 2 days

* Geostationary satellite, ** Commercial satellite, *** Satellite data that can be acquired at free of costs

LISS = Linear imaging Self Scanner, WV = World View, OLCI = Ocean and Land Colour Instrument, MSI = Multi-Spectral Imager, SEVIRI = Spinning Enhanced Visible and InfraRed Imager, COMS = communication, Ocean and Meteorological Satellite, AHI= Advanced Himawari Imager, GOCI = Geostationary Ocean Colour Imager, AVNIR = Advanced Visible and Near Infrared Radiometer, OLI = Operational Land Imager, MODIS = MODerate resolution Imaging Spectroradiometer, ALI = Advanced Land Imager, ASTER = Advanced Spaceborne Thermal Emission and Reflection Radiometer

2.5 TSS Algorithms

Algorithms used in mapping TSS via remote sensing methods can be broadly classified into three categories—empirical, bio optical and semi-analytic models. In this section, a brief discussion of TSS models is presented for each of the three categories. More detailed descriptions of TSS models with greater emphasis on Landsat and MODIS based satellite sensors is presented in Section 4.2.

2.5.1 Empirical models

The empirical TSS models are those models that are designed solely based on empirical data and established using a statistical relationship between the reflectance (water leaving (ρ_w), R_{rs} , r_{rs} or top of the atmosphere (ρ_{toa})) and TSS concentration through a linear or non-linear regression. The empirical models are the most common models in remote sensing of TSS in coastal waters because of their simplicity and ease in design, and also because such TSS models produce better results than semi-analytic or bio-optical models when the model is tuned to a particular region (Matthews, 2011). The design and the implementation of empirical TSS models in estimating TSS concentration from satellite sensors involves the following steps:

1. The concurrent measurement of the *in situ* TSS concentrations and optical properties (reflectance and/or radiance) of the regional waters;
2. The collected *in situ* data are processed and quality controlled to form a linear and/or non-linear relationship between the TSS concentration and highly correlated optical properties, usually the reflectance (R_{rs} and ρ_w) at a specific band or combination of bands through a statistical linear or nonlinear regression analysis;
3. The established relationship between TSS concentration and optical properties, the TSS model, is validated using *in situ* validation data to assess accuracy, and;

4. The validated TSS model is applied to satellite remote sensed and atmospherically corrected or top of atmosphere measured reflectance or radiances to generate the TSS concentration.

The form of the empirical relationships between TSS concentration and reflectance are typically either linear (Ayana et al., 2015; Kaba, Philpot, & Steenhuis, 2014; Miller et al., 2011), exponential (Feng, Hu, Chen, & Song, 2014; Hudson et al., 2014; Zhang, Shi, Zhou, Liu, & Qin, 2016a), polynomial (Giardino et al., 2014; Kumar, Equeenuddin, Mishra, & Acharya, 2016; Petus et al., 2014) or power (Chu et al., 2009; Espinoza Villar et al., 2013; Sokoletsky, Yang, & Shen, 2014). The form of the empirical relationships used in deriving TSS concentrations have an implication for their accuracy because most empirical relationship do not necessarily represent the actual relationships between TSS and reflectance in reality. Further, because such relationships are often determined on the basis of the highest regression coefficient obtained when performing the regression analysis between TSS concentration and reflectance, such methods may produce a bias in the TSS model that favours either high or low turbid waters if the full spectrum of TSS values are not used in parameterizing the TSS models. For example, for low TSS concentrations in the red and NIR bands, the TSS concentration does vary linearly with reflectance, but as the TSS concentration increases the linear relationship begins to break down and reflectance saturates at higher TSS concentrations (Mobley, 1994). TSS estimated with such a linear relationship would underestimate TSS concentration in highly turbid waters. Thus, in designing TSS models, it is important to sample waters that are representative of the full range of turbidity values in the region and select an appropriate form to generate an empirical relationship. In the case of high turbidity over a specific region, the studies by Feng et al. (2014) and Chen et al. (2015a) have shown that the use of different TSS models, possibly a split TSS algorithm for different turbidity regimes (high or low turbid waters) gives improved results compared to one general TSS model for the whole spectrum of turbidity.

The bands used in estimation of TSS concentration in empirical models ranges from the visible to the NIR regions of spectrum. However, the

most common bands used in the TSS models in the last decade were single red (Kumar et al., 2016; Lu, Chen, Tian, & Zhang, 2014; Shi et al., 2015; Zhang et al., 2016a) and NIR (Ayana et al., 2015; Cai, Tang, & Li, 2015b; Hicks, Stichbury, Brabyn, Allan, & Ashraf, 2013; Kaba et al., 2014) bands or combinations of red and NIR bands (Chen et al., 2015a; Hudson et al., 2014; Wang, Zhou, Liu, Zhou, & Zhao, 2012). There have been studies (Härmä et al., 2001; Sawaya, Olmanson, Heinert, Brezonik, & Bauer, 2003; Wang & Ma, 2001) where different band ratios in the visible and NIR spectral regions have been used in estimation of TSS concentration by taking advantage of the phytoplankton absorption minimum near 560 nm, which makes reflectance in that band relatively sensitive to the changes in TSS concentration (Matthews, 2011). In water where the expected variation of the sediment types (particle size and refractive indices) are high over the long timescales then the use of band-ratios in the NIR and green bands and NIR and red bands are shown to be more robust than single red or NIR band TSS models (Doxaran et al., 2009).

2.5.2 Bio-optical and semi-analytical models

In the bio-optical models, the biogeochemical properties (TSS in this case) of water are derived by seeking to model the ρ_w using the IOPs of water through radiative transfer modelling (Dekker et al., 2002). However, the IOPs of water are different for different geographical locations and the limitation of optical instruments to accurately measure the IOPs of the water column limits the development of a purely analytic model. Thus, different model-based approaches are derived using radiative transfer modelling to establish a relationship between biogeochemical properties of water and the reflectance through either ‘forward’ or ‘inverse’ modelling.

In a forward model, the r_{rs} or ρ_w are derived using the *in situ* bio-optical properties of water through an approximate solution, as in Equation (2.17), or a more accurate solution is generated by solving the RTE using a range of radiative transfer models such as HydroLight (Mobley, 1994) or Monte Carlo simulations (Gordon et al., 1988). In the ‘inverse’ model, the reflectance derived by satellite sensors is used in deriving the IOPs of the water using a

range of mathematical optimization techniques such as Levenberg-Marquardt or non-linear regression methods (IOCCG, 2000) to establish an analytical relationship between reflectance and IOPs, such as a_{ϕ} and b_{bp} , which generally have well established relationships with the CHL or TSS concentrations (Matthews, 2011).

The bio-optical models are desired over empirical models because bio-optical models are physically based on the principle of RTE and have the potential to accurately estimate biogeochemical parameters if IOPs of the water column are known. The complexity and difficulty in measurement of IOPs of the water column limits the development of robust analytical models, but the use of empirical data to establish a relationship between optical properties and the concentration of the biogeochemical parameters of interest have led to the development of “semi-analytical” models. The use of semi-analytical models to estimate the TSS concentrations have gained momentum over the years from a few early studies (Dekker, Vos, & Peters, 2001; Dekker et al., 2002; Gordon et al., 1988; Lee et al., 2002) to numerous recent studies (Chen et al., 2014a; Chen, Cui, Tang, & Song, 2014b; Chen, Cui, Qiu, & Lin, 2013a; Dorji & Fearn, 2016; Han et al., 2016; Nechad et al., 2010; Shen, Zhou, Peng, & Chen, 2014). The semi-analytic TSS models reviewed here are observed to derive the TSS concentration from the satellite reflectance (R_{rs} , ρ_w or r_{rs}) using a non-linear relationship with one or more coefficients statistically derived from a regional or global *in situ* IOP dataset.

The satellite sensor bands used in bio-optical or semi-analytic models to estimate TSS concentrations in coastal waters or highly turbid waters are usually a single red band (Han et al., 2016; Katlane, Nechad, Ruddick, & Zargouni, 2013; Vanhellemont & Ruddick, 2014) or NIR band (Chen, D'Sa, Cui, & Zhang, 2013b; Kong et al., 2015b; Shen et al., 2014) or a combination of red and NIR bands (Chen et al., 2013b), because particulate matter is known to dominate the backscattering in the red and NIR bands when compared with the optical response from other biogeochemical constituents (particularly phytoplankton). However, there are also semi-analytical TSS models that use different combinations of bands in the visible and NIR

spectral regions (Zhang et al., 2016b). Use of a single red or NIR band provides a robust and TSS sensitive algorithms in turbid waters, where optical properties in those bands are dominated by suspended sediments. But in optically complex water where TSS is not necessarily a dominating constituent then the use of band combinations in the visible and NIR regions can be useful in normalizing the optical effect of other constituents in estimation of TSS concentration (Kwiatkowska & Bonekamp, 2016).

2.6 Challenges and future direction

Satellite remote sensing has proven to be more effective in mapping TSS concentration at high spatiotemporal resolution than ever possible with traditional ground based sampling methods, but satellite remote sensing of TSS (or any other biogeochemical parameter) has its limitations and challenges. The challenges for remote sensing of TSS from satellite includes inherent limitations of radiometric, temporal, spatial and spectral resolution of satellite sensors themselves, the uncertainty in the TSS model that may be the result of inadequate calibration of the model because it is physically not possible to obtain a training dataset representative of all turbidity values of the region, and atmospheric effects on the signals collected at the satellite sensor (Gholizadeh et al., 2016).

2.6.1 Satellite sensor requirements and limitations

The design of satellite sensors is guided by the specific mission requirements and their applications; therefore, different satellite sensors have different spatial, spectral band and band widths, SNR, radiometric characteristics and temporal resolutions (CARSOCRO & National Research Council, 2011). Even in open Case-1 waters, the minimum number of spectral channels needed for retrieval of a CHL pigment index, sediment detection and assessment of aerosol is five channels, three in visible bands (438 - 448 nm, 485 - 495 nm, and 550 - 565 nm) and two in the NIR bands (744 - 757 nm and 855 – 890 nm) (IOCCG, 1998). In addition to the minimum of five spectral channels, the high SNR (Noise Equivalent Radiance of $0.035 \text{ W m}^{-2} \text{ sr}^{-1} \mu\text{m}^{-1}$ or lower in the visible bands and below

0.025 in the NIR bands) and the capability to maintain the minimum required radiometric stability and adequate dynamic range to differentiate between weak L_w with those of atmospheric contributions are necessary. Further, a mechanism to avoid sensor saturation from sun glint, adequate spatial resolution (~1 km) and temporal resolution (~2-3 days) are also needed as a required minimum for satellite a sensor designed for remote sensing of open Case-1 water (IOCCG, 1998).

For coastal water quality monitoring, an additional spectral channel in the SWIR (1040 - 1240 nm) is needed as well as the minimum bands required in Case-1 waters because the non-zero reflectance in the NIR bands over the Case-2 or coastal waters due to high sediment concentration renders the atmospheric correction scheme of Case-1 waters not applicable (IOCCG, 2000). The spatial and temporal resolutions required for coastal waters are also dependent on the intended applications. For example, in coastal ocean-colour applications involving the monitoring of river and tidal plumes, spatial resolutions in the range of 30 m – 1 km and temporal resolutions of hours are needed, while general coastal water quality monitoring would require spatial resolutions of 100 m – 1 km and temporal resolutions within days (IOCCG, 2000). The current existing polar orbiting sensors with dedicated ocean colour bands are MODIS-Aqua and Modis-Terra. MODIS sensors have adequate spatial, radiometric SNR and spectral channels needed for a general coastal-water quality monitoring, but capable of providing only one image per day or combined two images per day during cloud free days. Higher temporal resolution satellite sensors with adequate spatial resolution, such as the geostationary satellite sensor GOCI with the capability of acquiring 8 images per day at 500 m spatial resolution, can effectively map the temporal dynamics of coastal waters (Choi et al., 2014; Doxaran et al., 2014; Huang et al., 2015). However, GOCI currently only “looks” around the Korean Peninsula and lacks the SWIR band required to perform atmospheric correction over turbid regions. The Landsat-8 OLI sensor, though designed for terrestrial applications, has found uses in water quality monitoring due to its high spatial resolution which can effectively resolve and delineate fine turbidity features between the micro-tidal river and

offshore waters plumes (Ody et al., 2016). However, with a revisit frequency of every 16 days Landsat-8 OLI lacks the required temporal resolution to monitor the temporal dynamics of suspended sediments in the coastal environment.

The past and the existing satellite sensors have provided a wealth of information in qualitative and quantitative understanding of the dynamics of our coastal waters quality as a result of natural and anthropogenic processes. However, there are challenges in continuously monitoring the coastal waters quality due to the satellite sensor's spatiotemporal and radiometric limitations. The synergistic approach of using different satellite sensors in conjunction with each other has shown some potential in achieving the limitations of using only a single satellite sensor (Miller et al., 2011). However, some challenges still exist in multi-sensor data fusion resulting from different radiometric and spatial characteristics of each sensor. The availability of geostationary sensors, such as GOCI and SERIVI, has shown the potential of high temporal monitoring of water quality in coastal waters in regional waters. Thus, the possible future in coastal water quality lies in the availability of synchronized geostationary satellite with at least equivalent radiometric and spectral characteristics of MODIS or better. Further, the exploration of the application of other planned or already available geostationary sensors, like Himawari 8 & 9 and the third generation European Union's meteorological satellite sensor, with sufficient SNR and spectral bands is warranted to sustain the effort of water quality monitoring of highly dynamic coastal waters.

2.6.2 Limitations of TSS models

The complex nature of biogeochemical properties of coastal waters limits the general application of already developed and validated TSS models from one region to another. Further, the limitations of TSS models are also caused by the different errors associated with not only the simple statistical basis used in the empirical model and the simplified relationship generated using approximation and assumption between IOPs and biogeochemical properties in the bio optical and semi-analytical models, but

also from the atmospheric correction procedures and calibration errors in the model as a result of the *in situ* measurements and the difference between the temporal and spatial match between satellite and *in situ* measurements (IOCCG, 2000).

The atmospheric correction for Case-1 waters generally assumes zero contribution of L_w in NIR bands which has been proven to be an invalid assumption in coastal waters because suspended sediments also contribute to L_w in the NIR bands (Ruddick, Ovidio, & Rijkeboer, 2000). Failure to correct for atmospheric effects on the quantification of geophysical parameters was shown to be significant by Doxaran et al. (2002), who observed ρ_w in the NIR bands (700 – 900 nm) for TSS greater than 50 mg/L were not negligible, and Chen, Zhang, Cui, and Wen (2013c) also found that ρ_w at 748 nm was not insignificant (0.0012) when TSS concentration was moderate (8.13 mg/L). Thus, L_w in turbid coastal waters was shown to be not negligible, contrary to previous assumptions about ρ_w in NIR based atmospheric correction models. Further, it is well known that 5% uncertainty in reflectance translates to 5% error in the estimation of biogeochemical parameters (Gordon & Castaño, 1989).

The calibration of a part or whole of the parameters in both the empirical and semi-analytical TSS models requires accurate *in situ* measurements of optical properties or biogeochemical parameters, which are representative of the water conditions of the study region. However, accurate measurements of the optical properties using currently available optical instruments are limited by instrument's sensitivities, calibration, dark signal correction, data processing, and deployment strategy among other environmental and experimental procedures (IOCCG, 2006). Empirical TSS models which are usually calibrated using *in situ* measurements from the regional water are only valid for that particular region and time, depending on the general representativeness of the *in situ* data collected from that particular region. Apart from the different regional application of the developed TSS models, the application of developed regional TSS models is questionable at different time periods because IOPs of water are affected by the seasonal changes where one biogeochemical constituent's concentration

might be less or more dominant during a particular season (Xing et al., 2014). Further, the general applicability of TSS models is limited due to potential violation of physical relationships that exist between the TSS concentration and the optical properties the models assumes or approximates (IOCCG, 2000). In the case of the bio-optical and semi-analytical models, the development of TSS models usually assumes or approximates the physical relationship between biogeochemical properties and the IOPs to simplify the actual physical relationships which are more complex and interlinked than a decoupled relationship of a single or few parameters. Thus, the uncertainties in the semi-analytical model are as a result of the chosen relationship between the physical parameters and the optical properties and associated assumptions used in generation of those relationships.

In addition to the aforementioned uncertainties associated with both empirical and semi-analytical TSS models, the uncertainties in the remotely sensed L or ρ by the satellite sensor also affects the quantification of TSS concentrations. It has been reported that 5% calibration error of satellite sensor will result in 50% error in R_{rs} (Chen et al., 2015b) which can translate to 50% error in TSS concentration estimation even for a simple linear TSS model. The source of error in the validation of TSS models stems from the fact that *in situ* measurement are collected over small areas (usually a few square meters) while the satellite match-ups are generated from large areas (few hundreds square meters to a square kilometre) (IOCCG, 2006). Such validation methods are valid for the open ocean which is assumed to be relatively spatially homogenous, but such is not the case for turbid coastal waters. Despite the challenges and limitations faced by TSS models, more TSS models are developed where uncertainties associated with the model development are quantified through the use of advanced statistical methods, such as use of type II regression methods in the empirical models to account for the uncertainty associated with both the dependent (TSS concentration) and independent (reflectance) variables and non-linear adaptation in computation of the confidence interval for semi-analytical models (IOCCG, 2006).

Chapter 3

A Semi-Analytic Model for Estimating Total Suspended Sediment Concentration in Turbid Coastal Waters of Northern Western Australia Using MODIS-Aqua 250 m Data

This chapter has been published in the journal: Remote Sensing

Dorji, P., Fearn, P., & Broomhall, M. (2016). A Semi-Analytic Model for Estimating Total Suspended Sediment Concentration in Turbid Coastal Waters of Northern Western Australia Using MODIS-Aqua 250 m Data. *Remote Sensing*, 8(7), 556.

3.1 Abstract

Knowledge of the concentration of total suspended sediment (TSS) in coastal waters is of significance to marine environmental monitoring agencies to determine the turbidity of water that serve as a proxy to estimate the availability of light at depth for benthic habitats. TSS models applicable to data collected by satellite sensors can be used to determine TSS with reasonable accuracy and of adequate spatial and temporal resolution to be of use for coastal water quality monitoring. Thus, a study is presented here where we develop a semi-analytic sediment model (SASM) applicable to any sensor with red and near infrared (NIR) bands. The calibration and validation of the SASM using bootstrap and cross-validation methods showed that the SASM applied to Moderate Resolution Imaging Spectroradiometer (MODIS)-Aqua band 1 data retrieved TSS with a root mean square error (RMSE) and mean absolute relative error (MARE) of 5.75 mg/L and 33.33% respectively. The application of the SASM over our study region using MODIS-Aqua band 1 data showed that the SASM can be used to monitor the on-going, post and pre-dredging activities and identify daily TSS anomalies that are caused by natural and anthropogenic processes in coastal waters of northern Western Australia.

3.2 Introduction

The use of satellite remote sensing of coastal waters to derive their bio-geophysical properties provides marine scientists and managers with a relatively affordable alternative to *in situ* based sampling. Remote sensing has been used to map a wide array of coastal water's constituents, such as phytoplankton for biomass and primary production (Acker et al., 2005; Arrigo & McClain, 1994; Jutla et al., 2012; Sullivan et al., 1993), coloured dissolved organic matter (CDOM) for its effect on benthic habitats (Kutser et al., 2005; Loisel et al., 2014b; Tiwari & Shanmugam, 2011), and total suspended sediments (TSS) concentration as a measure of water quality (Ayana et al., 2015; Binding et al., 2005; Chen et al., 2007; Martinez, Guyot, Filizola, & Sondag, 2009; Park & Latrubesse, 2014). Many studies have been performed to derive TSS concentration via satellite remote sensing using different platforms: Sea-viewing Wide Field-of-view Sensor (SeaWiFS) (Doxaran et al., 2003; Vos et al., 2003), Landsat series (Kallio et al., 2008b; Vanhellemont & Ruddick, 2014; Wu et al., 2015; Wu et al., 2008; Zhang et al., 2014; Zhou et al., 2006), Medium Resolution Imaging Spectrometer (MERIS) (Chen et al., 2015b; Kratzer et al., 2008; Odermatt et al., 2008; Qing et al., 2014; Raag et al., 2013; Tarrant et al., 2010), Moderate Resolution Imaging Spectroradiometer (MODIS) (Ayana et al., 2015; Chen et al., 2015a; Chen et al., 2007; Hudson et al., 2014; Miller & McKee, 2004; Petus et al., 2014; Raag et al., 2013), "Système Pour l'Observation de la Terre" (SPOT) (Doxaran et al., 2002), and high resolution sensor IKONOS (Ekercin, 2007). Most models are developed to estimate TSS concentration by directly relating the remotely sensed reflectance with *in situ* measurements of the TSS concentration using statistical analysis, linear and non-linear regression. These models may use a single spectral band (Choi et al., 2014; Cui, Qiu, Fei, Liu, & Wu, 2013; Kaba et al., 2014; Shi et al., 2015; Tyler, Svab, Preston, Présing, & Kovács, 2006; Wang, Zhou, Xu, Song, & Wang, 2008; Wu et al., 2008) or combinations of different spectral bands (Chen et al., 2015a; Duan, Ma, Zhang, & Zhang, 2009; Espinoza Villar et al., 2013; Kallio et al., 2008b; Kratzer et al., 2008; Qiu, 2013; Shen et al., 2014) with regression analysis to predict the TSS concentration. Linear

approximations from regression analysis are valid for relatively low TSS concentrations but as the TSS concentration increases the linearity weakens and the reflectance saturates at high TSS concentration (Doxaran et al., 2003; Petus et al., 2010). The saturation of reflectance occurs at high TSS concentration because the increased water column scattering leads to a relative enhancement in absorption/attenuation of the backscattered light (Mobley, 1994). In such cases, a non-linear approximation such as a higher order polynomial or exponential function (Doxaran, Castaing, & Lavender, 2006; Doxaran et al., 2003; Hudson et al., 2014; Shi et al., 2015) is used to relate the TSS concentration to reflectance. Combinations of different spectral bands in visible and near infrared (NIR) spectral regions have been used to estimate the TSS concentration in coastal waters that varied vastly in concentrations, from less than 11.0 mg/L (Alikas & Reinart, 2008; Kutser et al., 2007; Raag et al., 2013; Sipelgas et al., 2006) to very high, greater than 2000 mg/L (Doxaran et al., 2003; Hu et al., 2004; Sokoletsky et al., 2014). Spectral bands in the blue and green spectral regions with (Chen et al., 2015b; Li, Gao, & Wang, 2010; Qiu, 2013; Zhang, Tang, Dong, Song, & Ding, 2010) or without (Jiang and Liu 2011 as cited in (Chen et al., 2015a),(Tang et al., 2013)) the combinations of red or NIR bands are used by many researchers to explore the potential of TSS mapping using different band combinations. However, more recently, single band estimations of the TSS concentration using the red or NIR bands have been widely used in TSS algorithms because of the particulates dominance in total backscattering when compared with the optical response of other components in these regions of the electromagnetic spectrum.

Empirical methods are most often used to estimate TSS concentration because of their simplicity in development. However, the lack of a physical basis in empirical models limits their general applicability to other than a local area where the algorithm was developed and ones confidence in extrapolating the model to higher or lower concentration than those on which it was developed (Chen et al., 2013b). In recent decades, physical and semi-analytical models relating inherent optical properties (IOPs) of water to apparent optical properties (viz. irradiance reflectance just beneath the water

surface) are used to estimate bio-geophysical parameters of interest (Ayana et al., 2015; Brando & Dekker, 2003; Chen et al., 2014b; Chen et al., 2013b; Dekker et al., 2002; Odermatt et al., 2008; Vanhellefont & Ruddick, 2014; Yang, Matsushita, Chen, & Fukushima, 2011). A physical model, which is based on radiative transfer theory, requires that the *in situ* inherent optical properties of water, atmospheric conditions and several other factors are accurately known to enable the determination of TSS concentration (Mobley, 1994). Use of semi-analytical models that combine both physical foundations and statistical analyses provide a promising method to estimate TSS concentration with limited knowledge of the *in situ* optical properties of the water body (Dekker et al., 2002; Lee et al., 1999; Nechad et al., 2010).

Semi-analytic TSS algorithms include model parameters that use *in situ* regional IOPs (Chen et al., 2013b), averaged IOPs representative of wider geographical locations (Nechad et al., 2010) or IOPs inverted from site specific satellite reflectance (Kong et al., 2015a). The site specific IOPs used in parameterizing these models are potentially the best for retrieving site-specific TSS. However, notwithstanding the inherent uncertainties and limitations of *in situ* IOP instruments, the acquisition of IOPs is also challenging due to financial, logistical and time factors for rapid assessment of TSS. The dependence of IOPs on site-specific water constituents limits the use of published IOPs from other areas as an alternative without compromising the quality of the derived TSS concentration. The IOPs obtained by inverting the site specific satellite reflectance are also not without limitations because the inverted IOPs are affected by not only the uncertainties of IOPs from inversion models but also uncertainties of the reflectance product from which the IOPs are derived. The study conducted by (Wang, Boss, & Roesler, 2005) to determine the uncertainties of IOPs derived from semi-analytic models quantified that 20% of derived absorption coefficients were outside the 90% confidence limit while for the backscattering coefficient ~50% were outside the 90% confidence limit.

In this study, we proposed a semi-analytic sediment model (SASM) that had a basis in radiative transfer theory and was locally tuned to the regional waters of northern Western Australia for MODIS-Aqua band 1 to monitor

TSS concentration in the region. The SASM was applied to the coastal waters of northern Western Australia using MODIS-Aqua 250 m data for mapping the TSS concentration in the region, which would serve as a baseline in future water quality monitoring of the region.

3.3 Materials and Methods

3.3.1 Study Site

Onslow waters fall within the Pilbara Coast West (from Exmouth to Karratha) of Western Australian centred at 21°35'00"S and longitude 115°05'00"E (Figure 3.1) and experience an annual average temperature of 29.2 °C and mean annual rainfall of 296 mm (Bureau of Meteorology, 2015a). The discovery of the Wheatstone gas field off the coast of Onslow in 2004 has led to the construction of 25 million tonnes per year gas processing plants (WAPC, 2011) with the dredging of a shipping access channel to the processing plants beginning from May 2013 till end of September 2013 in the location of the dredge area (DA) in Figure 3.1 (Chevron, 2014). The dredging operation was expected to generate 45 million m³ of dredge spoil (Chevron, 2014), and the activity has some level of impact on the marine ecosystem in the region.

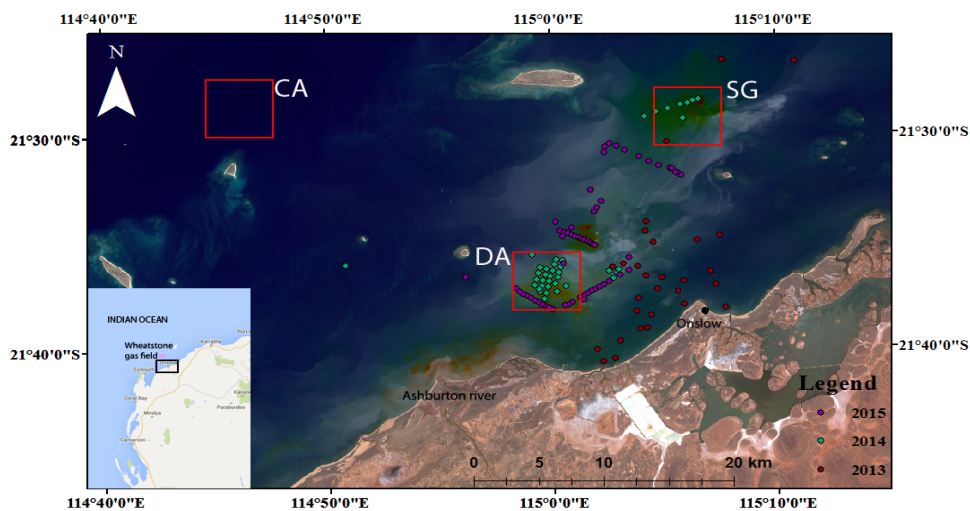


Figure 3.1: True colour 15 m pan sharpened Landsat OLI (Operational Land Imager) imagery showing study site and the locations of sampling stations. Red squares represent the locations of dredge area (DA), spoil ground (SG), and clean area (CA) used in the temporal analysis. Red, purple and green filled circles are the locations of water sampling stations in 2013, 2014 and 2015 respectively

3.3.2 *In situ* and Remote Sensing Data

The satellite-based remote sensing data for this study were MODIS-Aqua data spanning the years 2013 to 2015, acquired as Level 1B data from the NASA LAADS web (<http://ladsweb.nascom.nasa.gov/>). The *in situ* data of reflectance samples was collected using a hyperspectral radiometer, the “Dynamic above-water radiance and irradiance collector” (DALEC) and simultaneously, water samples were gathered for TSS measurements. In total three field campaigns were carried out in the study site collecting a total of 130 water samples. First two field campaigns were carried out on board the RV Linnaeus, operated by the Commonwealth Scientific and Industrial Research Organisation (CSIRO) during October 2013 and June 2014. The third field campaign was carried out in July 2015 on the Australian Institute of Marine Science (AIMS) RV Solander (Figure 3.1).

3.3.2.1 *The DALEC Radiometer*

The DALEC, a hyperspectral radiometer developed by “In situ Marine Optics” is used routinely for autonomous ship-based measurement of remote sensing reflectance (Brando et al., 2016). The DALEC takes coincident measurements of downwelling irradiance (E_d), upwelling radiance (L_u) and sky radiance (L_{sky}) with each sensor collecting spectral information in 256 spectral bins ranging from 380 nm to 900 nm. Measurement of radiance from the L_u and L_{sky} sensors and irradiance from the E_d sensor can be used to compute remote sensing reflectance (R_{rs}) using the ad hoc formula of Mobley (1999), as shown by Equation (3.1),

$$R_{rs}(\lambda) = \frac{L_u(\lambda) - \rho L_{sky}(\lambda)}{E_d(\lambda)} \quad (3.1)$$

where ρ is a correction factor which is dependent on sky radiance, θ_s , wind speed and the instrument’s viewing angle (Mobley, 1999). The value of ρ was set to 0.022 as prescribed by Mobley (1999) for uniform sky conditions and wind speed less than 5 ms^{-1} . DALEC data were collected between 10:00 am and 3:00 pm local time when cloud cover was below 10%, the wind speed less than 5 ms^{-1} and the sea waves and swell were below 0.5 m. As recommended by Mobley (Mobley, 1999), the DALEC’s azimuthal viewing

angle was maintained at 135° relative to the solar direction and the viewing angles of the L_u and L_{sky} sensors were set at 40° off nadir and zenith respectively to minimize the sun glint and instrument shading. The necessary adjustment to the orientation of the DALEC was carried out as and when the heading of the ship changed during the course of the measurements.

3.3.2.2 DALEC Data Collection and Analysis

The DALEC was mounted on the bow of the research vessel using a horizontal pole to a distance such that disturbance from the wake of the ship was avoided. The DALEC is capable of running continuously, and collecting individual spectra at integration times selected automatically in response to illumination conditions. On average DALEC was able to collect 11 reflectance spectrum per minute. The DALEC was operated whilst the boat was underway and also when “on station”, with the on station periods lasting at least 5 min to allow collection of TSS samples.

Despite taking necessary steps discussed above as recommended by Mobley (1999) to avoid specular reflection of sunlight from some wave facets for the reflectance measurements, still some spectra can be contaminated by the sun glint. These sun glint affected spectra are removed from the time series of data prior to subsequent analysis. After elimination of sun glint contaminated spectra there were at least 5 reflectance spectra per stations every minute. Typically, an average spectrum is derived from a set of measurements coinciding with the collection of the TSS sample. Analysis of the variation in reflectance spectra, by calculating the standard deviation for time periods of ± 1 min, ± 3 min, and ± 5 min from time when TSS sample was collected, showed that the standard deviation for each set of data was comparable. On average, we selected ± 3 min as the standard averaging period for all stations.

3.3.2.3. Water Sample Collection and Analysis

During the first two field trips we collected a minimum of two 1 litre sample bottles of water from ~ 0.5 – 1 m depth at each station while the boat was stationary. For the third field trip, we collected water samples using an

underway seawater sampling system on the AIMS RV Solander, which has a sea water intake system at a depth of ~1.9 m below the ocean surface.

All the water samples collected were processed for TSS concentration using the gravimetric method within six hours from the time the water samples were collected. Whatman GF/F filters (47 mm diameter, nominal pore size 0.7 μm) were pre-prepared in the laboratory by rinsing each filter with 50 mL of distilled/deionized water followed by drying at 60 °C in an oven for over 12 h. The water samples were filtered using low vacuum pressure and the filter flushed with 50 mL of deionized water to remove residual salt. The filtered TSS samples were stored in a cool dry place until being taken back to the laboratory where they were dried for at least 24 h at 60 °C. The dried filters were then repeatedly measured until the measured weight was constant within the tolerance weight limit of 0.001 mg/L.

Analysis of TSS samples collected during the third field trip showed that the TSS did not correlate with the reflectance measurements or other optical measurements. Collecting the water samples from a depth of ~1.9 m might have resulted in the *in situ* TSS concentration being different from the actual expected value at the surface (~0.5—1.0 m) if the water column is stratified. In fact, observations from acoustic instruments did often show strong stratification, with suspended sediment loads increasing with depth. Thus, data from the third field trip were excluded from the algorithm development or TSS product validation in this study with the exception of DALEC measurements of the remote sensing reflectance to be used in the validation of the atmospheric correction process because DALEC data on 6 July 2015 were acquired within 15 min from the MODIS-Aqua overpass. The details of water column stratification on the MODIS sensor at band 1 is discussed in Appendix B.

3.3.2.4. Satellite Data Acquisition

MODIS-Aqua level 1B images containing geo located at-aperture radiances for all 36 spectral bands were acquired from NASA LAADS web for the dates corresponding to all the field trips for the validation of the MODIS-Aqua derived TSS. The images were screened for sun glint

contamination and cloud cover over the study sites visually and found to be free of cloud and sun glint. In addition to the aforementioned MODIS-Aqua images, additionally 247 MODIS-Aqua images free of cloud and sun glint in the study site for the year 2013 coinciding with the dredge operation to construct access channels for a gas processing plant by Chevron Pty Ltd. (Perth, Australia) were also acquired for time series analysis. All MODIS-Aqua 1B images were processed for atmospheric correction, water pixel extraction for the validation, and spatial consideration for the temporal analysis.

3.3.2.5. Atmospheric Correction

For the atmospheric correction, the top of the atmosphere (TOA) radiance from the MODIS-Aqua Level 1B products were converted to atmospherically corrected, at-surface remote sensing reflectance using the multi-sensor Level 1 to Level 2 generator (l2gen) function which can be run as a stand-alone program or accessed through the SeaDAS 7.2 interface (Feldman & McClain, 2010). Among many atmospheric correction algorithms available for data processing in SeaDAS we considered two, the standard atmospheric correction method for MODIS high resolution data SWIR (Wang, 2007), and the MUMM (Ruddick et al., 2000) atmospheric correction method, because previous studies (Chen et al., 2014b; Ody et al., 2016; Ruddick et al., 2000; Wang, Son, & Shi, 2009c) have demonstrated that these two atmospheric correction algorithms are effective for turbid coastal waters. The SWIR atmospheric algorithm estimates the aerosol reflectance using the 1240 nm and 2130 nm MODIS bands while the MUMM atmospheric correction is based on the spatial homogeneity of water-leaving radiances and aerosol ratios for the MODIS 748 nm and 869 nm bands (Ody et al., 2016).

Both the MODIS high resolution and MUMM atmospheric correction were applied to MODIS-Aqua Level 1B data for 6 July 2015 because all the DALEC R_{rs} data collected on 6 July 2015 were within 15 min of MODIS overpass time compared to in excess of at least 90 min on other sampling dates. A comparative analysis of R_{rs} data from the two atmospheric

correction methods considered (results discussed in result Section 3.4.4.1) showed that MUMM is better at retrieving R_{rs} when compared with the standard MODIS high resolution SWIR atmospheric correction method for our study site. All MODIS-Aqua data were subsequently processed with the MUMM atmospheric correction approach. However, analysis of the products showed that MUMM's default cloud screening band at 869 nm caused the turbid plumes to be flagged as clouds, thus we applied the 2130 nm band instead.

3.3.2.6. Water Pixel Extraction and Analysis

For water pixel extraction, we used the geographical location of the *in situ* TSS sampling stations that were within ± 30 min, ± 60 min and ± 90 min from MODIS-Aqua overpass time. Herein, data are referred to as Aqua Validation Data (AVD) and followed by the suffix 30, 60 and 90 for data collected within ± 30 min, ± 60 min and ± 90 min of MODIS-Aqua overpass respectively. For the AVD30, AVD60 and AVD90 there were 18, 28 and 45 match-up pairs between MODIS-Aqua derived TSS and *in situ* TSS respectively. TSS from each location at the validation sites were extracted using the SeaDAS pixel extraction tool for window sizes of a single pixel, 3×3 pixels, and 5×5 pixels to account for the pixel variability in the error analysis.

For the selection of the location and the spatial extent in the MODIS derived TSS for performing the time series analysis, we focused on three different regions in the study site after careful analysis of the pan-sharped 15 m Landsat imagery to confirm appropriate locations to represent (1) clean area (CA); (2) dredge area (DA); and (3) spoil ground (SG). All three areas of interest were confined to a spatial extent of 25 km^2 after visually examining the high spatial resolution Landsat images. The CA was selected away from the main dredging area and further off the coast, the DA was selected at a location coincident with dredging operations, and the SG was selected at a location where spoils from the dredge operations were dumped. MODIS-derived TSS concentrations corresponding to each location were extracted

for MODIS-Aqua time series analysis. The spatial extent and the geographical locations of CA, DA and SG are shown in Figure 3.1.

3.3.3. SASM Model Formulations

The formulation of the SASM describes the relationship between TSS concentration and ocean reflectance, thus providing a means to estimate TSS concentration using remote sensing methods. The approach is based on general radiative transfer theory and the Quasi Analytic Algorithm of Lee et al. (2002).

3.3.3.1 Reflectance Model

Gordon et al. (1988) showed subsurface remote sensing reflectance (r_{rs}), is related to the total absorption coefficient, $a(\lambda)$, and total backscattering coefficient, $b_b(\lambda)$, through:

$$r_{rs}(\lambda) \approx \sum_{i=1}^2 g_i \left[\frac{b_b(\lambda)}{a(\lambda) + b_b(\lambda)} \right]^i \quad (3.2)$$

The coefficients g_i depend on solar angle, scattering phase function, bidirectional reflectance effects and water surface conditions. Gordon et al. (1988) gave $g_1 = 0.0949$ and $g_2 = 0.0794$ for Case-1 waters and Lee et al. (1999) demonstrated that $g_1 = 0.084$ and $g_2 = 0.17$ are more suitable for highly scattering coastal waters. In this study, we adopted the values of g_1 and g_2 provided by Lee et al. (1999).

The $R_{rs}(\lambda)$ which are measured by above-water radiometer can relate to $r_{rs}(\lambda)$ using the relationship from Lee et al. (1999) as shown in Equation (3.3).

$$r_{rs}(\lambda) = \frac{R_{rs}(\lambda)}{(0.52 + 1.7R_{rs}(\lambda))} \quad (3.3)$$

The total absorption coefficient is expressed as the sum of absorption coefficients for pure sea water ($a_w(\lambda)$), particulate matter ($a_p(\lambda)$), phytoplankton pigments ($a_\phi(\lambda)$), and coloured dissolved organic matter ($a_{cdom}(\lambda)$).

$$a(\lambda) = a_p(\lambda) + \underbrace{a_w(\lambda) + a_\phi(\lambda) + a_{cdom}(\lambda)}_{a_{other}} \quad (3.4)$$

The total backscattering coefficient is expressed as the sum of backscattering coefficients for pure sea water ($b_{bw}(\lambda)$), particulates ($b_{bp}(\lambda)$), and phytoplankton pigments ($b_{b\phi}(\lambda)$).

$$b_b(\lambda) = b_{bw}(\lambda) + b_{bp}(\lambda) + b_{b\phi}(\lambda) \quad (3.5)$$

Equation (3.2) representing the subsurface remote sensing reflectance as a function of the IOPs can be rewritten as a quadratic equation as follows:

$$r_{rs}(\lambda) = g_1x(\lambda) + g_2x^2(\lambda) \quad (3.6)$$

where

$$x(\lambda) = \frac{b_b(\lambda)}{a(\lambda) + b_b(\lambda)} \quad (3.7)$$

3.3.3.2 Inherent Optical Properties Model

In the IOPs model we represent the ratio of $b_b(\lambda)$ to $a(\lambda)$ as $\omega'_b(\lambda)$ as follows:

$$\omega'_b(\lambda) = \frac{b_b(\lambda)}{a(\lambda)} \quad (3.8)$$

For the case of turbid water, we adopt the following assumptions:

- For high-scattering coastal waters, $b_b(\lambda)$ is mainly due to the backscattering coefficient from particulate matter and water molecules, the backscattering coefficient contributions from other constituents are insignificant (Tiwari & Shanmugam, 2013). Further, in the red and NIR regions of the spectrum the scattering by water molecules becomes insignificant, thus we can make an assumption that total backscattering in the red and NIR regions is due to particulate matter only. Equation (3.5) can be approximated as:

$$b_b(\lambda) \approx b_{bp}(\lambda) \quad (3.9)$$

The assumption in Equation (3.9) can potentially be undermined for extreme concentrations of chlorophyll during phytoplankton blooms because in such cases, the backscattering from chlorophyll can be significant and cannot be ignored. HydroLight simulations show that even in the extreme

case of high chlorophyll concentration (10 mg/m^3) the backscattering contribution from chlorophyll constitute backscattering equivalent of TSS concentration of 3.4 mg/L and 3.6 mg/L at MODIS band 1 and 2 respectively. The backscattering contribution from pure water is calculated to be $\sim 20\%$ and $\sim 9\%$ of backscattering coefficient of MODIS band 1 and band 2 respectively than the TSS backscattering contribution even at TSS concentration of 0.2 mg/L . The coastal waters in Western Australia typically shows a seasonal cycle in chlorophyll with average low values of 0.24 mg/m^3 during summer and peaks in June with average values of 0.69 mg/m^3 (Moore li, Matear, Marra, & Clementson, 2007). Considering the concentration of chlorophyll is typically less than 1 mg/m^3 and its backscattering effect minimal even during the peak seasons in coastal waters of Western Australia, we can assume Equation (3.9) is valid for both MODIS band 1 and band 2. An added bonus that the aforementioned MODIS bands are both capable of is a 250 m spatial resolution.

- Following (Babin, Morel, Fournier-Sicre, Fell, & Stramski, 2003a; Babin et al., 2003b) we can assume the particulate backscattering coefficient ($b_{bp}(\lambda)$) and absorption coefficient ($a_p(\lambda)$) to be proportional to TSS concentration, via appropriate constants—the specific particulate backscattering coefficient ($b_{bp}^*(\lambda)$) and specific particulate absorption coefficients ($a_p^*(\lambda)$).

$$b_{bp}(\lambda) = b_{bp}^*(\lambda) \times TSS \quad (3.10)$$

$$a_p(\lambda) = a_p^*(\lambda) \times TSS \quad (3.11)$$

Taking into account the aforementioned assumptions, we can formulate Equation (3.8) into

$$TSS(\lambda) = \frac{C_1(\lambda)\omega_b'(\lambda)}{1 - C_2(\lambda)\omega_b'(\lambda)} \quad (3.12)$$

where $C_1(\lambda) = a_{\text{other}}(\lambda) / b_{bp}^*(\lambda)$ and $C_2(\lambda) = a_p^*(\lambda) / b_{bp}^*(\lambda)$.

Essentially, Equation (3.12) is equivalent to Equation (5) of Nechad et al. (2010). However, the difference between the two models lies in the approximation of $r_{rs}(\lambda)$ where we use the second order approximation of Gordon et al. (1988) and Nechad et al. (2010) make use of the first order

approximation of $r_{rs}(\lambda)$ from (Gordon et al., 1988). The difference in $r_{rs}(\lambda)$ between Nechad et al. (2010) and the SASM model stems from the computation of $\omega'_b(\lambda)$ by each individual model. The details of reflectance models comparison between Nechad et al. (2010) and SASM is presented in Appendix A.

3.3.3.3. Consolidation of Reflectance and Inherent Optical Properties Model

Equation (3.7) can be established in terms of $\omega'_b(\lambda)$ using the relationship from Equation (3.8) as follows:

$$x(\lambda) = \frac{\omega'_b(\lambda)}{1 + \omega'_b(\lambda)} \quad or \quad \omega'_b(\lambda) = \frac{x(\lambda)}{1 - x(\lambda)} \quad (3.13)$$

Substituting Equation (3.13) into Equation (3.12) gives:

$$TSS(\lambda) = \frac{C_1(\lambda) \left(\frac{x(\lambda)}{1 - x(\lambda)} \right)}{1 - C_2(\lambda) \left(\frac{x(\lambda)}{1 - x(\lambda)} \right)} \quad (3.14)$$

where $x(\lambda)$ is the positive root of the solution of the quadratic function shown as Equation (3.6), which is as follows:

$$x(\lambda) = \frac{-g_1 + \sqrt{(g_1)^2 + 4g_2r_{rs}(\lambda)}}{2g_2} \quad (3.15)$$

The constants $C_1(\lambda)$ and $C_2(\lambda)$ in Equation (3.14) will be derived using regression analysis between *in situ* TSS measurements and $x(\lambda)$.

3.3.4 Conversion of DALEC Remote Sensing Reflectance to Sub-Surface Remote Sensing Reflectance

Fact that DALEC and MODIS have different spectral resolutions and the SASM uses r_{rs} in its model, it is necessary to convert DALEC R_{rs} to MODIS equivalent below-water surface r_{rs} . Thus, *in situ* DALEC-measured R_{rs} were convolved to MODIS band 1 (B1) and band 2 (B2) equivalent R_{rs} using spectral response functions of the MODIS-Aqua following the method described in (Nechad et al., 2010). The MODIS B1 and B2 equivalent R_{rs} were then converted to r_{rs} using the relationship defined in Equation (3.3). Herein, *in situ* DALEC R_{rs} convolved to MODIS band equivalent R_{rs} and

converted to sub-surface remote sensing reflectance will be referred as $r_{rs}(B1)$ and $r_{rs}(B2)$ for MODIS band 1 and band 2 respectively.

3.3.5. Regional Empirical Model

Many regional algorithms that are used in estimating the TSS concentration from remote sensing image-derived reflectance or *in situ* reflectance use either linear or exponential models (Matthews, 2011). To compare the performance of the SASM with empirical models the simple form of linear and exponential models were selected as represented by Equations (3.16) and (3.17) respectively.

$$TSS(\lambda) = ax(\lambda) + b \quad (3.16)$$

$$TSS(\lambda) = ae^{bx(\lambda)} + c \quad (3.17)$$

where x is $r_{rs}(B1)$ and $r_{rs}(B2)$ and various combinations of the two bands and a , b , and c are coefficients derived from regression analysis between TSS and x .

3.3.6. Model Calibration and Model Uncertainty Estimates

To calibrate the SASM and empirical models in Equations (3.14), (3.16), and (3.17) we used TSS and $r_{rs}(B1)$ and $r_{rs}(B2)$ and various combinations of the two bands from the data of the first two field trips. From the 69 TSS samples collected during the first two field campaigns only 48 stations afforded the appropriate match-up pair with R_{rs} data collected by the DALEC. For all TSS and R_{rs} match-up pairs, the TSS concentrations varied from a minimum of 2.4 mg/L to a maximum of 69.6 mg/L and mean of 9.89 mg/L. In calibrating a model, it is desirable to have separate data sets for model calibration and testing collected independently of each other. However, due to the limitation of only acquiring 48 match-up pairs, we decided to use all 48 pairs for model calibration and validate using the leave-one-out cross-validation (LOOCV) procedure of Stone (1974). The LOOCV method is a commonly used statistical method in small sample size to allow for whole samples to be used in training and validations (Volpe, Silvestri, & Marani, 2011). In this procedure, one pair of data is left as a validation data set and the remaining data are used in calibrating the model. This procedure

is repeatedly executed excluding the pair that has been picked in previous validations and recalibrated using the new remaining data until all 48 pairs are validated.

Using all 48 match-up pairs the SASM in Equation (3.14) and empirical models in Equations (3.16) and (3.17) were calibrated. From the results discussed in Section 3.4.2, the different bands or their combinations were not at par in retrieving TSS when compared with the MODIS-Aqua band 1, thus we selected MODIS-Aqua band 1 for this study. Finally, all three calibrated models from Equations (3.14), (3.16), and (3.17) are presented below for MODIS-Aqua band 1.

$$TSS(B1) = \frac{23.47 \times \left(\frac{x(B1)}{1 - x(B1)} \right)}{1 - 0.69 \times \left(\frac{x(B1)}{1 - x(B1)} \right)}, (R^2 = 0.85) \quad (3.18)$$

$$TSS(B1) = 612.72 \times r_{rs}(B1) - 4.83, (R^2 = 0.85) \quad (3.19)$$

$$TSS(B1) = 2.41 \times \exp[40.12 \times r_{rs}(B1)] + 0.89, (R^2 = 0.85) \quad (3.20)$$

The LOOCV method provides overall model accuracy but does not produce assessment of uncertainty in the results derived by the model (Volpe et al., 2011). The bootstrap method of Efron (1979) as discussed in (Volpe et al., 2011) provides a means to generate the confidence in models as a result of uncertain determination of model parameters, uncertainties in *in situ* measurements, and assumptions in the model formulations (Volpe et al., 2011). Following Efron (1979), 1000 sets of data were generated using re-sampling via a re-substitution method, and 65% confidence limits and upper and lower bound of the derived TSS products were generated for all three models considered. The 65% confidence interval was obtained by the percentile method by taking the upper and lower 17.5% (the 17.5% and 82.5% quantiles) of the results from the bootstrap distribution.

3.3.7. Accuracy Assessment for Model Performance

The accuracy assessment was performed by comparing model-derived and *in situ* measurements with Root Mean Square Error (RMSE), the

correlation coefficient (r), and Mean Absolute Relative Error (MARE), which are defined in Equations (3.21)–(3.23).

$$\text{RMSE} = \sqrt{\frac{\sum_{i=1}^n (x_i - y_i)^2}{n}} \quad (3.21)$$

$$r = \frac{n \sum x_i y_i - \sum x_i \sum y_i}{\sqrt{n \sum x_i^2 - (\sum x_i)^2} \sqrt{n \sum y_i^2 - (\sum y_i)^2}} \quad (3.22)$$

$$\text{MARE} = \frac{\sum_{i=1}^n |(x_i - y_i) / y_i|}{n} \times 100\% \quad (3.23)$$

where n is the total number of samples, x_i is the model-derived TSS and y_i is the measured TSS.

3.4 Results and Discussion

3.4.1. Spectral Characterization of Field Spectral Measurements

The DALEC measured spectral reflectance signatures for different concentrations of TSS show that in the blue region of the spectrum (400–495 nm) there is little distinct separation between R_{rs} spectra for low and high TSS concentrations (Figure 3.2). In the green (495–570 nm) and the yellow (570–590 nm) spectral regions there are general trends in the increment of the magnitude of R_{rs} with increases in TSS concentration. In addition, there is a tendency for the wavelength of maximum R_{rs} to increase with increasing TSS concentration, from about 570 nm at 3 mg/L to 590 nm at 69.6 mg/L. For the red spectral region (620–750 nm), there is a distinct increment of the magnitude in R_{rs} spectra with increase in TSS concentration. For the case of the NIR region (>750 nm) there is no clear difference among R_{rs} spectra for TSS less than 13 mg/L, but for higher TSS there is a distinct increment in magnitude of R_{rs} with the NIR R_{rs} exhibiting an increasingly more distinct peak at ~810 nm.

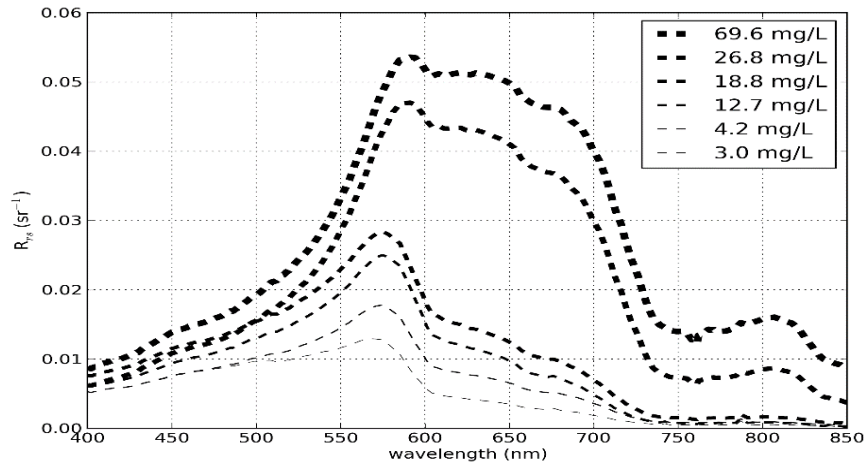


Figure 3.2: *In situ* DALEC spectral reflectance plots for different ranges of TSS concentration.

The selection of the red band and NIR bands for SASM are in agreement with (Kong et al., 2015a) in considering band's responsiveness to TSS concentration in establishing a good retrieval model. In our spectral data, the reflectance at the red and NIR bands responds well with TSS concentration, as shown by the distinct increase in the magnitude of red band reflectance with increase in TSS concentration for all TSS concentrations, while the NIR band shows distinct increments for TSS concentrations greater than 13 mg/L. The correlation coefficients (r) between R_{rs} and TSS at the blue, green, red, and NIR regions of the spectrum were 0.66, 0.42, 0.84, and 0.77 respectively, indicating the presence of a strong linear relationship between reflectance and TSS at red and NIR wavelengths.

3.4.2. SASM Calibration and Validation

The validation of the results for $r_{rs}(B1)$ and $r_{rs}(B2)$ and various band combination results obtained from the LOOCV method are shown in Table 3.1. The results in Table 3.1 show that $r_{rs}(B1)$ alone has better results than $r_{rs}(B2)$ or combinations of the two bands. The poor performance result for $r_{rs}(B2)$ may be because most of the available TSS measurements in our data set were lower. At low TSS concentrations and in the NIR wavelengths where the reflectance measurements are relatively low, results may be better modelled with a simple linear model which works well in low TSS

concentrations (Kutser et al., 2007; Miller & McKee, 2004). However, in the waters with higher TSS concentrations and spectral regions where reflectance are high, the reflectance are not linearly related to the TSS concentration (Li et al., 2010) so a different approach than a simple linear regression has to be taken. Thus, applying the SASM in MODIS band 1 to a region with low TSS concentration can avoid the lower reflectance issues in MODIS band 2 and also the SASM can address the problem of non-linearity between TSS and reflectance when using a simple linear model for higher TSS concentrations.

Table 3.1: Validation results from the LOOCV results for the SASM for MODIS-Aqua band 1, band 2 and their combinations.

Bands	$r_{rs}(B1)$	$r_{rs}(B2)$	$r_{rs}(B2/B1)$	$r_{rs}((B1+B2)/2)$
RMSE (mg/L)	5.75	28.66	15.95	6.32
MARE (%)	33.33	82.90	102.78	38.52
r	0.89	-0.51	0.08	0.86

The results of the SASM uncertainty obtained using the bootstrap method discussed in Section 3.3.6 is presented in Figure 3.3. The upper and lower bounds in Figure 3.3, shown by the grey shading represent the highest and the lowest TSS values obtained in the bootstrap results. The upper and lower bounds simply express the model uncertainty in deriving TSS concentration because of uncertainty in estimating model parameters from *in situ* data. The 65% confidence limit represented by dashed lines in Figure 3.3 defines a narrow band and closely follows the model curve indicating that the TSS retrieved by the SASM is closer to the expected TSS from the SASM. In Figure 3.3, the uncertainty estimates defined by the 65% confidence limits and upper and lower bounds are smaller at the lower concentration end of the curve and wider at the middle and upper part of the concentration curve. The smaller uncertainty at low TSS concentration is due to the availability of larger numbers of match-up (R_{rs} and TSS) pairs while the higher uncertainty at high TSS is due to the limited number of match-up pairs. The future endeavour in collecting *in situ* TSS and R_{rs} should be

focused on collection of more match-up pair that are evenly distributed throughout the range of different TSS concentrations.

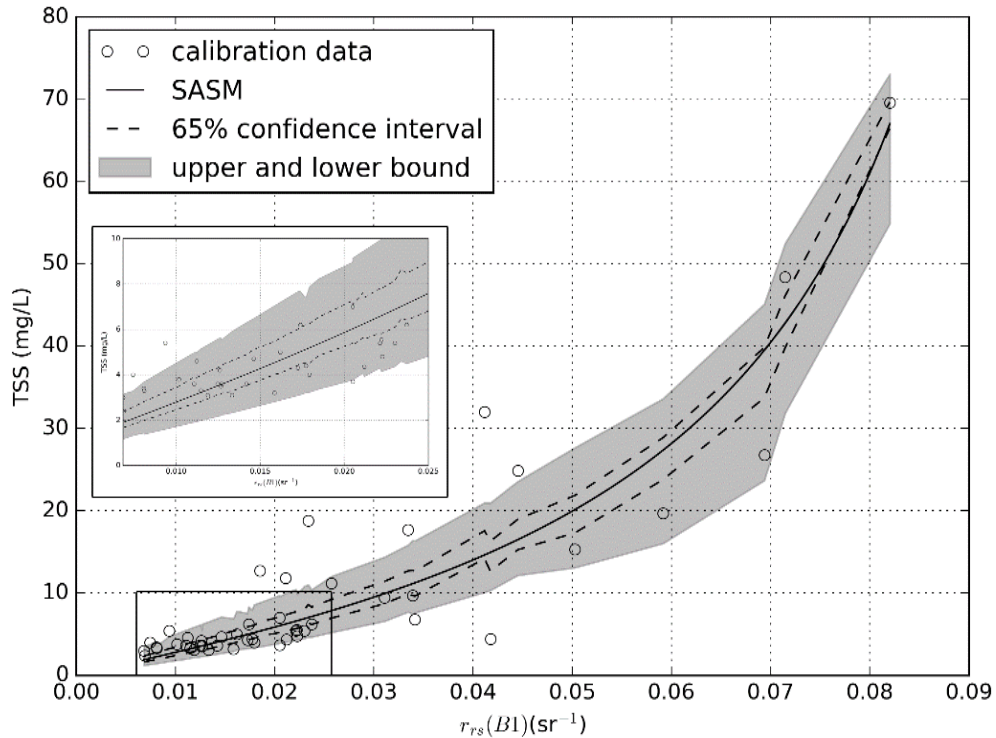


Figure 3.3: The SASM curve for $r_{rs}(B1)$ (Equation (3.18)) is shown by the solid line. The *in situ* data points are shown by open circles. The 65% confidence limits obtained through the bootstrap method are shown by dashed lines. The greyed region represents the upper and lower bound for 1000 bootstrap runs.

3.4.3. SASM Comparison with Empirical Models

The accuracy assessment results for the SASM, the linear, and the exponential models obtained through the LOOCV process described in Section 3.3.6 are presented in Table 3.2. The results show that the SASM and the exponential models perform relatively better than the simple linear model in all three accuracy assessment categories. The comparison between the SASM and the exponential model are quite similar, however the SASM performs marginally better than the exponential model in all three assessment categories. Figure 3.4 shows TSS values derived from each model using the LOOCV method with respect to the *in situ* TSS values. Assessment of Figure 3.4 shows that all three models underestimate TSS when compared with *in situ* TSS for TSS greater than 30 mg/L. We can speculate that underestimation is due to our calibration data set having more

low TSS values, 75% of *in situ* TSS data collected were less than 10 mg/L. Further, in the region where TSS were less than 30 mg/L there is no clear case supporting which model estimated TSS values better considering the large spread in the model-derived TSS by all three models.

Table 3.2: Results for the SASM, linear and exponential models for MODIS-Aqua band 1.

Model	MARE (%)	RMSE (mg/L)	r
SASM	33.33	5.75	0.89
Linear	59.17	7.39	0.80
Exponential	39.29	6.16	0.87

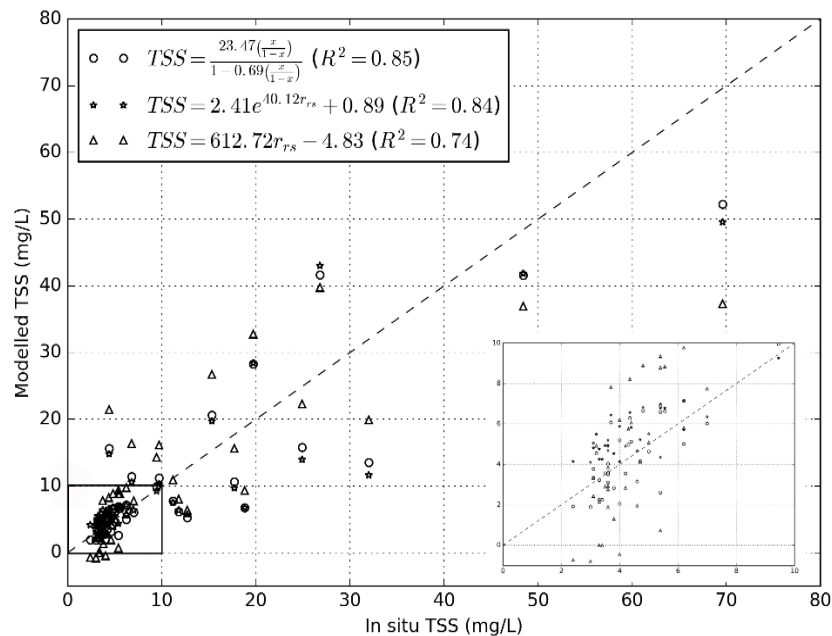


Figure 3.4: Validation results using the LOOCV method for the three models. The box at the bottom right is a blow out of the TSS < 10 mg/L and the dashed line is 1:1 line.

The results of model uncertainty defined by the upper, lower, and 65% confidence limits generated by the bootstrap method discussed in Section 2.6 are presented in Figures 3.5a and 3.5b for the linear and exponential models respectively. In addition to the confidence interval and the extreme bounds of each model, the relative errors (RE) for the lowest, median, and the largest TSS concentrations from the bootstrap distribution are also

presented in Table 3 for the SASM, linear, and exponential models. The median value of the bootstrap results was used because of the random re-sampling procedure employed in the bootstrap methods results of extreme cases (possibly outliers) that affects the mean of whole distributions. The median RE value for all three models are similar to the MARE from the LOOCV method (shown in Table 2) which agrees with the results from the bootstrap method.

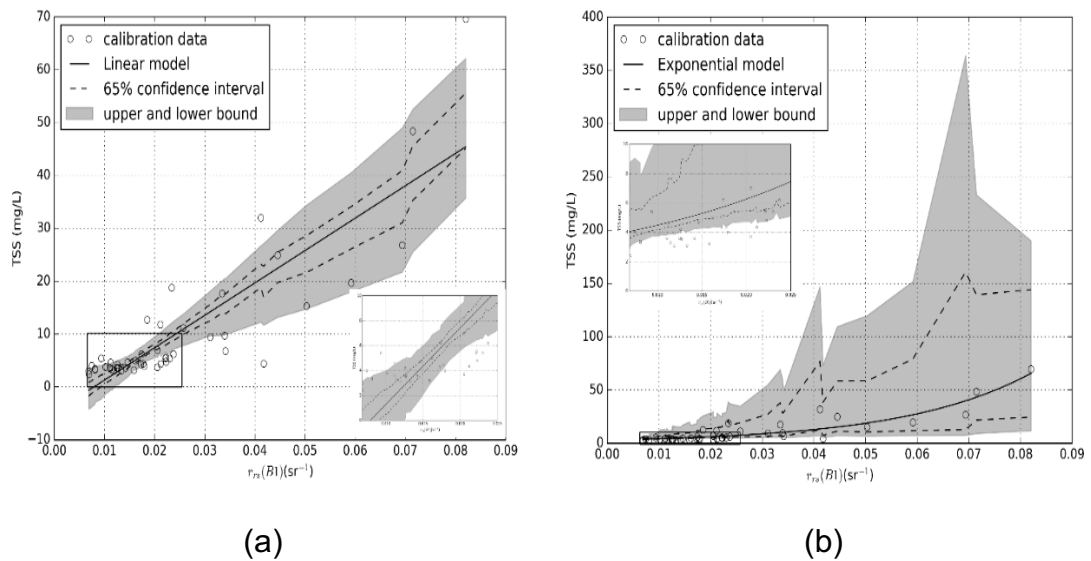


Figure 3.5: The empirical model curve for $r_{rs}(B1)$ is shown by the solid line, *in situ* data points shown by open circles for both (a) the linear model and (b) the exponential model. In both the figures the 65% confidence limit obtained through the bootstrap method are shown by dashed lines. The greyed region represents the upper and lower bound for 1000 bootstrap runs. The upper and lower bound for exponential model has been limited to 95% CI because few high values of TSS were in excess of several thousand mg/L. The box at the bottom right in (a) and middle left (b) is a blow out of the TSS < 10 mg/L and $r_{rs}(B1)$ < 0.025 sr⁻¹.

From the results in Table 3.3 we observe that the lowest and largest RE is slightly better for the exponential model when compared with the SASM, but the mean RE is better for the SASM when compared with the exponential. The RE results of the linear model are all lower than the SASM and exponential model in all three categories of RE results. The bootstrap results of RE indicate slightly better performance for the exponential model. However, on considering the 65% confidence interval and upper and lower bounds of the bootstrap results in Figures 3.3 and 3.5 we observe that the SASM has a smaller 65% confidence interval and significantly smaller upper and lower bounds when compared with the exponential model.

Table 3.3: Absolute relative error for the SASM, linear and exponential models derived from the bootstrap distribution of the TSS results.

Model	Lowest RE (%)	Median RE (%)	Largest RE (%)
SASM	1.20	30.93	228.15
Linear	2.20	53.64	349.90
Exponential	1.03	38.39	195.55

Considering the retrieval error of TSS concentrations from MODIS algorithms is in the range of ~18.0% to ~61% for many studies conducted in the last decade, all three models look feasible in estimating the TSS concentrations in the coastal waters of northern Western Australia. However, we must exercise caution when using any model, particularly when extending the application beyond the limits of the calibration data. A simple linear regression model depends on the linearity between TSS concentration and reflectance, which is observed to weaken as the turbidity of the water increases (Li et al., 2010). Without the proper calibration data for lower reflectance values, the linear model starts to yield negative TSS values at R_{rs} of $\sim 0.0042 \text{ sr}^{-1}$ in MODIS band 1 and underestimates TSS at higher R_{rs} values, as shown in Figure 3.5a. The exponential model gives closer values to the SASM than a simple linear model. Similar result between the SASM and exponential model might be because the non-linear relationship of reflectance and TSS concentration given by bio-optical models closely approximates the exponential curve (Dekker et al., 2002). However, we must caution using the exponential model within proper calibration data because for even zero R_{rs} the exponential model in our study gives minimum value of 3.308 mg/L for and over estimates TSS at higher R_{rs} values. In reality, even with the zero contributions from the constituents in the water there is still backscattering from water molecules, which when modelled using HydroLight gives R_{rs} of $\sim 0.000085 \text{ sr}^{-1}$ in MODIS band 1 for no contributions from in-water constituents. At this R_{rs} value the SASM, linear and exponential models give TSS of 0.002 mg/L, -4.778 mg/L, and 3.308 mg/L respectively. In real

world applications, the values provided by the linear and exponential models are not theoretically sensible whereas those TSS values provided by the SASM are closer to the values we would expect for near zero reflectance.

Considering the results from the LOOCV and bootstrap methods, the SASM is more suitable for the application of deriving TSS concentration using MODIS band 1 in coastal waters of northern Western Australia. However, when applied to sensors other than MODIS the SASM model would need to be recalibrated for that sensor. The collection of hyperspectral R_{rs} measurements using the DALEC and knowledge of the sensor band response functions makes this possible. We also have to be mindful that the error in TSS concentration is also impacted by factors such as atmospheric correction and sensor calibration, where a 5% error in radiance at-sensor results in 50 percent error in R_{rs} (Chen et al., 2015b).

3.4.4. Application to MODIS Imagery

3.4.4.1. Atmospheric Correction

The difference between the standard MODIS high resolution SWIR and MUMM atmospheric correction methods was significant, as shown in Figure 3.6 for 6 July 2015 R_{rs} data. The default MODIS I2gen atmospheric correction method for high resolution MODIS imagery underestimated R_{rs} on average by 39.2% while MUMM underestimated by only 5% in MODIS band 1 when compared with DALEC R_{rs} .

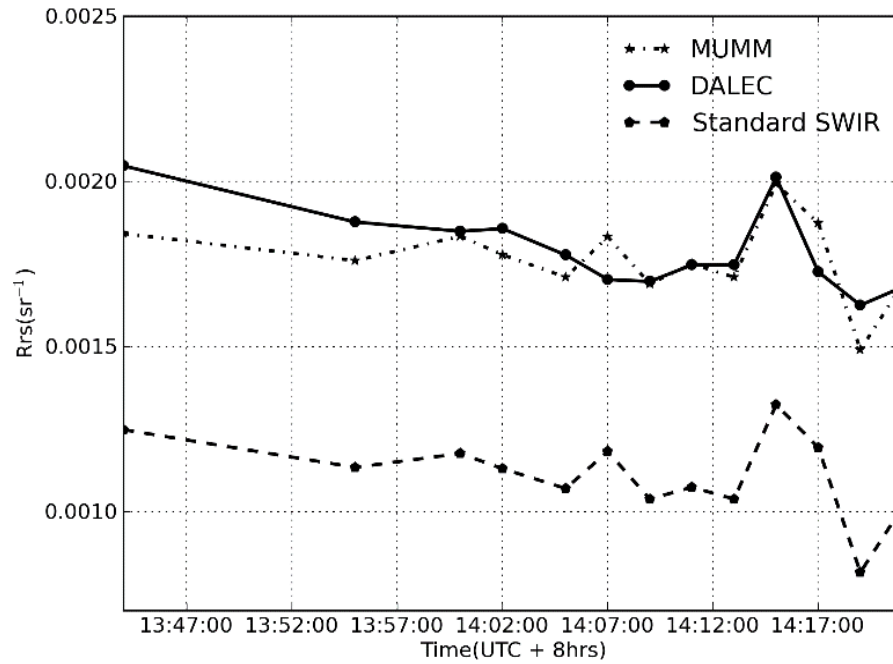


Figure 3.6: R_{rs} (B1) from the standard atmospheric correction method in SeaDAS SWIR and the MUMM atmospheric correction method in comparison with DALEC measurements for 6th July 2015.

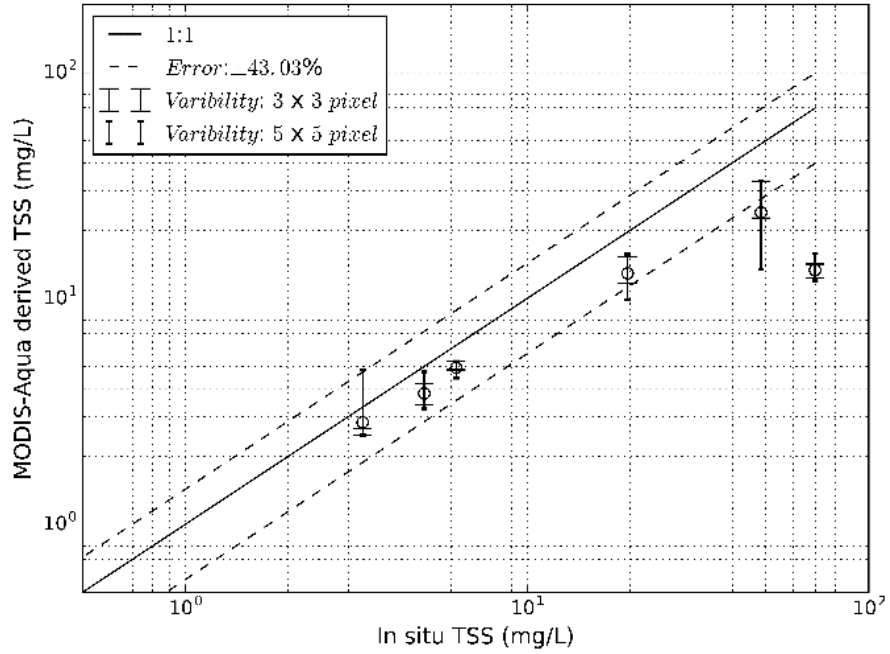
The analysis of the MODIS-Aqua band 1 data corresponding to AVD30, AVD60, and AVD90 to estimate the error in reflectance derived from the satellite resulted in AVD30 with the least error in satellite derived reflectance with MARE of 9.7% while the highest is for AVD90 with 27.58%, and AVD60 with MARE of 21.99%. The correlation coefficients between DALEC R_{rs} and MUMM derived R_{rs} were 0.98, 0.86, and 0.67 for AVD30, AVD60 and AVD90 respectively. Results shows that as time the difference between satellite sensors and DALEC measurement decreases the difference between DALEC measured R_{rs} and MODIS R_{rs} also decreases. These results support the view amongst the remote sensing community that comparison between satellite sensor and *in situ* measurement can be improved by narrowing the time difference between the two. For this study, we used respective error for each AVD to account for the atmospheric correction error in subsequent analysis of the results in estimation of the TSS concentration.

3.4.4.2. MODIS-Aqua Validation

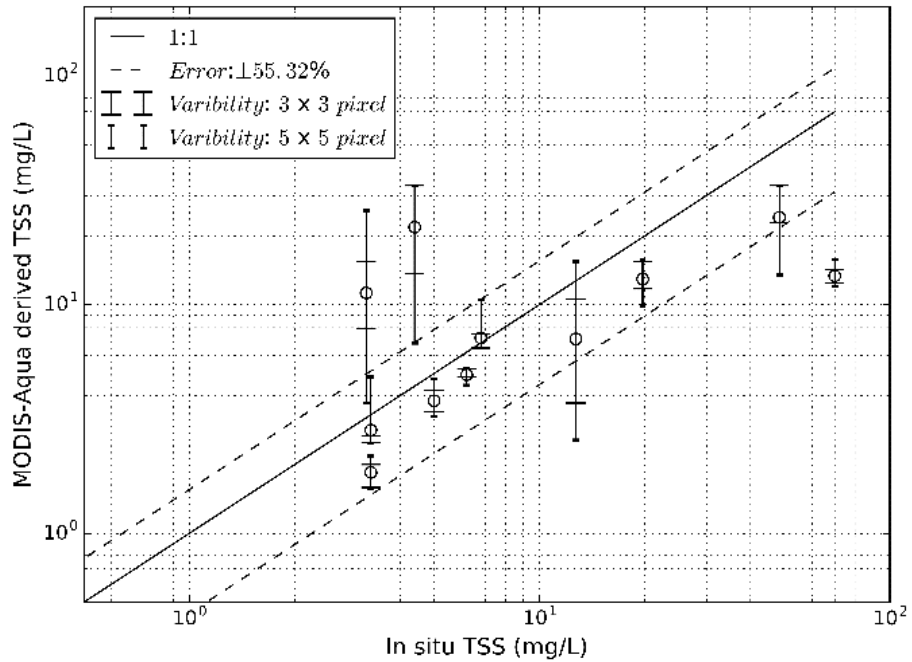
In order to consider the validation of the SASM results against the *in situ* TSS data, we have considered the contribution of two sources of error on the retrieval of TSS concentrations from MODIS-Aqua reflectance, namely the errors in the calibration of model parameters and errors arising from atmospheric correction. Notwithstanding the errors from other sources specifically, such as satellite sensor calibration, time difference between satellite image acquisition, and errors in *in situ* TSS measurements, the total error for AVD30, AVD60, and AVD90 were 43.03%, 55.32%, and 60.91% respectively. The total error is obtained from the following sources: MARE of 33.33% as a model error from the SASM in MODIS band 1 plus respective error for the AVD30, AVD60 and AVD90 from the atmospheric correction process presented in Section 3.4.1.

The validation of the TSS concentration derived using SASM in MODIS-Aqua band 1 shows that AVD30 has the better performance with a MARE of 35.39% while AVD60 and AVD90 had MARE of 94.38% and 78.62% respectively. As the duration between satellites overpass timing and measurement increases, the mismatch between the *in situ* and satellite derived TSS also increases depending on the spatial variability and water dynamics influenced by ocean currents and wind. To account for the source of error of TSS due to time difference between satellite image acquisition and *in situ* measurement, we calculated the average TSS for different pixel window widths. Figures 3.7a–c shows the validation results between the observed TSS and SASM-derived TSS for AVD30, AVD60 and AVD90 respectively. As the time difference between MODIS-Aqua overpass and *in situ* data collection increases the spatial variability in the SASM-derived TSS also increases, as indicated by the error bars displayed on each data point tending to lengthen as we move from AVD30 to AVD90. The effect of TSS spatial variability can be minimised by using an aggregate of larger pixel window sizes. However, using larger window width can also result in higher variability in TSS, especially in waters that vary rapidly in the spatial domain, a common characteristic of waters associated with dredging operations. For

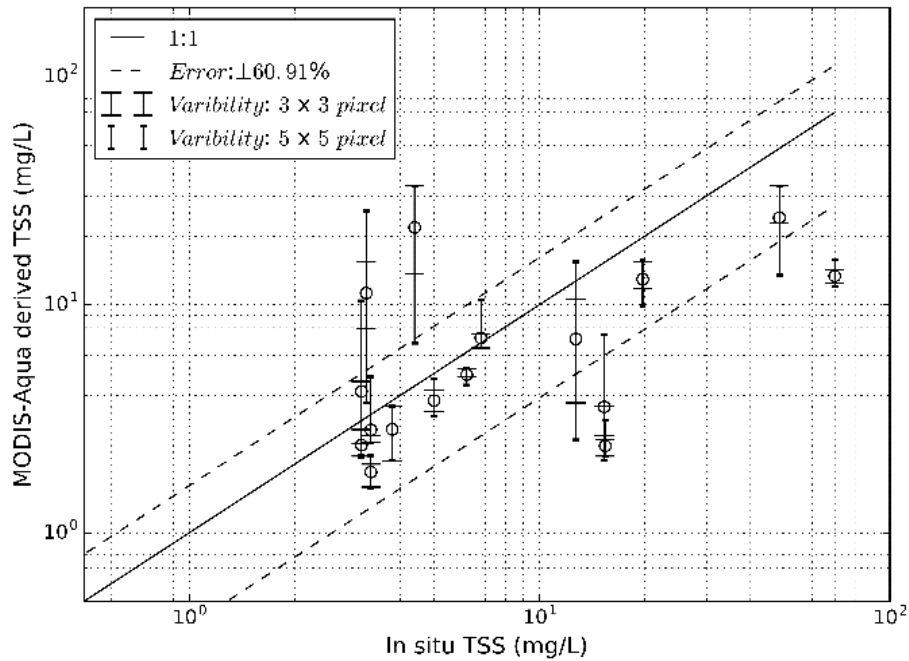
our study site, on the second field trip, we visually observed that high spatial variation in TSS was present in a small spatial domain.



(a)



(b)



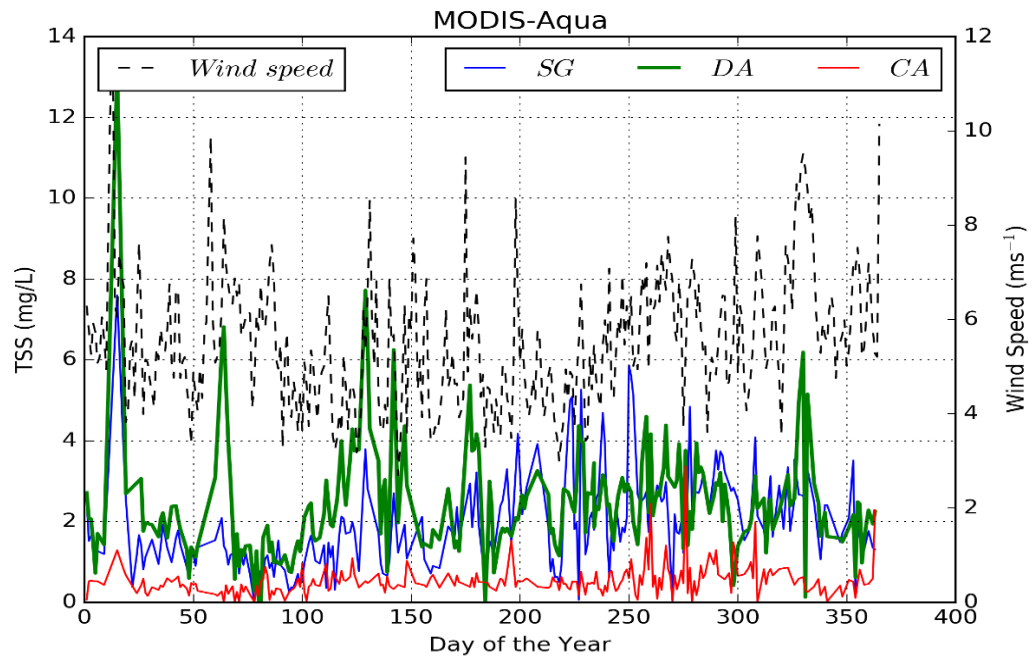
(c)

Figure 3.7: Validation between the SASM-derived TSS from MODIS-Aqua band 1 reflectance for (a) AVD30; (b) AVD60; and (c) AVD90. The error bar indicates the minimum and maximum TSS computed in 3×3 and 5×5 -pixel window widths.

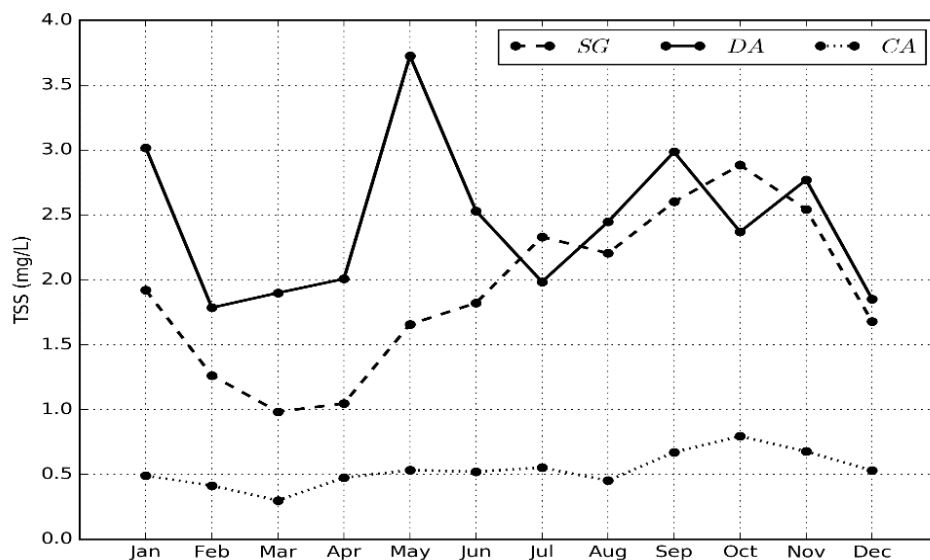
3.4.4.3. Temporal Analysis of 2013 MODIS Imagery

The daily and monthly TSS averages for SG, DA and CA were computed and are shown in Figures 3.8a and 3.8b respectively. In MODIS-Aqua daily TSS plots we see that SG and DA TSS are consistently higher than CA, which is expected because of the location of CA being further from the coast, further from the dredge operation, and in deeper waters thus have less re-suspension of TSS from local tidal influences. The monthly average of MODIS-Terra derived TSS in DA is higher than SG from the beginning of 2013 until June 2013 and then comparable to SG from July 2013 until the end of 2013. After June 2013, the MODIS-Aqua derived TSS in DA is slightly higher than SG for all months except July and October. However, the differences in monthly averaged TSS concentration between SG and DA after June 2013 are not different than monthly averaged TSS concentration before June 2013 (refer to Figures 3.8a, and 3.8b for details). The apparent shift in TSS, in MODIS-Aqua data, from SG being lower in the early half of 2013 and increasing in the later part of 2013 may be as a result of the increasing load of spoil in the SG. Further, the effect of river outflow from the

Ashburton River and intermediate streams created by heavy rain might be a cause of DA being higher in TSS when compared with SG during the early half of 2013. Rainfall data for Onslow Airport shows there was higher rainfall from January to June 2013 when compared with July to December (Bureau of Meteorology, 2015b).



(a)



(b)

Figure 3.8: (a) Daily and (b) monthly averaged TSS derived from the SASM for 2013 MODIS-Aqua data.

Figure 3.8a shows a number of anomalies in daily TSS when compared with the respective trend, apparent as “spikes” in the data. Such

anomalies were examined with respect to the wind speed of the study site to study the potential links to re-suspension of sediment in the water column. From the daily mean average wind speed in 2013 acquired from the Bureau of Meteorology (<http://www.bom.gov.au>) for Onslow Airport, we performed a correlation analysis between wind speed on different days and TSS for all three study regions. In general, for wind speeds less than 7 m s^{-1} there was no significant correlation between wind speed and TSS for any of the regions. For speeds greater than 8 m s^{-1} , and for two and three days before the TSS dates, there was strong correlation observed between TSS and wind speed at all three regions. The results show that for MODIS-Aqua derived TSS, a lag of three days gives the highest correlation ($r = 0.92$) for the DA. The correlation results between wind speed and TSS indicates that the re-suspension of sediments from wind speed greater than 8 m s^{-1} tends to take about three days to build to a maximum before settling down. Specific TSS anomalies in the time series, such as those observed on days 15 (15 January) and 61 (2 March) in Figure 3.8a correspond to the effects of tropical cyclone Narelle which moved as close as 330 km off the coast of Exmouth on 12 January 2013 and severe tropical cyclone Rusty which made landfall on 27 February 2013 in Port Hedland which is located at 389 km north east of Onslow (Bureau of Meteorology, 2015c).

Figure 3.9 show a series of monthly average TSS images spanning 2013 derived from MODIS-Aqua using the SASM. January was impacted by tropical cyclone Narelle, which crossed the study site on 11 and 12 January 2013, thus the average TSS levels are relatively high and widespread. The monthly images show that TSS levels in the SG and DA begin to increase from May and maintain high levels until October, then tend to decrease during November and December. The increase in TSS in both the SG and DA from May is likely due to dredging activities being carried out starting in May and continuing until October 2013. The maximum monthly TSS averages were observed in October in the SG with a TSS concentration of $2.88 \pm 0.52 \text{ mg/L}$, in the DA the maximum was $3.73 \pm 1.21 \text{ mg/L}$ in May, and the CA displayed a maximum of $0.79 \pm 0.04 \text{ mg/L}$ in October amongst the MODIS-Aqua derived monthly TSS averages. The monthly TSS averages

were higher in SG and DA from May to December than the January to March, despite the higher rainfall in the first six months of 2013 (Bureau of Meteorology, 2015b). This is a strong indication of the impact of the dredge process causing higher TSS concentrations.

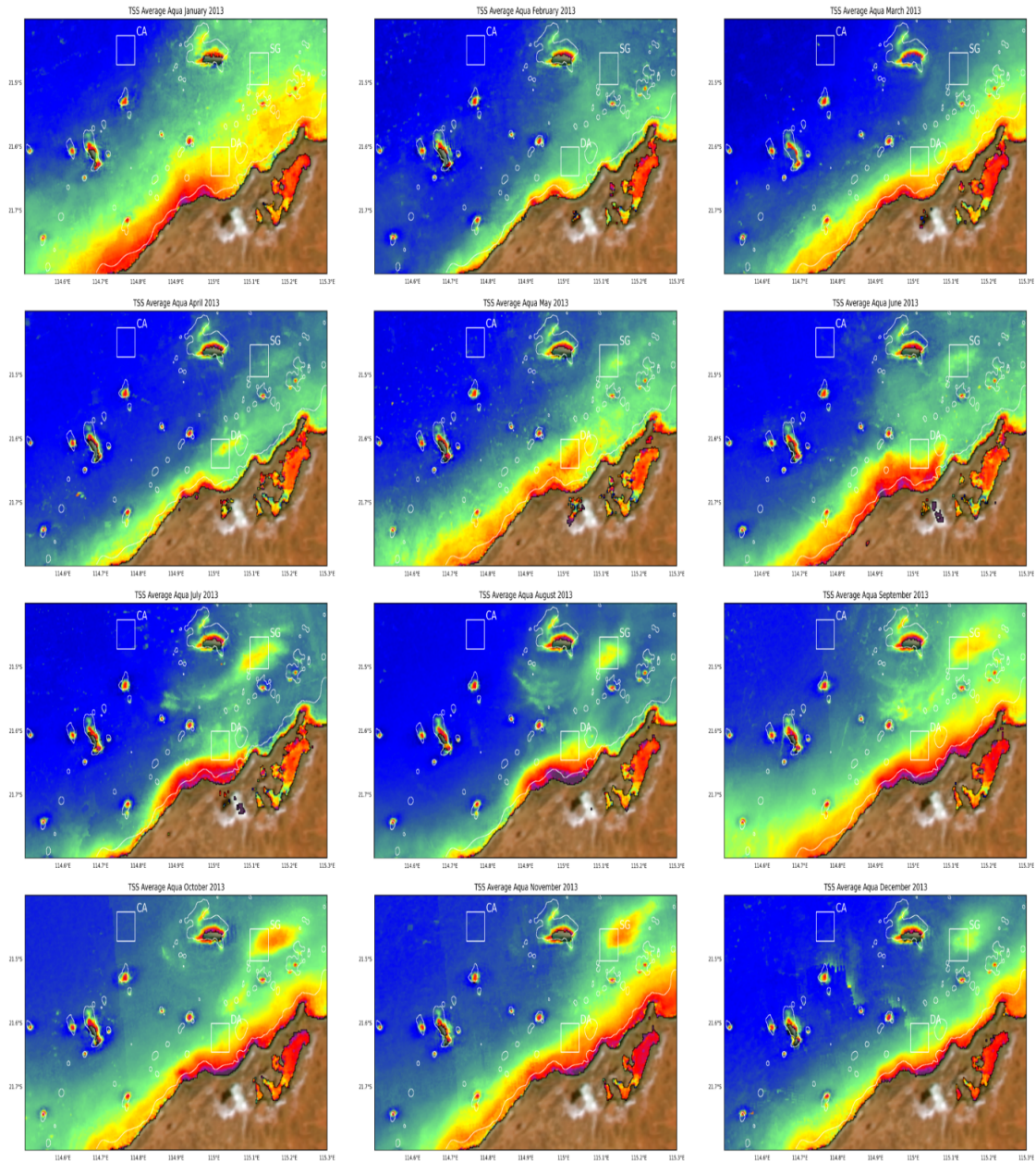


Figure 3.9: 2013 monthly averaged TSS images derived from MODIS-Aqua 250 m band 1 (January to December 2013). Rectangles represent locations for CA, DA, and SG.

3.5 Conclusions

In this paper we developed a semi-analytic sediment model (SASM) that is both physically sensible in its general form and adapted to the northern Western Australian coastal waters in retrieving TSS from 250 m MODIS-

Aqua band 1 reflectance. We assessed the inherent uncertainty due to combined model and atmospheric correction effects in the retrieved TSS product to be 43.03% to 60.91% for MODIS-Aqua. We demonstrated the application of the SASM TSS concentration product in analysing MODIS-Aqua data for 2013 and associated this with the dredge activities at Onslow in Western Australia. The 250 m imagery was successful at highlighting the impact of cyclones and dredge activities on dredge spoil grounds and dredge operation areas. Further, daily anomalies in temporal data were able to be linked to specific causes, including dredge activities, cyclone events, wind-induced re-suspension, and increased river outflow. Thus, we have shown that the SASM, in conjunction with an appropriate atmospheric correction method for MODIS-Aqua band 1, should be sufficient for monitoring TSS in Onslow waters or waters with similar optical properties before, during and after dredging operations. The SASM developed in this study can be applied to other regional waters of Western Australia or waters with similar optical properties, but the application of the SASM beyond the regional waters of Western Australia should be carried out with recalibration of the SASM parameters. The merits of the SASM are the ease in calibration using *in situ* TSS concentration for particular regions of interest, akin to fully empirical algorithm, but also the robustness based on a physical foundation of the radiative transfer theory.

Chapter 4

A Quantitative Comparison of Total Suspended Sediment Algorithms: A Case Study of the Last Decade for MODIS and Landsat-Based Sensors.

This chapter has been published in the journal: Remote Sensing

Dorji, P., & Fearn, P. (2016). A Quantitative Comparison of Total Suspended Sediment Algorithms: A Case Study of the Last Decade for MODIS and Landsat-Based Sensors. *Remote Sensing*, 8(10), 810.

4.1 Abstract

A quantitative comparative study was performed to assess the relative applicability of Total Suspended Solids (TSS) models published in the last decade for the Moderate Resolution Imaging Spectroradiometer (MODIS) and Landsat-based sensors. The quantitative comparison was performed using a suite of statistical tests and HydroLight simulated data for waters ranging from clear open ocean Case-1 to turbid coastal Case-2 waters. The quantitative comparison shows that there are clearly some high performing TSS models that can potentially be applied in mapping TSS concentration for regions of uncertain water type. The highest performing TSS models tested were robust enough to retrieve TSS from different water types with Mean Absolute Relative Errors (MARE) of 69.96%–481.82% for HydroLight simulated data. The models were also compared in regional waters of northern Western Australia where the highest performing TSS models yielded a MARE in the range of 43.11%–102.59%. The range of Smallest Relative Error (SRE) and Largest Relative Error (LRE) between the highest and the lowest performing TSS models spanned three orders of magnitude, suggesting users must be cautious in selecting appropriate models for unknown water types.

4.2 Introduction

The health of coastal waters not only determines the health of marine habitats in the region but also signifies the health of the nearby human inhabitants with nearly 60% of the earth's population settled in the coastal zones of our oceans and seas, and over 90% of the world's fish caught for consumption being sourced from coastal waters (Bukata, 2005). The health of water systems is typically determined from a key indicator, the water clarity (turbidity) which is influenced by the amount of dissolved matter and total suspended solids (TSS) comprising organic matter such as algae and other micro-organisms and inorganic particulate matter from minerals (Macdonald, Ridd, Whinney, Larcombe, & Neil, 2013). Monitoring TSS along with other water quality parameters is crucial for coastal ecology because TSS can directly affect the turbidity and colour of water (Miller & McKee, 2004) and turbidity determines the amount of light availability at depth for primary production (Chen et al., 2010; Havens et al., 2011; Shi et al., 2014).

Monitoring the temporal and spatial distribution of TSS in the coastal environment can be a huge undertaking and nearly impossible in terms of financial and time resources if performed using traditional *in situ* water sampling methods (Kong et al., 2015a) unless coupled with satellite-based remote sensing. Since the early space-borne sensors of the 1970s there has been, and continues to be, a great improvement in the spectral, spatial and temporal resolutions (Chang, Imen, & Vannah, 2015). For example, the Landsat-based series of sensors has evolved over the years from three (red, green and blue) spectral bands with spatial resolutions of 185 m and a revisit time of 18 days to the newest Landsat-8 with 11 spectral bands (433–12,500 nm) with spatial resolutions of 30 m (and 15 m panchromatic) and a revisit time of 16 days. The shortcoming of the long revisit time for Landsat can be filled by the readily available MODIS-Aqua and Terra sensors which have shorter revisit times of one day, and with 36 spectral bands (405–14,385 nm) and spatial resolutions from 250 m to 1000 m.

Since the launch of the early remote sensing satellites in the early 1970s many studies have been conducted in remotely mapping TSS, driven in part by the capability of satellite remote sensing to cover large spatial

domains in near real time (Kong et al., 2015a). Considering the past decade, remote sensing studies of the spatial and temporal mapping of TSS have utilized moderate resolution sensors including Landsat (Olmanson et al., 2008; Vanhellemont & Ruddick, 2014; Wang, Lu, Liew, & Zhou, 2009b; Wu et al., 2015; Wu et al., 2008; Zhang et al., 2014; Zhou et al., 2006), MERIS (Alikas & Reinart, 2008; Chen et al., 2015b; Raag et al., 2013; Shen, Verhoef, Zhou, Salama, & Liu, 2010; Shi et al., 2014; Yang et al., 2011), MODIS (Chen et al., 2015a; Chen, Huang, Chen, & Chen, 2011a; Hudson et al., 2014; Kutser et al., 2007; Raag et al., 2013; Shi et al., 2015; Sipelgas et al., 2006; Wang & Lu, 2010), and high resolution sensors including SPOT (Doxaran et al., 2002), IKONOS (Ekercin, 2007), and THEOS (Lim et al., 2013). Further, the TSS mapping studies encompassed waters with diverse optical and physical properties, from inland lakes and river systems (Kaba et al., 2014; Park & Latrubesse, 2014; Shi et al., 2015; Wang, Han, Kung, & Van Arsdale, 2006; Wang & Lu, 2010) to coastal waters (Chen, Huang, Chen, & Wang, 2011b; Choi et al., 2014; Feng et al., 2014; Nechad et al., 2010; Petus et al., 2014) and from different geographical locations including America (Miller & McKee, 2004; Park & Latrubesse, 2014; Son & Wang, 2012), Africa (Ayana et al., 2015; Kutser et al., 2007), Asia (Chen et al., 2015b; Choi et al., 2014; Islam et al., 2001), Australia (Evans et al., 2012; Islam et al., 2007), and Europe (Hudson et al., 2014; Petus et al., 2014; Raag et al., 2013; Sipelgas et al., 2006).

The majority of the models developed in retrieving TSS by remote sensing methods are typically locally tuned to a regional water or waters with similar optical properties. Regional tuning of a TSS model is necessary because of the potentially large variation in the inherent optical properties (IOPs) of the water constituents. The theoretical basis of ocean colour remote sensing has shown that sensor-measured reflectance of the water is related to the IOPs of the water—absorption and scattering coefficients. IOPs vary with the types and amounts of the water's constituents, such as sediments, phytoplankton, detrital matter and CDOM (Brewin et al., 2015) which may be different for different sediment types and phytoplankton types in different regions. In addition, factors such as water depth, viewing

geometry, and atmospheric conditions all add to the complexity of the relationship between the measurement of reflectance of the water surface and the IOPs and concentrations of constituents (Curran & Novo, 1988).

TSS models are generally classified into three categories, (1) an empirical model where TSS is modelled directly using a statistical analysis to relate the apparent optical properties (AOPs); (2) an analytic model that relates the IOPs and AOPs of water through radiative transfer theory to derive TSS; and (3) a semi-analytic model that is partly based on the empirical analysis and grounded on the radiative transfer theory (Kong et al., 2015a). Individual TSS model designs have their own limitations and advantages. An empirical model is often sought for its simplicity and explanatory power because unique properties of local waters are tuned to each model, but it may lack general applicability. An analytic model is potentially applicable to other water bodies because it is not dependent on the *in situ* water constituents, but it requires accurate knowledge of water column properties which is often difficult to acquire. The semi-analytic model has both the limitations and advantages associated with the first two models, and it is generally preferred because it has higher explanatory power and is more convenient than the analytic model (Chang et al., 2015; Kong et al., 2015a).

In the last decade, various TSS models have been developed (Feng et al., 2014; Nechad et al., 2010; Petus et al., 2014; Qiu, 2013; Wang, Lu, Liew, & Zhou, 2010b) and applied to their respective regions with a wide range of success with reported retrieval errors ranging from lows of ~18% to highs of ~61%. Considering each model is developed and tuned for a specific region, water type and its associated IOPs, the application or transferability of the models to other regions is limited, and the likely accuracy of the results unknown. Even when an existing TSS model is applied to waters in similar regions it is often first re-calibrated before being applied. The availability of many TSS algorithms for different regions and sensors warrants one to ask if we can use someone else's algorithm to estimate TSS in regions where we do not have any *in situ* observations? For the cross applicability of TSS models between different regions the design of

a TSS algorithm has to either be based on analytic methods and grounded on theoretical functions of radiative transfer theory, or the waters must be assumed to have similar optical and physical properties. However, considering the vast number of TSS models that have been developed across different geographical regions with different optical and physical properties we can seek to establish the robustness in the applicability of these existing TSS algorithms for different regions.

A recent study by Brewin, et al. (2015) developed an objective methodology where comparison of different bio-optical algorithms are quantitatively and qualitatively considered for use in climate studies. Following the methods of Brewin, et al. (2015) and their quantitative methodology to rank the algorithms, in this study we objectively compare the performance of TSS algorithms for MODIS and Landsat sensors developed during the last decade using HydroLight simulated data for different water and sediment types. If shown to be robust, these algorithms would provide marine remote sensing scientists and coastal managers some level of confidence in their ability to assess the quality of water with minimal resource for coastal monitoring of optically unexplored waters. Specifically, this study aims to quantitatively assess the applicability of established TSS algorithms to different water types and quantify the variability in retrieving TSS when using off the shelf TSS algorithms for MODIS and Landsat sensors.

4.3. Materials and Methods

4.3.1. Dataset

4.3.1.1. HydroLight Simulation

A set of ocean reflectance spectra were derived using the radiative transfer numerical model HydroLight 4.2 (Sequoia Scientific, Inc., Bellevue, WA 98005, United States of America) in the four component Case-2 waters mode. Using a forward model HydroLight solves radiance distributions and derives reflectance and radiance for water bodies with specific inherent optical properties (SIOPs) for given sky and water state conditions (Mobley,

1994). Sub-surface remote sensing reflectance's (r_{rs}) were computed for infinitely deep water using a range of SIOPs, sea-state, and sky conditions. The spectral range for r_{rs} from HydroLight was simulated for wavelengths (λ) in the range of 400 nm–800 nm at a nominal bandwidth of 4 nm.

For all the HydroLight simulations the sea state was chosen to have a wind speed of 5 m s^{-1} and the sky radiance computed using the Harrison and Coombes (1988) normalized radiance model for a clear sky. The diffuse and direct sky irradiances were computed using the Gregg and Carder (1990) irradiance model for a solar zenith angle of 30° (Mobley & Sundman, 2001). The four components, pure water, chlorophyll (CHL), coloured dissolved organic matter (CDOM), and mineral (TSS) were modelled in varying concentrations, presented in Table 4.1, to be representative of open ocean to turbid coastal waters. For the TSS component, five different sediment types were used, namely (1) brown earth; (2) calcareous sand; (3) yellow clay; (4) red clay; and (5) Bukata from the default database of HydroLight. The phase functions for the components were modelled as Rayleigh like phase function for pure water, Fournier-Forand phase function with $b_b(\lambda)/b(\lambda)$ of 0.01 for CHL, and Petzold “average particle” phase function for TSS for all the aforementioned HydroLight simulations. In addition to the aforementioned parameters for HydroLight simulations, we further carried out additional simulations using the parameters outlined above but with solar zenith angles of 15° , 30° , 45° , and 60° and $b_b(\lambda)/b(\lambda)$ ratios of 0.001, 0.01, 0.018, 0.05, and 0.1 for calcareous sand to study the robustness of TSS models to changes in solar angles and the backscattering ratios.

Table 4.1: Concentration of coloured dissolved organic matter (CDOM), chlorophyll (CHL), and total suspended solids (TSS) used in HydroLight modelling. The pure water component in all the HydroLight runs remains unchanged.

CHL (mg/m ³)	CDOM (m ⁻¹)	TSS (mg/L)
		0.01–1.00 at 0.01 interval
		1.00–10.00 at 0.1 interval
		10.00–50.00 at 1.0 interval
		50.00–100.00 at 2.0 interval
0.01, 3.0, 20.0	0.001, 1.0, 10.0	100.00–250.00 at 5.0 interval
		250.00–500.00 at 10.0 interval
		500.00–2000.00 at 50.0 interval
		2000.00–7000.00 at 250.0 interval

The IOP models used in this HydroLight simulation are described by Equations (4.1) and (4.2). The total absorption coefficient ($a(\lambda)$) is the sum of absorption coefficients of pure water ($a_w(\lambda)$), CHL ($a_\phi(\lambda)$), CDOM ($a_{\text{cdom}}(\lambda)$) and TSS ($a_p(\lambda)$):

$$a(\lambda) = a_w(\lambda) + a_\phi(\lambda) + a_{\text{cdom}}(\lambda) + a_p(\lambda) \quad (4.1)$$

The total scattering coefficient (b) is the sum of scattering coefficients of pure water ($b_w(\lambda)$), CHL ($b_\phi(\lambda)$), and TSS ($b_p(\lambda)$):

$$b(\lambda) = b_w(\lambda) + b_\phi(\lambda) + b_p(\lambda) \quad (4.2)$$

The total backscattering coefficient is expressed as the sum of backscattering coefficients for pure sea water ($b_{\text{bw}}(\lambda)$), particulates ($b_{\text{bp}}(\lambda)$), and phytoplankton pigments ($b_{\text{b}\phi}(\lambda)$).

$$b_b(\lambda) = b_{\text{bw}}(\lambda) + b_{\text{bp}}(\lambda) + b_{\text{b}\phi}(\lambda) \quad (4.3)$$

The SIOP models allow the scaling of the IOP of each component with concentration (X):

$$a_i(\lambda) = a_i^*(\lambda) \times X_i \quad (4.4)$$

$$b_i(\lambda) = b_i^*(\lambda) \times X_i \quad (4.5)$$

where i is the component and $a_i^*(\lambda)$ and $b_i^*(\lambda)$ are component specific absorption and scattering coefficients.

The SIOP of each component was either obtained from HydroLight's default dataset or modeled using established models. For the specific absorption and scattering coefficients: the absorption coefficient for pure water was obtained from Pope and Fry (1997) (Pope & Fry, 1997) and mass-scattering coefficient from Smith and Baker (1981) (Smith & Baker, 1981), the CHL mass-specific absorption coefficient ($a_\phi^*(\lambda)$) from Prieur-Sathyendranath (1981) (Prieur & Sathyendranath, 1981) and the CHL mass-specific scattering coefficient modeled using Equation (4.6), the CDOM mass-specific absorption was modeled using Equation (4.7) and CDOM was considered to be a non-scattering component, and the mineral mass-specific absorption and scattering coefficients were obtained from HydroLight's default dataset for brown earth, calcareous sand, yellow clay, red clay, and Bukata. Figure 4.1a and 4.1b shows the mass-specific absorption and scattering coefficients of the five different minerals used in the HydroLight modelling of water reflectance.

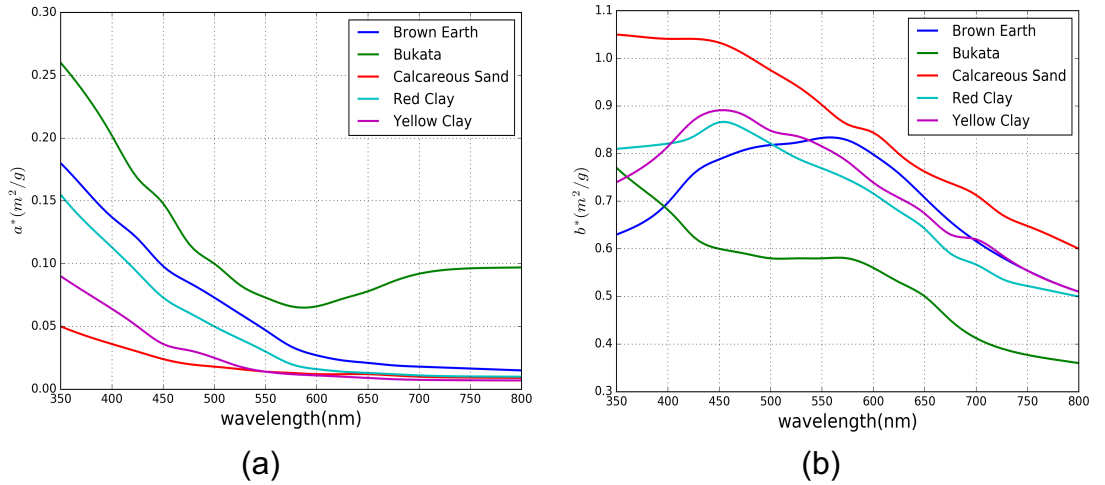


Figure 4.1:(a) Mineral mass-specific absorption and (b) scattering coefficients.

$$b_\phi^*(\lambda) = 0.407CHL^{0.795} \left(\frac{600}{\lambda} \right) \quad (4.6)$$

$$a_{cdom}^*(\lambda) = 0.1 \exp(-0.014 \times (\lambda - 440)) \quad (4.7)$$

4.3.1.2 Extrapolation of Simulated Dataset

The IOP data output by HydroLight do not extend beyond 800 nm, however some of the TSS algorithms for MODIS and Landsat utilize bands beyond the 800 nm reflectance data generated by the HydroLight simulations. To include algorithms which utilize bands in the NIR region of the electromagnetic spectrum, we extrapolated the $r_{rs}(\lambda)$ data from HydroLight to 1300 nm using Equation (4.1) of the quasi-analytical model of Lee et al. (2002) at a nominal wavelength of 1.0 nm:

$$r_{rs}(\lambda) = g_1 \left(\frac{b_b(\lambda)}{a(\lambda) + b_b(\lambda)} \right) + g_2 \left(\frac{b_b(\lambda)}{a(\lambda) + b_b(\lambda)} \right)^2 \quad (4.8)$$

where g_1 and g_2 are assigned either $g_1 = 0.0949$ and $g_2 = 0.0794$ for oceanic Case-1 water (Gordon et al., 1988), $g_1 = 0.084$ and $g_2 = 0.17$ for coastal water, or averaged values of $g_1 = 0.0895$ and $g_2 = 0.1247$ for coastal and Case-1 waters (Lee et al., 2002). The selection of values for g_1 and g_2 were based on the condition that the selected values provided the minimum Mean Absolute Relative Error (MARE) as defined in Equation (E1) in the Appendix E between HydroLight and Equation (4.8) $r_{rs}(\lambda)$ spectra.

To model the $r_{rs}(\lambda)$ spectra to 1300 nm using Equation (4.8), we used the following IOPs—the total absorption coefficient was computed using Equation (4.1) while the total backscattering coefficient was computed using Equation (4.2). Equations (4.4) and (4.5) were used to compute individual component-specific absorption and scattering coefficients using the respective component concentration and the phase function used in the HydroLight simulations as mentioned in Section 4.3.1.1. The total backscattering coefficient in Equation (4.8) was computed from the respective backscattering components in Equation (4.3) which in turn were computed using respective scattering components from Equation (4.2) and scattering phase functions and backscattering ratios discussed in Section 4.3.1.1. The mineral specific absorption and backscattering coefficients were spline extrapolated to 1300 nm to compute the mineral-specific absorption and backscattering coefficients required in Equations (4.4) and (4.5). The $r_{rs}(\lambda)$ spectra generated using HydroLight and modelled using Equation (4.8)

had MARE of 1.6% to 13.73%. The higher relative error was toward the blue end of the spectral region.

4.3.1.3. Grouping of Datasets

Using the extrapolation methods discussed in Section 4.3.1.2, in total 2.2×10^4 $r_{rs}(\lambda)$ spectra were generated for the spectral range of 350 nm to 1300 nm at the nominal wavelength of 1.0 nm for the parameters discussed in Section 4.3.1.1. The water, from the point of view of remote sensing, can be classified into Case-1 and Case-2 water types: Case-1 waters are optically dominated by phytoplankton (CHL) while Case-2 waters are more optically complex with varying concentrations of CHL, CDOM and TSS that are region specific (Curran & Novo, 1988; Doxaran et al., 2002). With respect to modelling the water types, it is not feasible to model each water type that is optically similar to the optical properties of the water where each individual TSS model was developed. The TSS models that are robust enough in one region can often fail when applied to other regions because each TSS model is typically tuned to a specific region where the waters are optically unique. Thus, due to the problem of accurately modelling the waters to suit any specific TSS model, and acknowledging the fact that we cannot simulate all the conditions and compositions of ocean constituents for different regions, we resorted to five different classes (shown in Table 4.2) to represent varying cases of water where concentrations of one ocean constituent might dominate the others or there are different degrees of contributions from each constituent. CLASS I from the water classification in Table 4.2 represents high CHL and low CDOM concentration which in a physical world would be associated with high phytoplankton blooms in eutrophic lakes where concentration of CHL dominates other optically active substances (Arst, 2003). CLASS II with high CDOM and low CHL represents water where CDOM dominates other optically active substances, which is the case in lakes where CHL is generally low, for example as in the case in lakes in boreal regions and waters off the coast in the Baltic Sea (Arst, 2003). CLASS III and IV represent the extreme cases where both CDOM and CHL are either high or low, which can be associated with high phytoplankton blooms

in coastal waters for CLASS III and open ocean water with low CHL for CLASS IV. CLASS V represents a general case of coastal waters where CHL and CDOM are moderate. For all the classes of water discussed above, the TSS is varied in its concentration independent of different water cases considered.

Table 4.2: Five different water classes.

CLASS	CDOM (m ⁻¹)	CHL (mg/m ³)
I	0.01	20.0
II	10.0	0.1
III	10.0	20.0
IV	0.01	0.1
V	1.0	5.0

4.3.1.4. HydroLight-derived Reflectance to Sensor Equivalent Reflectance

The TSS retrieval algorithms developed by various researchers use different types of reflectance measurements to relate to TSS concentrations. The most common choice among all the TSS algorithms considered here is the remote sensing reflectance ($R_{rs}(\lambda)$), which is defined by Equation (4.9).

$$R_{rs}(\lambda) = \frac{L_w(0^+, \lambda)}{E_d(0^+, \lambda)} \quad (4.9)$$

where $L_w(0^+, \lambda)$ is the water leaving radiance and $E_d(0^+, \lambda)$ is the downwelling irradiance evaluated above the water surface. The HydroLight generated $r_{rs}(\lambda)$ was converted to $R_{rs}(\lambda)$ following Lee et al. (2002) as defined by Equation (4.10).

$$R_{rs}(\lambda) = \frac{0.52r_{rs}(\lambda)}{1 - 1.7r_{rs}(\lambda)} \quad (4.10)$$

After converting $r_{rs}(\lambda)$ to $R_{rs}(\lambda)$, depending on the sensor and the bands used by particular TSS algorithms, we convolved $R_{rs}(\lambda)$ from Equation (4.10) to each sensor's respective band reflectance using the spectral response function of the sensor in their respective bands using Equation (4.11).

$$R_{rs}^k = \frac{\int_{\Delta k} R_{rs}(\lambda) s(\lambda) d\lambda}{\int_{\Delta k} s(\lambda) d\lambda} \quad (4.11)$$

where R_{rs}^k is the band averaged R_{rs} for each band, k , with band width Δk and spectral response function $s(\lambda)$ of the sensor.

The next common reflectance type used in TSS algorithms is a normalized water-leaving reflectance which is related to $R_{rs}(\lambda)$ as follows:

$$\rho_w(\lambda)|_N = \pi R_{rs}(\lambda) \quad (4.12)$$

There are also algorithms which employ normalized water leaving radiance which is calculated using Equation (4.13).

$$L_w(\lambda)|_N = \frac{\rho_w(\lambda) \times F_o(\lambda)}{\pi} \quad (4.13)$$

where $F_o(\lambda)$ is the extraterrestrial solar irradiance band averaged to each sensor's band using their respective band spectral response functions.

4.3.2. TSS Models

This section lists the available TSS algorithms from 2000–2015 that are empirical and semi-analytic in their design for MODIS and Landsat-based sensors. We made an effort to select all the available TSS algorithms for the sensors considered in this study using a search database 'Scopus' (<https://www.scopus.com/>), but we acknowledge that some of the literature for TSS algorithms, which were not present in the database, might have been missed. However, within the limitation of our search capability we made an effort to use other science databases and discovered 42 MODIS empirical models and 7 semi-analytical models, 22 Landsat empirical models and 5 semi-analytical models. The summaries of each TSS algorithm are provided in Table B1. Semi-analytical models described in this section encompass all the semi-analytical models from MODIS (MOD-A) and Landsat (LAN-A). Models are considered semi-analytic because they are derived based on a physical form (Chen et al., 2013a) or one or more parameters in the TSS algorithms are either parameterized using site-specific or global in-water bio-optical properties (Nechad et al., 2010). Semi-analytic algorithms for the two sensors considered here consist of algorithms that are based on radiative transfer modelling to relate the dependence of

geo-physical properties of the water, TSS in our case, to the reflectance via IOPs of the water.

Empirical models consist of TSS algorithms that are directly related with *in situ* AOPs of water and the TSS using linear or non-linear regression methods. For the two optical sensors considered here the empirical algorithms from MODIS (MOD-E) and Landsat (LAN-E) will be collectively known as empirical algorithms unless otherwise stated explicitly. The form of the equations used in the empirical methods ranged from simple linear (Kutser et al., 2007; L & Mckae, 2004; Liu, He, Li, & Ren, 2006; Raag et al., 2013), exponential (Choi et al., 2014; Hu et al., 2004; Shi et al., 2015; Wu et al., 2015), power (Qiu, 2013; Wang et al., 2012; Zhang et al., 2014) and other polynomial relationships (Chen, Tingwei, Zhongfeng, & Changsong, 2014c; Chen, Huang, Wang, & Li, 2009; Ondrusek et al., 2012) using single, multiple or combinations of different bands in band ratio or self-formulated indexes. To differentiate the algorithms within each sensor, algorithms will be labelled with a respective number following each sensor's name, MOD-A1 and MOD-E1 will represent MODIS semi-analytic algorithm 1 and MODIS empirical algorithm 1 respectively; likewise, a similar naming convention is followed for TSS algorithms for Landsat-based sensors.

4.3.3. Statistical Tests and Scoring System

The statistical tests used to evaluate the performance of each TSS algorithm for different types of water described in Section 4.3.1.3 are based on the statistical tests used by Brewin et al. (2015). Further, to objectively rank the TSS algorithms we used the point scoring system of Brewin et al. (2015). The details of each statistical test and scoring system of each test adopted from Brewin et al. (2015) are described in the following sections. Further, to contain the effect of spurious TSS generated by some of the TSS models being applied outside their range, we only included TSS estimations that were between a lower bound available in each TSS model (zero for the TSS models which did not contain the lower bound) and an upper bound of twice the highest TSS concentration reportedly used to calibrate each TSS model.

4.3.3.1. Pearson Correlation Coefficient (r) Test

The point scoring system for the r test involves determining if the r -value for each TSS algorithm is statistically significant when compared with the mean r -value for all TSS algorithms. The statistical significance is determined through z -scores and the z -score is computed through Fisher's r -to- z transformation using relationships between the r -values of two models and the total number of samples used to determine the r -values, described in Brewin et al. (2015) as:

$$z_1 = 0.5 \log\left(\frac{1+r_1}{1-r_1}\right) \quad (4.14)$$

$$z_2 = 0.5 \log\left(\frac{1+r_2}{1-r_2}\right) \quad (4.15)$$

$$z_{score} = \frac{z_1 - z_2}{\sqrt{\frac{1}{n_1 - 3} + \frac{1}{n_2 - 3}}} \quad (4.16)$$

where r_1 is the r -value of a specific TSS algorithm and r_2 is the mean of all r -values from all the TSS algorithms. Similarly, n_1 is the number of samples in a specific TSS algorithm and n_2 is the mean number of samples from all TSS algorithms.

For algorithm comparison, a two-tailed test was performed using the Z -score to determine the p -value. If the p -value was less than 0.05 then the r -values were considered as statistically significant and for each TSS algorithm that were statistically significant the following scores were assigned comparing the r -value and the mean r -value (\bar{r}) of all TSS algorithms:

$$r\text{-test} \left\{ \begin{array}{ll} 0 \text{ points} & \text{if } r < \bar{r} \\ 1 \text{ point} & \text{if } r = \bar{r} \\ 2 \text{ points} & \text{if } r > \bar{r} \end{array} \right. \quad (4.17)$$

4.3.3.2. Root Mean Square Error (ψ) Test:

The Root Mean Square Error (ψ) of a model estimate, y_i , with respect to a true value, x_i , can be computed using Equation (4.18):

$$\psi = \sqrt{\frac{1}{N} \sum_{i=1}^N (y_i - x_i)^2} \quad (4.18)$$

The 95% confidence intervals were also calculated for each TSS algorithm and the mean of all TSS algorithms. For each TSS algorithm, the following scoring points were assigned according to the conditions in Equation (4.19):

$$\psi\text{-test} \begin{cases} 0 \text{ points} & \text{if } \psi - \psi_{95\%CI} > \bar{\psi} + \bar{\psi}_{95\%CI} \\ 1 \text{ point} & \text{if } \bar{\psi} - \bar{\psi}_{95\%CI} \leq \psi - \psi_{95\%CI} \leq \bar{\psi} + \bar{\psi}_{95\%CI} \text{ or } \bar{\psi} - \bar{\psi}_{95\%CI} \leq \psi + \psi_{95\%CI} \leq \bar{\psi} + \bar{\psi}_{95\%CI} \\ 2 \text{ points} & \text{if } \psi + \psi_{95\%CI} < \bar{\psi} - \bar{\psi}_{95\%CI} \end{cases} \quad (4.19)$$

where $\psi_{95\%CI}$ and $\bar{\psi}_{95\%CI}$ is the 95% confidence interval of ψ and mean $-\psi$ ($\bar{\psi}$) of all TSS algorithms respectively.

Figure 4.2 shows an example of scoring point classification for Landsat algorithms used in retrieving TSS concentration for the ψ -test.

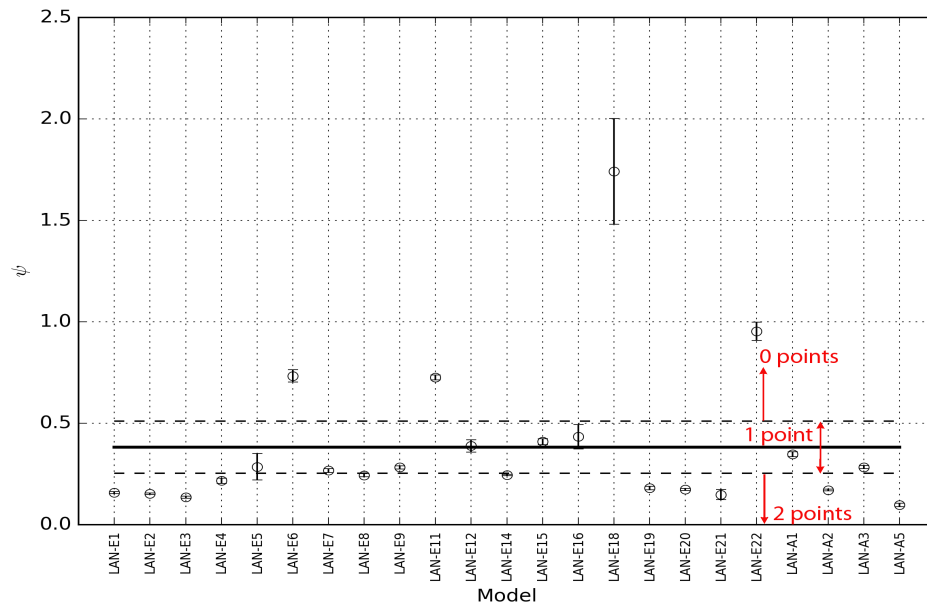


Figure 4.2: Point classification for Landsat algorithms using the Root Mean Square Error (RMSE) Test. The upper and lower dashed lines indicate the mean \pm 95% confidence limits and the solid horizontal line is the mean RMSE of all the TSS algorithms. Unfilled circles are RMSE of each TSS algorithm with respective \pm 95% confidence limits shown by error bars.

4.3.3.3. The Bias (δ) Test

The bias (δ) of model estimate y_i and true x_i is calculated using Equation (4.20):

$$\delta = \frac{1}{N} \sum_{i=1}^N (y_i - x_i) \quad (4.20)$$

For each TSS algorithm, following score points were awarded according to the conditions in Equation (4.21):

$$\delta\text{-test} \begin{cases} 0 \text{ points} & \text{if } \delta_{95\%CI} > \bar{\delta}_{95\%CI} \text{ AND } \delta - \delta_{95\%CI} > 0 + \delta_{95\%CI} \text{ or } \delta + \delta_{95\%CI} > 0 - \delta_{95\%CI} \\ 1 \text{ point} & \text{if } \delta_{95\%CI} < \bar{\delta}_{95\%CI} \text{ or } 0 - \bar{\delta}_{95\%CI} \leq \delta + \delta_{95\%CI} \leq 0 + \bar{\delta}_{95\%CI} \text{ or } 0 - \bar{\delta}_{95\%CI} \leq \delta - \delta_{95\%CI} \leq 0 + \bar{\delta}_{95\%CI} \\ 2 \text{ points} & \text{if } \delta_{95\%CI} < \bar{\delta}_{95\%CI} \text{ AND } 0 - \bar{\delta}_{95\%CI} \leq \delta - \delta_{95\%CI} \leq 0 + \bar{\delta}_{95\%CI} \text{ or } 0 - \bar{\delta}_{95\%CI} \leq \delta + \delta_{95\%CI} \leq 0 + \bar{\delta}_{95\%CI} \end{cases} \quad (4.24)$$

where $\delta_{95\%CI}$ and $\bar{\delta}_{95\%CI}$ is the 95% confidence interval of mean $-\delta$ ($\bar{\delta}$) of all TSS algorithms respectively. Further, to score one point only one conditions must be satisfied while to score two points both the conditions must be satisfied.

4.3.3.4. The Center-Pattern Root Mean Square Error (Δ) Test:

The center-pattern Root Mean Square Error (Δ) is calculated using Equation (4.22):

$$\Delta = \sqrt{\frac{1}{N} \sum_{i=1}^N \{(y_i - \bar{y}) - (x_i - \bar{x})\}^2} \quad (4.22)$$

The 95% confidence intervals were also calculated for each TSS algorithm and the mean of all TSS algorithms. For each TSS algorithm, the following scores were assigned according to the conditions in Equation (4.23):

$$\Delta\text{-test} \begin{cases} 0 \text{ points} & \text{if } \Delta - \Delta_{95\%CI} > \bar{\Delta} + \bar{\Delta}_{95\%CI} \\ 1 \text{ point} & \text{if } \bar{\Delta} - \bar{\Delta}_{95\%CI} \leq \Delta - \Delta_{95\%CI} \leq \bar{\Delta} + \bar{\Delta}_{95\%CI} \text{ or } \bar{\Delta} - \bar{\Delta}_{95\%CI} \leq \Delta + \Delta_{95\%CI} \leq \bar{\Delta} + \bar{\Delta}_{95\%CI} \\ 2 \text{ points} & \text{if } \Delta + \Delta_{95\%CI} < \bar{\Delta} - \bar{\Delta}_{95\%CI} \end{cases} \quad (4.23)$$

where $\Delta_{95\%CI}$ and $\bar{\Delta}_{95\%CI}$ is the 95% confidence interval of Δ and mean $-\Delta$ ($\bar{\Delta}$) of all TSS algorithm respectively.

4.3.3.5. The Slope (S) and Intercept (I) of a Type-2 regression Test

The Slope (S) and Intercept (I) of a type-2 regression (Glover, Jenkins, & Doney, 2011) were calculated using Equation (4.24):

$$Y = X \times S + I \quad (4.24)$$

where Y is the TSS estimates derived from the TSS algorithms and X the true TSS. The following scores were assigned by comparing the S —value of each TSS algorithm and mean— S (\bar{S}) value of all TSS algorithms.

$$S\text{-test} \begin{cases} 0 \text{ points} & \text{if } \sigma_s > \sigma_{\bar{s}} \text{ AND } S - \sigma_s > 1 + 2\sigma_{\bar{s}} \text{ or } S + \sigma_s < 1 - 2\sigma_{\bar{s}} \\ 1 \text{ point} & \text{if } \sigma_s < \sigma_{\bar{s}} \text{ or } 1 - 2\sigma_{\bar{s}} \leq S - \sigma_s \leq 1 + 2\sigma_{\bar{s}} \text{ or } 1 - 2\sigma_{\bar{s}} \leq S + \sigma_s \leq 1 + 2\sigma_{\bar{s}} \\ 2 \text{ points} & \text{if } \sigma_s < \sigma_{\bar{s}} \text{ AND } 1 - 2\sigma_{\bar{s}} \leq S - \sigma_s \leq 1 + 2\sigma_{\bar{s}} \text{ or } 1 - 2\sigma_{\bar{s}} \leq S + \sigma_s \leq 1 + 2\sigma_{\bar{s}} \end{cases} \quad (4.25)$$

where $\sigma_{\bar{s}}$ is the standard deviation of \bar{S} from all TSS algorithms.

For the I parameter, for each TSS algorithm, the following scores were assigned according to the conditions in Equation (4.26).

$$I\text{-test} \begin{cases} 0 \text{ points} & \text{if } \sigma_I > \sigma_{\bar{I}} \text{ AND } I - \sigma_I > 0 + 2\sigma_{\bar{I}} \text{ or } I + \sigma_I < 0 - 2\sigma_{\bar{I}} \\ 1 \text{ point} & \text{if } \sigma_I < \sigma_{\bar{I}} \text{ or } 0 - 2\sigma_{\bar{I}} \leq I - \sigma_I \leq 0 + 2\sigma_{\bar{I}} \text{ or } 0 - 2\sigma_{\bar{I}} \leq I + \sigma_I \leq 0 + 2\sigma_{\bar{I}} \\ 2 \text{ points} & \text{if } \sigma_I < \sigma_{\bar{I}} \text{ AND } 0 - 2\sigma_{\bar{I}} \leq I - \sigma_I \leq 0 + 2\sigma_{\bar{I}} \text{ or } 0 - 2\sigma_{\bar{I}} \leq I + \sigma_I \leq 0 + 2\sigma_{\bar{I}} \end{cases} \quad (4.26)$$

where $\sigma_{\bar{I}}$ is the standard deviation of mean— I (\bar{I}) from all TSS algorithms.

Further, in the S and I —test in Equations (4.25) and (4.26), to score one point only one of the two conditions must be satisfied while to score two points both the conditions must be satisfied.

4.3.3.6. Percentage of Possible Retrievals (η):

The percentage of possible retrievals (η) was calculated using Equation (4.27):

$$\eta = \frac{N^E}{N^M} \times 100\% \quad (4.27)$$

where N^E is the total number of TSS retrieved using each TSS algorithm from the total number of TSS concentrations (N^M) considered in the study. For the point scoring system the following basis was followed:

$$\eta\text{-test} \begin{cases} 0 \text{ points} & \text{if } \eta < \bar{\eta} - \sigma_{\bar{\eta}} \\ 1 \text{ point} & \text{if } \bar{\eta} - \sigma_{\bar{\eta}} \leq \eta \leq \bar{\eta} + \sigma_{\bar{\eta}} \\ 2 \text{ points} & \text{if } \eta > \bar{\eta} + \sigma_{\bar{\eta}} \end{cases} \quad (4.28)$$

where $\bar{\eta}$ and $\sigma_{\bar{\eta}}$ is the mean η -value and its standard deviation for all TSS algorithm in η -test.

4.3.3.7. Total Points

For objective comparison the performance of each TSS algorithm with respect to different water types, all points from each statistical test were added and normalized by the mean score of all TSS algorithms. Thus, a score of zero indicates that the TSS algorithm is performing lower than the mean of all TSS algorithms, a score of one indicates that the TSS algorithm is at par with the average of all TSS algorithms, and a score of 2 means the TSS algorithm is better than the mean of all TSS algorithms.

Further, to test the stability of the scoring systems used in this study, we used a bootstrap method (Efron, 1979), with 1000 runs and each time generating a new dataset by resampling via the replacement method for model generated TSS and HydroLight TSS. Each new dataset was tested using the statistical tests and scored using the scoring system described in Section 4.3.3. The results reported in the Section 4.4 are the mean values of the total points from the bootstrapping method with 2.5 and 97.5 percentiles reported as uncertainty estimates for 95% confidence limits.

4.3.3.8. Mean of Total Points

The mean of total points is achieved by averaging the score of each TSS model across different sediment types or solar zenith angles or backscattering ratios for the particular water classes described in Section 4.3.1.3. For example, in the case of different sediment types in CLASS-I water, the mean of total points in CLASS-I is an aggregate of total scores of each TSS model for different sediment types. For the case of different backscattering ratios and solar zenith angle, the mean of total points is an aggregate of each TSS model for different backscattering ratios and solar zenith angles, respectively, for a specific sediment type in a particular water class. The error bars in the mean of total points are the mean of uncertainty estimates of the total points obtained from the 95% confidence limit from the bootstrapping method.

4.3.3.9. Final Score

The final score is the aggregate of the mean of total points across all water classes for different sediment types, backscattering ratios and solar zenith angles. For example, the final score for MOD-E1 is derived as the mean from the aggregate score of MOD-E1 at five different sediment types, backscattering ratios, and solar zenith angles across all five different water classes. The error bars are the standard deviation of errors from the mean of total points across all five different water classes. Figure 4.3 shows an illustration of the point score system adapted from Brewin et al. (2015) and used in comparing TSS models in this study. The error bars in the Final score are the mean of uncertainty estimates from the mean of total points.

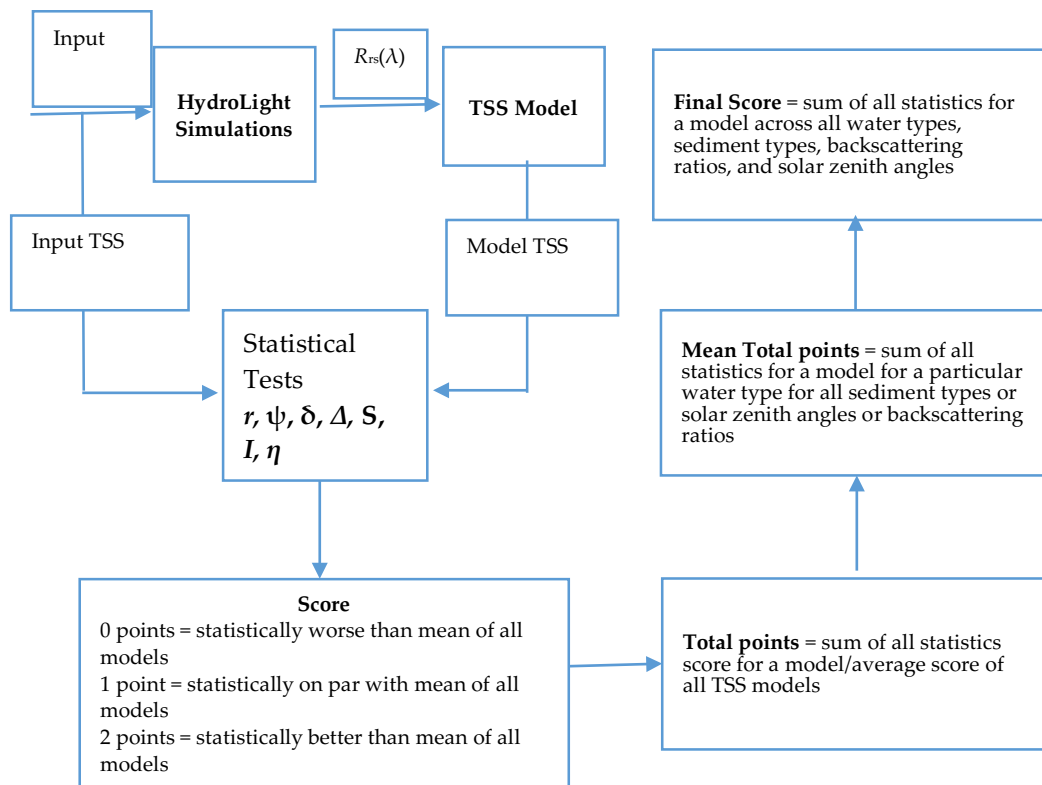


Figure 4.3: Flow diagram showing the methodology of the point scoring system described in Section 4.3.3.

4.4 Results

4.4.1. TSS Model Comparisons

Figures 4.4 and 4.5 show the quantitative comparison between the models using the final scores which are aggregates of the total scores from

different sediment types, backscattering ratios, and solar zenith angles across all five different water classes for MODIS and Landsat-based models respectively. The final results presented in Figures 4.4 and 4.5 are indications of the overall performance of the TSS models when weighted across different water types, sediment types and backscattering ratios. The detailed results of individual model performance in respective sediment types, backscattering ratios, and water types are presented in Appendix F. In addition, the Supplementary A1-A10 also provide the detailed statistical test results for each TSS model.

From the final scores displayed in Figures 4.4 and 4.5 we can visually observe that there are clearly high and low performing models. The high performing MODIS TSS models with final scores greater than 1.5, in the order of highest to lowest final score, are MOD-E6, MOD-A1, MOD-E28, MOD-A4, MOD-E10, and MOD-E42 and low performing MODIS TSS models with scores less than 0.5 are MOD-E8, MOD-E2, MOD-E24, MOD-E22 and MOD-E32. For the Landsat TSS models, LAN-E3, LAN-A4, LAN-E9, LAN-A5, and LAN-A1 have final scores greater than 1.5 while LAN-E11, LAN-E22, LAN-E16, and LAN-E18 have final scores less than 0.5. In the final scores of low performing TSS models, the LAN-E18 model has scores of zeros which shows that LAN-E18 failed to derive TSS within the acceptable TSS bounds of 0.4–5.8 mg/L. We suspect the published algorithm includes an error. The overall ranking of the TSS models using the final scores for each TSS model is also presented in Tables C1 and C2 for MODIS and Landsat respectively. Further, Tables D1 and D2 provides mean total scores for different sediment types, backscattering ratios, and solar zenith angles in all five water classes for respective TSS model.

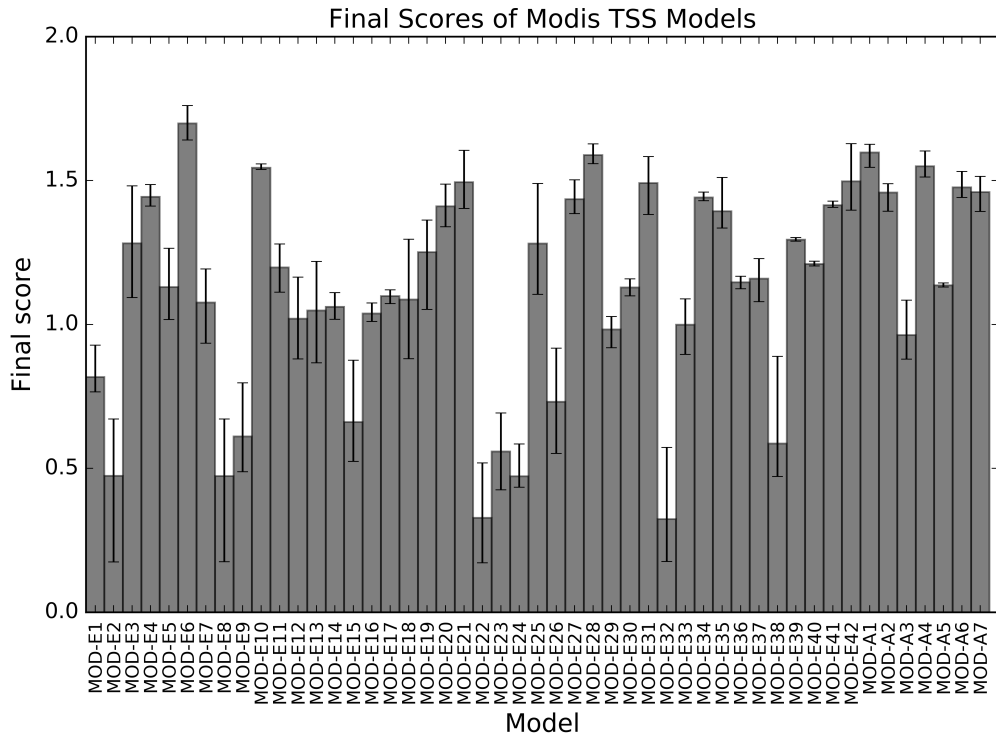


Figure 4.4: Final scores of MODerate resolution Imaging Spectroradiometer (MODIS) TSS models.

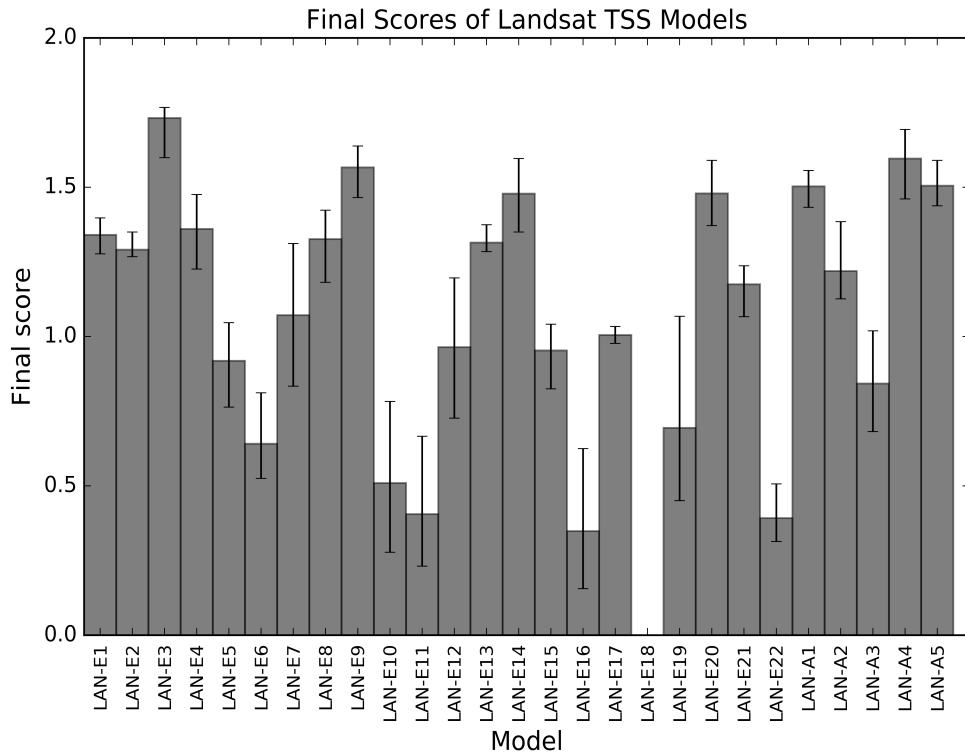


Figure 4.5: Final scores of Landsat TSS models.

With respect to the results displayed in Figures 4.4 and 4.5, without the inclusion of error bars the distinction between the high performing TSS models is clear and we can easily compare the scores of each TSS model to obtain a ranking. For instance, in Figures 4.4 and 4.5, the MOD-E6 and LAN-E3 are the highest scoring models with final scores of 1.70 and 1.73 respectively. However, on inclusion of the error bars, all high performing TSS models may be considered comparable and difficult to separate in terms of robustness, thus may all be ranked equally. Likewise, the case is similar for low performing TSS models where their error bars overlap. Further, we observe that two and three of the top five high scoring TSS models in MODIS and Landsat respectively are semi-analytic while none of the semi-analytic models were in the bottom five low scoring models.

4.4.2. Evaluation of Models

4.4.2.1. Model Evaluation Using HydroLight Data

The five high and low scoring models from MODIS and Landsat TSS models were selected to further evaluate their performance. From all available HydroLight data discussed in Section 4.3.1.1, the aforementioned high scoring TSS models were evaluated for their Relative Error (RE) between model-derived and HydroLight TSS. From the results presented in Table 4.3 we observe that there is high variability in the RE results amongst the respective MODIS and Landsat TSS models. The differences in the Smallest Relative Error (SRE) for high scoring TSS models were not as large as the differences within the MARE and Largest Relative Error (LRE). The MARE ranged from a low of 69.96% to a high of 481.82% while the SRE and LRE ranged from 15% to 63.14% and 139.35% to 1109.80% respectively. In the low scoring models, the high variability in the RE was observed with the MARE for low performing models ranging from 106.43% to 1832.79% while the SRE and LRE ranged from 39.90% to 213.54% and 118.16% to 6778.93% respectively. In both MODIS and Landsat high scoring models, the LRE results were for backscattering ratios of 0.001 and for Bukata type sediment. The SRE results were for backscattering ratios of 0.01 and calcareous sand sediment. Further, for the SRE in both the high and low

performing TSS models, we observe that the high and low performing TSS models scored reasonably well in either one of the categories in sediment types, backscattering ratios, solar zenith angle and water classes. For instance, the low performing LAN-E22 scored higher than most of the high scoring TSS models in SRE results which indicated that LAN-E22 retrieves better in one of the water types.

The TSS derived using real satellite-data are bound by uncertainty related to observational, instrumental, measurement and data processing errors, the latter largely associated with the atmospheric correction procedure (Chen, Lee, Hu, & Wei). Thus, to assess the tolerance of high and low performing TSS models to the uncertainties in R_{rs} , which is the key input in derivation of the TSS concentration, we simulated the effect of R_{rs} uncertainty (ΔR_{rs}) by varying the R_{rs} by $\pm 10\%$, $\pm 20\%$ and $\pm 50\%$ of the HydroLight generated R_{rs} at each of the MODIS and Landsat bands. The $R_{rs} \pm \Delta R_{rs}$ was used in deriving TSS concentration and compared with HydroLight input TSS to calculate the Absolute Relative Error (ARE) of the TSS model. Table 4.3 reports the ARE and the MARE of HydroLight Data Validation as defined in Equation E2 in Appendix E. In general, we observe that with the increase in ΔR_{rs} the ARE also increases and the errors are higher for $+\Delta R_{rs}$ than $-\Delta R_{rs}$. The ARE for high scoring TSS models ranged from 33.14% to 1974.47% while for low scoring TSS models it ranged from 82.69% to 12747.84% which shows both high and low performing TSS models are not impervious to uncertainty in R_{rs} measurements. However, high scoring TSS models show better tolerance to ΔR_{rs} than the low scoring TSS models. The details of the TSS models deviation in estimating TSS concentration from the error-free HydroLight data with ΔR_{rs} are shown in Table 4.3.

Table 4.3: Relative Error and ΔR_{rs} Uncertainty Tolerance results for the highest and lowest scoring models' evaluation using HydroLight Data. The highest scoring models are in bold text and the lowest scoring models are in regular italic text. The results provided in parenthesis represent the $+\Delta R_{rs}$ and '-' indicates the model failed to provide TSS estimation within acceptable bounds. SRE: Smallest Relative Error. LRE: Largest Relative Error. MARE: Mean Absolute Relative Error. ARE: Absolute Relative Error.

Model	Relative Errors from HydroLight Data Validation			ARE from R_{rs} Uncertainty (%)		
	SRE (%)	MARE (%)	LRE (%)	- (+) 10% ΔR_{rs}	- (+) 20% ΔR_{rs}	- (+) 50% ΔR_{rs}
MOD-E6	59.35	94.30	139.35	70.46 (113.02)	44.59 (129.11)	91.94 (170.65)
MOD-A1	15.00	75.56	151.14	39.24 (126.59)	38.89 (182.84)	97.92 (294.93)
MOD-E28	51.61	148.62	191.97	97.96 (211.76)	49.89 (271.68)	53.30 (497.21)
MOD-A4	63.14	257.59	386.87	157.51 (346.27)	68.10 (410.35)	96.13 (530.23)
MOD-E10	32.17	92.42	171.47	53.64 (149.97)	33.54 (242.01)	49.85 (396.29)
<i>MOD-E8</i>	<i>189.55</i>	<i>220.69</i>	<i>344.16</i>	<i>244.77 (197.29)</i>	<i>268.89 (180.18)</i>	<i>341.16 (164.68)</i>
<i>MOD-E2</i>	<i>189.55</i>	<i>220.69</i>	<i>344.16</i>	<i>244.77 (197.29)</i>	<i>268.89 (180.18)</i>	<i>341.16 (164.68)</i>
<i>MOD-E24</i>	<i>77.87</i>	<i>141.49</i>	<i>218.80</i>	<i>10824.61 (9960.40)</i>	<i>11278.06 (9549.92)</i>	<i>12747.84 (8416.88)</i>
<i>MOD-E22</i>	<i>42.31</i>	<i>1832.79</i>	<i>5403.47</i>	<i>2461.87 (1149.55)</i>	<i>1369.44 (1306.50)</i>	<i>187.31 (1206.94)</i>
<i>MOD-E32</i>	<i>39.90</i>	<i>1717.85</i>	<i>6778.93</i>	<i>2575.05 (1067.58)</i>	<i>1381.65 (1385.73)</i>	<i>184.20 (288.28)</i>
LAN-E3	59.31	120.37	166.68	69.03 (170.14)	33.14 (220.15)	76.58 (387.62)
LAN-A4	57.05	197.26	266.40	134.36 (262.03)	72.73 (331.63)	74.29 (541.89)
LAN-E9	23.52	481.82	1109.80	171.42 (857.00)	51.00 (1167.00)	92.43 (1974.47)
LAN-A5	62.86	244.28	362.44	149.20 (341.63)	66.53 (414.85)	95.90 (543.85)
LAN-A1	16.07	69.96	141.53	38.02 (115.85)	39.00 (169.17)	97.78 (286.31)
<i>LAN-E10</i>	<i>76.17</i>	<i>106.43</i>	<i>118.16</i>	<i>88.74 (126.91)</i>	<i>82.69 (161.62)</i>	<i>-(357.92)</i>
<i>LAN-E11</i>	<i>213.54</i>	<i>241.28</i>	<i>337.58</i>	<i>260.07 (22.48)</i>	<i>278.86 (203.89)</i>	<i>335.21 (177.52)</i>
<i>LAN-E22</i>	<i>19.41</i>	<i>110.69</i>	<i>164.56</i>	<i>110.70 (110.688)</i>	<i>110.64 (110.72)</i>	<i>196.66 (110.60)</i>
<i>LAN-E16</i>	<i>77.55</i>	<i>135.45</i>	<i>222.93</i>	<i>150.00 (109.18)</i>	<i>151.20 (103.59)</i>	<i>223.24 (85.67)</i>
<i>LAN-E18</i>	-	-	-	-	-	-

4.4.2.2. Model Evaluation Using In situ Data

As part of a regional water monitoring program, *in situ* reflectance and TSS measurements were carried out for the waters off the coast of northern Western Australia to develop regional TSS models (see MOD-A1 and LAN-A1 in Appendix C)(Dorji et al., 2016). The details of the *in situ* measurements and regional TSS model developed using *in situ* data can be obtained from (Dorji et al., 2016). A set of high scoring models (MOD-E10, MOD-A4, LAN-E9, and LAN-A5) and low scoring models (MOD-E1, MOD-E38, LAN-E6, and LAN-A3) were selected to compare with MOD-A1 and LAN-A1 in the context of *in situ* data comparisons. These subsets of models were selected because the reflectance bands used by other high scoring models were beyond the available reflectance bands in the *in situ* data. Table 4.4 shows the Mean RE results obtained from each of the model evaluations against *in situ* data. Table 4.4 displays a high variability in the Mean RE for model comparisons

for high scoring models with *in situ* data, from a low of 43.11% for LAN-E9 to a high of 102.59% for LAN-A5. When compared with the regional model's MOD-A1 and LAN-A1 MARE results, we see that both the high scoring TSS models MOD-E10 and LAN-E9 and low scoring TSS models LAN-E6 and LAN-A3 were comparable. However, the results presented in Table 4.4 also show the extreme variability observed in the Mean RE for the low scoring models with a low of 35.62% and a high of 256%.

Table 4.4: The MARE for high and low scoring models for *in situ* data. The high scoring models are in bold text and the low scoring models are in italics.

Error/ Model	MOD- E10	MOD- A1 *	MOD- A4	<i>MOD- E1</i>	<i>MOD- E38</i>	LAN- E9	LAN- A1 *	LAN- A5	<i>LAN- E6</i>	<i>LAN- A3</i>
MARE (%)	46.20	33.33	100.85	<i>341.04</i>	<i>256.00</i>	43.11	33.36	102.59	55.23	35.62

* MARE was obtained using the leave-one-out cross validation method discussed in (Dorji et al., 2016).

4.5 Discussion

4.5.1. Data and Methodological Limitation

The data used in this study to quantitatively compare TSS models have been generated using the widely used (Albert & Mobley, 2003; Du, Lee, & Carder, 2006) in-water radiative transfer model HydroLight 4.2. The simulated data do not encompass all different water types in which each TSS model was developed to be used, however, it does provide us with a dataset that is independent of the data that has been used to parameterize the models to avoid biases in the results. To include all the models in comparisons, the simulated data were extrapolated to the NIR region of the spectrum using the methods discussed in Section 4.3.1.2. The extrapolation of reflectance data can introduce unrealistic values if the underlying assumptions of the spline extrapolation methodology does not hold true for the NIR regions. The extrapolation of the data is not ideal when used in modelling remote sensing products but the error for extrapolation had a MARE of 4.0% which was

considered to be acceptable for this study. The ideal case for data for model comparisons would be to use a real global water database, which is currently not available. The NOMAD dataset (<http://seabass.gsfc.nasa.gov/>) that is currently the most extensive dataset of *in situ* reflectance measurement and in-water variables did not contain the TSS measurements essential for this study.

The use of the objective methodology Brewin et al. (2015) of comparing models, used in this study to compare TSS models, can aid users in selection of TSS models that are best suited for waters of regional interest in the absence of means and a method to produce their own regionally tuned TSS algorithms. However, the objective methodology used here is not without limitations, as discussed by Brewin et al. (2015) with respect to using average performance to classify between high and low performing models. The very low performance of one particular model would affect the average of all other models to the extent that it becomes difficult to differentiate scores between models. For example, in Figure F1 for the score of MODIS TSS models in yellow clay, MOD-E1-2, E8-9, E15, E22-24, E32, and E38 all have low scores which increases the score of other TSS models making it difficult to differentiate among high scoring models. This problem is further exacerbated when the majority of TSS models score low which makes the few remaining high scoring models to appear similar in score, which is the case in Figure F22 for b_b/b of 0.001.

The objective classification was conducted on a case by case basis for different water types, sediment types, solar zenith angles, and backscattering ratios. The overall low performance of models in the final scores in Figures 4.4 and 4.5 does not necessarily mean that low performing TSS models scored less in all the categories used in deriving the final score. For example, in Figure 4.5, LAN-E22 scored a very low final score when compared to other TSS models, but when considering specific results as presented in Figures F16 to F20, LAN-E22 received a score at least comparable with most of the best performing models in all water classes for the red clay sediment type. Likewise, similar cases can be ascertained for all the respective TSS model's scores for specific water classes, sediment

types, backscattering ratios and solar zenith angle (Results provided as Appendix F for other overall low scoring TSS models in Figures 4.4 and 4.5). An additional disadvantage of the objective methodology used here is that the final score does not necessarily show the performance of all models in different categories considered, it shows only the relative performance of models in comparison with the mean scores of TSS models. In Figure F1, we observe that almost all TSS models score relatively higher total points for brown earth and lower for Bukata sediment types when compared with other sediments.

To account for the methodological uncertainties from the range of univariate statistical tests described in Section 4.3.3, we used a bootstrapping method (Brewin et al., 2015; Efron, 1979) which generates the confidence limit in the final score. The results from the 1000 bootstrap runs presented in all the score charts shows that the mean score of models did not vary significantly for each different run, the ranges of 95% confidence limits were smaller for most of the models. Further, to limit the effect of spurious TSS values derived by some of the models, especially models with exponential and power functions, we filtered out any derived TSS value below a minimum of 0.001 mg/L and greater than a twice the maximum TSS concentration of each TSS model. Filtering out the spurious results can artificially inflate the final scores because only values that are within the upper and lower bounds would be considered for statistical tests. However, the possible percentage retrieval test discussed in Section 4.3.3.6 negate such an effect because filtering out spurious results would result in lower possible percentage retrieval and lower score in the percentage retrieval test.

4.5.2. TSS Model Selection Guidelines

Even though there were clearly distinct higher and lower performing TSS models from the final score chart presented in Figures 4.4 and 4.5, the performance of individual models varied widely when viewed against respective water types, sediment types, and backscattering ratios. The results presented in Figures 4.4 and 4.5 can be of use to the end-users who

are clearly interested in TSS models that are robust enough to be used in waters for which they have little or no information of their optical and physical properties to generate TSS products. Figures 4.4 and 4.5 indicate that the MODIS TSS models MOD-E6, MOD-A1, MOD-E28, MOD-A4 and MOD-E10 and the Landsat TSS models LAN-E3, LAN-A4, LAN-E9, LAN-A5 and LAN-A1 are ranked the highest in terms of likely suitability for estimating TSS concentration of unknown water types. An example of the selection of high performing TSS models using a real water dataset was demonstrated in Section 4.4.2.2 and it can be seen that the results varied widely among the high scoring TSS models, with MOD-E10 and LAN-E9 producing results within a MARE of 46.20% and 43.11% and other higher scoring models producing results as high as 102.59%. Considering the retrieval error of TSS concentrations from MODIS algorithms are typically reported as in the range of ~18.0% to ~61% for many studies conducted in the last decade (Feng et al., 2014; Nechad et al., 2010; Petus et al., 2014; Qiu, 2013; Wang et al., 2010b), we consider the regional TSS models MOD-A1 and LAN-A1, and the empirical models MOD-E10 and LAN-E9 as being the most appropriate for the waters in the north of Western Australia.

However, readers with prior information of water and sediment types can use information provided in S4.11, and Tables D1 and D2 as a guideline in selecting the model that is best suited for that particular water type. The difference in Relative Error between the high and low scoring models validated using HydroLight data and the *in situ* data showed that there is a huge difference between the two. The best performing model from the high scoring models shows that TSS can be estimated with a Mean RE between 69.96% and 481.82% (for different water conditions), but the low scoring model's results can vary dramatically within a Mean RE ranging from 106.43% to 1832.79%. The high Mean RE for low scoring models does not necessarily mean that the low scoring model performs low for all water types. The low scoring TSS model's performance in one category or more can be significantly better than other models, but overall on average the model performs poorly when compared with high scoring models across all water types. For example, the low scoring model LAN-E22 displays the

Smallest RE of 19.41% which is certainly better than the Smallest RE of most of the high scoring model's Smallest RE. Thus, with prior knowledge of water types and bio-geochemical properties of the region, we can select a TSS model from both high and low performing TSS models presented in Tables D1 and D2 that have higher scores in the water that are similar to the region where TSS model would be applied.

The results also showed that semi-analytic models were generally higher in ranking when compared with empirical models. The reason for most semi-analytic models performing better than empirical models can be attributed to the fact that semi-analytic models, by design, were based on radiative transfer theory (Nechad et al., 2010; Passang, Peter, & Mark, 2016) and one or more parameters were calibrated using general *in situ* bio-optical properties representative of a wide range of global waters (Kong et al., 2015a; Nechad et al., 2010).

4.6. Conclusions

In summary, in this study we have applied an objective methodology to compare the TSS models and their suitability in use for retrieving TSS in the absence of a regionally tuned TSS model. From the study we have identified the MODIS TSS models MOD-E6, MOD-A1, MOD-E28, MOD-A4 and MOD-E10 and the Landsat TSS models LAN-E3, LAN-A4, LAN-E9, LAN-A5 and LAN-A1 as suitable for estimating TSS concentration in waters with no prior knowledge of bio-optical or bio-geochemical properties. The results from this study highlighted the impact of "local tuning" of algorithms, showing that some low scoring models performed better than the high scoring models in one or more specific sediment, backscattering, solar zenith and water types. The results from this study can be used to ascertain which TSS models perform well in particular water types, sediment types and backscattering ratios for use in aiding the selection of a TSS model suited for use in a particular water type. In addition, the results also show that the semi-analytic TSS models are generally better than empirical TSS models in deriving TSS estimation in unknown water types.

Chapter 5

Impact of the Spatial Resolution of Satellite Remote Sensing Sensors in the Quantification of Total Suspended Sediment Concentration: A Case Study in Turbid Waters of northern Western Australia.

This chapter has been published in the journal: PLoS One

Dorji, P., & Fearn, P. (2017). Impact of the Spatial Resolution of Satellite Remote Sensing Sensors in the Quantification of Total Suspended Sediment Concentration: A Case Study in Turbid Waters of northern Western Australia, *PLoS One*, 12(4), e0175942.

5.1 Abstract

The impact of anthropogenic activities on coastal waters is a cause of concern because such activities add to the total suspended sediment (TSS) budget of the coastal waters, which have negative impacts on the coastal ecosystem. Satellite remote sensing provides a powerful tool in monitoring TSS concentration at high spatiotemporal resolution, but coastal managers should be mindful that the satellite-derived TSS concentrations are dependent on the satellite sensor's radiometric properties, atmospheric correction approaches, the spatial resolution and the limitations of specific TSS algorithms. In this study, we investigated the impact of different spatial resolutions of satellite sensor on the quantification of TSS concentration in coastal waters of northern Western Australia. We quantified the TSS product derived from MODerate resolution Imaging Spectroradiometer (MODIS)-Aqua, Landsat-8 Operational Land Image (OLI), and WorldView-2 (WV2) at native spatial resolutions of 250 m, 30 m and 2 m respectively and coarser spatial resolution (resampled up to 5 km) to quantify the impact of spatial resolution on the derived TSS product in different turbidity conditions. The results from the study show that in the waters of high turbidity and high spatial variability, the high spatial resolution WV2 sensor reported TSS concentration as high as 160 mg/L while the low spatial resolution MODIS-

Aqua reported a maximum TSS concentration of 23.6 mg/L. Degrading the spatial resolution of each satellite sensor for highly spatially variable turbid waters led to variability in the TSS concentrations of 114.46%, 304.68% and 38.2% for WV2, Landsat-8 OLI and MODIS-Aqua respectively. The implications of this work are particularly relevant in the situation of compliance monitoring where operations may be required to restrict TSS concentrations to a pre-defined limit.

5.2 Introduction

Global coastal marine ecology is at ever increasing risk because of the increase of impacts due to the demands of maritime trade, supporting population growth which necessitates land reclamation, maintenance and capital dredging for ports, dredging for offshore resources, and placing of sub-sea transport pipelines (Evans et al., 2012; Mostafa, 2012). The Australian economy is heavily dependent on maritime links because of its geographical remoteness from other continents. One third of its GDP is based on sea-borne trade, and the existing ports that support this high volume of shipping traffic require constant maintenance dredging of existing shipping channels and frequent large capital dredging projects (Australia, 2014). The environmental effects of dredging on the coastal marine ecology are diverse, with dredging potentially resulting in either partial reduction or complete loss of marine habitat through the physical removal of substratum biota from the sub-sea surface and immediate burial due to sedimentation of the dredged materials (Erftemeijer, Riegl, Hoeksema, & Todd, 2012). Further, increase in turbidity caused by dredging significantly attenuates the amount of light reaching the benthic habitat for primary productivity (Chen et al., 2010; Havens et al., 2011; Shi et al., 2014). The environmental cost of dredging and the need for coastal development poses a challenge to environmental monitoring agencies, marine ecologists and coastal infrastructure developers who aim to find a balance between the two (Erftemeijer et al., 2012).

Coastal water quality monitoring of the effects of anthropogenic processes aims to provide immediate and appropriate responses, but often

requires continuous ground based monitoring, which is typically resource intensive, to maintain and only provides information on limited specific geographical locations (Etcheber et al., 2011; Gernez et al., 2015). The availability of satellite remote sensing platforms has provided coastal managers with tools and capabilities to effectively monitor the coastal environment at spatial and temporal scales previously unconceivable from the perspective of traditional *in situ* based observation methods (Peta, 2001). Coastal water quality in the form of water turbidity or Total Suspended Sediment (TSS) concentration has been widely studied across diverse geographical locations (Acker et al., 2005; Binding et al., 2005; Burenko, Ershova, Kopelevich, Sheberstov, & Shevchenko, 2001; Ekercin, 2007; Koponen et al., 2007; Miller & McKee, 2004; Min, Ryu, Lee, & Son, 2012; Ouillon & Petrenko, 2005; Tang et al., 2013; Wang et al., 2008) by using a suite of remote sensing sensors such as, Landsat (Brezonik et al., 2005; Doxaran et al., 2006; Kallio et al., 2008a; Kloiber, Brezonik, Olmanson, & Bauer, 2002; Olmanson et al., 2008; Onderka & Pekárová, 2008; Östlund et al., 2001; Wang et al., 2009b; Wu et al., 2008; Zhou et al., 2006), MEdium Resolution Imaging Spectrometer (MERIS) (Koponen et al., 2002; Kratzer et al., 2008; Odermatt et al., 2008; Shi et al., 2014), MODerate resolution Imaging Spectroradiometer (MODIS) (Chen et al., 2014b; Chen et al., 2007; Doxaran et al., 2009; Hu et al., 2004; Li et al., 2010; Miller & McKee, 2004; Min et al., 2012; Petus et al., 2010; Wang et al., 2008; Wang et al., 2009a; Wang & Lu, 2010; Wang et al., 2009c; Wu et al., 2008; Wu et al., 2009; Zhang et al., 2010), and Sea-viewing Wide Field-of-view Sensor (SeaWiFS) (Binding, Bowers, & Mitchelson-Jacob, 2003; Burenko et al., 2001; Fettweis, Nechad, & Van den Eynde, 2007; Gordon & Wang, 1994b; Myint & Walker, 2002; Ruddick et al., 2000). In addition to these most commonly used and “free to ground” sensors, commercial high spatial resolution sensors such as Systèm Pour l’Observation de la Terra (SPOT) (Dekker et al., 2002; Doxaran et al., 2006; Doxaran et al., 2002), IKONOS (Ekercin, 2007) and WorldView-2 (WV2) (Eugenio, Martin, Marcello, & Bermejo, 2013) are also employed to map the TSS.

The high spatial resolution commercial satellite sensors such as IKONOS, WV2, and GeoEye-1 can provide data at spatial resolutions of approximately 0.5 m – 4.0 m with temporal resolutions of ~1–8 days (DigitalGlobe, 2017). The freely available remote sensing data of MODIS and MERIS from the National Aeronautics and Space Administration can provide near-daily TSS estimates at 250 m – 300 m resolution and Landsat at 30 m but with a monitoring frequency of 16 days. Previous studies (Evans et al., 2012; Gernez et al., 2015; Miller et al., 2011; Ody et al., 2016) conducted in mapping TSS for water quality monitoring have studied the spatial extent of suspended sediment plumes using one or more satellite sensors and the common consensus is that the higher spatial resolution satellite sensors are able to resolve finer details of suspended sediment plumes while the lower spatial resolution sensors lose the finer details. However, only a few studies (Miller et al., 2011; Ody et al., 2016) have been conducted to study the impact of using different spatial resolution sensors in estimation of TSS in sediment plumes where the water can be spatially variable in TSS concentration, even at sub-pixel level. Ody et al. (Ody et al., 2016) showed that in the Gulf of Lion, France, the variability in the TSS concentration at the turbid fronts and edges of the river plume was estimated to be around 7 mg/L and 10 mg/L for 250 m and 1.0 km spatial resolution respectively. Further, the lower spatial resolution sensor SERVI (Spinning Enhanced Visible and Infrared Imager) at 3.0 x 5 km² was shown to have TSS concentration variability due to different spatial resolution were as high as 20 mg/L. The two studies (Miller et al., 2011; Ody et al., 2016) indicated that the quantification of TSS concentrations using remote sensing sensors are not only determined by the spatial resolution of the sensors, but also the TSS variability of the region itself. Generally, the coarser spatial resolution sensors would produce higher TSS variability but the magnitude of TSS variability depended on the variability of the TSS concentration of the sampled region.

In Western Australia, specifically the Pilbara region, the last decade and a half has seen substantial capital dredging projects with the total volume of dredged material in excess of ~70 million m³ and the recent

Wheatstone gas field project is expected to add another ~45 million m³ of dredge spoils to this total (Hanley, 2011). Compliance monitoring of large volume capital dredging and/or frequent maintenance dredging is typically carried out using *in situ* data loggers that measure a range of water quality parameters (TSS concentration, turbidity, light, and sedimentation rate) (SKM, 2013). In compliance monitoring of dredge operations in Western Australia, it is required of dredging companies to perform environmental impact assessment studies using hydrodynamic modelling of sediment plumes to identify zones of impact and trigger values derived in relation to a water quality parameter and sensitivity to benthic communities (WA EPA, 2011). For instance, in the Wheatstone gas field project, a zone of high impact (mortality rate > 50%) was identified along the dredge channels and spoil area. The hydrodynamic model was used to identify trigger values to prompt management responses, with thresholds of TSS > 25 mg/L for more than 14% of the time, >10 mg/L for more than 38% of the time, and > 5 mg/L for more than 63% (WA EPA, 2011). The TSS levels set to trigger a management response are monitored using point measurement from the *in situ* data loggers, accepted as providing very accurate and reliable data. However, *in situ* data loggers cannot provide a synoptic view of TSS concentration at reasonable costs over a large spatial extent, which has led environmental managers adopting remote sensing technologies which can provide a synoptic view of plume dynamics and TSS concentration at reasonable costs (Islam et al., 2007).

Despite the benefits of satellite remote sensing in water quality monitoring, the environmental protection agencies tasked with monitoring the coastal water quality should be aware of potential discrepancies in satellite derived TSS concentration as a result of different satellite sensors and different spatial resolutions. The impact of significant spatial variability in the TSS concentration can affect the results of the satellite derived TSS concentration used in monitoring the water quality. In effect, the monitoring of dredging activity with different satellite-based remote sensing sensors can produce different TSS concentrations even in the same spatial region and depends on which satellite sensor is employed for the compliance

monitoring. Thus, this work was carried out to study the variability in TSS concentration at different spatial resolutions in the waters of the Onslow region in northern Western Australia using WV2, Landsat-8 OLI (Operational Land Imager) and MODIS-Aqua data. Specifically, first we tested the capabilities of WV2, Landsat-8 OLI and MODIS-Aqua in resolving the spatial features in areas of sediment plumes caused by dredging activities and river outflows. Second, we quantified the range of TSS concentration variability in the region of the sediment plumes and background waters by degrading the native spatial resolution of each sensor to coarser spatial resolutions. Finally, we discuss the impact of using different spatial resolution sensors in monitoring of water quality as a result of findings from this study.

5.3 Materials and Methods

5.3.1 Study Site and Context

The study area, the coastal waters of Onslow, fall within the Pilbara region, in Western Australia (see Figure 5.1). The coastal area of Onslow generally experiences a mean annual temperature of 29.2 °C and mean annual rainfall of 296 mm (Bureau of Meteorology, 2015a). The study area is generally sheltered from the prevailing south-west winds and sea-swells from the Indian ocean by Barrow Island and the shoals of Lowendal and Montebello Islands, however, the area experiences locally wind-driven waves and seasonal tropical cyclones (Chevron, 2014). The topography of the coastal area generally drives the ebb and flood tides easterly and westerly along the coastline with the flow occasionally disturbed by the locally wind-driven currents. The tides around the shoreline are semi-diurnal with the spring tide ranging from a mean high of 2.5 m to a mean low of 0.6 m (Chevron, 2014).

The discovery of the Wheatstone gas field, located at the edge of the continental shelf 200 km off the coast of Onslow (located approximately 1390 km from Perth, Western Australia), has led to the construction of offshore platforms and onshore gas processing plants (Chevron, 2014). The turbidity of the coastal waters of Onslow was previously only affected by natural processes, including seasonal tropical cyclones and episodic river outflows

from the Ashburton river which can range the TSS concentration from 15 mg/L to 5000 mg/L (with higher TSS concentration closer to the river mouth) with river flow rates of 30 m³/s to 250 m³/s (URS, 2014). The dredging activity in the near-shore waters of Onslow occurred from May 2013 to December 2015 with an estimated 45 million m³ of dredge spoil generated (WAPC, 2011). Such large volumes of dredge spoil are expected to have immediate impact in the immediate area of the dredging and also have some level of impact on the marine habitat in the vicinity of the dredging locations.

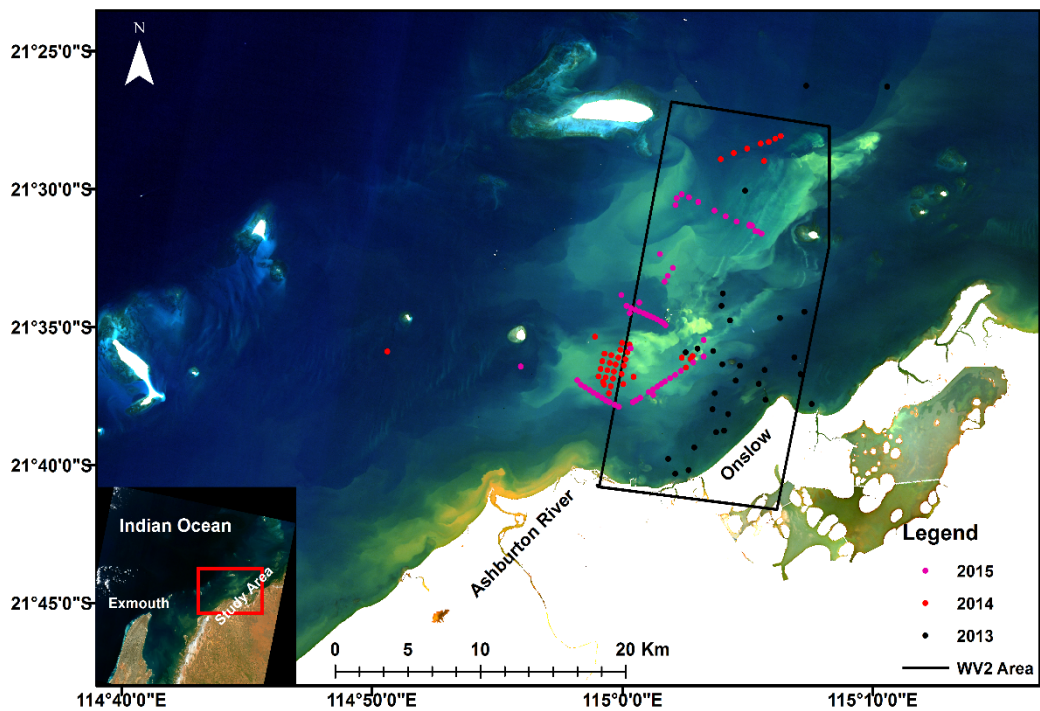


Figure 5.1: Study Site. True colour imagery Landsat OLI showing the locations of field sites in the waters off the coast of Onslow, Western Australia. True colours image of the study site is reprinted from Figure 1 in Dorji et al., (2016) under a Creative Commons Attribution (CC-BY) license (<http://creativecommons.org/licenses/by/4.0/>). The black polygon added in Figure 5.1 represents the area where WorldView 2 data were captured on June 13th 2014. The coloured dots represent locations of *in situ* data with colours indicating the year of data acquisition.

5.3.2 Field Remote Sensing Reflectance and TSS Measurements

As part of the Dredging Science Node project 2/3 (WAMSI, 2014) funded by the Western Australian Marine Science Institution three field campaigns were carried out in October 9th – 31th, 2013, June 7th – 21st, 2014

and July 3rd – 13th 2015 onboard RV Linnaeus operated by the Commonwealth Scientific and Industrial Research Organization and RV Solander operated by the Australian Institute of Marine Science. The ship-based “Dynamic Above-water radiance (L) and irradiance (E) Collector” (DALEC) (Brando et al., 2016) was used to measure the remote sensing reflectance (R_{rs} , in sr^{-1}) and *in situ* water sampling methods were used in measuring TSS concentrations. A brief description of the *in situ* R_{rs} measurements using the DALEC and sampling of TSS concentration are provided below. Further details of the R_{rs} and TSS concentration data used in this study, including the data collection procedure and data quality control measures, are discussed in depth in Dorji et al. (2016).

5.3.2.1 DALEC and TSS Data Collection and Analysis

The DALEC, developed by “In situ Marine Optics”, is an autonomous ship based hyperspectral upwelling radiance (L_u), sky radiance (L_{sky}) and downwelling irradiance (E_d) collector which takes coincident measurements in 256 spectral bins in the 380 nm – 900 nm spectral range. The L_u , L_{sky} and E_d measurements from the DALEC can be used to compute R_{rs} using an ad-hoc R_{rs} formulation from Mobley (Mobley, 1999) for a uniform sky condition and wind speed less than 5 m s^{-1} , as presented in Equation (5.1).

$$R_{rs}(\lambda) = \frac{L_u(\lambda) - 0.022L_{sky}(\lambda)}{E_d(\lambda)} \quad (5.1)$$

The quality of DALEC data were maintained at two stages. 1) During the data collection stage, we positioned the DALEC instrument at an azimuth angle of $\sim 135^\circ$ relative to solar direction while the viewing angle of the L_u and L_{sky} sensors were maintained at 40 off nadir and zenith respectively to minimize the sun glint and instrument shading. 2) During the data analysis stage, we visually inspected the L_u and L_{sky} spectra and removed any spectra that were contaminated by sun glint. The remaining spectra free of sun glint were averaged within ± 3 min from TSS sample collection time to generate an average R_{rs} spectrum corresponding to that TSS sample.

For *in situ* TSS concentration measurement, we collected a minimum of two 1-liter samples of sea water at a depth of approximately 0.5 m – 1 m

at each TSS sample location (see Figure 5.1). The TSS samples were filtered using a Whatman GF/F filters (47 mm diameter, nominal pore size of 0.7 μm) pre-prepared in the laboratory by flushing the filters with 50 mL of deionized water and drying in an oven at 60 °C for 24 hrs. The filtered TSS samples were flushed with 50 mL of deionized water to remove salt from the seawater, then dried in the oven at 60 °C for 24 hrs and repeatedly measured and dried until consistent measurements were obtained within the tolerance limit of 0.001 mg/L. After performing the quality checks of the *in situ* data there were 48 (R_{rs} and TSS) match-up pairs that were selected to establish a TSS algorithm. The range of TSS concentrations used in the algorithm development varied from a low of 2.5 mg/L to a high of 69.9 mg/L.

5.3.2.2 Satellite Remote Sensing Data

5.3.2.2.1 Satellite Data Acquisition and Atmospheric Correction

The satellite data used in this study comprise MODIS-Aqua, Landsat-8 OLI and WV2 acquired around the time when the second field campaign was carried out in June 7th - 21st 2014. Due to the temporal limitation of the Landsat-8 OLI of 16 days we could not acquire data for all three satellites contemporaneously. However, we acquired three concurrent sets of Landsat OLI and MODIS-Aqua data for May 23, July 10 and July 26 that were free of clouds and sun glint. The MODIS-Aqua and WV2 data were acquired for June 13, 2014, which was when the WV2 image was requisitioned over the study region. The spectral bands and the spatial resolutions used in mapping the TSS concentrations were band 1 (620 – 670 nm) at 250 m, band 4 (640 – 670 nm) at 30 m and the ‘red band’ (630 – 690 nm) at 2 m for MODIS-Aqua, Landsat-8 OLI and WV2 respectively.

For this study we used the top of the atmosphere radiance data from MODIS-Aqua available from the NASA LAADS web (<http://ladsweb.nascom.nasa.gov/>) as geo-located Level 1B data in all 36 spectral bands. All the MODIS-Aqua Level 1B data were atmospherically corrected using the MUMM (Ruddick et al., 2000) atmospheric correction as implemented in SeaDAS (version 7.2) (Feldman & McClain, 2010). The MUMM atmospheric correction, based on the spatial homogeneity of water

leaving radiance and constant aerosol ratios in MODIS 748 nm and 869 nm bands (Ody et al., 2016), was demonstrated to perform well in the waters over our study region (Dorji et al., 2016).

Radiometrically and geometrically corrected Level 1T Landsat-8 OLI data were obtained from USGS archives using the EarthExplorer (<http://earthexplorer.usgs.gov/>). The Level 1T Landsat-8 OLI data were atmospherically corrected to marine remote sensing reflectance using the ACOLITE software (available at <https://odnature.naturalsciences.be/remsem/software-and-data/acolite>) (Vanhellemont & Ruddick, 2014). Two atmospheric correction algorithms are available in ACOLITE, the NIR and SWIR algorithm: the NIR algorithm is based on the selection of the red (655 nm) and NIR (865 nm) bands to account for the aerosol contributions, the SWIR algorithm uses the SWIR1 (1608.5 nm) and SWIR2 (2200.5 nm) bands available on the Landsat-8 OLI sensor. For this study, we selected the SWIR algorithm because it is valid for turbid waters (Vanhellemont & Ruddick, 2015), which is the case for our study site where *in situ* TSS concentration was measured as high as 69.6 mg/L in the vicinity of dredging areas and it is likely higher in the area of the dredge plumes (Dorji et al., 2016). Further, the SWIR algorithm was shown to be an improvement over the NIR band based atmospheric correction algorithm (Vanhellemont & Ruddick, 2014) that was valid for only moderately turbid waters (Ody et al., 2016; Vanhellemont & Ruddick, 2015).

The WV2 image covered an area of 331 km² over the study area (see Figure 5.1 for the spatial extent in the study area and the WV2 image). The WV2 data comprise spectral bands in the blue (450 - 510 nm), green (510 - 580 nm), red (630 - 690 nm) and NIR1 (770 - 895 nm) and are supplied as ortho ready standard WV2 satellite image data at 2 m spatial resolution. The SeaDAS and ACCOLITE platforms were specifically designed and adapted to process, among others, MODIS and Landsat-8 OLI satellite sensor data, but they are not designed to process WV2 data. A study by Martin et al. (Martin, Eugenio, Marcello, & Medina, 2016) demonstrated the success of 6S (Second Simulation of a Satellite Signal in the Solar Spectrum) radiative transfer code in the atmospheric correction of satellite data captured in turbid

coastal waters. The 6S code predicts the satellite signals at the top of atmosphere between 250 - 4000 nm based on geometrical conditions, atmospheric models for gaseous components, the aerosol model, spectral conditions, and ground reflectance (Zhao, Tamura, & Takahashi, 2001). Thus, we applied the 6S atmospheric correction method of Kotchenova et al. (Kotchenova, Vermote, Matarrese, & Klemm, 2006) and obtained the marine surface reflectance using the following input parameters: 1) geometrical conditions were obtained from the solar zenith angle, solar azimuth angle, satellite zenith angle, satellite azimuth angle, image acquisition day and month that was supplied with the WV2 image, 2) the atmospheric model was selected as the Tropical atmospheric model, 3) the aerosol model was selected as the 'Continental' aerosol model with visibility of 15 km, 4) The spectral band used was equivalent to the red band of WV2 and ground reflectance was modeled as a homogenous ocean BRDF model with wind speed of 5 m s^{-1} , wind azimuth of 220° from North, salinity of 35 psu and pigment concentration of 0.5 mg/m^3 . The input parameters in 6S were selected to match closely with the conditions over the study region.

5.3.2.2.2 Validation of Atmospheric Correction Methods

For the *in situ* validation of the atmospheric correction method, only MODIS-Aqua provided concurrent measurements to the DALEC-measured R_{rs} . The MODIS-Aqua overpass time over the study region on July 13th 2014 was at 06:30 hrs (UTC) while *in situ* TSS and DALEC R_{rs} were collected between 02:00 – 07:30 hrs (UTC). The WV2 and Landsat-8 OLI data were not concurrent with the DALEC-measured R_{rs} during any of the Landsat-8 OLI and WV2 overpass times in the study region, thus no *in situ* validation is performed for Landsat-8 OLI and WV2-derived R_{rs} . The time difference between DALEC R_{rs} measurements and MODIS-Aqua overpasses used in the validation was constrained to ± 90 min. As a validation of atmospheric correction for Landsat-8 OLI and WV2-derived R_{rs} , an inter comparison of R_{rs} with reference to MODIS-Aqua was performed for the WV2 and Landsat-8 OLI derived R_{rs} over the study site for selected locations (see light cross

marks in Figure 5.2a and Figures 5.2c–e) representing a range of TSS concentrations.

An inter satellite sensor comparison can show significantly different R_{rs} values over the same region due to the time difference of data acquisition and the dynamic water conditions where water masses can move and evolve rapidly (Ody et al., 2016), thus to minimize the effect of satellite data acquisition time difference we used the aggregates of pixel values in a selection of square boxes of 2.5 km in length that represented waters ranging from clear to highly turbid in the image. The length of 2.5 km was chosen because the minimum size of the plumes in the area of study were at least 5 km in length, and the intent was to incorporate pixels within the plumes which are expected to display a small range in R_{rs} values. For the MODIS-Aqua and WV2-derived R_{rs} comparison, we selected 12 square box regions after visually identifying the areas that ranged in different turbidity from the WV2 image for June 13, 2014 (see white cross marks for central locations of each box in Figure 5.2a). For the MODIS-Aqua and Landsat-8 OLI derived R_{rs} comparison, we selected 12 square boxes per image after visually identifying the areas representing a range of different turbidity levels using Landsat-8 OLI imagery for May 23, July 10 and July 26, 2014 (see white cross marks in Figures 5.2c–e).

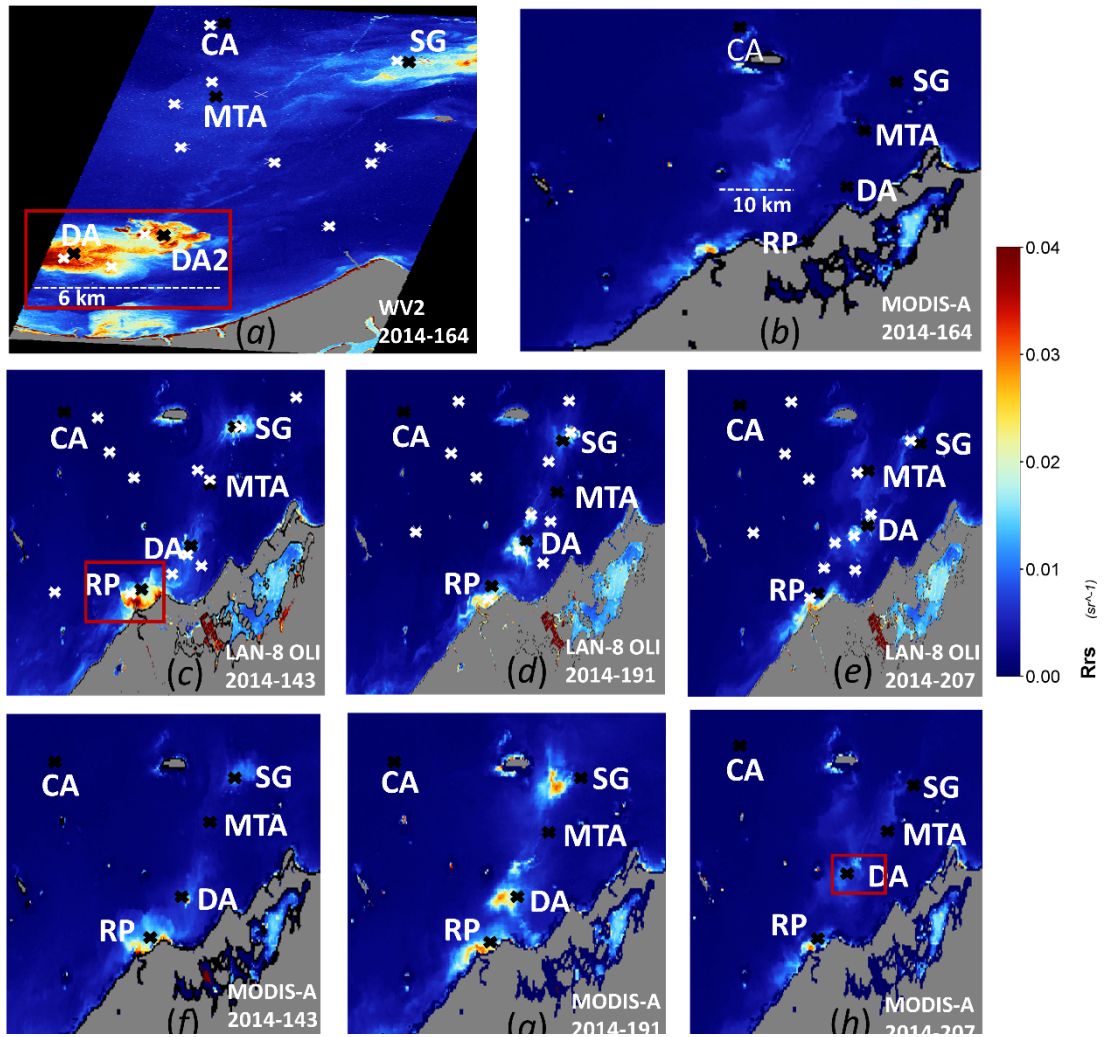


Figure 5.2: The atmospherically corrected R_{rs} (red band) product. (a) and (b) WV2 and MODIS-Aqua on 13th June 2014; (c)-(e) Landsat-8 OLI and (f)-(h) MODIS-Aqua on 23rd May, 10th July and 26th July 2014 respectively. The white cross mark on (a), (c)-(e) are the locations of the central pixel of 2.5 km square used in R_{rs} product validation. The black cross mark are locations corresponding to Dredged Areas (DA and DA2), Spoil Ground (SG), Clean Area (CA), River Plume (RP) and Moderate Turbid Area (MTA) in each image.

5.3.2.2.3 Degrading the Satellite Spatial Resolution

Quantification of the variability in TSS concentration derived from sensors with different spatial resolutions was assessed by spatially degrading the satellite sensor's derived TSS products to coarser spatial resolutions than their respective native resolutions of 250 m, 30 m and 2 m for MODIS-Aqua, Landsat-8 OLI and WV2 data respectively. The degradation of the spatial resolution depended on the respective sensor's native resolution, the MODIS-Aqua TSS data were degraded to 500 - 5000

m at 500 m intervals, the Landsat-8 OLI TSS data were degraded to 60 - 4800 m at 60 m intervals, and the WV2 TSS data were degraded to 4 - 5000 m at 2 m intervals. The spatial resolution was degraded using the aggregate of all available pixel values in a selected region. For example, if MODIS-Aqua 250 m data were to be degraded to 1000 m spatial resolution then all pixels confined within the 1000 m by 1000 m (equivalent to 4 × 4 250 m spatial grids) would be averaged. The locations and size of each selected area were determined visually by assessment of the uniformity of TSS in the region and the spatial resolution of degradation. For each MODIS-Aqua and Landsat-8 OLI TSS image we selected 5 locations, the 1) the center of the dredge area (DA), 2) center of the spoil ground (SG), 3) moderately turbid but spatially uniform area (MTA), 4) clean area (CA) and 5) center of the river plume (RP). For the WV2 TSS image, we also selected 5 locations, but replaced the location of the river plume with the second dredge area (DA2) because the area of the river plume was not covered by the WV2 image (see black cross marks in Figure 5.2 for the locations).

In addition, the data to visually examine the spatial characteristic of the sediment plumes were generated by spatially degrading the TSS product for all of the study regions from each sensor's native spatial resolution. The high spatial resolution 2 m WV2 TSS product was degraded to 30 m, 250 m, 500 m, and 1000 m, the spatial resolution of the 30 m Landsat-8 OLI TSS product was degraded to 250 m, 500 m, and 1000 m, and the coarser 250 m spatial resolution of MODIS-Aqua was degraded to 500 m and 1000 m. For the examination of the plume features we focused on the area where the plume was visually evident (see red box in Figures 5.2a, c, and h) for the TSS product of June 13th 2014 for WV2, May 23rd for Landsat-8 OLI and July 10th 2014 for MODIS-Aqua.

5.3.2.3 Calibration and Validation of Multi-Sensor TSS Algorithm

The TSS algorithm used in this study is the Semi-Analytic Sediment Model (SASM) from Dorji et al. (2016) where the physical form of SASM is based on the principle of radiative transfer and it has been shown that the SASM performs better in the study region compared with simple linear and

exponential models. Further, SASM is based on a red spectral band which suits our purpose because all three satellite sensors considered here have red bands which are proven to be effective in mapping TSS concentrations in the turbid region. To calibrate the SASM model, the DALEC measured R_{rs} was convolved to the respective sensors band's spectral response functions and then converted to equivalent sub-surface remote sensing reflectance (r_{rs}). Then all the 48 (r_{rs} and TSS) match-up pairs were used in re-calibration of the general form of the SASM in Equation (14) of Dorji et al. (2016). The recalibrated model was validated using the method of Leave-one-out cross-validation (LOOCV) (Stone, 1974) where all but one (r_{rs} and TSS) match-up pairs were used in calibration and the remaining one was used in validation until all the match-up pairs were exhausted. The SASM re-calibrated to the respective red bands of MODIS-Aqua, Landsat-8 OLI and WV2 are presented below in Equations (5.2), (5.3), and (5.4) for MODIS-Aqua in band 1, Landsat-8 OLI in band 4 and WV2 in the red band respectively.

$$TSS = \frac{23.47 \times \left(\frac{x}{1-x} \right)}{1 - 0.69 \times \left(\frac{x}{1-x} \right)}, \quad (R^2=0.85) \quad (5.2)$$

$$TSS = \frac{25.34 \times \left(\frac{x}{1-x} \right)}{1 - 0.69 \times \left(\frac{x}{1-x} \right)}, \quad (R^2=0.85) \quad (5.3)$$

$$TSS = \frac{26.37 \times \left(\frac{x}{1-x} \right)}{1 - 0.69 \times \left(\frac{x}{1-x} \right)}, \quad (R^2=0.89) \quad (5.4)$$

where $x = \frac{-g_1 + \sqrt{(g_1)^2 + 4g_2 r_{rs}(\lambda)}}{2g_2}$, and $r_{rs}(\lambda) = r_{rs}(\text{band1})$ for MODIS-Aqua, $r_{rs}(\text{band 4})$ for Landsat-8 OLI and $r_{rs}(\text{red band})$ for WV2, $g_1 = 0.084$ and $g_2 = 0.17$

5.3.3 Mapping of TSS Concentration

The R_{rs} derived from the atmospherically corrected reflectance of MODIS-Aqua in band 1, Landsat-8 OLI in band 4 and WV2 in the red band for all the corresponding dates of image acquisition were used in mapping the TSS concentration. The respective satellite derived R_{rs} were converted to

r_{rs} using Equation (5.5) (Lee et al., 1999) then, the resultant r_{rs} was used in the respective satellite sensor's TSS algorithm given by Equations (5.2), (5.3) and (5.4) for MODIS-Aqua, Landsat-8 OLI and WV2 respectively.

$$r_{rs}(\lambda) = \frac{R_{rs}(\lambda)}{(0.52 + 1.7R_{rs}(\lambda))}, \quad (5.5)$$

5.3.4 Accuracy Assessment

The common accuracy assessment methods, Mean Absolute Relative Error (MARE), Absolute Relative Error (ARE) and Root Mean Square Error (RMSE) employed in remote sensing by numerous studies (Forkuor, Hounkpatin, Welp, & Thiel, 2017; Shi et al., 2017; Sun et al., 2013) were used in this study to compare model-derived and 'true' R_{rs} and TSS values. In this study we refer to 'true' value as the *in situ* measurements or MODIS-Aqua derived R_{rs} or TSS values. We also considered the correlation coefficient (r) defined in Equation (5.9), although r cannot be strictly used in assessing the accuracy between two models because a high r value does not necessarily mean a better prediction because the systematic model error can also lead to over and/or under prediction (Forkuor et al., 2017). We used r to gauge the presence of positive correlation between the models. RMSE, as defined in Equation (5.8), is the most common accuracy assessment used to indicate average error of a model. Because of its susceptibility to outliers we resorted to using RMSE to evaluate *in situ* validation of TSS algorithms only, where in the *in situ* model validation the model-derived TSS concentration is not expected to deviate significantly from the *in situ* TSS measurements. However, in the accuracy assessment of TSS concentration derived from the satellite images, the TSS concentration can be highly variable and possibly include outliers, which can limit the use of RMSE accuracy assessment in such cases. Thus, the MARE and ARE as defined in Equations (5.6) and (5.7) respectively, were deemed more appropriate for satellite image derived TSS comparison. Further, the MARE and ARE are scale independent and provide errors in percentages, which better facilitates the comparative study of TSS concentrations produced by different satellite sensors. Thus, accuracy assessment for quantitative comparison of TSS

concentration derived from different sensors was performed using MARE and ARE. However, it should be noted that negative or zero, model-derived or ‘true’ values can result an unreliable accuracy estimates in MARE and ARE calculation. In this study, in the atmospheric correction process of the satellite images, the R_{rs} values were tested for negative or zero values to be flagged as ‘bad’ pixels and removed from subsequent analysis

$$\text{MARE} = \frac{\sum_{i=1}^n |(x_i - y_i) / y_i|}{n} \times 100\% \quad (5.6)$$

$$\text{ARE} = \frac{|x_i - y_i|}{y_i} \times 100\% \quad (5.7)$$

$$\text{RMSE} = \sqrt{\frac{\sum_{i=1}^n (x_i - y_i)^2}{n}} \quad (5.8)$$

$$r = \frac{n \sum x_i y_i}{\sqrt{n \sum x_i^2} \sqrt{n \sum y_i^2}} = \frac{\sum x_i \sum y_i}{(\sum x_i)^2 (\sum y_i)^2} \quad (5.9)$$

where n is the total number of samples, x_i is the model-derived TSS and y_i is the ‘true’ TSS.

5.4 Results

5.4.1 Validation of TSS Algorithms

The result from the LOOCV method used in calibration and validation of the TSS algorithms in Equations (5.2), (5.3) and (5.4) are presented in Table 5.1. Further, the corresponding TSS model curves for MODIS-Aqua in band 1, Landsat-8 OLI in band 4 and WV2 in the red band are shown in Figure 5.3. The results from all three sensor’s TSS algorithms produce similar results in terms of MARE, RMSE and r values. The similar results between all three TSS algorithm’s validation are expected because all three algorithms use the respective sensor’s red band with slight variation in spectral response function of each sensor.

Table 5.1: Validation results for MODIS-Aqua, Landsat-8 OLI, and WV2 TSS algorithms.

SASM Model	MARE (%)	RMSE (mg L ⁻¹)	<i>r</i>
Modis-Aqua	33.33	5.75	0.89
Landsat-8 OLI	33.36	5.73	0.89
WorldView 2	33.34	5.68	0.89

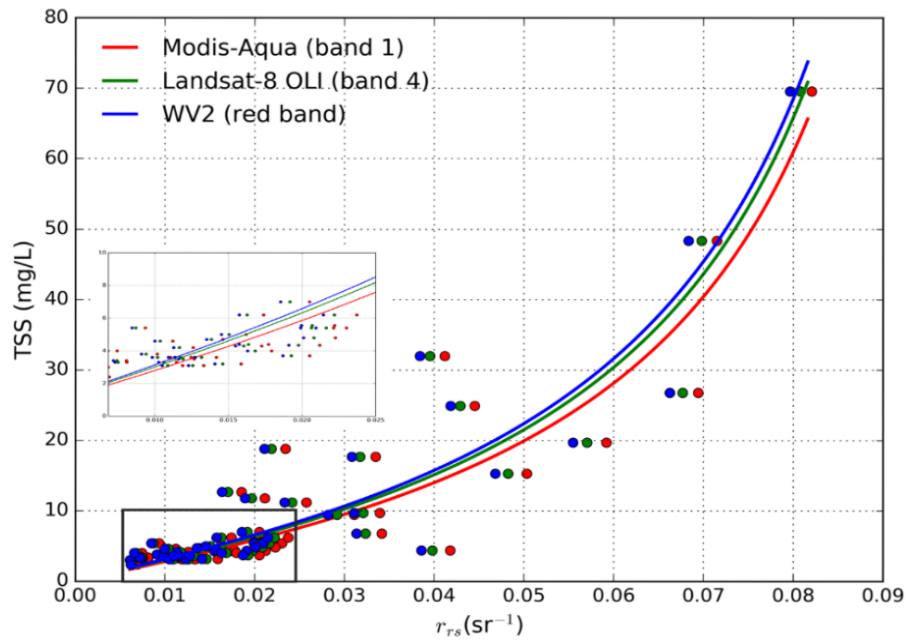


Figure 5.3: The TSS model curves for MODIS-Aqua (blue), Landsat-8 OLI (green) and WV2 (red). The *in situ* data points are shown by filled circles with the same colour profile as respective TSS model curves. The data for TSS < 10 mg/L and $r_{rs} < 0.025 \text{ sr}^{-1}$ are also shown in the blow out version of the plot.

5.4.2 Multi-Sensor Atmospheric Correction Validations

Validation of the atmospheric correction methods for the different satellite sensors involved two methods: 1) *in situ* validation for MODIS-Aqua atmospheric correction methods and 2) inter-sensor R_{rs} validation between MODIS-Aqua, WV2 and Landsat-8 OLI. In both the validation methods, type-II linear regression from (Glover et al., 2011) was used because type-I regression typically assumes the dependent variable (‘true’) is error free, but this is not the case even in *in situ* measurements (Brewin et al., 2015).

The *in situ* atmospheric correction validation result for MODIS-Aqua using the DALEC-derived R_{rs} is shown in Figure 5.4. The error bars on the data points in Figure 5.4 indicate the minimum and maximum values of R_{rs} within 3×3 and 5×5 pixel extents. In Figure 5.4 we observe that the majority of the data points were within the 1:1 line considering the error bars from R_{rs} variability in a 5 by 5-pixel window. However, there are also a few data points whose error bars do not overlap with the 1:1 line and resulted in ARE as high as 109.64% between the *in situ* DALEC R_{rs} measurement and MODIS-Aqua derived R_{rs} . The overall MARE of all data points was 34.82% with slope of 0.67, intercept of 0.0018 and R^2 of 0.54 as obtained from Type-II regression. Additional observation we can make from Figure 5.4 are that as the pixel window increases from a 3×3 to a 5×5 pixel window, the upper and lower error bounds also increase, showing that the water is highly variable in R_{rs} values. This spatial variability in R_{rs} is associated with the spatial variability in TSS.

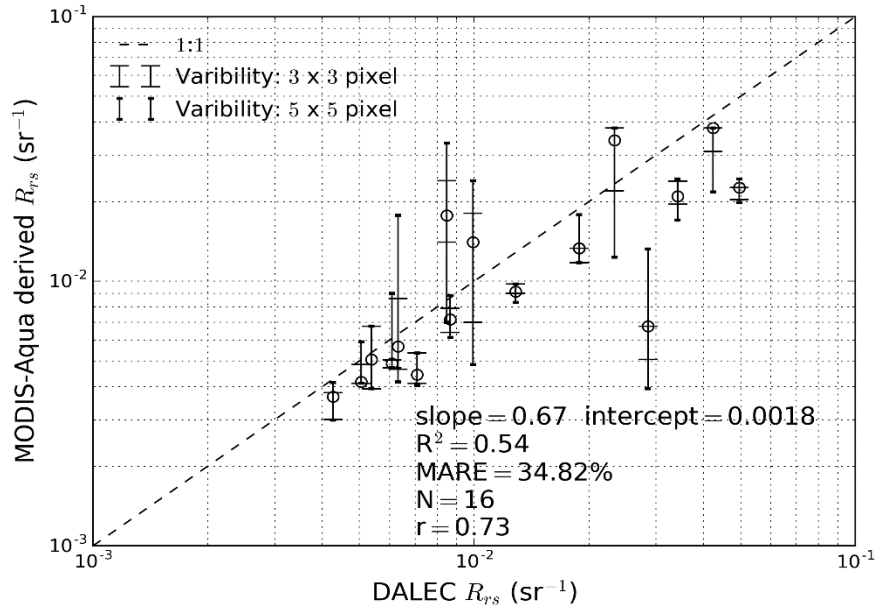
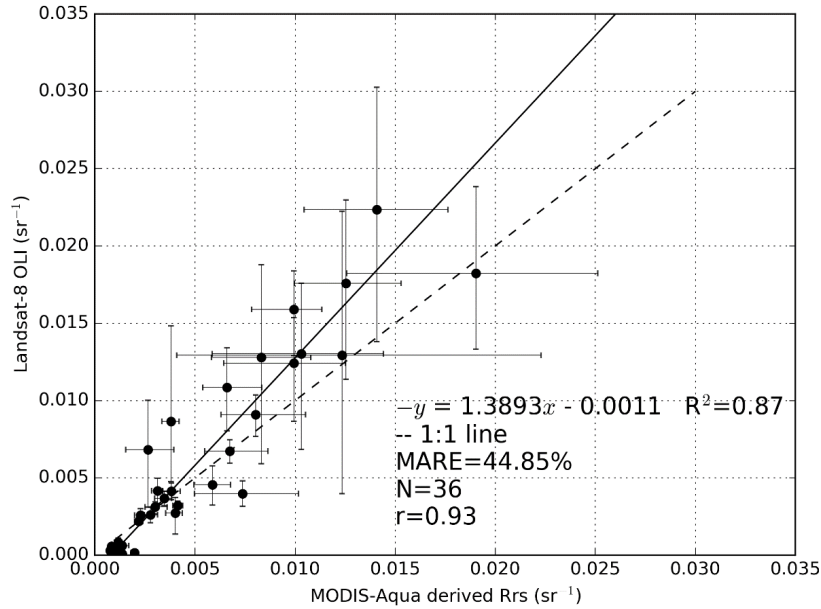


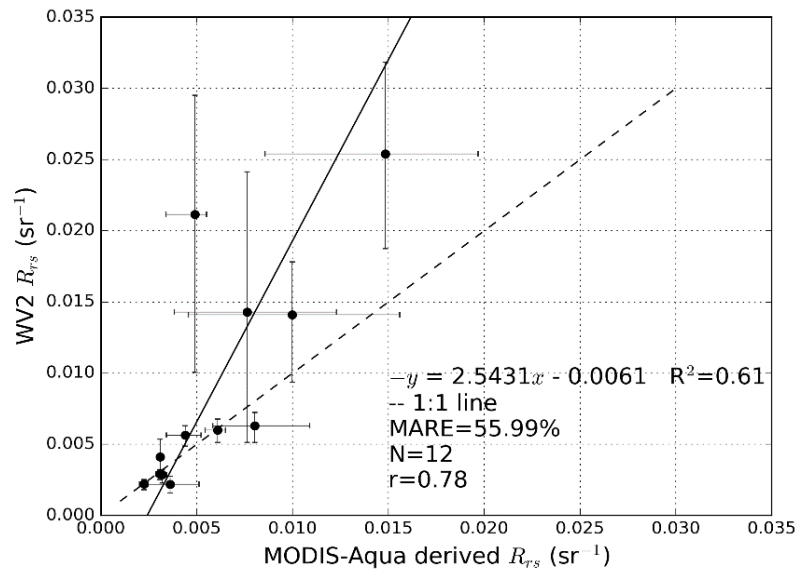
Figure 5.4: *In situ* validation of DALEC-measured R_{rs} and MODIS-Aqua derived R_{rs} for match-up data within ± 90 min from the satellite overpass. The error bars indicate the maximum and minimum MODIS R_{rs} values in 3×3 and 5×5 pixel extents. The R_{rs} bands were red bands of the respective sensors.

The result of the inter-sensor validation of the R_{rs} product is shown in Figures 5.5a and b. From Figures 5.5a and b we observe that the inter-sensor R_{rs} product validation of MODIS-Aqua vs Landsat-8 OLI (Figure 5.5a) with MARE of 44.85 % showed a better result than MODIS-Aqua vs WV2 (Figure 5.5b) with a MARE of 55.99%. In addition, the ARE results in Figure 5.5a were also better with the smallest ARE and largest ARE of 0.15% and 158.11% while in Figure 5.5b the smallest ARE and largest ARE were 1.20% and 332% respectively. Further, in Figure 5.5a the type-II linear regression indicates that there is high correlation, with $R^2 = 0.87$, between MODIS-Aqua and Landsat-8 OLI derived R_{rs} , with most data points falling along the 1:1 line, considering the R_{rs} variability within a 2.5 km width square box (indicated by error bars in Figures 5.5a and b with the 17.5 and 82.5 percentile R_{rs} values). The correlation between MODIS-Aqua and WV2, as shown in Figure 5.5b, was lower, with $R^2=0.61$ with some data points failing to fall within the 1:1 line even after considering the errors from R_{rs} variability in the 2.5 km square box. However, the majority of the data points in both Figures 5.5a

and b show that MODIS-derived R_{rs} are lower than either WV2 or Landsat-8 OLI derived R_{rs} for $R_{rs} > 0.005 \text{ sr}^{-1}$.



(a)



(b)

Figure 5.5: Inter-satellite R_{rs} product validation results. (a) MODIS-Aqua vs Landsat-8 OLI R_{rs} product validation from May 23rd, July 10th and July 26th 2014; (b) MODIS-Aqua vs WV2 R_{rs} product validation for R_{rs} from June 13th 2014. The error bars indicate the 17.5 percentile (lower limit) and 82.5 percentile (upper limit) of pixel values from a 2.5 km width box for each respective satellite sensors derived R_{rs} . Dashed lines indicate the 1: 1 relationship. The R_{rs} bands were red bands of the respective sensors.

5.4.3 Sediment Plume Features Examination

Few selected regions within the study sites in Figure 5.1 (shown by red boxes in Figures 5.2a, 5.2c, and 5.2h) which are spatially degraded to lower spatial resolutions are shown in Figures 5.6a-c for WV2, Landsat-8 OLI and MODIS-Aqua sensors respectively. Subsequent images from the top row to bottom row in Figures 5.6a-c are spatially degraded to a coarser spatial resolution. In Figure 5.6a, showing WV2 at 2 m spatial resolution, we are able to visually identify even the fine spatial features in the sediment plumes adjacent to the large turbidity features which are very evident. Similar spatial features as those observed at 2 m spatial resolution are still evident in the degraded lower spatial resolution of 30 m. As the spatial resolution is degraded to 250 m and 500 m the fine spatial features which were evident at 2 m and 30 m spatial resolution are no longer visible, but we can still identify the two large distinct plume regions (DA and DA2 in Figure 5.6a) which are visible enough to be distinguished as two separate regions of plume when compared with the surrounding areas in DA and DA2.

In the lowest spatial resolution of 1000 m, we can no longer clearly discern even the two distinct DA and DA2 plumes observed at the 250 m and 500 m spatial resolutions. The separate regions of DA and DA2 are fused together to appear as one large region of turbid plume when compared with the surrounding background data. In Figure 5.6b, showing Landsat-8 OLI data at 30 m spatial resolution, we can distinguish the fine features of the river plume, but as the spatial resolution is degraded to 250 m, 500 m and 1000 m only the larger boundaries of the sediment plumes remain visible as the finer features are replaced by the coarser grids at degraded spatial resolutions. Similarly, in Figure 5.6c showing MODIS-Aqua data, we can clearly observe the dredge plume in the 250 m and 500 m spatial resolution images, but the 1000 m spatial resolution image loses the details that are observed at the higher spatial resolutions.

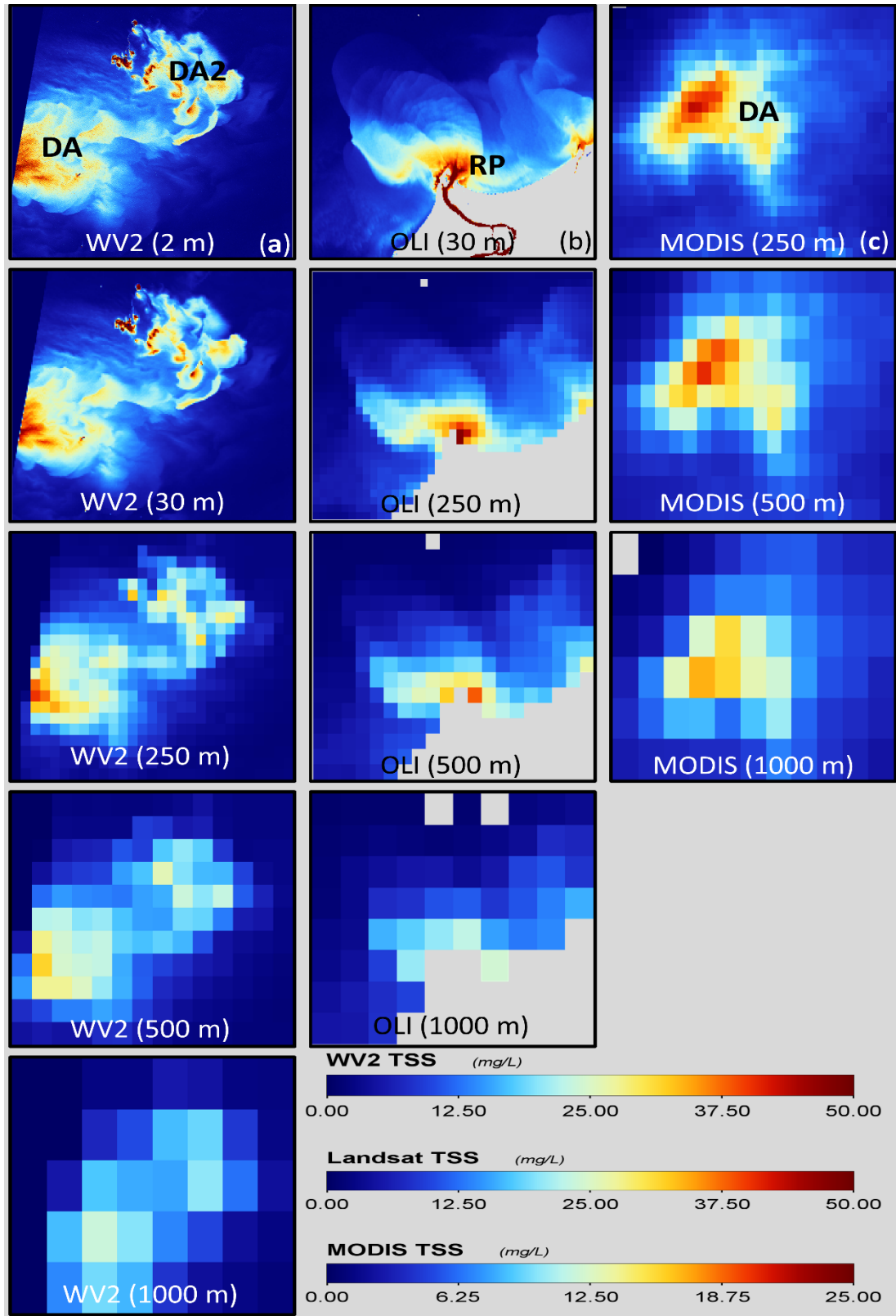


Figure 5.6: Spatially degraded images of the dredge area (DA) and river plume (RP): Extracted from images in Figures 5.2a, d, and i corresponding to (a) WV2, (b) Landsat-8 OLI and (c) MODIS-Aqua.

5.4.4 Quantification of TSS in Sediment Plumes

Figures 5.7a and 5.7b show the histograms of TSS concentrations derived from pixels located within the clean area (CA) which represents the background water to the turbid dredged area (DA) for all the images at MODIS-Aqua and WV2 sensor's native spatial resolution as well as spatially degraded resolutions respectively. The degraded resolutions encompass more pixels and the histogram shows the average TSS value of each area, with the error bars indicating the maximum and minimum TSS values of the native resolution pixels within each area. The comparative results between MODIS-Aqua and WV2 for the June 13th 2014 show that MODIS-Aqua derived average TSS values are relatively lower than WV2 derived average TSS for the regions DA, RP, SG and MTA. At sensor native resolution (2 m for WV2 and 250 m for MODIS-Aqua) the MODIS-Aqua derived TSS for the turbid regions (DA, SG and RP) were ~8.5 times less than WV2 derived TSS concentrations. In terms of average TSS derived at different spatial resolutions for the WV2 image (Figure 5.7b) we observe that in the plume/turbid areas (DA), the average TSS concentration decreased as the spatial resolution became coarser and the MARE between average TSS derived from 2 m and 2000 m spatial resolution in DA was 114.46%. Likewise, a similar trend was observed for the MODIS-Aqua images, with the MARE between 250 m and 5000 m spatial resolutions of 30.80% for MODIS-Aqua.

The variability in TSS concentration in different regions is represented by error bars (minimum and maximum TSS concentration in each spatial grid) in Figures 5.7a and 5.7b. The error bars in Figures 5.7a and 5.7b show that for all regions considered, the range of TSS variability increases as spatial resolution gets coarser and the area encompassed increases. In the region of the dredge plume (DA) the TSS concentration ranged from a low of 2.3 mg/L to a high of 160 mg/L for the WV2 image at the spatial resolution of 2000 m while for MODIS-Aqua, at a spatial resolution of 5000 m, by contrast only displayed TSS in the range of 1.4 mg/L to 6.6 mg L.

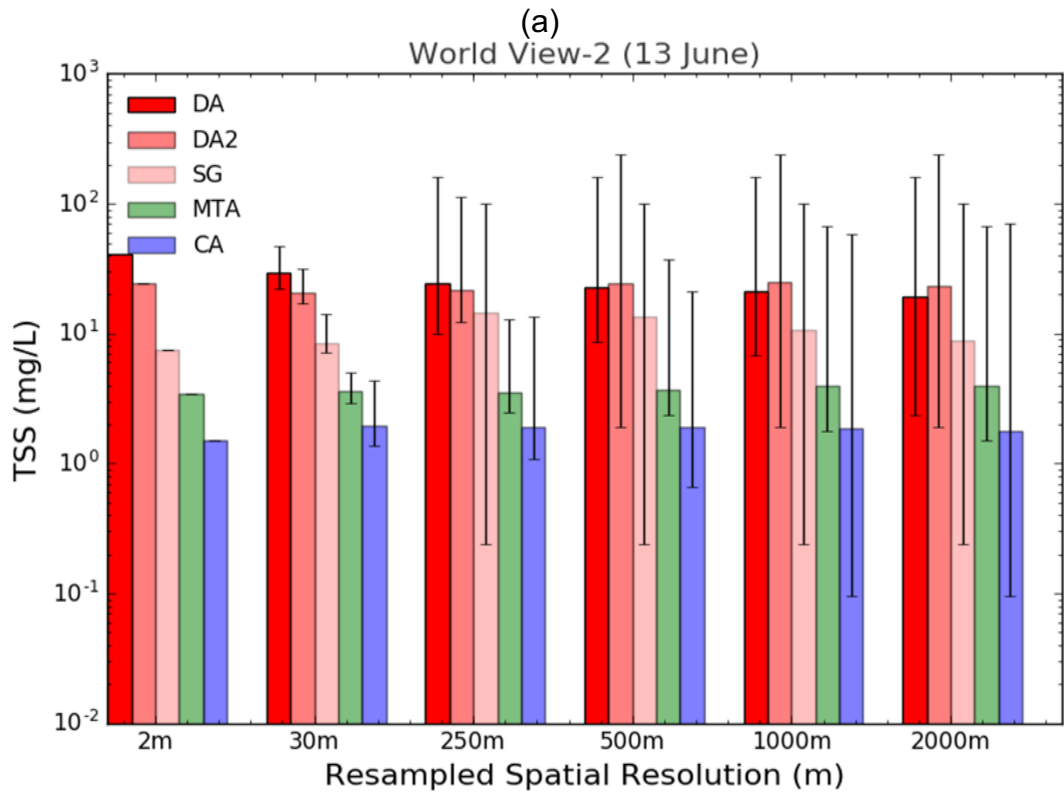
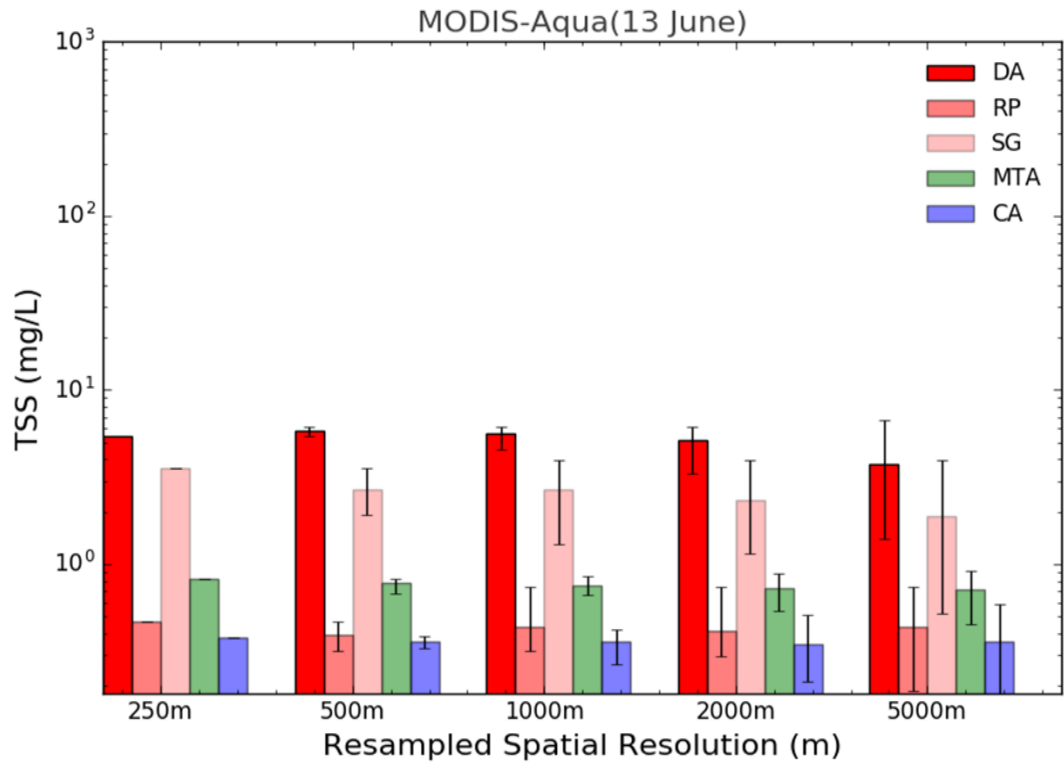


Figure 5.7. (a) MODIS-Aqua and (b) WV2 at their respective native and degraded spatial resolutions, averaged over the areas: dredge plume (DA and DA2), Spoil Ground (SG), River Plume (RP), Moderate Turbid Area (MTA) and Clean Area (CA). The error bars indicate the minimum and maximum TSS concentrations in each spatial grid.

Figures 5.8a-f show histograms of the TSS concentration derived using Landsat-8 OLI and MODIS-Aqua data for May 23rd, July 10th and July 26th 2014 for regions DA, CA, MTA, RP and SG at native and degraded spatial resolutions. For all three dates, the TSS concentration derived using Landsat-8 OLI images were higher than the MODIS-Aqua for the turbid (DA, SG and RP) and moderately turbid (MTA) regions while the MODIS-Aqua derived TSS was higher than the Landsat-8 OLI for the clean area (CA). For the turbid regions (DA, RP and SG) the ARE between MODIS-Aqua and Landsat-8 OLI derived TSS ranged from 2.3% to 304.68% with higher ARE at the higher spatial resolution for all Landsat-8 OLI and MODIS-Aqua image pairs. For the regions of moderately turbid (MTA) and clean area (CA) the ARE in TSS concentration ranged from 44.22% to 82.08% with a maximum of 4% variability in ARE for all different spatial resolutions within any Landsat-8 OLI and MODIS-Aqua image pair.

In general, apart from the MODIS-Aqua image of the May 23rd 2014 (Figure 5.8d) all TSS concentrations derived for turbid regions (DA, SG and RP) show general trends in which the mean TSS concentrations of the coarser spatial resolution grid are lower than the mean TSS concentrations derived at higher spatial resolution. Further, the variability in TSS concentration as represented by minimum and maximum TSS concentrations in the spatial grid increases as the spatial grids get coarser and cover a larger extent. The range of TSS concentration as derived by Landsat-8 OLI and MODIS-Aqua varied from 5.59 mg/L to 29.15 mg/L and 3.9 mg/L to 6.31 mg/L in the turbid regions (DA, SG and RP) respectively while the TSS concentration ranged from 0.38 mg/L to 0.43 mg/L for MODIS-Aqua and 0.14 mg/L to 0.30 mg/L for Landsat-8 OLI in the background waters (CA).

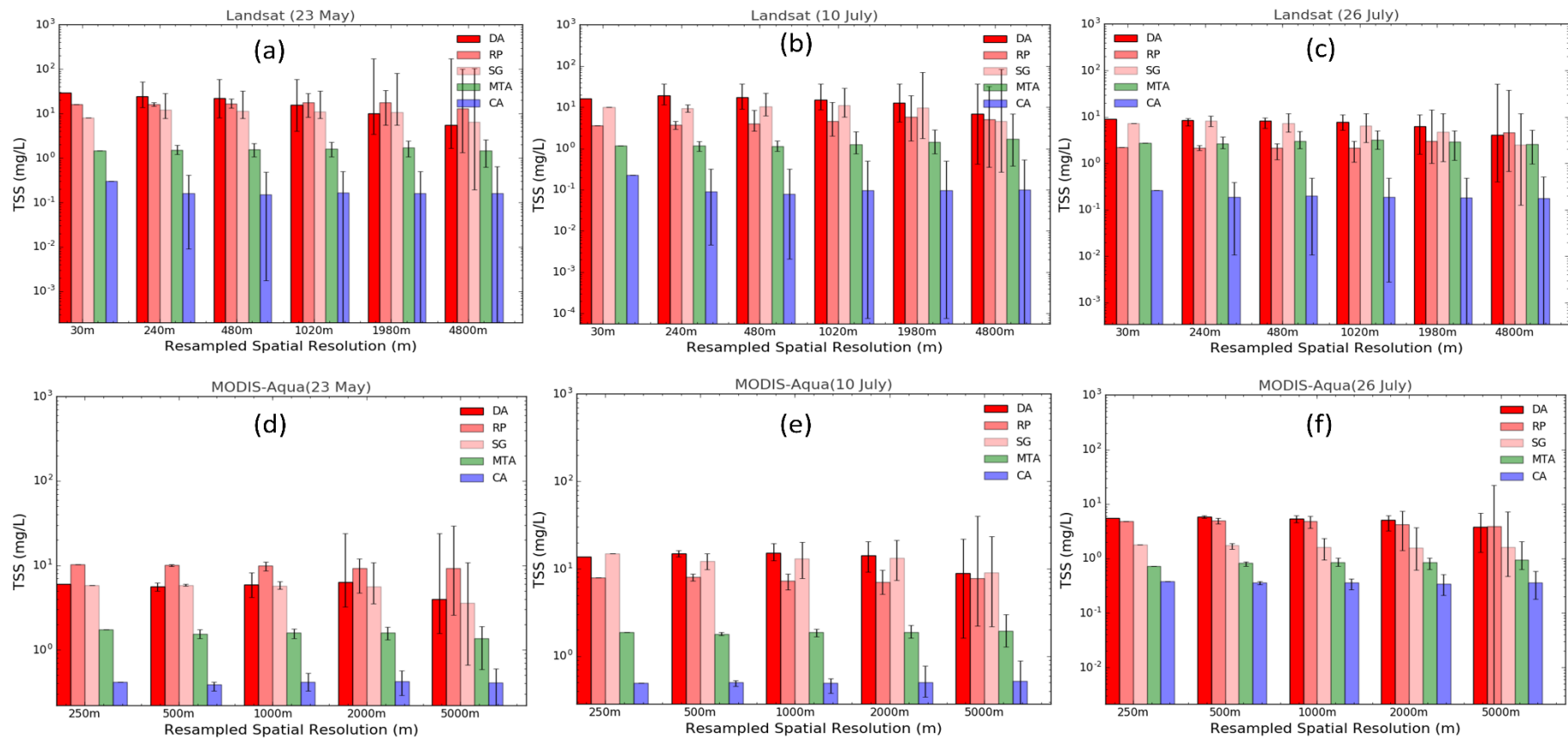


Figure 5.8: Average TSS concentration. (a)—(c) Landsat-8 OLI and (d)—(f) MODIS-Aqua at their respective native and degraded spatial resolutions in the dredge plume (DA), Spoil Ground (SG), River Plume (RP), Moderate Turbid Area (MTA) and Clean Area (CA). The error bars indicate the minimum and maximum TSS concentrations in each spatial grid.

5.5 Discussion

5.5.1 Data and Methodological Limitations

The results presented demonstrate the differences observed in remotely sensed TSS concentrations for three different sensors and for varying spatial scales of monitoring. The remote sensing instruments, WV2, MODIS-Aqua and Landsat-8 OLI considered in this study have their own radiometric characteristics and atmospheric correction methods that are best suited to each individual sensor. Apart from the radiometric and atmospheric correction methodologies considered for each sensor we also have to take into account the different image acquisition times when attempting to compare the results of the different sensors. The miss-match between the different sensor image acquisition times leads to the situation where the water mass, or the feature of interest such as a sediment plume, may move and alter in spatial distribution, thus the comparison of the R_{rs} was based on a spatial subset of pixels contained within a square region of length 2.5 km, the average distance the surface current for June 13th 2014 in the study region was estimated to move a water mass within the acquisition time differences (P. Branson, personal communication, July 4th 2016). Further, the effect of pixel resolution and the size of the spatial domain on the TSS product was studied by degrading the spatial resolution of the TSS products for each sensor to coarser and larger grids.

The inter-sensor TSS algorithms considered in this study were all calibrated using the same *in situ* TSS and R_{rs} measurements in the red bands of the respective sensors and the *in situ* validation result of the TSS algorithms for all three satellite sensors were within MARE of 33.33% to 33.36%. Figure 5.3 shows the close similarity in the algorithm curves for each sensor, with a maximum relative difference of ~10% between TSS values occurring at higher R_{rs} . However, comparison between TSS algorithm curves should take into account the differences in the spectral response of each sensor, thus the R_{rs} value for the same body of water would be

expected to be slightly different for each sensor, as indicated by the horizontal displacement of the individual data points in Figure 5.3. Nonetheless, the value of 10% is a reasonable estimate of the upper limit of the differences in TSS to be expected simply due to differences between sensor algorithms. The use of different atmospheric correction methods for different sensors can cause discrepancies in the final derived TSS products, thus it is vital to account for such discrepancies in atmospheric correction methods. The R_{rs} results for the MODIS-Aqua which were validated using the *in situ* R_{rs} data showed that MODIS-Aqua had MARE of 33.82%. The WV2 and Landsat-8 OLI atmospheric correction results which were “validated” against the MODIS-Aqua R_{rs} data had MARE of 55.99% for WV2 vs. MODIS-Aqua, and 44.85% for MODIS-Aqua vs. Landsat-8 OLI. The high MARE values of inter sensor validation may be expected because of the acquisition time differences between satellite sensor data that were in excess of 3 hrs between MODIS-Aqua and WV2, and 3.75 hrs between MODIS-Aqua and Landsat-8 OLI. In areas of the turbid dredged plumes (DA and DA2 in Figure 5.2a) the MODIS-Aqua R_{rs} derived using the MUMM atmospheric correction method is particularly low when compared with R_{rs} derived from WV2 using the 6S atmospheric correction method. The highest ARE were between the R_{rs} derived from the MUMM and 6S atmospheric correction methods at 332% while the lowest ARE of 1.2 % were observed in the region of the background waters (CA in Figure 5.2a). The underestimation of R_{rs} by the MUMM atmospheric correction method could be because it was designed for moderately turbid waters (Vanhellemont & Ruddick, 2014) and fails to retrieve R_{rs} correctly in highly turbid waters of the dredge plumes. Similar under estimation of R_{rs} in the turbid region (DA in Figures 5.2c-h) by the MUMM atmospheric correction method applied to the MODIS-Aqua image was observed when compared with R_{rs} derived from the SWIR atmospheric correction applied to the Landsat-8 OLI which was adapted for the turbid waters (Vanhellemont & Ruddick, 2015).

5.5.2 General Observation and Recommendations

The effect of different spatial resolutions of the satellite sensors on identifying and mapping the fine features in the dredge plumes are evident from the results. The higher spatial resolution satellite sensors, no doubt, have the benefit of identifying even the fine features in the sediment plumes. For the size and scale of images displayed, the 30 m Landsat-8 OLI and 2 m WV2 TSS products shows similarly fine features, but as the spatial resolution is degraded to larger pixel sizes the fine features are no longer visible, as seen in images with the spatial resolution greater than 250 m (see Figure 5.6). The fine details observed with the high spatial resolutions of WV2 at 2 m and Landsat-8 OLI and 30 m native spatial resolution makes these two sensors capable of resolving fine spatial details in the surface turbidity features and shows the capability of their application in spatial features/extent mapping of the sediment plumes when compared with MODIS-Aqua sensors. From the perspective of dredge plume monitoring for environmental impact assessment or compliance, the finer details available in the higher resolution satellite data provide better resolution of the spatial extent of dredge plumes, and this in turn translates to a higher confidence in the product. For instance, the extent of the dredge plume in the lateral direction when measured with the high resolution WV2 image was ~6 km, while the MODIS-Aqua derived measurement was ~10 km. However, marine and environmental protection agencies should carefully weigh the cost and benefit of using different spatial resolution sensors. Both the WV2 and Landsat-8 OLI data are able to identify the fine features of the dredge plume, but users should be mindful that the WV2 data are not freely accessible, as is Landsat-8 OLI. Further, if the requirement of the agencies were just to map the extent of dredge plume then MODIS 250 m spatial resolution shows similar capability in mapping the larger TSS spatial features, but not the fine features and details as seen in the high resolution WV2 and Landsat-8 OLI images.

The general trend observed in quantified TSS concentration (Figures 5.7 and 5.8) is that as the spatial resolution gets coarser and the spatial

extent increases the mean TSS concentration decreases for all three different sensors for turbid regions (DA, SG and RP) while the mean TSS concentrations for CA and MTA remain relatively uniform. Depending on the spatial resolution, the mean TSS concentration results for different spatial resolutions by the same satellite sensors are different and it is shown to decrease as spatial resolution gets coarser for turbid regions. The decrease in TSS concentration with coarser spatial resolutions are observed because of the inclusion of background and lower turbid waters in averaging as the spatial grids get larger. In monitoring of TSS concentration in turbid regions it is important for environmental agencies to be mindful of the result from this study where it shows the effect of the coarser spatial resolution sensors in inclusion of background and lower TSS concentration neighboring pixels producing a lower average TSS concentration than the TSS concentration of the sediment plume over a small spatial extent, particularly when the size of the sediment plume is smaller than the spatial resolution of the satellite sensor. However, our results did not show that such an effect is observed in regions where the turbidity is uniformly distributed over a relatively large spatial extent.

The quantification of TSS concentrations variability results (see Appendix G for details) show that in the background, CA (see Figure G3), spatially uniform and moderately turbid waters, MTA (see Figure G2), the TSS variability remains similar across different spatial resolutions for each sensor. The TSS variability across different spatial resolutions (250 m – 2000 m) for CA and MTA were mostly below ~5% from the mean TSS concentrations of the respective region, with the exception of Landsat-8 OLI in MTA which had TSS variability of 10.39%. The low TSS variation is expected in the CA and MTA regions because the CA, which is approximately 30 km from the dredge region, is expected to remain undisturbed by the dredging activities and has a natural background level of TSS concentration without disturbance from anthropogenic processes. Further, the MTA region, which has spatially uniform TSS concentration, is expected to show minimum variance when spatially degraded to represent

coarser spatial resolution. However, in the turbid regions (DA, SG and RP) the TSS variability was higher, with 16.96%, 54.09%, and 12.05% for MODIS-Aqua, Landsat-8 OLI and WV2 respectively. The higher TSS variability in the turbid regions, the regions of dredge and river plumes, can be associated with higher TSS gradient in each region. The mean TSS concentration derived by different satellite sensors was also different for each sensor.

The MODIS-Aqua sensor produced mean TSS concentrations of 12.67 ± 2.15 mg/L, 1.89 ± 0.04 mg/L, and 0.51 ± 0.02 mg/L for the DA, MTA and CA regions respectively. Likewise, for Landsat-8 OLI and WV2 sensors, the mean TSS concentrations in the DA, MTA and CA regions were quantified to be 11.34 ± 6.13 mg/L, 1.61 ± 0.07 mg/L, and 0.16 ± 0.02 mg/L for Landsat-8 OLI and $22.04.34 \pm 2.65$ mg/L, 3.85 ± 0.19 mg/L, and 1.84 ± 0.06 mg/L for WV2. Thus, in monitoring TSS concentration, it should be noted that the TSS variability observed by the satellite sensors is not only associated with the different satellite sensor's spatial resolution, but also the horizontal spatial distribution of TSS as well.

5.6 Conclusion

The aim of this study was to highlight the effect of the sensor spatial resolution on quantification of TSS concentration in turbid sediment plumes. Results from this study show that different satellite sensors with different spatial resolutions can produce different TSS concentrations, particularly in regions of spatially variable TSS. The WV2 sensor, with 2 m spatial resolution, was shown to generate TSS concentrations as high as 160 mg/L in the region of the dredge plumes while the highest TSS concentration generated by MODIS-Aqua with 250 m spatial resolution was 23.6 mg/L. Even for the same satellite sensor degraded to different spatial resolutions, the TSS concentrations in the non-uniform turbid regions varied by 114.46%, 304.68% and 38.2% for WV2, Landsat-8 OLI and MODIS-Aqua respectively as the sensor resolution was degraded and the spatial extent increased. In the region of background water and uniformly turbid waters, the mean TSS

concentration was observed to be uniform as the sensor resolution was degraded and the spatial extent was increased. Thus, in the context of TSS monitoring of the coastal waters, and particularly for environmental compliance monitoring for dredge operations, users must be mindful of the fact that different satellite sensors produce different TSS concentrations with higher spatial resolution satellite sensors reporting higher TSS values. Also, higher spatial resolution sensors are able to resolve fine turbidity features while lower spatial resolution sensors are only able to resolve the larger spatial extent of the sediment plumes.

Chapter 6

Mapping Total Suspended Sediment in Near Real Time: A Preliminary Assessment of the AHI sensor on board the geostationary Himawari-8 satellite for Coastal Waters of Western Australia.

This chapter has been submitted in the journal: Remote Sensing of Environment

Dorji, P., & Fearn, P. (2017). Mapping Total Suspended Sediment in Near Real Time: A Preliminary Assessment of Geostationary Satellite (Himawari-8) in Coastal Waters of Western Australia. *Remote Sensing of Environment, (Submitted).*

6.1 Abstract

Recent studies in the application of geostationary satellite sensors, such as the Spinning Enhanced Visible and InfraRed Imager (SEVIRI) onboard the European Union's meteorological satellite, and the Geostationary Ocean Colour Imager (GOCI) from South Korea, to monitor the Total Suspended Sediment (TSS) in coastal waters have shown that the higher temporal dynamics in the coastal processes can be better achieved through the use of high temporal resolution geostationary satellite sensors. The availability of the geostationary satellite, Himawari-8 carrying the Advanced Himawari Imager (AHI) sensor with visible, Near InfraRed (NIR) and Shortwave InfraRed (SWIR) bands over the coastal waters of Australia has prompted this study to test the feasibility of AHI in studying the coastal TSS dynamics in Western Australian waters. In this study, we show that diurnal variability in TSS concentration in coastal waters of northern Western Australia can be observed using the AHI sensor for TSS concentrations greater than ~0.15 mg/L and when solar zenith angles (θ_0) are less than 60°. In addition, the diurnal variations of TSS concentration in the region showed

that the TSS concentration of water near the coast decreased by a factor of ~2 between the lowest and highest tidal elevation point. Also, *in situ* validation performed on the atmospherically corrected water leaving reflectance (ρ_w) showed that atmospheric correction performed on AHI data using SWIR bands in aerosol estimations performed better than using a combination of NIR and SWIR bands. Further, cross-validation of AHI derived TSS concentration with MODIS-Aqua and Landsat-8 Operational Land Imager (OLI) data showed good correlation, with correlation coefficients $r = 0.71$ and $r = 0.91$ respectively.

6.2 Introduction

Monitoring the status of ocean colour in the past has been mostly met by low altitude, polar orbiting satellites with either a dedicated ocean colour sensor or sensors that were primarily designed for terrestrial monitoring (IOCCG, 2000). Widely used historical ocean colour sensors with dedicated ocean colour bands employed in mapping Total Suspended Sediment (TSS) included the Coastal Zone Colour Scanner (CZCS) (Viollier & Sturm, 1984), Sea-Viewing Wide Field-of-view Sensor (SeaWiFS) (Binding et al., 2003; Burenko et al., 2001; Fettweis et al., 2007; Myint & Walker, 2002), and the Medium Resolution Imaging Spectrometer (MERIS) (Doxaran et al., 2014; Kratzer et al., 2008; Odermatt et al., 2008). The currently operational polar orbiting sensor with dedicated ocean colour bands used in TSS mapping is the MODerate resolution Imaging Spectrometer (MODIS) on board the Terra and Aqua satellites (Constantin et al., 2016; Li et al., 2010; Miller & McKee, 2004; Wang et al., 2009a) and the recently launched Sentinel-3A in February 2016 with Ocean and Land Colour Instrument (OLCI) as part of the European Commission's Copernicus programme (EUMETSAT, 2017). The MODIS instruments have passed their designed life-spans (MODIS Web, 2017). Landsat based sensors, which were primarily designed for use in terrestrial monitoring, have also been extensively used in marine applications. For example, TSS mapping in coastal environments was carried out using the earliest Multispectral Scanner (MSS) and Thematic

Mapper (TM) aboard Landsat satellites 1 to 5 (Kim, 1980; Klemas et al., 1973; Wang et al., 2006; Zhou et al., 2006) and more recently using the currently operational Landsat sensors, Enhanced Thematic Mapper Plus (ETM+) (Kallio et al., 2008a; Wang et al., 2009b) and Operational Land Imager (OLI) (Cai et al., 2015b; Ody et al., 2016; Vanhellemont & Ruddick, 2014, 2015; Zhang et al., 2016b) aboard Landsat-7 and Landsat-8 respectively.

The advantage of low earth orbiting satellite sensors are numerous, and have far surpassed the spatiotemporal limitations inherent in the traditional *in situ* sampling methods used in water quality monitoring. Further, notwithstanding the availability of the high spatial resolution (~1.5-10 m) of commercial satellite sensors such as WorldView 2-4, Satellite Pour l'Observation de la Terre (SPOT) 6-7, and Advanced Land Observing Satellite (ALOS) 2, the freely accessible low earth orbiting sensors such as MODIS-Aqua/Terra and Landsat-7 and Landsat-8 with global spatial coverage, provide ocean colour data for mapping TSS concentration at adequate spatial resolutions from 30 m to 0.25 – 1.0 km respectively. However, the temporal resolutions of MODIS and Landsat sensors are generally ~1-2 days and ~16 days respectively, thus data from these sensors are sufficient to differentiate, at best, daily TSS variability during cloud free periods, or seasonal variability of TSS concentration for most open ocean waters (Neukermans et al., 2009). In contrast, most coastal waters are characterized by highly energetic environments that undergo frequent horizontal advection and vertical resuspension from the influence of wind driven and tidal currents, thus the variability in biogeochemical processes occurs at relatively short timescales (Van Raaphorst, Malschaert, & Van Haren, 1998). For instance, Thompson et al. (2011) reported that apart from the wind driven waves, the resuspension due to tidal forcing alone can account for from approximately 8% to 13% for a short (< 30 min) duration timescale. The temporal resolution needed to discern such diurnal variability from daily or seasonal variation in TSS concentration is much higher than currently afforded by low earth orbiting satellite sensors. Satellite sensors

with the capability of acquiring numerous images per day, currently available only through high earth orbiting geostationary satellite sensors, can provide the high temporal resolution required for studies of coastal dynamics.

First of the pioneering studies in estimating TSS using a geostationary satellite sensor was carried out by Neukermans et al. (2009) using the Spinning Enhanced Visible and InfraRed Imager (SEVIRI) onboard the European Union's meteorological satellite (EUMETSAT). Following Neukermans et al. (2009), a limited number of studies have been carried out using the SIVIRI sensor (Neukermans et al., 2012; Salama & Shen, 2010) and the dedicated ocean colour sensor, Geostationary Ocean Colour Imager (GOCI) (Choi et al., 2014; Doxaran et al., 2014; Huang et al., 2015), on board the Communication, Ocean and Meteorological Satellite (COMS) operated by South Korea. The SERIVI was primarily developed for meteorological purposes with broad spectral resolution in the visible and near infrared (NIR) bands, thus it has limitations in general ocean colour monitoring. Nonetheless, SERIVI has shown promise in the study of the temporal dynamics of coastal waters because of its high temporal resolution (data available every 15 min) and its ability to map TSS concentration using just a single Red or NIR band at a spatial resolution of 3.0 x 6.5 km (Neukermans et al., 2009). The GOCI sensor, primarily developed for ocean colour applications with six visible (412, 443, 490, 555, 660, and 680 nm) and two NIR (745 and 865 nm) bands, has shown that it can be used in mapping the dynamics of TSS concentration in coastal waters at high temporal resolution (eight images per day) (He et al., 2013), but the absence of spectral bands in short-wave infrared (SWIR) bands has proven challenging in atmospheric correction of data collected over highly turbid coastal waters (Wang et al., 2013).

This study was prompted by the success of the SERIVI and GOCI sensors in mapping TSS concentration in coastal waters. We explore the feasibility of the Advanced Himawari Imager (AHI) on board the Japanese meteorological agency's geostationary meteorological satellite, Himawari-8, in mapping the temporal dynamics of TSS variability in coastal waters of

Western Australia. The AHI sensor has the required spectral bands and the spatiotemporal resolution needed for the detection of high temporal dynamics in coastal waters in Western Australia. Further, there are planned missions involving geostationary satellite sensors with the required ocean colour bands, such as GOCI-II by South Korea, GEO-CAPE by the United States, Geo-Oculus by Europe, Himawari-9 by Japan, and HR-GEO by India (IOCCG, 2012). The current geostationary sensors, and the planned missions, provide the needed incentive in conducting more studies in ocean colour mapping using Geostationary satellite sensors. As far as we know, no study has been conducted using the AHI sensor in mapping TSS concentration, although feasibility studies in ocean colour estimation—the mapping of chlorophyll-a (Chl-a), were conducted by Murakami (2016) using AHI observations. Specifically, this study will aim to answer following two questions: 1) are AHI data capable of mapping TSS concentration in coastal waters of Western Australia, and 2) are AHI data able to discern diurnal TSS variability in the region.

6.3. Materials and Methods

6.3.1. Study area

The study area chosen for this study falls along the Pilbara coast, which extends between the Exmouth Gulf ($22^{\circ} 25' 00''$ S and $114^{\circ} 25' 00''$ E) and Onslow ($21^{\circ} 35' 00''$ S and $115^{\circ} 05' 00''$ E) in Western Australia (see Figure 6.1 for details). The coastline of the Pilbara region is dominated by river deltas and tidal flats which are more than 2 km wide from the coastline in the majority of the region (Stul, Gozzard, Eliot, & Eliot, 2014). The shallow waters in the Exmouth Gulf and the Onslow region extend approximately 50 km from the coastline, with water depths less than 30 m, while the waters that extends greater than 50 km from the coast can range in depth from 30 m, depending on their proximity to the coast, to greater than 1000 m for offshore waters (Department of Environment, 2007). A significant source of sediments in the coastal waters of the Pilbara region is the

Ashburton River (22° 42' S and 114° 55' 00'' E) which discharges large quantities of sediment laden water with TSS concentration ranging from 15 to 5000 mg L⁻¹ with higher concentration closer to the river mouth (URS, 2014). The vertical mixing of waters in the Pilbara coastal regions is generally caused by the combination of tidal current, wind-driven waves and episodic seasonal cyclones (Department of Environment, 2007). The average rainfall in the Exmouth Gulf and Onslow region is approximately 300 mm annually with mean annual temperatures in the range 21.5 to 29 °C and with mean summer wind speeds between 7 and 9 m s⁻¹ and winter wind speeds of only 3 m s⁻¹ in variable directions (Bureau of Meteorology, 2015a).

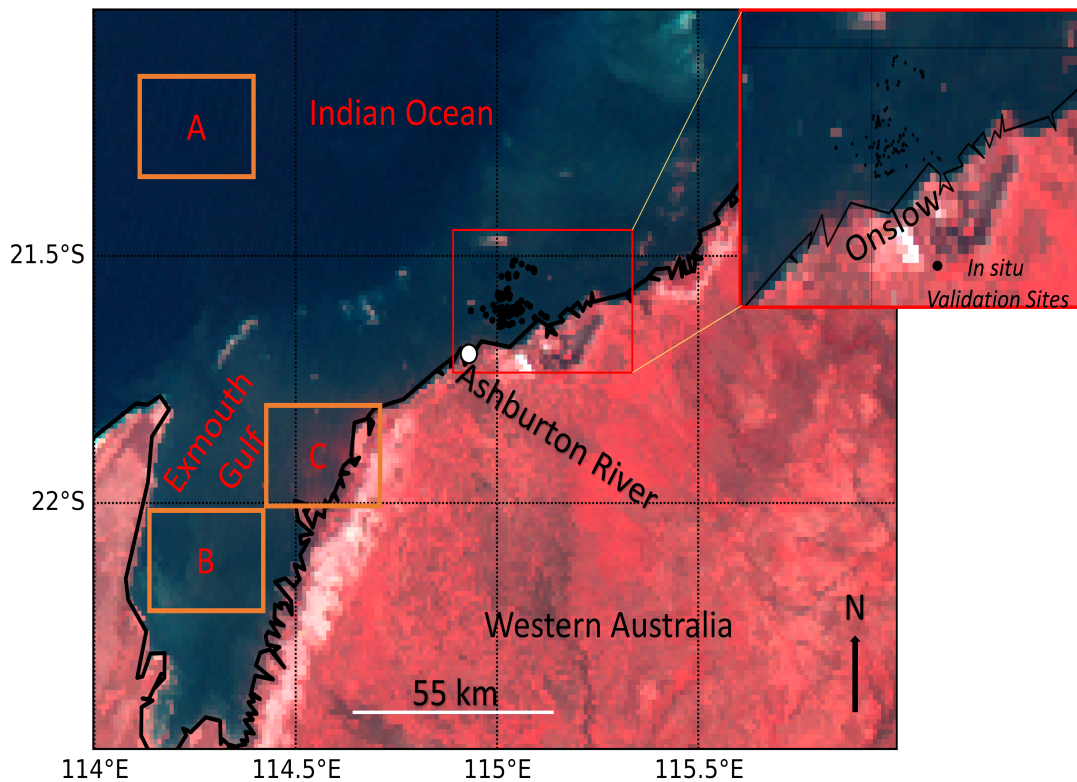


Figure 6.1: True colour image of the study site (RGB = AHI Band 3, 2, 1). Black filled circles are the *in situ* validation points collected during the field campaign on July 4th – July 10th 2015 (shown in blow-out version on the right for greater details). Box A corresponds to homogenous clear water area; Box B corresponds to homogenous region within the Exmouth Gulf; Box C corresponds to turbid waters near the coast.

6.3.2 Himawari-8 (AHI) overview

Himawari-8, stationed above the equator at 140.7 °E, is a Japanese meteorological satellite that was primarily designed for meteorological purpose and was launched on October 7th 2014, becoming fully operational from July 7th 2015 (Murakami, 2016). The AHI sensor onboard Himawari-8 has 16 spectral channels, with three that collect data in visible bands (470.3, 510.5, and 639.9 nm), one NIR (856.3 nm), two SWIR bands (1609.8, and 2257 nm), and 10 bands in thermal infrared (TIR) regions (~3.9 – 13.3 μm). Spatial resolution at the sub satellite point of the first two visible bands (blue and green) and the NIR band is 1 km, while the third visible band (red) is 0.5 km. The spatial resolution of the SWIR and TIR bands is 2 km. Himawari-8 collects data at three different temporal resolutions that depend on the sampled regions, divided into the whole earth disk, three target regions, and two landmark areas (see Figure 6.2 for details). The full disk of the earth as seen from the satellite is collected every 10 min while two target regions focused on north eastern and south western Japan with one flexible target region which can be changed depending on the needs of meteorological conditions are collected every 2.5 minutes, and two landmark regions which are also flexible to enable the prompt and rapid assessment of meteorological conditions are collected every 0.5 minutes (Japan Meteorological Agency, 2015).

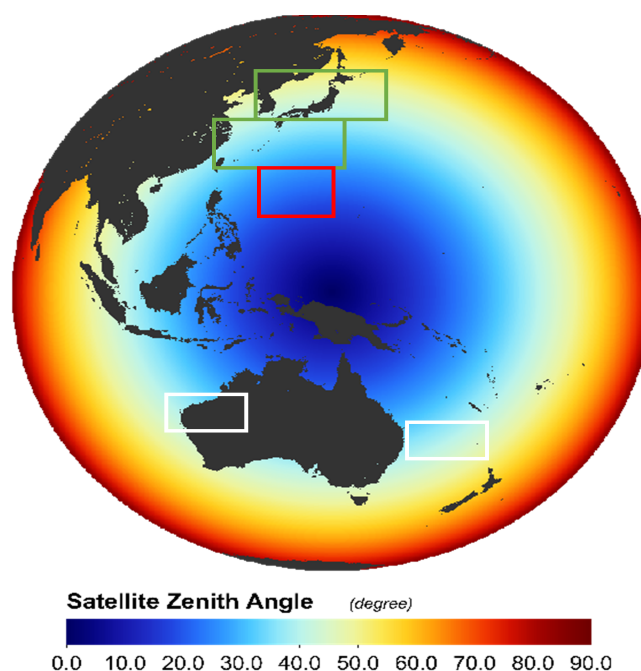


Figure 6.2: Full disk view of earth as seen from Himawari-8 with different target areas (green rectangles (top) North-Eastern Japan Area and (bottom) South-Western Japan Area, red square flexible target area and white rectangles are flexible Landmark areas). The satellite view angle is show for the whole disk with satellite zenith at 140.7°E.

6.3.3. Satellite sensor dataset acquisition and atmospheric correction

The satellite dataset used in this study are from Himawari-8 AHI, Landsat-8 OLI and MODIS-Aqua acquired for the dates shown in Table 6.1.

Table 6.1: Data Acquisition dates for Himawari-8, Landsat and MODIS-Aqua

Satellite Sensor	Date/Time
Himawari-8 AHI	July 4 –10 th , 2015 (10:00 am – 4: 00 pm at every 10 mins)
Modis-Aqua	July 4 –6 th and July 8-10 th , 2015 (1:00 pm – 2:35pm)
Landsat-8 OLI	July 29 th , 2015 (10:20 pm)

6.3.3.1 Himawari-8 AHI data acquisition and atmospheric correction

The first six bands, three visible, one NIR and two SWIR, of full disk data were used in this study. The Himawari Standard Data (HSD) of the AHI sensor for July 4 – 10th, 2015 were obtained from the Australian Bureau of Meteorology through the National Computational Infrastructure facilities

(<http://nci.org.au/>). HSD data files contain all the necessary metadata for calibration and projection parameters in the header section along with the raw binary data available in the main HSD block. The calibration parameters were applied to the raw counts to produce at-satellite radiance (L_{toa}) for fixed grids, which are defined by fixed pixel locations relative to an ideal geostationary satellite viewpoint (Japan Meteorological Agency, 2015). The L_{toa} was converted to reflectance at top of the atmosphere (ρ_{toa}) using Equation (6.1), spatially resampled from 0.5 km in the red band and 1 km in the blue, green and NIR band to a standard 2 km as in SWIR and TIR bands. The AHI derived L_{toa} data were converted to a CF-complaint NetCDF-4 files using a 'hsd2netcdf' source code written in C (available at <http://www.data.jma.go.jp/>) which was developed by Japanese Meteorological Satellite Center to convert the HSD to a NetCDF file.

$$\rho_{\text{toa}} = \frac{\pi d^2 L_{\text{toa}}}{F_0 \cos \theta_0} \quad (6.1)$$

Where d is the sun-earth distance in astronomical units, θ_0 is the solar zenith angle and F_0 is spectral solar irradiance at top of the atmosphere (in $\text{W m}^{-2} \mu\text{m}^{-1}$).

For the atmospheric correction, the ρ_{toa} can be decomposed into following contributions as shown in Equation (6.2) (Neukermans et al., 2009; Vanhellefont & Ruddick, 2014).

$$\rho_{\text{toa}} = \rho_a + \rho_r + \rho_{\text{ra}} + \rho_g + t_0 t_v (\rho_w + \rho_{\text{wc}}) \quad (6.2)$$

where ρ_a and ρ_r are reflectance from Rayleigh and aerosol scattering respectively, ρ_{ra} is the contribution as a result of interaction between aerosol and molecules. Typically, ρ_{ra} is included in the ρ_a estimation, so it can be excluded from Equation (6.2). ρ_g is the sun-glint contribution, t_0 and t_v are sun-sea and sea-sensor total diffuse transmittance, $\rho_w = \pi L_w(0^+) / E_d(0^+)$ and ρ_{wc} are water-leaving reflectance and white caps reflectance of the sea surface respectively. ρ_g is only significant when the satellite zenith angle (θ_v) is close to θ_0 and relative azimuth angle ($\Delta\varphi = |\varphi_0 - \varphi_v|$) is close to 180° (Neukermans et al., 2009). For the whole of our study region (Figure 6.1), the

θ_v and satellite azimuth (φ_v) angle varied between 39°- 40° and 53°- 54° respectively and $\Delta\varphi$ varied from ~15° - 123° between 10 am to 3 pm, so ρ_g was assumed to be negligible in Equation (2) for the study site. Further, ρ_{wc} for our study site was also assumed to be negligible because wind speed for the dates considered in this study was less than 10 m s⁻¹, as according to Gordon and Wang (1994a) the ρ_{wc} should be accounted for in the aerosol correction for wind speeds higher than 10 m s⁻¹. Thus, after considering the negligible contributions from ρ_g and ρ_{wc} , the Equation (6.2) can be rewritten as,

$$\rho_{toa} = \rho_a + \rho_r + t_0 t_v \rho_w \quad (6.3)$$

The t_0 and t_v can be decomposed separately into the effects from the atmospheric gases (ozone, water vapor, methane, oxygen, and carbon monoxide and carbon dioxide), aerosol and air molecules as shown in Equation (6.4).

$$t_0 = t_0^a t_0^r t_0^g \quad \text{and} \quad t_v = t_v^a t_v^r t_v^g \quad (6.4)$$

where $t_0 = t_0^a, t_0^r, t_0^g$ are transmittance factors for sun-sea for aerosol, Rayleigh and atmospheric gasses respectively and $t_v = t_v^a, t_v^r, t_v^g$ are for sea-sensor for aerosol, Rayleigh and atmospheric gasses respectively. The Rayleigh corrected reflectance (ρ_c) can be computed as shown in Equation (6.5) if ρ_r is known a priori.

$$\rho_c = \rho_{toa} - \rho_r = \rho_a + t_0 t_v \rho_w \quad (6.5)$$

The unknown parameters ρ_r , t_0 and t_v in Equation (6.5) were generated as a look-up-table (LUT) using the Second Simulation of a Satellite Signal in the Solar Spectrum Vector Version 1.1 (6SV1.1) developed by Vermote, Tanre, Deuze, Herman, and Morcette (1997) for the parameters shown in Table 6.2 for the first six AHI bands. The satellite geometry, θ_v and φ_v , used in generating the LUT was maintained constant at 39.2° and 53.6° respectively, which are the mean values of satellite geometry of the study site. Further, the range of satellite geometry, both θ_v and φ_v varied by only ~1° for the whole

study site. For the atmospheric model, we only varied water vapor and ozone concentration because these two parameters are known to exhibit higher spatial and temporal variability than other gases which are considered well mixed in both the spatial and temporal domains (Proud, Fensholt, Rasmussen, & Sandholt, 2010). In addition, we used a tropical aerosol model for the aerosol model type required as input for the 6SV1.1. For the cloud and land mask for AHI data for our study region we used AHI Band 5 in the SWIR region with a threshold of $\rho_c^5 > 0.0215$ as it is shown to be effective in classifying cloud and land from water pixels even in turbid coastal water (Vanhellemont & Ruddick, 2015; Wang & Shi, 2006).

Table 6.2: Parameters and values used in generating LUT using 6SV

Parameters	Values
Solar Zenith Angle	0,5,10,15,20,25,30,35,40,45,50,55,60,70
Solar Azimuth Angle	0,15,30,45,60,90,120,150,180,210,240,270,300,330,360
Water Vapor (g/cm ²)	0,0.5,1.0,2.0,3.0,4.0,5.0
Ozone(cm/atm)	0,0.1,0.2,0.25,0.3,0.4,0.45,0.5,1.0
AOT (550 nm)	0.0,0.001,0.01,0.05,0.1,0.15,0.2,0.3,0.4,0.5,1.0

The aerosol, ρ_a , correction in Equation (6.5) was performed using two aerosol estimation methods: 1) SWIR bands (Band 5 = 1609.8 nm and Band 6 = 2257 nm) and 2) one NIR (Band 4 = 860 nm) and one SWIR band (Band 5 = 1609.8 nm). Hereafter, the first aerosol correction method will be referred to as the SWIR method and the second as the NIR-SWIR method. In the SWIR bands ρ_w is negligible even for very turbid water cases, with essentially zero contribution from ρ_w because of strong absorption by water molecules in the SWIR bands (Gordon & Wang, 1994b; Vanhellemont & Ruddick, 2015). In the NIR bands ρ_w is not negligible in turbid waters, but for clear water pixels that are farther away from the coast ρ_w can be assumed to be

negligible even in the NIR bands. With $\rho_w = 0$, we can reformulate Equation (6.5) for AHI Band 4, Band 5 and Band 6 as follows:

$$\rho_c^4 = \rho_{\text{toa}}^4 - \rho_r^4 = \rho_a^4; \quad \rho_c^5 = \rho_{\text{toa}}^5 - \rho_r^5 = \rho_a^5; \quad \text{and} \quad \rho_c^6 = \rho_{\text{toa}}^6 - \rho_r^6 = \rho_a^6 \quad (6.6)$$

In the SWIR and NIR-SWIR aerosol correction methods, the ratio of aerosol reflectance $\varepsilon^{(5,6)}$ for AHI Band 5 and Band 6 and $\varepsilon^{(4,5)}$ for AHI Band 4 and Band 5 are computed using Equation (6.7) as follows:

$$\varepsilon^{(5,6)} = \frac{\rho_a^5}{\rho_a^6} = \frac{\rho_c^5}{\rho_c^6}; \quad \text{and} \quad \varepsilon^{(4,5)} = \frac{\rho_a^4}{\rho_a^5} = \frac{\rho_c^4}{\rho_c^5} \quad (6.7)$$

The ratios $\varepsilon^{(5,6)}$ and $\varepsilon^{(4,5)}$ were computed on an image-by-image basis for all available AHI data over the clear water pixels (Box A in Figure 6.1) using Equation (6.7). The distribution of aerosol reflectance ratios was observed to be normal (see Figure 6.3), thus the median values of $\varepsilon^{(5,6)}$ and $\varepsilon^{(4,5)}$ computed from each image were used for each AHI scene with the assumption that the aerosol scattering ratio was spatially homogenous for our study region. Further, 1 standard deviations (STD) of the respective $\varepsilon^{(5,6)}$ and $\varepsilon^{(4,5)}$ values were taken as the uncertainties in aerosol reflectance ratios. For all available AHI dates in Table 6.1, the $\varepsilon^{(5,6)}$ and $\varepsilon^{(4,5)}$ values were calculated to be 1.12 ± 0.65 and 1.82 ± 0.84 respectively.

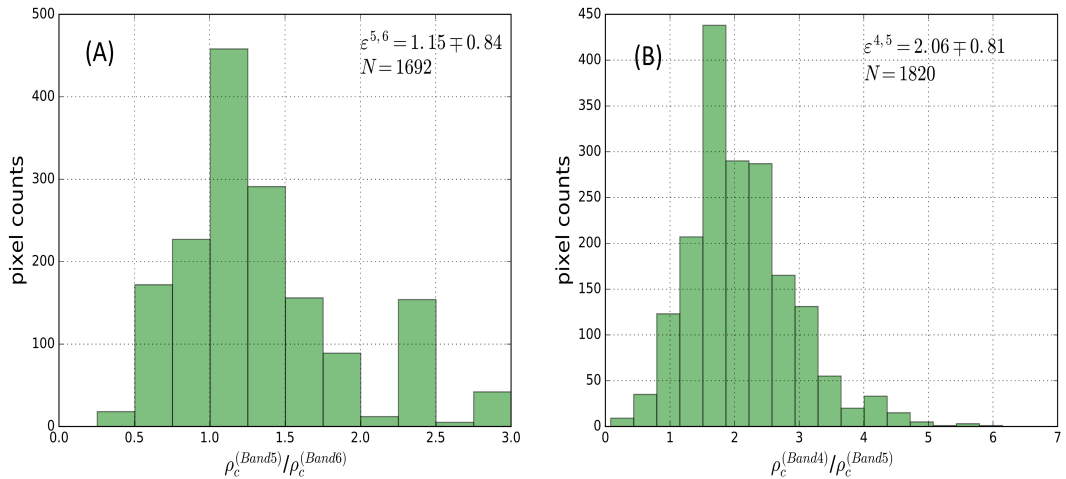


Figure 6.3: Histogram of aerosol reflectance ratio derived from clear water pixels of AHI data on July 9th 2015 at 2:00 UTC (A) $\varepsilon^{(5,6)}$ and (B) $\varepsilon^{(4,5)}$ from rayleigh corrected reflectance (N is the total number of pixels).

By replacing ρ in Equation (6.5) with ρ^4 to denote AHI Band 4 in the NIR-SWIR method and ρ^5 to denote Band 5 in the SWIR method, we can combine Equation (6.5) and Equation (6.7) to compute atmospherically corrected ρ_w^4 and ρ_w^5 as follows:

$$\begin{aligned}\rho_w^4 &= \frac{\rho_c^4 - \rho_a^4}{t_0^4 t_v^4} = \frac{\rho_c^4 - \varepsilon^{(4,5)} \rho_a^5}{t_0^4 t_v^4} \\ \rho_w^5 &= \frac{\rho_c^5 - \rho_a^5}{t_0^5 t_v^5} = \frac{\rho_c^5 - \varepsilon^{(5,6)} \rho_a^6}{t_0^5 t_v^5}\end{aligned}\quad (6.8)$$

In both the SWIR and NIR-SWIR methods, knowing the aerosol reflectance in longer wavelengths (ρ_a^5 and ρ_a^6) allows for ρ_w^i ($i = \text{other bands}$) to be computed as:

$$\begin{aligned}\text{SWIR: } \rho_w^i &= \frac{\rho_c^i - \varepsilon^{(i,6)} \rho_a^6}{t_0^i t_v^i} \\ \text{NIR-SWIR: } \rho_w^i &= \frac{\rho_c^i - \varepsilon^{(i,5)} \rho_a^5}{t_0^i t_v^i}\end{aligned}\quad (6.9)$$

where $\varepsilon^{(i,5)}$ and $\varepsilon^{(i,6)}$ can be derived using simple exponential extrapolation from (Gordon & Wang, 1994b) as follows:

$$\begin{aligned}\varepsilon^{(i,5)} &= \left(\varepsilon^{(4,5)} \right)^{\delta i} ; \delta i = \frac{\lambda_5 - \lambda_i}{\lambda_5 - \lambda_4} \\ \varepsilon^{(i,6)} &= \left(\varepsilon^{(5,6)} \right)^{\delta i} ; \delta i = \frac{\lambda_6 - \lambda_i}{\lambda_6 - \lambda_5}\end{aligned}\quad (6.10)$$

6.3.3.2 MODIS-Aqua data acquisition and atmospheric correction

Data from the MODIS sensor onboard the Aqua (EOS PM) satellite was used in this study to validate and compare the data from the AHI sensor. MODIS Level 1B data, which are geo-located and calibrated L_{toa} data from MODIS in 36 spectral channels, were downloaded from the NASA LAADS web (<http://ladsweb.nascom.nasa.gov/>) for the dates provided in Table 6.1. Atmospheric correction of MODIS-Aqua level 1B data was performed using a standard MUMM atmospheric correction methods available in SeaDAS version 7.2 (Feldman & McClain, 2010). The MUMM atmospheric correction

method is based on the assumption that the ratio of multiple-scattering aerosols and aerosol-Rayleigh reflectance at MODIS NIR bands (MODIS Band 15 and Band 16) in the sub-scene of interest is spatially homogeneous (Ruddick et al., 2000). The only deviation from the standard MUMM method was that we employed the SWIR (2130 nm) band instead of the NIR (869 nm) for cloud detection. A study by Dorji et al. (2016) found that, for our study site, the SWIR band was more suited for cloud detection as reflectance in the NIR band was occasionally impacted by significant reflectance and thus highly turbid waters were flagged as clouds. Validation of atmospherically corrected remote-sensing reflectance (R_{rs}) from MODIS-Aqua data in our study site was performed by Dorji et al. (2016) who showed that MUMM underestimated R_{rs} by approximately 5% when compared with *in situ* R_{rs} . MUMM atmospherically corrected, MODIS-Aqua Band 1 data were resampled to 2000 m spatial resolution to be used for validation of AHI results in this study.

6.3.3.3 Landsat-8 OLI data acquisition and atmospheric correction

In addition to MODIS-Aqua data, Landsat-8 OLI data were also used for comparison with the results from the AHI sensor. Landsat-8 OLI data from the United States Geological Services were obtained using EarthExplorer (<http://earthexplorer.usgs.gov/>) as radiometrically and geometrically corrected level 1T data for July 29th 2015. Only the July 29th 2015 image was cloud free over the study site during that month. The atmospheric correction of Landsat-8 OLI data was performed using the atmospheric correction platform for Landsat and Sentinel sensors, ACOLITE, available from <https://odnature.naturalsciences.be/remsem/software-and-data/acolite>.

ACOLITE includes several methods for atmospheric correction which are similar in design to the Rayleigh and other atmospheric effects corrections of (Gordon & Wang, 1994b; Neukermans et al., 2009; Ruddick et al., 2000). For aerosol corrections, different methods are available in ACOLITE, using either two SWIR bands or a combination of one NIR and one SWIR band. In the combination of two SWIR bands method, the added advantage is that the ϵ

for the whole scene can either be computed for every pixel, or one constant value for the whole scene can be estimated using either mean or median ϵ values (Vanhellemont & Ruddick, 2015). For our study, we selected two SWIR bands from Landsat-8 OLI (SWIR1 = 1608.5 nm and SWIR2 = 2200.5 nm) for aerosol corrections and chose to select a median value for the aerosol scattering ratio between SWIR1 and SWIR2 to represent the whole of our study region, an approach adopted in previous studies by (Ody et al., 2016; Vanhellemont & Ruddick, 2015) and shown to work better for coastal waters. The TSS product derived from the atmospherically corrected Landsat-8 OLI Band 4 (655 nm) and resampled to 2000 m was used to compare with the results of the AHI sensor.

6.3.4 AHI sensor noise estimation

To test the feasibility of the AHI sensor in mapping TSS concentration, we assessed the signal to noise ratio (SNR) and noise equivalent radiance (NE_L) of the AHI sensor using a method described in Hu et al. (2012). In brief, the method involves first selecting a region of cloud free clear ocean water pixels in each AHI image from all available images in the AHI dataset. The clear ocean region is labelled as 'Box A' in our study region (see Figure 6.1). This area was visually determined after examining the true colour images and also based on the fact this region is a significant distance from the shore, thus unlikely to be influenced by near-coast TSS dynamics. Secondly, the clear water pixels were further screened using a window of 3 x 3 pixels to segregate the real variation in the ocean or atmosphere from sensor noise. The threshold derived from the ratio of maximum/minimum L_{toa} of the whole of Box A pixels was used to quality control pixels for the SNR calculation by discarding 3 x 3 pixel windows whose maximum/minimum ratios were greater than the ratio for the whole of Box A. Finally, the mean of the qualified pixels from the 3 x 3 pixel windows was accepted as the typical at sensor radiance ($L_{typical}$) in an image, and 1 STD as the noise (L_{std}), which is essentially the NE_L value due to AHI sensor artifacts. Further, for all the above steps, all the clear water pixels were grouped according to discrete θ_0

($40^\circ \pm 1^\circ, 45^\circ \pm 1^\circ, 50^\circ \pm 1^\circ, 55^\circ \pm 1^\circ, 60^\circ \pm 1^\circ$, and $65^\circ \pm 1^\circ$) because θ_0 can vary significantly during the course of an entire day and L_{typical} values are known to vary as a function of θ_0 (Hu et al., 2012). The SNR was computed by dividing L_{typical} from clear water pixels by L_{std} . Further, the computed NE_L was converted to noise equivalent reflectance (NE_ρ) as a function of different θ_0 using the following Equation (6.11).

$$NE_\rho = \frac{\pi d^2 NE_L}{F_0 \cos \theta_0} \quad (6.11)$$

where d and F_0 are as defined in Equation (6.1).

For noise equivalent TSS concentration (NE_{TSS}) for AHI sensor, we used NE_ρ of AHI Band 3 at different θ_0 to estimate NE_{TSS} using a single red band TSS algorithms from Dorji et al. (2016).

6.3.5 *In situ* validation dataset

For *in situ* validation data, concurrent measurements of R_{rs} using a “dynamic above-water radiance and irradiance collector” (DALEC) (Brando et al., 2016) were available for July 4–10th, 2015. The details of R_{rs} collection using a DALEC, quality control and analysis methods are described in Dorji et al. (2016). To get the match-up data corresponding to the AHI dataset, we selected the R_{rs} data that were within ± 3 min of the Himawari-8 overpass time. In total, we selected 167 DALEC and AHI derived R_{rs} match-up pairs to perform the *in situ* validation. Unfortunately, the range of *in situ* R_{rs} data were limited to only $0.0003 - 0.0227 \text{ sr}^{-1}$ for the entire dataset at AHI Band 3 (~640 nm). Further, the majority of the data were in the lower range of R_{rs} value, with a mean of only $0.0026 \pm 0.0018 \text{ sr}^{-1}$. In contrast, other data collected in the same region, but not at appropriate times for AHI validation, displayed R_{rs} as high as 0.05 sr^{-1} in the red band (Dorji et al., 2016). Our limited range of *in situ* R_{rs} validation data may have an impact on the validation of the atmospheric correction of AHI data. The entire *in situ* R_{rs} validation dataset used in this study has been interpolated to 1 nm and is shown in Figure 6.4.

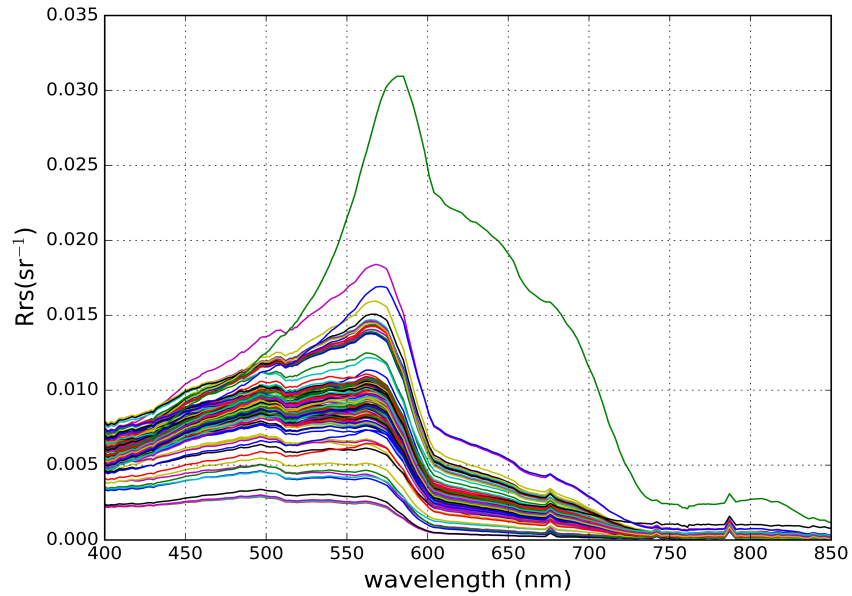


Figure 6.4: *In situ* DALEC measured R_{rs} used in validation of AHI derived R_{rs}

6.3.6. Single red band TSS algorithm

The single red band multi-sensor TSS algorithm developed by Dorji et al. (2016) for coastal waters of northern Western Australia is used in this study. The single red band MODIS-Aqua TSS algorithm from Dorji et al. (2016) was recalibrated to Landsat-8 OLI Band 4 and AHI Band 3 using an *in situ* dataset comprising 48 match-up pairs of sub-surface remote sensing reflectance (r_{rs}) and TSS concentration from Onslow regional waters within the study site (see Figure 6.1). The TSS algorithms, recalibrated and convolved to the spectral response functions for Landsat-8 OLI Band 4 and AHI Band 3 along with MODIS-Aqua Band 1, from Dorji et al. (2016) are shown below:

$$\text{MODIS-Aqua: } TSS = \frac{23.47 \times \left(\frac{x}{1-x} \right)}{1 - 0.69 \times \left(\frac{x}{1-x} \right)}, \quad (R^2=0.85) \quad (6.12)$$

$$\text{Landsat-8 OLI: TSS} = \frac{25.34 \times \left(\frac{x}{1-x} \right)}{1 - 0.69 \times \left(\frac{x}{1-x} \right)}, \quad (R^2=0.85) \quad (6.13)$$

$$\text{AHI: TSS} = \frac{22.12 \times \left(\frac{x}{1-x} \right)}{1 - 0.71 \times \left(\frac{x}{1-x} \right)}, \quad (R^2=0.89) \quad (6.14)$$

where $x = \frac{-g_1 + \sqrt{(g_1)^2 + 4g_2 r_{rs}(\lambda)}}{2g_2}$, and $r_{rs}(\lambda) = R_{rs}(\lambda)/(0.52 + 1.7R_{rs}(\lambda))$, $\lambda = \text{Band 1}$

for MODIS-Aqua, $\lambda = \text{Band 4}$ for Landsat-8 OLI and $\lambda = \text{Band 3}$ for AHI, $g_1 = 0.084$ and $g_2 = 0.17$.

The TSS products from Landsat-8 OLI and MODIS-Aqua were derived for all dates and times shown in Table 6.1 at the sensors red band's native spatial resolution, 30 m and 250 m respectively, and resampled to a spatial resolution of 2000 m of AHI derived TSS for quantitative analysis.

6.3.7. Accuracy assessment

The accuracy assessment used in comparing the AHI-derived product with *in situ* or other sensor derived products includes: 1) Mean Absolute Relative Error (MARE), 2) Absolute Relative Error (ARE), 3) Root Mean Square Error (RMSE), and 4) correlation coefficient (r) as defined by Equations (6.15) - (6.18).

$$\text{MARE} = \frac{\sum_{i=1}^n |(x_i - y_i)/y_i|}{n} \times 100\% \quad (6.15)$$

$$\text{ARE} = \frac{|x - y|}{y} \times 100\% \quad (6.16)$$

$$\text{RMSE} = \sqrt{\frac{\sum_{i=1}^n (x_i - y_i)^2}{n}} \quad (6.17)$$

$$r = \frac{n \sum x_i y_i - \sum x_i \sum y_i}{\sqrt{n \sum x_i^2 - (\sum x_i)^2} \sqrt{n \sum y_i^2 - (\sum y_i)^2}} \quad (6.18)$$

where n is the total number of samples, y_i is the AHI-derived products (reflectance or TSS concentrations) and x_i is either *in situ*, MODIS-Aqua or Landsat-8 OLI derived products.

6.4 Results

6.4.1. Quantitative comparison of water leaving reflectance derived from the SWIR and NIR-SWIR aerosol estimation methods

The quantitative comparisons of ρ_w estimated using SWIR and NIR-SWIR aerosol reflectance estimation methods are presented in Table 6.3. The ρ_w data presented in Table 6.3 include the mean and STD of all AHI images from July 04 –10th, 2015. The mean and STD of each individual AHI image was computed for all the pixels within the Boxes A, B and C (see Figure 6.1). Boxes A, B and C correspond to a homogenous offshore region (clear water), gulf region (moderate turbid) and a near coastal region (turbid water) respectively. Table 6.3 shows that for all AHI Bands 1, 2, 3 and 4, the ρ_w was consistently higher for the SWIR method than the NIR-SWIR method. The ARE calculated from the ρ_w of the SWIR and NIR-SWIR methods shows that in AHI Band 1, the SWIR method produced higher ARE (57.1% - 63.84%) in all three regions (Boxes A, B and C). Likewise, similar observations were observed in other bands, where the SWIR method estimated ρ_w higher than the NIR-SWIR method by 31.03% - 37.73%, 43.69% - 113.10%, and 63.57% - 211.75% in Bands 1, 2 and 3 respectively. The overall ρ_w comparison result using the SWIR and NIR-SWIR methods is shown in Figure 6.5. We observe from Figure 6.5 that ρ_w results computed from the SWIR method are all above the 1:1 line with an overall RMSE of

0.0046. In addition, the simple linear regression analysis shows that ρ_w obtained by the SWIR and NIR-SWIR methods are well correlated with slope of ~ 1.0 and R^2 of 0.94, but slightly positively biased toward the SWIR aerosol estimation method.

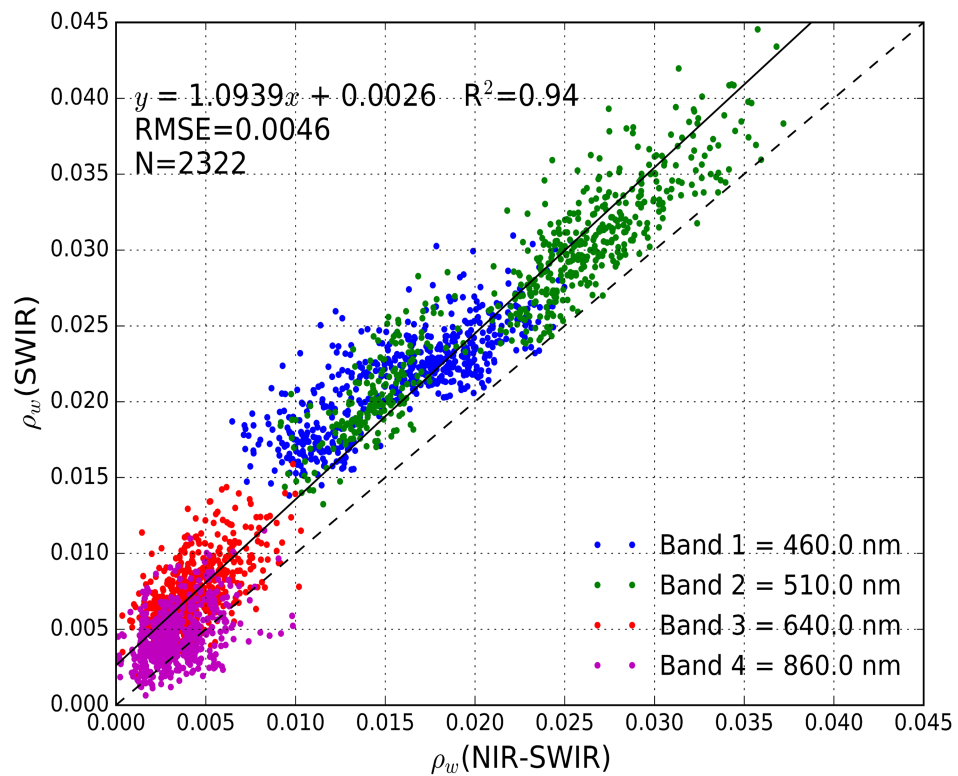


Figure 6.5: Scatter plot of ρ_w computed using a SWIR and NIR-SWIR atmospheric correction method. Solid line is line of best fit and broken line is 1:1 line.

Table 6.3: Water leaving reflectance (ρ_w) of AHI sensor in Band 1, 2, 3 and 4 computed for different atmospheric correction methods (NIR-SWIR and SWIR aerosol correction methods). The mean and STD ρ_w results are determined from all pixels within Box A, B and C for all available AHI data. The ARE are determined as the absolute relative error between NIR-SWIR and SWIR results.

Band	ρ_w	Box A		Box B		Box C	
		NIR-SWIR	SWIR	NIR-SWIR	SWIR	NIR-SWIR	SWIR
1	Mean (STD)	0.0112 (0.0018)	0.0176 (0.0018)	0.0177 (0.0035)	0.0299 (0.0016)	0.0151 (0.0029)	0.0247 (0.0024)
	ARE	57.1%		69.12%		63.84%	
2	Mean (STD)	0.0144 (0.0022)	0.0199 (0.0030)	0.0314 (0.0037)	0.0423 (0.0037)	0.0291 (0.0023)	0.0381 (0.0028)
	ARE	37.73%		34.75%		31.03%	
3	Mean (STD)	0.0031 (0.0012)	0.0067 (0.0021)	0.0109 (0.0043)	0.0205 (0.0047)	0.0176 (0.0111)	0.0252 (0.0111)
	ARE	113.10%		87.10%		43.69%	
4	Mean (STD)	0.0030 (0.0016)	0.0050 (0.0018)	0.0018 (0.0014)	0.0056 (0.0016)	0.0031 (0.0019)	0.0061 (0.0023)
	ARE	63.57%		211.75%		96.56%	

The underestimation of ρ_w by the NIR-SWIR method can be attributed to higher ρ_a estimated by the NIR-SWIR method. The ρ_a in all AHI bands considered here (Bands 1- 4) were consistently estimating high aerosol reflectance as a result of the NIR-SWIR method. The results shown in Table 6.4 for the ρ_a obtained using the SWIR and NIR-SWIR methods shows that in Band 1, the NIR-SWIR method estimated ρ_a higher than the SWIR method by 60.78% - 75.50% in Boxes A, B and C. Likewise, in Bands 2, 3 and 4, the NIR-SWIR method estimated ρ_a higher by 59.16% - 74.71%, 54.70% - 72.34% and 46.03% - 67.51% respectively in all the Boxes A, B, and C.

Table 6.4: Aerosol reflectance (ρ_a) of AHI sensor in Band 1, 2, 3 and 4 computed for different atmospheric correction methods (NIR-SWIR and SWIR aerosol correction methods). The mean and STD ρ_a results are determined from all pixels within Box A, B and C for all available AHI data. The ARE are determined as the absolute relative error between NIR-SWIR and SWIR results.

Band	ρ_a	Box A		Box B		Box C	
		NIR-SWIR	SWIR	NIR-SWIR	SWIR	NIR-SWIR	SWIR
1	Mean	0.0059	0.0023	0.0121	0.0030	0.0119	0.0042
	(STD)	(0.0016)	(0.0008)	(0.0030)	(0.0006)	(0.0027)	(0.0007)
	ARE	60.78%		75.50%		64.31%	
2	Mean	0.0056	0.0023	0.0115	0.0029	0.0114	0.0042
	(STD)	(0.0012)	(0.0007)	(0.0028)	(0.0006)	(0.0025)	(0.0007)
	ARE	59.16%		74.71%		62.90%	
3	Mean	0.0050	0.0023	0.0101	0.0028	0.0099	0.0041
	(STD)	(0.0012)	(0.0007)	(0.0022)	(0.0005)	(0.0019)	(0.0007)
	ARE	54.70%		72.34%		58.83%	
4	Mean	0.0040	0.0022	0.0080	0.0026	0.0079	0.0038
	(STD)	(0.0009)	(0.0007)	(0.0015)	(0.0005)	(0.0012)	(0.0006)
	ARE	46.03%		67.51%		51.53%	

6.4.2. *In situ* validation of water leaving reflectance derived from SWIR and NIR-SWIR aerosol estimation methods

The *in situ* validation of ρ_w derived using the AHI sensor was performed for ρ_w obtained using both the SWIR and NIR-SWIR atmospheric correction methods. The DALEC measured (*in situ*) reflectance data which were within ± 3 min of the AHI image acquisition time were selected for the validation analysis. A 5 x 5-pixel window from the AHI image was selected after matching the geographical location of the *in situ* data with the closest latitude and longitude space of the AHI image. The AHI Band's *in situ* validation results are provided in Table 6.5 for Bands 1, 2 3 and 4. The accuracy assessment, r , MARE, and RMSE described in Section 6.3.7 were used in the *in situ* validation. The correlation coefficients, r , for all four bands show very poor correlation (< 0.3) for both the SWIR and NIR-SWIR methods. This poor result for r can be attributed to the fact that all *in situ* validation data points were within a very narrow range. For instance, in Band 3 the highest ρ_w was only ~ 0.07 and more than 95% of the ρ_w data were all below 0.015. However, the MARE results were better for Bands 1, 2 and 3

with all bands combined MARE values ranging from 22.17% - 47.76% and 23.78% - 69.81% for the NIR-SWIR and SWIR atmospheric correction methods respectively. The results of the MARE in Band 4 were larger by comparison with the MARE observed to be greater than 300% for both atmospheric correction methods.

Table 6.5: *In situ* validation of water leaving reflectance (ρ_w) derived from AHI in Band 1, 2, 3 and 4 using SWIR and NIR-SWIR atmospheric correction method. LRE = Largest Relative Error and SRE = Smallest Relative Error are the extreme points within the Absolute Relative Error (ARE) generated from whole of AHI dataset.

ρ_w	Band 1		Band 2		Band 3		Band 4	
	NIR-SWIR	SWIR	NIR-SWIR	SWIR	NIR-SWIR	SWIR	NIR-SWIR	SWIR
r	0.34	0.33	0.18	0.11	0.09	0.10	0.15	0.09
MARE (%)	47.76	25.57	22.71	23.78	44.22	69.81	388.85	504.73
LRE (%)	75.65	150.00	180.06	284.64	326.02	869.41	1881.12	3286.00
SRE (%)	3.02	1.33	0.4	0.09	0.3	0.1	8.23	12.21
RMSE	0.0133	0.0067	0.0068	0.0069	0.0059	0.0059	0.0019	0.0027

In addition to the individual band's accuracy assessment, we also performed over all accuracy assessment for all the bands together and spectral feature comparison of AHI derived ρ_w in Bands 1-4. The overall *in situ* ρ_w validation scatter plots for the SWIR and NIR-SWIR results are shown in Figure 6.6A and B respectively. General visual observation from Figure 6.6A shows that the majority of validation points in AHI Bands 1, 2 and 3 for the SWIR atmospheric correction method (see Figure 6.6A) were underestimated when compared with *in situ* ρ_w . For the NIR-SWIR atmospheric method, Figure 6.6B still shows underestimation of ρ_w in Band 1, but the majority of the validation points in Band 2, 3 and 4 were over estimated. The results from the simple regression analysis and RMSE of all the data in Bands 1-4 indicates that the NIR-SWIR method performed better

than the SWIR method. The RMSE, regression slope, and R^2 were better for the SWIR method, with RMSE = 0.0058, slope = 0.78 and $R^2=0.79$ compared to the NIR-SWIR method with RMSE = 0.0081, slope = 0.67 and $R^2=0.75$.

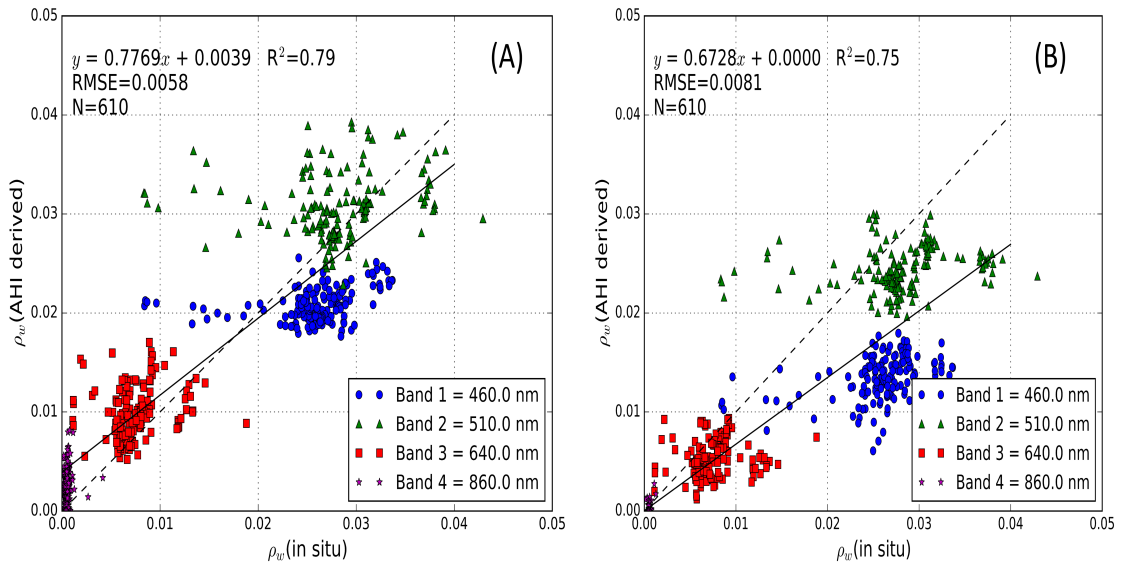


Figure 6.6: *In situ* validation of ρ_w for all available match-up data points for (A) SWIR and (B) NIR-SWIR atmospheric correction method.

The spectral shapes of atmospherically corrected ρ_w in AHI Bands 1-4 are shown in Figures 6.7A and 6.7B for two *in situ* data points, one close to the coast and one further away from the coast. Additional spectral shapes for rest of the validation data points are presented in Appendix I. In Figures 6.7A and 6.7B we observe spectrally both the NIR-SWIR and SWIR derived ρ_w closely match the spectral features of the *in situ* ρ_w , however it appears that the atmospheric correction processes both overcorrect AHI Band 1 in Figure 6.7A, corresponding to water closer to the coast. In particular, in Figure 6.8(A) we observe both the magnitude of SWIR and NIR-SWIR corrected ρ_w closely matches with *in situ* reflectance in Band 2-4. The SWIR method has slightly higher magnitude than *in situ* ρ_w while the magnitude of NIR-SWIR slightly was slightly lower. However, in Figure 6.7B we observe that both the SWIR and NIR-SWIR methods produced slightly lower ρ_w in magnitude than *in situ*, but generally good agreement is observed between all bands (Bands 1-4). The good spectral match between *in situ* and atmospherically corrected ρ_w provides some confidence in our atmospheric correction process of the

AHI data, although based on the relative errors shown in Table 6.5, we may conclude that the confidence in Band 4 is somewhat lower than bands 1-3.

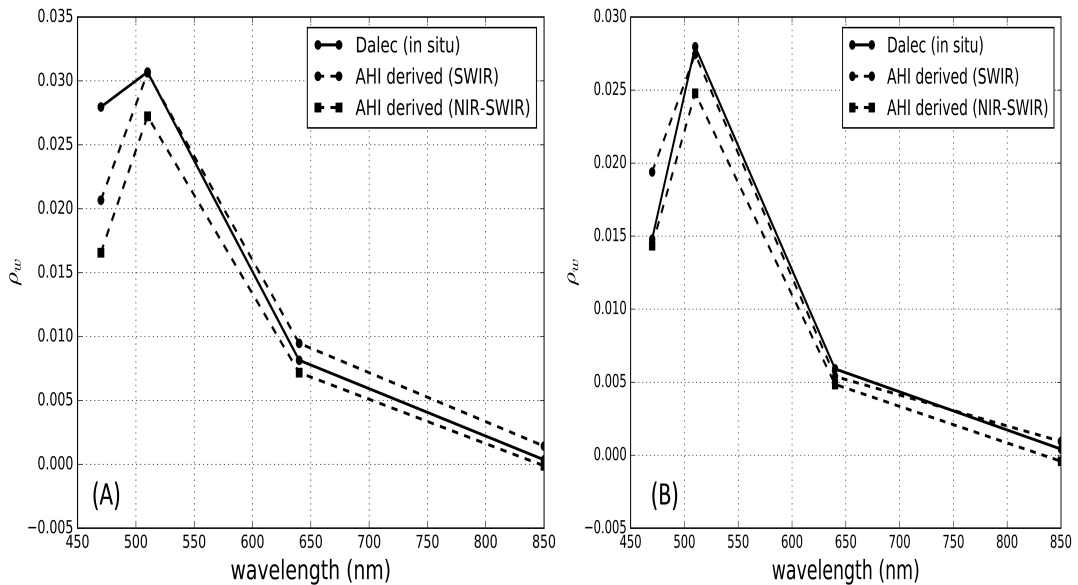


Figure 6.7: Spectral plot of atmospherically corrected ρ_w in AHI Band 1-4 using SWIR and NIR-SWIR methods and *in situ* data at (A) pixel close to the coast and (B) farther away from the coast.

6.4.3 Uncertainty of AHI sensor noise and comparison with the sensor noise of MODIS-Aqua and Landsat-8 OLI sensors

The results of the AHI sensor noise estimation determined using the method discussed in Section 6.3.4 are shown in Figures 6.8A-C. We have also presented in Table 6.6 the details of L_{typical} , NE_L , and SNR for AHI Bands 1-6 at θ_0 ranging from 45° - 65° . The statistics in Table 6.6 were calculated from all available AHI data in Table 6.1 and provided as an overall mean and STD (provided in parenthesis) at discrete θ_0 . Figure 6.8A shows that the typical radiance values, L_{typical} , observed in clear water pixels from 10:00 am – 5:00 pm local time over the study site varied throughout the day, with the general trend displaying a decrease in L_{typical} with an increase in θ_0 . It was observed that from $\theta_0 = 45^\circ$ - 65° , L_{typical} ranged from $56.61 - 36.00 \text{ Wm}^{-2} \mu\text{m}^{-1}\text{sr}^{-1}$, $37.96 - 24.52 \text{ Wm}^{-2} \mu\text{m}^{-1}\text{sr}^{-1}$, $13.24 - 9.01 \text{ Wm}^{-2} \mu\text{m}^{-1}\text{sr}^{-1}$, $2.86 - 2.20 \text{ Wm}^{-2} \mu\text{m}^{-1}\text{sr}^{-1}$, $0.16 - 0.13 \text{ Wm}^{-2} \mu\text{m}^{-1}\text{sr}^{-1}$, and $0.028 - 0.025 \text{ Wm}^{-2} \mu\text{m}^{-1}\text{sr}^{-1}$ in AHI Bands 1 – 6 respectively. The NE_L for Bands 1-6, shown in Figure 6.8B,

also vary from $0.18 - 0.26 \text{ Wm}^{-2} \mu\text{m}^{-1}\text{sr}^{-1}$, $0.17 - 0.22 \text{ Wm}^{-2} \mu\text{m}^{-1}\text{sr}^{-1}$, $0.23 - 0.26 \text{ Wm}^{-2} \mu\text{m}^{-1}\text{sr}^{-1}$, $0.17 - 0.20 \text{ Wm}^{-2} \mu\text{m}^{-1}\text{sr}^{-1}$, $0.004 - 0.01 \text{ Wm}^{-2} \mu\text{m}^{-1}\text{sr}^{-1}$, and $0.001 - 0.004 \text{ Wm}^{-2} \mu\text{m}^{-1}\text{sr}^{-1}$ respectively. Likewise, Figure 6.8C shows that the SNR calculated for a clear water pixel at L_{typical} values varied for different θ_0 , with the AH1 Bands 1-6 SNR ranging from 200.55 – 243.89, 123.16 – 182.14, 39.41 – 50.11, 11.20 – 16.00, 14.77 – 36.71 and 7.42 – 22.34 respectively. There was no general trend observed in NE_L or SNR for different θ_0 , thus we used the mean value calculated from SNR and NE_L for $\theta_0 = 45 - 60^\circ$ for computation of NE_p and NE_{TSS} .

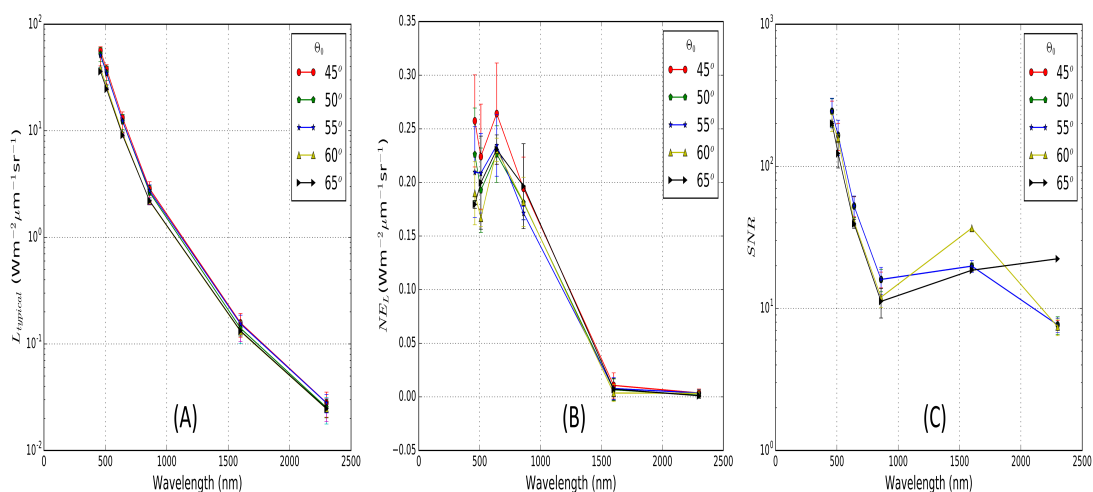


Figure 6.8: Plot of a (A) L_{typical} , (B) NE_L , and (C) SNR calculated from a clear water pixel location (Box A in Figure 6.1) for AH1 Band 1-6 at different θ_0 . Note that the SNR were calculated at L_{typical} values.

Table 6.6: Mean (1 STD) values of SNR, L_{typical} and NE_L derived from the clear water pixels of AHI sensor for all the dates provided in Table 6.1.

Band	$\lambda(\mu\text{m})$	L (Wm^{-2} $\mu\text{m}^{-1}\text{sr}^{-1}$)	θ_0				
			45°	50°	55°	60°	65°
1	0.46	L_{typical}	56.61 (3.09)	52.36 (7.80)	51.10 (10.38)	38.70 (0.62)	36.00 (0.57)
		NE_L	0.26 (0.04)	0.23 (0.04)	0.21 (0.04)	0.19 (0.03)	0.18 (0.004)
		SNR	219.93 (43.80)	231.56 (54.57)	243.89 (57.41)	203.83 (28.24)	200.55 (5.97)
2	0.51	L_{typical}	37.96 (2.16)	35.10 (5.33)	34.49 (7.16)	26.16 (0.52)	24.52 (0.48)
		NE_L	0.22 (0.05)	0.19 (0.04)	0.21 (0.04)	0.17 (0.01)	0.20 (0.04)
		SNR	169.43 (35.56)	182.14 (47.50)	165.32 (46.04)	156.95 (9.89)	123.16 (25.77)
3	0.64	L_{typical}	13.24 (0.87)	12.27 (1.96)	12.04 (2.72)	9.41 (0.35)	9.01 (0.33)
		NE_L	0.26 (0.05)	0.23 (0.03)	0.23 (0.03)	0.23 (0.01)	0.23 (0.01)
		SNR	50.11 (8.40)	54.20 (8.81)	52.58 (9.16)	40.85 (2.45)	39.41 (2.75)
4	0.86	L_{typical}	2.86 (0.25)	2.64 (0.40)	2.74 (0.59)	2.18 (0.16)	2.20 (0.16)
		NE_L	0.19 (0.03)	0.18 (0.02)	0.17 (0.01)	0.18 (0.02)	0.20 (0.04)
		SNR	14.72 (2.03)	14.60 (2.89)	16.00 (3.49)	12.00 (1.83)	11.20 (2.64)
5	1.6	L_{typical}	0.16 (0.03)	0.14 (0.02)	0.15 (0.04)	0.13 (0.03)	0.13 (0.03)
		NE_L	0.011 (0.023)	0.007 (0.002)	0.008 (0.003)	0.004 (0.002)	0.007 (0.003)
		SNR	14.77 (1.05)	21.03 (1.00)	19.84 (1.88)	36.71 (0.00)	18.56 (0.28)
6	2.3	L_{typical}	0.028 (0.006)	0.025 (0.006)	0.028 (0.008)	0.025 (0.008)	0.025 (0.007)
		NE_L	0.004 (0.0031)	0.002 (0.0004)	0.004 (0.0005)	0.003 (0.0003)	0.001 (0.0005)
		SNR	7.81 (0.57)	16.23 (1.08)	7.65 (0.90)	7.42 (0.99)	22.34 (0.00)

Comparison of NE_{TSS} derived using AHI data with MODIS-Aqua and Landsat-OLI data was performed using published parameters to calculate SNR at a reference radiance (L_{ref}) for the respective red bands of each sensor. The parameters L_{ref} , SNR and F_o shown in Table 6.7, as required for NE_p computation for Landsat-8 OLI, were obtained from Irons, Dwyer, and Barsi (2012). The MODIS-Aqua's parameters were sourced from Franz et al. (2006) and AHI's L_{ref} and SNR were those listed in Table 6.6 while F_o for the

AHI sensor was obtained from the Japan Meteorological Agency (2015). By using the respective parameters (L_{ref} , SNR, F_o and $d = 1$) for all three sensors considered here, first $NE_L = L_{\text{ref}}/\text{SNR}$ was computed, then NE_ρ at different θ_0 was calculated using Equation (6.11). Following the computation of NE_ρ , NE_{TSS} was calculated using the respective sensor's TSS algorithms, as described in Section 6.3.6. The NE_{TSS} for the red bands of AHI (Band 3), MODIS-Aqua (Band 1 and Band 13), and Landsat-8 OLI (Band 4) is shown in Figure 6.9. For all sensors, the general observation is that with increasing θ_0 , NE_{TSS} also increases gradually for $\theta_0 < 50^\circ$ and increases rapidly for higher θ_0 . As expected, from the four sensors considered here the lowest NE_{TSS} was observed for MODIS-Aqua Band 13 because of its high SNR, having been specifically designed for ocean applications. NE_{TSS} was less than 0.0041 mg/L for $\theta_0 < 50^\circ$ and the highest NE_{TSS} was 0.015 mg/L for $\theta_0 = 80^\circ$. The MODIS-Aqua Band 1 and Landsat-8 OLI Band 4, which were designed for terrestrial mapping, produced NE_{TSS} values between those of MODIS-Aqua Band 13 and AHI Band 3, with both curves for MODIS-Aqua Band 1 and Landsat-8 OLI Band 4 in Figure 6.9 following closely to one another. The NE_{TSS} for $\theta_0 < 50^\circ$ was less than 0.06 mg/L for both MODIS-Aqua Band 1 and Landsat-8 OLI Band 4 while the maximum was 0.23 mg/L and 0.21 mg/L at $\theta_0 = 80^\circ$ for MODIS-Aqua Band 1 and Landsat-8 OLI Band 4 respectively. The AHI sensor, designed specifically for meteorological purposes but with visible bands for true colour weather applications, had the highest NE_{TSS} in AHI Band 3 with the NE_{TSS} for $\theta_0 < 50^\circ$ less than 0.12 mg/L and the highest NE_{TSS} was 0.43 at $\theta_0 = 80^\circ$. Even though the AHI sensor here shows high NE_{TSS} due to sensor noise, it has been shown that temporal averaging of images can be used in reducing the noise. For instance, Vanhellefont et al. (2014) showed that NE_{TSS} in SEVIRI images can be reduced by a factor of $\sqrt{5}$ when 5-images were temporally averaged and still retained temporal dynamics of TSS concentration due to tidal processes. With similar temporal averaging (6 images), we have shown in Figure 6.9 that AHI Band 3 can effectively have similar or lower NE_{TSS} when compared with MODIS-Aqua Band 1 and Landsat-8 OLI Band 4.

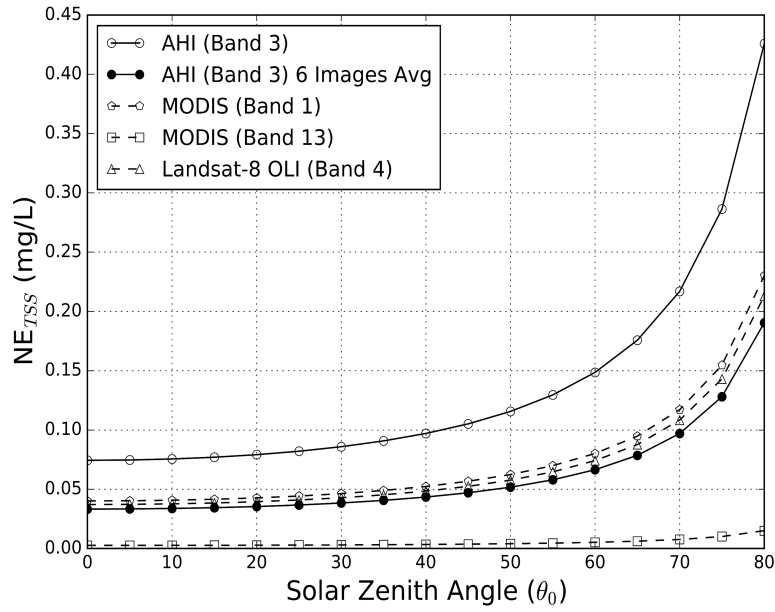


Figure 6.9: NE_{TSS} at different solar zenith angle, θ_0 , for MODIS-Aqua Band 1 (250 m) and Band 13 (1000 m), Landsat-8 OLI Band 4 (30 m) and AHI Band 3 (2000 m).

Table 6.7: Parameters used in the computations of NE_p and NE_{TSS} .

Sensor (Band #)	L_{ref} ($Wm^{-2} \mu m^{-1} sr^{-1}$)	F_o ($Wm^{-2} \mu m^{-1}$)	NE_L ($Wm^{-2} \mu m^{-1} sr^{-1}$)	SNR
AHI (Band 3)	11.74	1631	0.24	49.44
MODIS-Aqua (Band 1)	16.5	1578	0.1179	140
MODIS-Aqua (Band 13)	14.7	1523	0.0074	1962
Landsat-8 OLI (Band 4)	22	1549	0.0991	222

6.4.4 Cross-validation of AHI derived TSS concentration with MODIS-Aqua and Landsat-8 Sensors

Figures 6.10A-6.10D shows a spatial comparison between AHI derived TSS maps with MODIS-Aqua and Landsat-8 OLI derived TSS maps, all produced at 2000 m spatial resolution. Figures 6.10A and 6.10B correspond to AHI and MODIS-Aqua derived TSS maps of the 9th July 2014 at 02:40 pm and 02:35 pm local time respectively. From Figures 6.10A and 6.10B, we observe both AHI and MODIS-Aqua derived TSS maps have similar spatial patterns, higher TSS concentration near the Exmouth Gulf

region, particularly higher TSS concentration in the Box C region than the off-shore waters in Box A (Box regions displayed in Figure 6.1). Also, we note that the AHI derived TSS maps (Figures 6.10A and 6.10C) have higher spatial noise than the MODIS-Aqua or Landsat-8 OLI derived TSS maps (Figures 6.10B and 6.10D). Figures 6.10C and 6.10D, which correspond to AHI and Landsat-8 OLI derived TSS maps of the 29th July 2015 at 10:20 am also show similar spatial patterns, with higher TSS concentration near the coastal region than offshore waters. The Landsat-8 OLI derived TSS were higher than AHI-derived TSS concentration near the coast but the opposite was the case for offshore waters. We also observe in Figures 6.10A-6.10D that some inland pixels were classified as TSS due to presence of inland water masses which were discarded in cross-validation analysis.

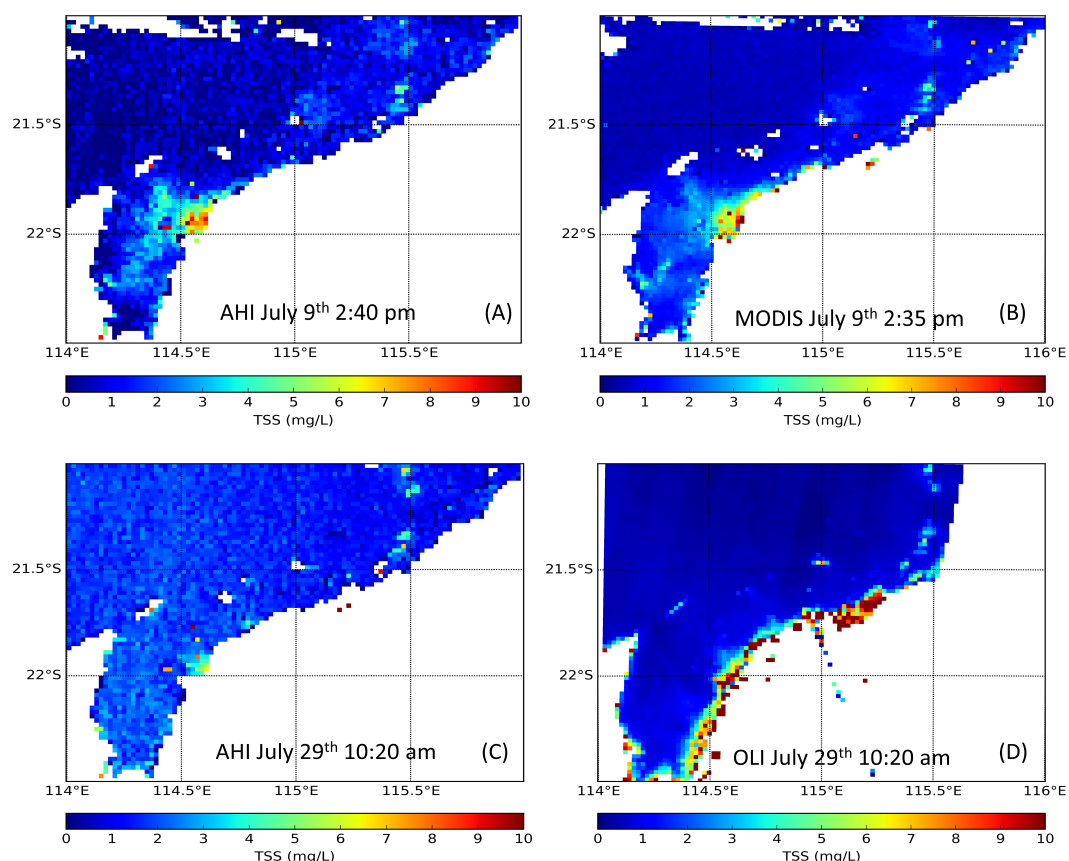


Figure 6.10: Spatial maps of TSS concentration derived from (A) AHI Band 3 on July 9th 2015 at 02:40 pm, (B) MODIS-Aqua Band 01 on July 9th 2015 at 02:35 pm, (C) AHI Band 03 on July 29th 2015 at 10:20 am and (D) Landsat-8 OLI Band 4 on July 29th 2015 at 10:20 am.

The quantitative cross validation was performed between AHI and MODIS-Aqua TSS concentration derived for July 4-6th and 8-10th 2015, and AHI and Landsat-8 OLI products of 29th July 2015. Figures 6.11A and 6.11B show linear regression results between AHI and Landsat-8 OLI, and AHI and MODIS-Aqua respectively. In Figure 6.11A, the cross-validation result shows that there is a good correlation between AHI and Landsat-8 OLI derived TSS concentration with $r= 0.90$ and the coefficient of determination, $R^2=0.81$, regression slope of 0.91 and an offset of 0.45 at low concentrations. The data in Figure 6.11B for the cross-validation of AHI and MODIS-Aqua derived TSS concentrations show a correlation coefficient of $r= 0.71$, $R^2=0.50$, slope of 0.74 and intercept of 0.17. Certainly, discrepancies are present between AHI and MODIS-Aqua or Landsat-8 OLI derived TSS products which could be caused by different native spatial resolution of the sensor and (or) as a result of atmospheric correction processes and different band response functions of individual sensors (Dorji & Fearn, 2017).

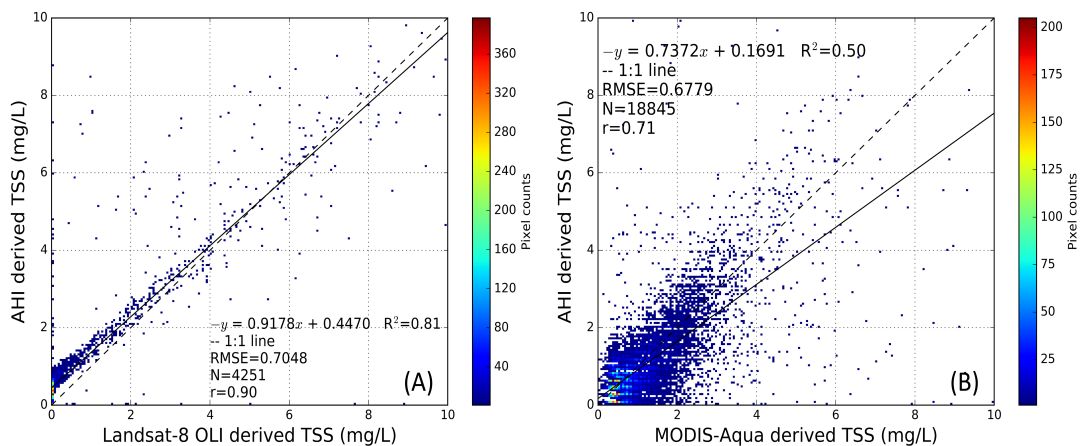


Figure 6.11: A linear regression between (A) AHI and Landsat-8 OLI derived TSS concentration on July 29th 2015 and (B) AHI and MODIS-Aqua derived TSS concentration on July 4th-6th and 8th-10th, 2015.

6.4.5 TSS Concentration Mapping and Temporal Dynamics

The TSS concentration maps of the study site derived from AHI Band 3 are shown in Figure 6.12 for July 5th 2015 at every 30 min from 10:00 am to 03:30 pm local time at spatial resolution of 500 m. From Figure 6.12, we observe that the spatial distribution of TSS concentration in the study site is similar to a previous study by Dorji et al. (2016), where higher TSS

concentration was observed closer to the coast and decreased in moving further away from the coast. For the quantitative analysis, TSS concentrations were computed for three different locations using the SWIR and NIR-SWIR atmospheric correction methods for all available AHI images in Table 6.1 at three different regions, Box A, B and C (see Figure 6.1). It was found that TSS concentration for the NIR-SWIR and SWIR atmospheric methods in Boxes A, B and C were 0.50 ± 0.19 mg/L, 1.72 ± 0.68 mg/L and 2.79 ± 1.97 mg/L and 1.06 ± 0.33 mg/L, 3.26 ± 0.78 mg/L and 4.05 ± 2.07 mg/L respectively. Similar TSS concentration were observed by Dorji et al. (2016) in Onslow waters ($21^{\circ} 35' S$, $115^{\circ} 05'' E$) where TSS concentration was 0.79 ± 0.04 mg/L in the offshore waters and 3.73 ± 1.21 mg/L closer to the coast.

From visual inspection of Figure 6.12, we observe that the temporal dynamics of TSS concentration are discernable during the course of the day. As observed at the near coastal region (see 'Box C' in Figure 6.12), the TSS concentration varied from high in the morning (10:00-11:30 hrs Local Time) to gradually decreasing in the early afternoon (12:00 – 14:30 hrs) and increasing slightly toward the late afternoon (15:00 – 15:30 hrs). In Box B, the changes in TSS concentration were present with a similar trend to Box C, although changes were very subtle and not easily discernable using visual inspection. In Box A, the changes in TSS concentration were negligible during the course of 10:00 – 15:30 hrs. Further for Box A, we observe background spatial noise to be more noticeable and increased toward the late afternoon. The sensor noise equivalent TSS concentration (Section 6.3.4) of AHI in Band 3 was estimated to be around 0.12 mg/L for $\theta_0 < 50^{\circ}$ (corresponded to 10:30 – 15.00 hrs in the study site) and around 0.40 mg/L for $\theta_0 > 70^{\circ}$ (corresponded to later than 15:00 hrs in the study site).

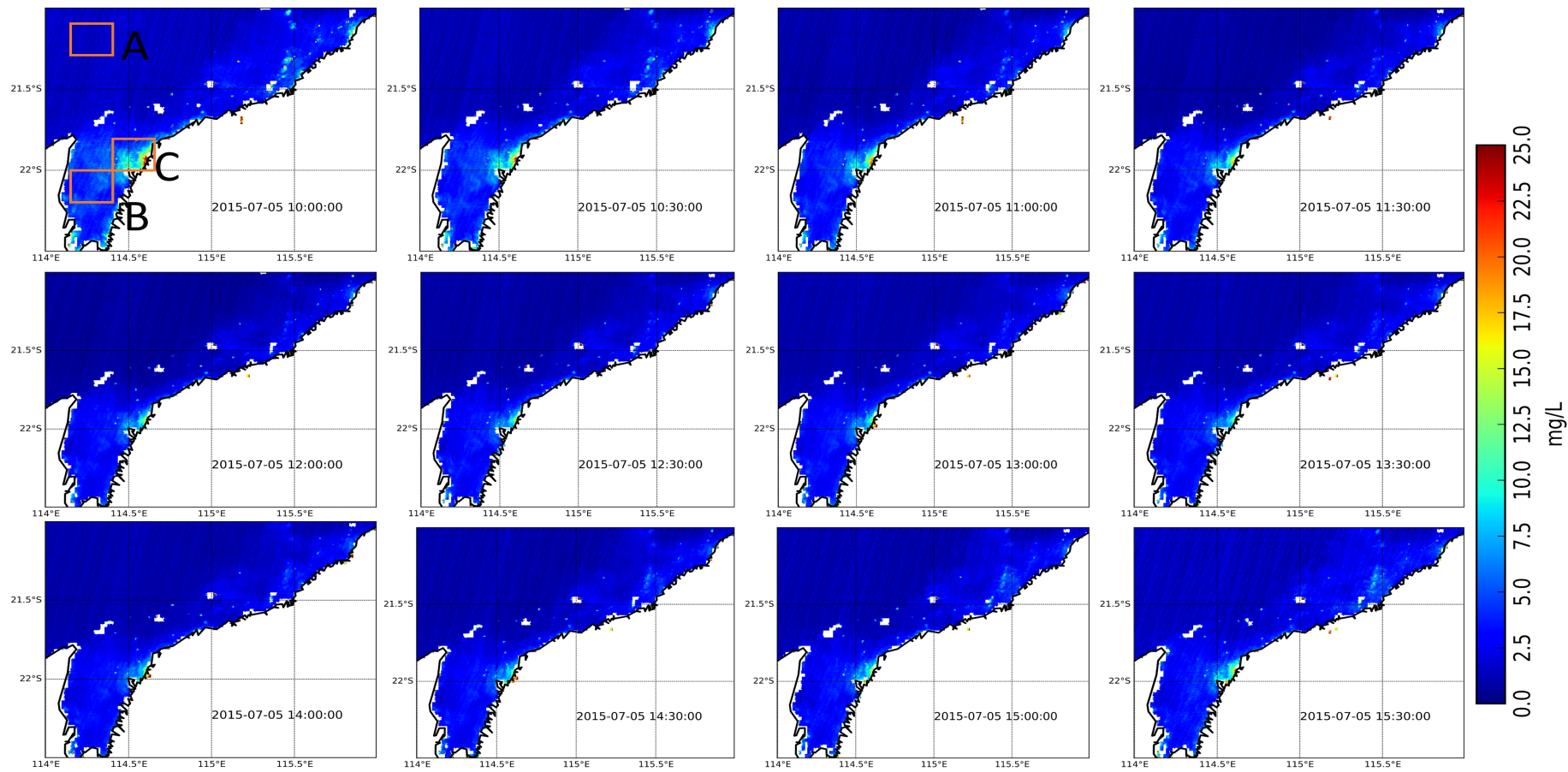


Figure 6.12: Every 30 min TSS concentration derived by AHI on July 5th 2015 from 10:00 – 15:30 hrs. TSS was derived using SWIR atmospheric correction method described in Section 6.4.1.

From visual inspection of the TSS maps in Figure 6.12, it is evident that diurnal TSS variations are noticeable near the coast, around the location of Box C. To further verify the diurnal TSS variation, quantitative analyses were performed by analysing every 10 min of AHI-derived TSS data from July 04th – July 10th 2015 at three locations (Boxes A, B and C). In addition, TSS variations were qualitatively compared with the tidal cycle in the area. Figures 6.13A-6.13C show TSS variation at the aforementioned locations on July 4th, July 08th and July 10th 2015, each representing a different period of the tidal cycle. The error bars displayed for each TSS variation curve in Figures 6.13A-6.13C were calculated from uncertainties associated with NE_L and the aerosol correction methods.

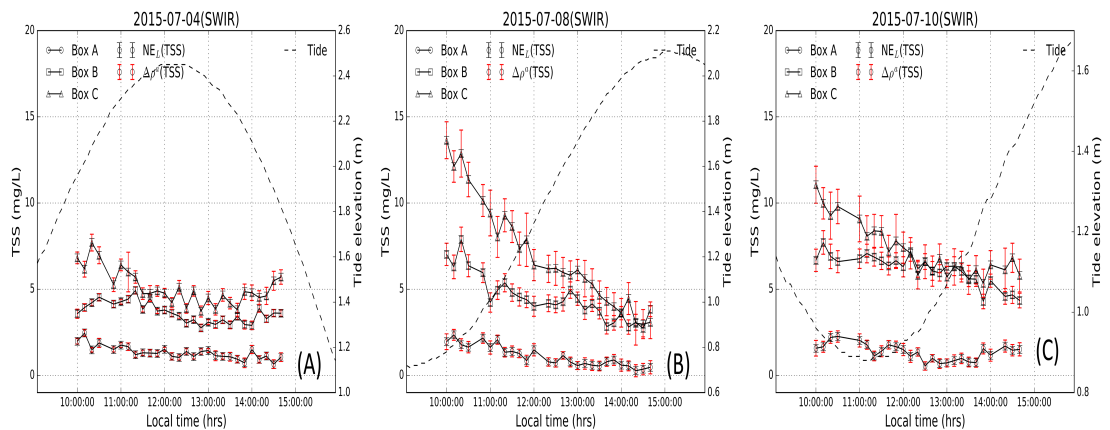


Figure 6.13: Daily TSS concentration from 10:00 hrs – 15:00 hrs at Boxes A, B and C (see Figure 6.12) derived using the SWIR atmospheric correction method for (A) July 4th 2015, (B) July 8th 2015, and (C) July 10th 2015. NE_L (TSS) and $\Delta\rho_a$ (TSS) are errors derived from AHI sensor noise and aerosol estimation.

In Figure 6.13A, which corresponds to TSS derived for July 4th 2015, we observe that in Boxes A and B that TSS concentration varied only slightly or remained relatively constant throughout the day, but in Box C, TSS concentration decreased at 10:00 am from ~7.0 mg/L to ~4.0 mg/L around 13:00 hrs and then increased to ~6.0 mg/L at 15:00 hrs. Figure 6.13B, showing TSS concentration derived for July 8th 2015, shows that in Boxes B and C the TSS concentrations were highest, ~7.0 mg/L and 14.0 mg/L respectively, at 10:00 hrs. By 15:00 hrs the TSS concentration in both Boxes

B and C decreased to ~3.50 mg/L. Similarly, but less pronounced, there was a decrease in TSS concentration in Box A from ~2.0 mg/L at 10:00 hrs to ~1.0 mg/L at 15:00 hrs. Likewise, in Figure 6.13C for July 10th, we observe the TSS variations were similar to those shown in Figure 6.13B for Boxes B and C with a gradual decrease from morning towards late afternoon. By 12:00 hrs the TSS concentrations in both Boxes B and C were similar, but both continued to decrease, although with a less pronounced decrease evident for Box C. With respect to the TSS variations portrayed in Figures 6.13A –6.13C, and considering the gradient of TSS plots, we observe that Box C usually had a steeper gradient than Boxes A and B. Further, visually comparing the TSS curves with the tidal elevation, the magnitude of TSS concentration in Boxes B and C was observed to be higher when tide elevation was lower, and lower TSS concentration during flooded periods corresponding to the highest tidal elevation of the day. In Box A however, corresponding to a location further from coast where the water is generally deeper and the impact of tidal currents is assumed to be lower, the tidal level seems to have little or no direct effect on TSS concentration, where the TSS concentration variously increases, decreases or remains constant. Similar observations were made for TSS variation derived using the NIR-SWIR atmospheric correction methods, but with lower magnitude in TSS concentrations. The results for TSS variations derived for other dates, not presented in this section, for both SWIR and NIR-SWIR atmospheric correction methods are presented in Appendix H.

6.5 Discussion

In this study, we have shown that the AHI sensor onboard Himawari-8 can be used in mapping of TSS concentration in the coastal waters of northern Western Australia at high temporal resolution, with the possibility of discerning temporal dynamics of TSS concentration of the region. The atmospheric correction of high temporal resolution daily data is usually challenged by varying solar geometry observed during the course of the day, which can have considerable impact on the derived products if geometrical

effects are not taken into account during the atmospheric correction process. For instance, L_{toa} in AHI Band 3 varied by 31.94% (from 13.24 to 9.01 $\text{Wm}^{-2} \mu\text{m}^{-1}\text{sr}^{-1}$) between 10:00 hrs and 15:00 hrs. Such a variation, without taking into account the geometrical effect in the atmospheric correction, would result in ~66% relative error in the final AHI derived TSS concentration.

The use of different aerosol calculation methods in the AHI atmospheric correction process, using AHI SWIR bands (4 and 5) and NIR-SWIR bands (5 and 6), resulted in different aerosol reflectance, ρ_a . For all three different regions considered (Boxes A, B and C) we observed that ρ_a values in AHI Bands 1 to 4 derived by the SWIR method were lower than those derived using the NIR-SWIR method. On average, ρ_a estimated by the SWIR method was ~60 – 66% lower than for the NIR-SWIR method. In the NIR-SWIR aerosol correction method, which is based on the assumption that ρ_w is effectively zero, visual selection of clear water pixels from Box A might have resulted in inclusion of pixels with ρ_w not equal to zero, potentially inflating the estimation of $\epsilon^{(4,5)}$. Further, using a single median value of ϵ as a representative of the whole image might also have contributed to discrepancies in ρ_a between the SWIR and NIR-SWIR methods because ϵ can potentially be different for every pixel, especially near the coast where ρ_a are not necessarily spatially homogenous. It was noted by Neukermans et al. (2009) and Vanhellemont and Ruddick (2015) that a combination of longer wavelength bands (SWIRs) resulted in lower values of ϵ than a combination of shorter and longer wavelength bands (NIR-SWIR), as was the case in this study with $\epsilon^{(5,6)}$ and $\epsilon^{(4,5)}$ values calculated to be 1.12 ± 0.65 and 1.82 ± 0.84 respectively. As a result of lower ρ_a in the SWIR aerosol correction method, the ρ_w and resulting TSS concentration were calculated to be higher than for the NIR-SWIR aerosol correction method.

The validation of AHI derived ρ_w with DALEC measured (*in situ*) ρ_w produced MARE in the range of 22.17% - 47.76% and 23.78% - 69.81% for the NIR-SWIR and SWIR atmospheric correction methods respectively. Higher accuracy was obtained for the NIR-SWIR atmospheric correction method than the SWIR atmospheric correction method when validated with

in situ ρ_w , but validation was only limited to low turbidity values. Thus, a higher turbidity range of *in situ* validation data is needed to rigorously validate the results in this study, and to better understand the effect of atmospheric correction methods considered in this study. However, the ALI-derived TSS validation using MODIS-Aqua and Landsat-8 OLI data did produce better correlation values, with $r = 0.71$ and $r = 0.91$ respectively. From the cross-validation results using both the *in situ* ρ_w and satellite-derived TSS concentrations we have shown that AHI-derived TSS products can be generated at high temporal resolution with reasonable accuracies.

The TSS variation results presented in Section 6.4.5 show that the AHI-derived TSS can be used to discern diurnal TSS variation in the region, especially near the coast (Location B and C) even after taking into account uncertainty from sensor noise and atmospheric correction. It should be noted that bidirectional variability in ρ_w can also contribute to discrepancies in the observed satellite reflectance (Vanhellemont et al., 2014). For this study we have not applied bidirectional correction in our analysis due to unavailability of such bidirectional reflectance data for the study site.

Considering the offshore waters represented by Box A, the TSS variation during the course of the day cannot be separated from climatological influence and sensor noise, especially at high θ_0 . The changes in TSS concentration that could be mapped by AHI data was limited by the $NE_{TSS} = \sim 0.15$ mg/L for θ_0 greater than 60° , which makes it difficult to study the variation in TSS concentration in offshore waters where TSS variations over relatively short time spans are typically less than ~ 0.1 mg/L. However, as discussed in Section 3.3, the NE_{TSS} can be reduced to ~ 0.06 mg/L even at high solar angles if the 10 min data are averaged into approximately hourly data.

6.6 Conclusion

The temporal analysis of TSS variation using AHI data was only performed for a one week period, from July 4th to July 10th 2015. This study has not assessed TSS variation due to climatological influences, seasonal

variation or the impact of varying solar geometry over the course of a year. We have shown that two widely used aerosol correction methods, the NIR-SWIR and SWIR methods, can produce reasonable atmospherically corrected AHI ρ_w at visible and NIR bands. We have demonstrated application of a TSS algorithm to the red band ρ_w to provide a TSS product at 10 minute intervals throughout the day. In general we have shown that temporal variation in daily TSS concentration can be observed in AHI derived TSS products, and specifically, we can conclude from this study that the Himawari-8 geostationary satellite can be used in mapping TSS concentration in northern Western Australia at high temporal resolution with AHI Band 3 data, and diurnal TSS variability can only be discerned for TSS variability greater than ~ 0.15 mg/L for $\theta_0 < 60^\circ$ for 10 min data and ~ 0.06 mg/L for temporally averaged ~ 1 -hour data.

Chapter 7

Conclusion and Future Work

7.1 Conclusion

The principle aim of this thesis was to develop a generic multi-sensor satellite TSS algorithm for the coastal waters of northern Western Australia. The developed TSS model was to be based on the principle of radiative transfer theory where the established relationship between TSS concentration and reflectance in the model was physically sensible. Further, in development of the TSS model for the coastal waters of northern Western Australia, the general aims were also to: (1) explore the feasibility of established TSS models and methods employed in TSS estimation that might be applicable to coastal waters of Western Australia, (2) examine the implication of using different satellite sensors in TSS estimation as satellite sensors are limited by their design, particularly the radiometric, spatial and temporal characteristics, and (3) explore the feasibility of a high temporal resolution geostationary satellite, which was primarily designed for meteorological purposes, for monitoring TSS dynamics in coastal waters.

The monitoring of water quality for large spatial scales is currently challenging, but nonetheless it is progressively addressed by the advancement in remote sensing technologies and improved TSS models. Most of the TSS models employed in estimation of TSS concentration are generally based on a simple linear or exponential relationship established between TSS concentration and reflectance measurements. The implication of using wholly empirical relationships in TSS estimation are significant considering that in the physical world, the reflectance versus TSS concentration does not necessarily follow a simple linear or exponential relationship. Simple linear or exponential relationships, as shown in Chapter 3, either overestimate or underestimate the TSS concentration by significant amounts if empirical models are not adequately tuned. In this thesis, we have developed a generic red band semi-analytic sediment model (SASM) for the coastal waters of northern Western Australia, the SASM being

physically based on the principle of radiative transfer, is physically sensible and performs relatively better than simple linear or exponential TSS models. The SASM developed in this thesis was further adapted to include different satellite sensors, MODIS-Aqua, Landsat-8 OLI, WV-2 and Himawari-8. This thesis has demonstrated that if adequately tuned to the regional waters, the SASM can be used to monitor TSS concentration using just a single red or NIR band of the various satellite sensors studied. The application of SASM using MODIS-Aqua 250 m data in the coastal waters of north Western Australian water was able to discern daily TSS anomalies of the region. Currently, the SASM is adopted by the Western Australian Marine Science Institute in the Dredging Science Node Project to study the coastal water quality to better understand the impact of dredging activities in northern Western Australia.

Due to the significance of coastal water quality monitoring, numerous TSS algorithms have been developed across the globe. In Chapter 4, we listed 76 TSS algorithms which were developed in the last decade for just the MODIS and Landsat sensors, but the majority of the TSS algorithms were regionally tuned to specific water types and mostly empirical in design. In this thesis, through rigorous statistical comparative analysis, we have shown that there are few developed TSS algorithms that can be employed to estimate TSS concentration in optically unknown water types. In Chapter 4, the application of high scoring TSS models in northern Western Australian coastal waters resulted in MARE of only 43.11% - 102.59%. Considering the MARE of previous studies for even the regionally tuned TSS algorithms were within $\sim 18\% - 61\%$, we can propose that the high performing TSS algorithms can be used in optically unknown waters types where regional TSS algorithms are not available. Further, the prior knowledge of the waters can also be used in selection of previously developed TSS algorithms presented in Chapter 4 to reduce the error and select more appropriate TSS models. However, it is not advisable to use any random TSS models without prior knowledge because the errors were shown to potentially exceed in excess of three orders of magnitudes for some cases.

Progress in remote sensing technologies has led to rapid adoption of remote sensing in water quality assessment. However, the inherent radiometric, spatial, temporal and spectral characteristics of satellite sensors can have implications on the derived TSS concentration. In Chapter 5, we have quantified the effect of using different satellite sensors with different spatial resolutions. The results from Chapter 5 qualitatively reconfirmed the results of previous studies in asserting the benefit of high spatial resolution satellite sensors being visually superior in assessing the sediment plume and ability to discern high turbidity gradients within the larger sediment plumes. However, added value was that the results in Chapter 5 also showed the quantified evidence of the effect from different satellite sensors in estimation of TSS concentration. It was observed in Chapter 5 that there was significant differences in the derived TSS concentration between high and low spatial resolution sensors. The WV2 sensor was observed to estimate TSS concentration as high as 160 mg/L while low spatial resolution MODIS-Aqua estimated only 23.6 mg/L. Further, it was observed the differences in TSS estimated by different satellite sensors were more evident in regions of high turbidity gradient than spatially homogenous regions.

The remote sensing sensors, MODIS and Landsat, currently employed to study the TSS dynamics in the coastal waters of northern Western Australia are limited by their temporal resolution, at best to map the daily TSS variability. Thus, we have explored the feasibility of using Himawari-8, a geostationary satellite with high temporal resolution (~10 min) to study the coastal dynamics of TSS variation in the region. The feasibility study in Chapter 6 showed that daily TSS dynamics can be ascertained from Himawari-8 over the coastal waters of northern Western Australia. However, the limitation of employing a geostationary satellite designed primarily for meteorological purpose was that the SNR of the bands required to discern TSS variability limits its application to TSS concentrations $> \sim 0.15$ mg/L. Thus, application of Himawari-8 in open ocean waters where TSS concentration is < 0.15 mg/L must be cautioned or applied only after temporally averaging the data to reduce the effect of SNR. Further, it was

observed that applicability of Himawari-8 was limited to 10:00 am – 3:00 pm when $\theta_0 < 60^\circ$.

7.2 Limitations

In Chapter 3, in the formulation of SASM, the simplification of the optical model by assuming all the backscattering in the red and NIR regions in turbid waters (see Equation 3.9) was predominantly due to TSS concentration limits the application of this model to waters where CHL concentration is low, relative to the TSS concentration. However, even in high CHL dominated waters (CHL ~ 10 mg/m³), the TSS concentration to produce an equivalent backscattering effect at 650 nm to the CHL was estimated to be only ~ 3.4 mg/L. In addition, the data collected to calibrate the SASM were limited to only 48 match-up pairs (TSS and R_{rs} pairs) with TSS in the range of only 2.4 – 69.6 mg/L. Further, most of the calibration data were in the lower spectrum of the TSS concentration range. Thus, the SASM model, when applied in regions where TSS concentrations are beyond the calibration range, may have an impact on the accuracy of derived TSS concentration.

In Chapter 4, the limitation stems from the data used to compare the TSS algorithms. The data used in the comparative study were simulated using HydroLight for four discrete optical constituents (CHL, TSS, CDOM and Pure Water). However, the simulated datasets may not necessarily be representative of all the waters in the physical world. Further, due to the limitation of HydroLight 4.2 to simulate data for wavelengths greater than 800 nm we employed extrapolation methods which introduced errors ($\sim 1 - 4\%$) in the longest wavelengths (~ 1300 nm).

In Chapter 5, the limitation of the study was mainly due to the time difference in image acquisition by the satellite sensors. The time differences between different satellite sensors were in excess of ~ 3 hrs. Such large time differences make image comparison difficult, particularly in highly dynamic coastal waters where components of water can change completely between the two satellite overpass times.

In Chapter 6, the limitation of the study can result from the aerosol estimation method employed in atmospheric correction of the AHI dataset. The ratio of aerosol reflectance between two methods, the SWIR (Band 5 and Band 6) method and the NIR-SWIR (Band 4 and Band 5) method, was assumed to constant over the whole study region and only one single median value was used to derive aerosol reflectance. The aerosol reflectance ratio is not necessarily spatially homogenous as assumed in this study, but can vary across different pixel locations, particularly near the coastal land and waters. The assumption of spatially homogenous aerosol reflectance ratios over a large spatial extent can possibly result in discrepancies in the atmospheric correction process and the derived products. However, the limitations discussed in aforementioned sections were carefully considered and their implications discussed in each individual chapter.

7.3 Future work and recommendations

The work pursued in development of SASM reinforces the need for larger datasets to adequately calibrate the SASM to be representative of generalized TSS algorithms for the whole of Western Australian coastal waters, or indeed for waters further afield. The data used in calibrating the SASM was sourced from one site over the course of three years, thus larger datasets comprising data from different sites in the coastal waters of Western Australia, and across different seasons, are needed to make SASM more robust to seasonal TSS variability and applicable to the extended coastal waters of Western Australia. In future, to limit the inaccuracies of the SASM associated with the parameterization, parameters of the SASM as defined in Equation (3.14) will be calibrated directly with *in situ* IOPs of the coastal waters in Western Australia. The IOPs are not depended on the ambient light fields, thus it has the potential to limit uncertainties associated with varying light fields in the water. The application of SASM in waters optically different than northern Western Australia should be performed only after calibration with *in situ* regional parameters.

In Chapter 4, the comparative analysis of decadal TSS algorithms for MODIS and Landsat sensors also suggest an avenue of potential future work. The quantitative methodology adopted in scoring the algorithms was based on the comparison of average performances which were susceptible to very low or high scores of the individual algorithms. Further, the same weight was assigned for different statistical tests which can bias the results when one test is more or less significant than others in a comparative analysis. Thus, to compare the models, the development of a better quantitative methodology is needed that is not depended on the average performance, but on the significance of the tests. In addition, the validation of high scoring models needs to be validated with different *in situ* datasets to confirm their reliability because in our study we only performed validation using an *in situ* dataset of our study site. The general recommendation from Chapter 4 would be to select an appropriate TSS model through proper validation if *in situ* datasets are available or at least consider historical or neighbouring water's biogeochemical properties to aid in selection of appropriate 'off the shelf' TSS algorithms.

The results from Chapter 5 showed that the difference in spatial resolutions of satellite sensors have an effect in the final derived TSS concentrations. Similarly, other attributes of the satellite sensors, such as radiometric and spectral characteristics can also significantly affect the final derived TSS product. Future work resulting from Chapter 5 will be in quantifying the uncertainties associated with different satellite sensors, in terms of radiometric and spectral bands. In addition, the communication of uncertainties associated with satellite remote sensing as a result of satellite sensors are important to make informed decisions of the final derived product, especially for coastal water quality monitoring agencies. Further, inter-sensor comparison of the final derived TSS products in Chapter 5 were dependent on the proper atmospheric correction of each individual satellite sensor, which is often challenging considering the different sensors have different radiometric properties. Thus, for inter-sensor comparative analysis it is important to take into account uncertainties associated with different

atmospheric corrections and quantitatively validate with *in situ* datasets to make reasonable comparison of the derived products between the sensors.

The TSS feasibility study in Chapter 6, being carried out for the first time, has resulted in subsequent possible future work. First, we adapted the widely used 6S radiative transfer methods of atmospheric correction, but with changes in the aerosol correction methods which were based on the satellite image itself. The two different SWIR and NIR-SWIR aerosol correction methods employed showed discrepancies between the two methods, but due to the lack of adequate validation data, we were unable to show which method was more valid for our study region. In future, we plan to collect a wide range of *in situ* aerosol data over the study region and validate the aerosol correction method best suited for our study region. The uncertainty in the final derived TSS product from individual ~10 min AHI data was considerable in clear waters, because the NE_{TSS} of 10 min AHI data were ~0.15 mg/L, which is considerable in open waters where TSS concentrations are minimal. Thus, sensor noise reduction methods need to be explored for the AHI sensor, such as the image aggregation method discussed in Chapter 6 which showed that aggregation of 10 min data to ~ 1 hour have potential to limit sensor noise to NE_{TSS} of ~ 0.06 mg/L.

7.4 Concluding remark

In this thesis, we have achieved the four main objectives outlined in Chapter 1, as we have in:

- Chapter 3: developed a TSS algorithm (SASM) for the coastal waters of northern Western Australia which is semi-analytic in design and physically based on the principle of radiative transfer theory. The developed SASM was tuned for the turbid coastal waters of northern Western Australia and recalibrated to be operational for Landsat-8 OLI, MODIS-Aqua, WV2 and Himawari-8 sensors;
- Chapter 4: quantitatively assessed published TSS algorithms from the last decade for the widely used MODIS and Landsat based sensors. In addition, we also identified TSS algorithm(s) that are best

suites for optically unknown water types and validated using *in situ* data of northern Western Australia;

- Chapter 5: quantified the effect of different spatial resolutions of WV2, Landsat-8 OLI and MODIS-Aqua satellite sensors on derived TSS concentration. The implications of using different satellite sensors were also qualitatively presented to support coastal managers in making informed decisions on water quality monitoring, and;
- Chapter 6: Himawari-8, a high temporal resolution geostationary satellite was found to be feasible to study the high temporal dynamics of TSS variation in the coastal waters of northern Western Australia.

Appendix A

A1. Comparison of Reflectance Models for Nechad et al. (2010) and SASM

The $\omega'_b(\lambda)$ by definition can be used as a proxy for reflectance because it is a ratio of the amount of light backscattered to the amount of light absorbed by water and its constituents Nechad et al. (2010), hereafter referred as NRP. Thus, $\omega'_b(\lambda)$ from both the NRP and SASM model is used here for the comparative analysis using HydroLight-simulated data for different water types. From the HydroLight simulations, we generate r_{rs} for given IOP models representing different water types (Mobley, Stramski, Bissett, & E, 2004) to be inverted to compute $\omega'_b(\lambda)$ for use in model comparisons between NRP and SASM derived estimates of $\omega'_b(\lambda)$. Each model derived $\omega'_b(\lambda)$ is then validated using the true $\omega'_b(\lambda)$ given by Equation (3.8). The true $\omega'_b(\lambda)$ are calculated from the $a(\lambda)$ and $b_b(\lambda)$ we used as the inputs in the HydroLight simulation.

A1.1. NRP Reflectance Model:

The reflectance model used in the formulation of $r_{rs}(\lambda)$ by NRP assumes $r_{rs}(\lambda)$ is based on the first order approximation of Gordon, *et al.* (1988):

$$r_{rs}(\lambda) = \frac{f' b_b(\lambda)}{Q a(\lambda) + b_b(\lambda)} = \frac{f' \omega'_b(\lambda)}{Q 1 + \omega'_b(\lambda)} \quad (\text{A1})$$

where f' is a varying dimensionless factor described by Morel and Gentili (1991) and Q is the ratio of subsurface upwelling irradiance to the subsurface upwelling radiance. The ratio of the total backscattering coefficient to total absorption coefficient ($\omega'_b(\lambda)$) is related to subsurface remote sensing reflectance as follows:

$$\omega'_b(\lambda) = \frac{\rho_w(\lambda)}{\gamma - \rho_w(\lambda)} \quad (\text{A25})$$

where $\rho_w(\lambda) = \pi \mathfrak{R} r_{rs}(\lambda)$ and $\gamma = \pi \mathfrak{R} r_{rs}(\lambda) f' / Q \approx 0.216$ with $\mathfrak{R} = 0.529$ and

$f'/Q = 0.13$ (refer to (Nechad et al., 2010) for details)

A1.2. SASM Reflectance Model:

SASM computes r_{rs} based on the second order approximation of Gordon et al. (1988) as shown in Equation (3.2) using coefficients g_1 and g_2 from Lee et al. (1999) optimized for turbid waters. In the SASM, $r_{rs}(\lambda)$ is related to $\omega'_b(\lambda)$ as follow:

$$\omega'_b(\lambda) = \frac{x(\lambda)}{1 - x(\lambda)} \quad (\text{A3})$$

where x is given by Equation (3.15).

A2. HydroLight Simulation

HydroLight 4.2 was used to simulate Case-2 water R_{rs} for infinitely deep water using a four components model. The four components were: 1) pure water (W), 2) pigmented particles or chlorophyll (CHL), 3) coloured dissolved organic matter (CDOM) and 4) mineral particles (TSS).

For all HydroLight simulations, the following details were kept unchanged: the phase function for component 1 was a Rayleigh-like phase function, components 2 and 4 used Petzold “average particle” phase functions, and component 3 used an isotropic phase function. Standard (IOP) models from HydroLight were used to compute components’ scattering and absorption coefficients: the component 1 absorption coefficient was from and the scattering coefficients were from (Smith & Baker, 1981). The component 2 absorption coefficient for a chlorophyll-specific absorption was derived from and the scattering coefficient was computed using the (Loisel & Morel, 1998) near surface power law model. The specific absorption for component 3 was computed using an exponential decay model and the component 4 specific absorption and scattering coefficients were from HydroLight data for Calcareous sand.

HydroLight simulations were performed for a solar zenith angle of 30° , wind speed of 5 m s^{-1} , and for a clear sky using Harrison and Coombes’ sky model for different TSS concentration, CHL concentration, and CDOM

absorption. TSS concentration values ranged from 0–200 mg/L. For the range 0–50 mg/L the TSS concentration was increased at the rate of 0.2 mg/L and for the 50–200 mg/L range the rate of increment was 2.0 mg/L. The concentration of chlorophyll was set at 0.1 mg/m³, 1 mg/m³, 5 mg/m³ and 10 mg/m³ and CDOM absorption of 0.1 m⁻¹ and 1.0 m⁻¹ were used in the simulation. The combinations of CHL and CDOM were used to define 6 different water types, shown in Table A1.

Table A.1: Six different water types grouped based on CHL concentration and CDOM absorption.

CHL (mg/m ³) and CDOM (m ⁻¹)	Water type
CHL 0.1 and CDOM 0.1	I
CHL 1.0 and CDOM 0.1	II
CHL 5.0 and CDOM 0.1	III
CHL 10.0 and CDOM 0.1	IV
CHL 0.1 and CDOM 1.0	V
CHL 10.0 and CDOM 1.0	VI

A3. Reflectance Model Evaluation

We present $\omega'_b(\lambda)$ modelled using Equations (A2) and (A3) for the 6 different water types as a function of TSS concentration, compared with HydroLight simulated $\omega'_b(\lambda)$. The details of the results from model evaluation are presented in Table A2, Table A3, Table A4, and Table A5 for blue (494 nm), green (566 nm), red (650 nm), and NIR (790 nm) wavelength respectively. For all bands and different water types, $\omega'_b(\lambda)$ was approximated better by the reflectance model in the SASM when compared with that in the NRP model. In comparison, the highest MARE was given by the NRP model for the green band (~75%) for water type I whereas the highest MARE of the SASM was ~4.5% in the blue band for water type V.

Since both the NRP and SASM are based on the assumption that red and NIR wavelengths are optimal for the estimation of TSS, we make a detailed comparative analysis between NRP and SASM in the red and NIR spectral regions. In the red spectral region, we find that the NRP model better estimates $\omega'_b(\lambda)$ when CHL and CDOM are increased: MARE

improved by 6.0% from type I to type VI, while for the SASM the MARE performance decreases by 0.48% from water type I to type VI. Likewise, in the NIR band, the shift in improvement over different water types is ~1.0% for the NRP model and ~0.17% for the SASM. However, comparing the red and NIR bands, the NRP model performs better for the NIR band with the MARE ~15.0% lower than the red band. For the SASM, the performance is better in the red band by ~1.0 %. Illustration of the differences between the NRP model and the SASM for their performance in estimating $\omega'_b(\lambda)$ with respect to HydroLight-modelled $\omega'_b(\lambda)$ is shown in Figures A1 (a) and A2 (a) for red and NIR bands respectively for water type VI. For the variation of $\omega'_b(\lambda)$ as a function of TSS, Figure A1 (b) for the red band and Figure A2 (b) for the NIR band shows that the accuracy of the estimation of $\omega'_b(\lambda)$ decreases with increasing TSS concentration for the NRP model. The estimation of $\omega'_b(\lambda)$ by the NRP model deviates by more than 25% for TSS concentrations greater than 100 mg/L. The $\omega'_b(\lambda)$ are estimated better by the SASM for the whole range of TSS when compared with the NRP for all spectral bands with maximum deviation of only 4.53% in the blue band.

Table A.2: Comparative $\omega'_b(494\text{nm})$ results for the NRP and SASM models (all $p < 0.005$).

Water Type	NRP			SASM		
	RMSE (sr^{-1})	MARE (%)	r	RMSE (sr^{-1})	MARE (%)	r
I	0.53	57.41	0.99	0.01	1.00	1.00
II	0.49	53.70	0.99	0.01	1.15	1.00
III	0.37	41.86	0.99	0.01	2.15	1.00
IV	0.28	32.91	0.99	0.02	2.98	1.00
V	0.23	26.00	0.99	0.02	4.53	1.00
VI	0.17	20.55	0.99	0.02	4.13	1.00

Table A.3: Comparative $\omega_b(566\text{nm})$ results for the NRP and SASM models (all $p < 0.005$).

Water Type	NRP			SASM		
	RMSE (sr^{-1})	MARE (%)	r	RMSE (sr^{-1})	MARE (%)	r
I	0.83	74.71	0.98	0.02	2.08	1.00
II	0.81	73.31	0.98	0.02	2.05	1.00
III	0.73	66.86	0.98	0.02	1.92	1.00
IV	0.64	59.85	0.99	0.02	1.88	1.00
V	0.52	49.24	0.98	0.02	2.25	1.00
VI	0.45	43.06	0.98	0.02	2.66	1.00

Table A.4: Comparative $\omega_b(650\text{nm})$ results for the NRP and SASM models (all $p < 0.005$).

Water Type	NRP			SASM		
	RMSE (sr^{-1})	MARE (%)	r	RMSE (sr^{-1})	MARE (%)	r
I	0.36	35.91	0.98	0.02	3.07	1.00
II	0.35	35.26	0.98	0.02	3.11	1.00
III	0.32	32.64	0.99	0.02	3.24	1.00
IV	0.29	29.62	0.99	0.02	3.44	1.00
V	0.33	33.09	0.98	0.02	3.27	1.00
VI	0.27	27.76	0.99	0.02	3.55	1.00

Table A.5: Comparative $\omega_b(790\text{nm})$ results for the NRP and SASM models (all $p < 0.005$).

Water Type	NRP			SASM		
	RMSE (sr^{-1})	MARE (%)	r	RMSE (sr^{-1})	MARE (%)	r
I	0.04	21.70	0.99	0.01	4.00	1.00
II	0.04	21.57	0.99	0.01	4.00	1.00
III	0.04	20.84	0.99	0.01	3.92	1.00
IV	0.04	20.13	0.99	0.01	3.83	1.00
V	0.04	21.87	0.99	0.01	4.00	1.00
VI	0.04	20.15	0.99	0.01	3.83	1.00

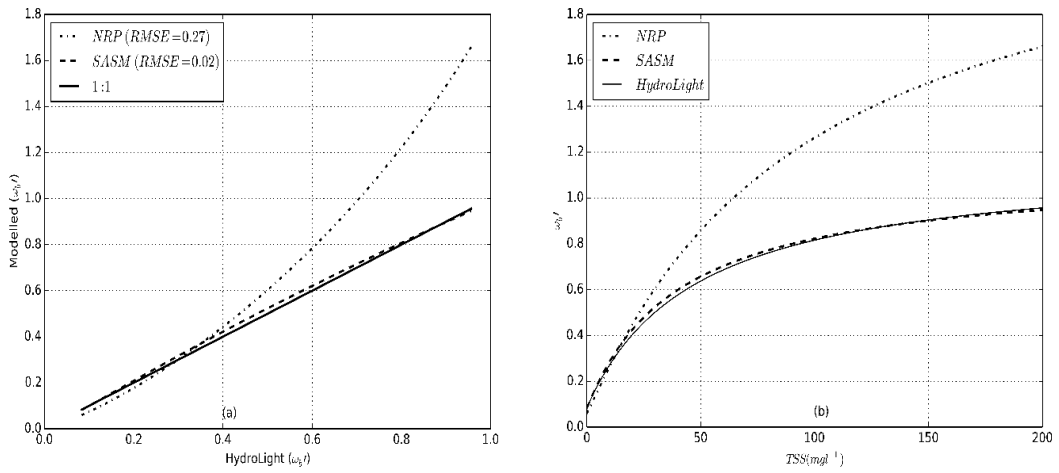


Figure A.1: (a) Scatter plot for modelled and HydroLight ω_b' (650nm); (b) ω_b' (650nm) as a function of TSS.

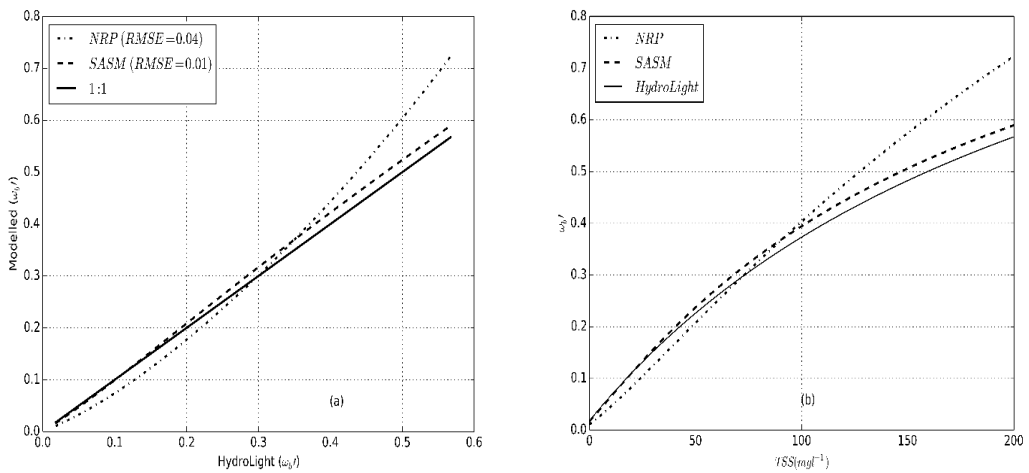


Figure A.2: (a) Scatter plot for modelled and ω_b' (790nm); (b) ω_b' (790nm) as a function of TSS

Appendix B

To ascertain how far below the water's surface MODIS can "see" in MODIS band 1, we simulated diffuse attenuation coefficients (K_d) for the near surface waters for different chlorophyll (CHL) and CDOM for a range of TSS concentrations using HydroLight 4.2 (Mobley, 1994). From the simulated K_d results, with the assumption that 90% of the diffuse light comes from a water column of depth of $1/K_d$ (Mishra, Narumalani, Rundquist, & Lawson, 2005), MODIS band 1 can only penetrate 1.9 m at a TSS concentration of 3.9 mg/L for even very low CHL and CDOM. For high CHL and CDOM concentrations, the penetration depth of MODIS band 1 is only 1.5 m even for zero TSS. Thus, the TSS data collected from a depth of ~1.9 m may be unsuitable for remotely sensed TSS algorithm development or validation.

Appendix C

Table C.1: The summary of TSS algorithms mentioned in Section 4.3.2

Algorithm	Reference	Location	TSS Range (mg/L)	Bands/Algorithms	Regression Coefficient (R ²)	Error	N
MOD-E1	Kumar et al. (2016)	Chilika Lagoon, India	3.9–161.7	$TSS = 13181 R_{rs}(B1)^2 - 1408.6 R_{rs}(B1) + 44.15$	0.915	RMSE = 2.64 mg/L	54
MOD-E2	Ayana et al. (2015)	Gumera catchment, Lake Tana, Ethiopia	~5–255	$TSS = 2371\rho(B2) - 62.8$	0.95	SE = 10.77 mg/L	54
MOD-E3	Chen et al. (2015a)	Estuary of Yangtze River and Xuwen Coral Reef, China	5.8–577.2	$\log(TSS) = \frac{-b + \sqrt{b^2 - 4a(c-y)}}{2a} \left. \begin{array}{l} R_{rs}(B1) < 0.025 \\ R_{rs}(B1) > 0.025 \end{array} \right\}$ $a = -0.334, b = 1.0046, c = 0.8251, (b^2 - 4a(c-y)) \geq 0$ $y = \log(Rrs(B2)) / \log(Rrs(B1))$	0.752	RMSE = 2.1mg/L RMSE = 38.6mg/l	40
MOD-E4	Zhang et al. (2016a) and Shi et al. (2015)	Lake Taihu, China	1.7–343.9	$TSS = 9.65 \exp(58.81 R_{rs}(B1))$	0.70	RMSE = 14.0mg/L	150
MOD-E5	Choi et al. (2014)	Mokpo coastal area, Korea	1.03–193.10	$TSS = 1.545 \exp(179.53 R_{rs}(B1))$	0.92	-	96

MOD-E6	Feng et al. (2014)	Yangtze estuary	4.3–1762.1	$TSS_{low} = 2.49 \exp(97.19 R_{rs}(B1)) \} TSS < 10(mg/l)$ $TSS_{high} = 57.58 \exp(3.48(R_{rs}(B2)/R_{rs}(B1))) \} TSS > 150(mg/l)$ $TSS_{mid} = \alpha \times TSS_{low} + \beta \times TSS_{high} \} 50 < TSS < 150(mg/l)$ $\alpha = \frac{\ln(TSS_{low}/50)}{\ln(150/50)}, \beta = \frac{\ln(150/TSS_{low})}{\ln(150/50)}$	0.88 (low) 0.93 (high)	RMSE = 27.7%	78
MOD-E7	Hudson et al. (2014)	Fjord in Southwest Greenland	1.2–716	$TSS = 1.80 \exp(19.11(R_{rs}(B1) + R_{rs}(B2)))$	0.84	-	143
MOD-E8	(Kaba et al., 2014)	Lake Tana, Ethiopia	~5–255	$TSS = 2371 \times \rho(B2) - 62.8$	0.95	RMSE = 16.5 mg/L	54
MOD-E9	(Lu et al., 2014)	Bohai Sea, China	~<160	$TSS = \exp\left(\frac{R_{rs}(B1) - 0.0123}{0.0038}\right)$	0.75	RE = < 20%	627
MOD-E10	(Park & Latrubesse, 2014)	Amazon River system	30–150	$TSS = 27.05 \exp(7.83\rho(B1))$	0.88	RMSE = 6.2 mg/L	232
MOD-E11	(Sokoletsky et al., 2014)	Yangtze river estuary	0–2500	$TSS=10^{2 \times [R_{rs}(B1)/R_{rs}(B4)]}$	-		361
MOD-E12	(Chen et al., 2014c)	Bohai Sea	4–106.4	$TSS = 3 \times 10^8 x^3 - 2 \times 10^6 x^2 + 5453.3x + 3.8825$ $x = \rho_w(B15) - 1.107\rho_w(B16)$	0.954	RMS = 30.12%	48
MOD-E13	(Cui et al., 2013)	Ponyang lake, China	0–141.9	$TSS = 1.063 \exp(27.859\rho(B1))$	0.91	SE = 11.20 mg/L	54
MOD-E14	(Kazemzadeh, Ayyoubzadeh, & Moridnezhad, 2013)	Bahmanshir River, Iran	30–500	$TSS=22.92\rho(B1)^{0.82}$	0.63	RMSE = 261.84	23
MOD-E15	(Raag et al., 2013)	Pakri Bay, of Gulf	0–10	$TSS = 592.54\rho(B1) + 1.1136$	0.52		77

Finland								
MOD-E16	(Qiu, 2013)	Yellow River Estuary, China	1.9–1896.5	$TSS = \exp\left(1.1932\left(\frac{Rrs(B12)}{Rrs(B14)}\right)^{0.875}\right)$	0.95	MAE = 24.5 mg/L	81	
MOD-E17	(Espinoza Villar et al., 2013)	Maderia River	25–622	$TSS = 1020\left(\frac{Rrs(B2)}{Rrs(B1)}\right)^{2.94}$	0.62	-	282	
MOD-E18	(Min et al., 2012)	Saemangeum coastal area, Korea	0.1–55	$TSS = 0.24 \exp(188.3 R_{rs}(B12))$	0.90	-	88	
MOD-E19	(Ondrusek et al., 2012)	Chesapeake Bay	4.5–14.92	$TSS = 3.8813(nL_w(645))^3 - 13.822(nL_w(645))^2 + 19.61(nL_w(645))$	0.95	MPD = 4.2%	35	
MOD-E20	(Son & Wang, 2012)	Chesapeake Bay	1.0–20	$TSS = 1.7 + 5.263 K_d(490)$	0.77	STD = 0.48	15,720	
MOD-E21	(Wang et al., 2012)	Hangzhou Bay, China	133–1,950	$TSS = 1.4599\left(\frac{Rrs(B1)}{Rrs(B2)}\right)^{2.3874}$	0.82		35	
MOD-E22	(Chen et al., 2011a)	Apalachicola Bay, USA	1.29–208	$\log(\rho(B2) / \log(\rho(B1))) = -0.1325 \log(TSS)^2 + 0.7429 \log(TSS) + 0.6768$	0.86	RMSE = 4.76 mg/L	32	
MOD-E23	(Chen et al., 2011b)	Apalachicola Bay, USA	1.29–208	$\log(\rho(B2) / \log(\rho(B1))) = 0.4339 \log(TSS) + 0.8288$	0.8	RMSE = 4.79	25	
MOD-E24	Jiang and Liu (2011) as cited in (Chen et al., 2015a)	Poyang Lake, China	0–40	$TSS = 1365.5x^2 - 369.08x + 27.216$ $x = Rrs(B3) + Rrs(B4)$	0.81	-	27	
MOD-E25	(Siswanto et al., 2011)	Yellow and East China Sea	0.04–340.07	$TSS = 10^{\left(0.649 + 25.623(Rrs(B12) + Rrs(B13)) - 0.646\left(\frac{Rrs(B10)}{Rrs(B12)}\right)\right)}$	0.92	RPD = 15.7%	223	
MOD-E26	(Zhao, Chen, Walker, Zheng, & MacIntyre,	Mobile Bay estuary, Alabama	0–87.8	$TSS = 2.12 \exp(42.92 \rho(B1))$	0.781	RMSE = 5.42	63	

	2011)							
MOD-E27	(Petus et al., 2010) and (Petus et al., 2014)	Bay of Biscay, France	0.3–145.6	$TSS = 12450 Rrs(B1)^2 + 666.1Rrs(B1) + 0.45$	0.97	RMSE = 61%	74	
MOD-E28	(Wang & Lu, 2010)	Yangtze River, China	45–909	$TSS = 61.369 \exp(0.2623x)$ $x(\%) = \rho(B2) - \rho(B5)$	0.78	RRMSE = 36.5%	35	
MOD-E29	(Wang et al., 2010a)	Apalachicola Bay, USA	1–64	$\log(TSS) = 1.5144(\log(\rho(B2))/\log(\rho(B1))) - 0.5755$	0.72	-	16	
MOD-E30	(Wang et al., 2010b)	Middle and Lower Yangtze River, China	75–881	$TSS = 60.24x - 23.03$ $x(\%) = \rho(B2) - \rho(B5)$	0.73	RMSE = 29.7%	153	
MOD-E31	(Zhang et al., 2010)	Yellow and East China Sea	0.68–27.2	$\log(TSS) = s_0 + s_1(Rrs(B4) + Rrs(B1)) + s_2(Rrs(B10)/Rrs(B4))$ $s_0 = 0.6311, s_1 = 22.2158, s_2 = -0.5239$	0.87	ARE = 26%	81	
MOD-E32	(Chen et al., 2009)	Apalachicola Bay, USA	1.29–208	$\log(\rho(B2)/\log(\rho(B1))) = -0.1356 \log(TSS)^2 + 0.7402 \log(TSS) + 0.6836$	0.853	RMSE = 5.5mg/L	25	
MOD-E33	(Chu et al., 2009)	Kangerlussuaq Fjord, Greenland	~500	$TSS = 10^{\left(\frac{Rrs(B1)-1.6}{7.5}\right)}$	-	-	-	
MOD-E34	(Doxaran et al., 2009)	Gironde Estuary, France	77–2182	$TSS = 12.996 \exp(Rrs(B2)/(0.189Rrs(B1)))$	0.89	RMSE: 18%–22%	204	
MOD-E35	(Jiang, Tang, Zhang, Ma, & Ding, 2009)	Taihu Lake, China	0–170	$TSS = 10^{(0.3568 \ln(Rrs(B2)) + 3.3431)}$	0.81	ARE = 20.5%	56	
MOD-E36	Liu and Rossiter (2008) as cited in (Chen et al., 2015a)	Poyang Lake, China	15.6–518.8	$TSS = 7167 \rho(B1) - 42.0$	0.91	-	25	

MOD-E37	(Wang et al., 2008)	Hangzhou Bay, China	17–6949	$TSS = \exp(43.233Rrs(B2) + 1.396)$	0.76	RMSE = 424mg/L	25
MOD-E38	Wu and Cui (2008) as cited in (Chen et al., 2015a)	Poyang Lake, China	0-142	$TSS = 86236.23(Rrs(B1))^3 - 15858.70(Rrs(B1))^2 + 1005.29(Rrs(B1)) - 15.67$	0.92	-	42
MOD-E39	(Kutser et al., 2007)	Muuga and Sillmae Port, Estonia	2–8	$TSS = 349.83\rho(B1) + 2.9663$	0.86	-	11
MOD-E40	(Liu et al., 2006)	Middle Yangtze River, China	23.4–61.2	$TSS = \exp(2.495x + 1.81)$ $x = \frac{\rho(B1) - \rho(B2)}{\rho(B1) + \rho(B2)}$	0.72	RE = 34.7%	41
MOD-E41	(Sipelgas et al., 2006)	Parki Bay, Finland	3–10	$TSS = 110.3\rho(B1) + 2.0$	0.58	-	48
MOD-E42	(Miller & McKee, 2004)	Northern Gulf of Maxico, USA	1.0–55.0	$TSS = 1140.25 \times Rrs(B1) - 1.91$	0.89	RMSE = 4.74mg/L	52
MOD-A1	(Dorji et al., 2016)	Onslow, Western Australia	2.4–69.6	$TSS = \frac{23.47 \left(\frac{x(B1)}{1-x(B1)} \right)}{1-0.69 \left(\frac{x(B1)}{1-x(B1)} \right)}$ $x(B1) = \frac{-g1 + \sqrt{(g1)^2 + 4g2r_{rs}(B1)}}{2g2}$ $g1 = 0.084, g2 = 0.17, \text{ and } r_{rs}(B1) = Rrs(B1)/(0.52 + 1.7Rrs(B1))$	0.85	MARE = 33.33%	48

MOD-A2	(Han et al., 2016)	Europe, French Guiana, Vietnam, North Canada, and China	0.154–2627	$TSS = \frac{W_L \cdot TSS_L + W_H \cdot TSS_H}{W_L + W_H}$ $W_L = \begin{cases} 1, & \text{if } Rrs(B1) \leq 0.03 \text{ sr}^{-1} \\ 0, & \text{if } Rrs(B1) \geq 0.04 \text{ sr}^{-1} \\ \log_{10}(0.04) - \log_{10}(Rrs(B1)), & \text{otherwise} \end{cases}$ $W_H = \begin{cases} 0 & \text{if } Rrs(B1) \leq 0.03 \text{ sr}^{-1} \\ 1, & \text{if } Rrs(B1) \geq 0.04 \text{ sr}^{-1} \\ \log_{10}(Rrs(B1)) - \log_{10}(0.03), & \text{otherwise} \end{cases}$ $TSS_L = \frac{404.4 \rho_w(B1)}{1 - \rho_w(B1)/0.5}$ $TSS_H = \frac{1214.669 \rho_w(B1)}{1 - \rho_w(B1)/0.3394}$	-	MRAD = 51.9-59%	TSS _L = 366 TSS _H = 46
MOD-A3	(Shen et al., 2014)	Yangtze estuary, China	-	$Rrs = \frac{\alpha \beta \times TSS}{1 + \beta \times TSS + \sqrt{1 + 2 \beta \times TSS}}$ $Rrs(B2) \left\{ \alpha = 0.1038, \beta = 1.8042 \right.$	0.91	RMSE = 0.0048 (sr ⁻¹)	144
MOD-A4	(Vanhellemon t & Ruddick, 2014)	Southern North Sea, UK	0.5–100	$TSS = \frac{258.85 \rho(B1)}{1 - \rho(B1)/0.1641}$ $\rho(B1) = 0.529 \times \pi \times r_{rs}(B1)$	-	-	-
MOD-A5	(Chen et al., 2013a)	Changjiang River Estuary, China	70–710	$TSS = 1.7492 (Rrs(B16)^{-1} - Rrs(B15)^{-1})^{-1} + 0.0912$	0.89	MRE = 28.99%	20
MOD-A6	(Katlane et al., 2013)	Gulf of Gabes	0.7–30	$TSS = 62.86 \left(\frac{\rho(B1)}{(0.1736 - \rho(B1))} \right)$ $\rho(B1) = \pi Rrs(B1)$	-	-	56
MOD-A7	(Nechad et al., 2010)	Southern North Sea	1.24–110.27	$TSS = \frac{400.75 \rho(B1)}{1 - \rho(B1)/0.1774} + 1.02$ $\rho(B1) = 0.539 \times \pi r_{rs}(B1)$	0.80	RMSE = 11.23 mg/L MRE = 38.9%	72
LAN-E1	(Cai et al., 2015b)	Hangzho Bay, China	203–481	$\ln(TSS) = 0.01113115 \times L(TM4) + 4.794229$	0.951	-	35
LAN-E2	(Cai, Tang, Levy, & Liu, 2015a)	Hangzho, Bay	179–389.58	$TSS = 314.435 \rho(TM3) + 3805.982 \rho(TM4) + 28.54$	0.976	-	27

LAN-E3	(Kong et al., 2015a)	Gulf of Bohai Sea	2.1–208.7	$TSS = 5.184 + 1349.63R_{rs}(TM4) + 614561.673[R_{rs}(TM4)]^2$	0.844	RMSE = 5.59	70
LAN-E4	(Kong et al., 2015b)	Caofeidian, Bohai Sea	4.3–104.1	$TSS = 296.29x^2 - 272.62x + 70.939$ $x = R_{rs}(TM3) / R_{rs}(TM2)$	0.977	RMSE = 7.22 mg/L MRE = 25.35	
LAN-E5	(Lim & Choi, 2015)	Nakdong River, South Korea	~3–14	$TSS = 11.80 - 50.608\rho(OLI2) + 14.58\rho(OLI5) - 4.764\rho(OLI5) / \rho(OLI3)$	0.74	RMSE = 1.40	48
LAN-E6	(Wu et al., 2015)	Dongting Lake, China	0–63.2	$TSS = 1.1034 \times \exp(23.61 \times \rho(OLI4))$	0.91	RMSE = 4.41 mg/L	52
LAN-E7	(Zheng et al., 2015)	Dongting Lake, China	4.0–101	$TSS = 4616.4 \times R_{rs}(TM4) - 4.362$	0.82	MAPE = 21.3% RMSE = 7.01 mg/L	42
LAN-E8	(In-Young, Lang, & Vermote, 2014)	Old Women Creek Estuary, Ohio, US	1.0–278	$Turb = 14.44 \times \rho(\%, ETM4) + 7.61$ $Turb = 1.03TSS - 3.54$	0.65		11
LAN-E9	(Zhang et al., 2014)	Yellow river estuary	1.0–1500	$\log_{10}(TSS) = 44.072 \times R_{rs}(TM3 + 0.1591)$	$\frac{0.967}{2}$	MRE = 26.1%	44
LAN-E10	Hao, et al. (2013)	Yangtze Estuary, China	~40.0–750	$R(B4) = 0.0444 + 32.7736 \times \left[\frac{TSS}{(51.6753 + TSS)} \right]$ $-32.7260 \times \left[\frac{TSS}{(51.6753 + TSS)} \right] \times \exp(-0.0000012081 \times TSS)$	$\frac{0.817}{5}$	ARE = 36.83	17
LAN-E11	(Hicks et al., 2013)	Waikato River, New Zealand	2.0–962	$TSS = -52.817 + 1449.4\rho(ETM4)$	0.939	RMSE = 21.3	35
LAN-E12	(Min et al., 2012)	Saemangeum coastal area, Korea	0.1–55	$TSS = 0.24 \exp(188.3R_{rs}(TM2))$	0.90	-	88
LAN-E13	(Miller et al., 2011)	Albemarle-Pamlico Estuarine System, North Carolina,	~5.0–30	$TSS = 1.7 + 684.76\rho(\%, ETM3)$	0.87	-	599

USA								
LAN-E14	(Li et al., 2010)	Changjiang Estuary	~1.5–560	$\log_{10}(TSS) = 0.892 + 6.2244x$ $x = \frac{[\rho(ETM2) + \rho(ETM3)]}{[\rho(ETM2) / \rho(ETM3)]}$	0.915	-		21
LAN-E15	(Wang et al., 2009b)	Yangtze river, China	22–2610	$\ln(TSS) = 3.18236 \times \ln(\%, \rho_w(ETM4))$	0.88	MRE = 14.83%		24
LAN-E16	(Onderka & Pekárová, 2008)	Danube River, Slovakia	19.5–57.5	$TSS = 4.17 \times L(ETM4) - 43.22$	0.93	SE = 3.2 mg/L		10
LAN-E17	(Teodoro et al., 2008)	Douro River and Mira Lagoon, Portugal	14–449	$TSS = 15.483 - 12.688\rho(TM1) + 44.495\rho(TM3)$	0.995	RMSE = 25.3 mg/L		11
LAN-E18	(Alparslan, Aydöner, Tufekci, Tufekci, 2007)	Omerli Dam, Turkey	0.4–2.9	$TSS = 42.2671 - 0.8694\rho(ETM1) - 0.3716\rho(ETM2) + 1.05\rho(ETM3) + 0.1247\rho(ETM4)$	0.99	SE = 0.0085mg/L		6
LAN-E19	(Wang, Lu, & Zhou, 2007)	Yangtze River, China	0–900	$TSS = 71.392 \times \rho(\%, ETM4) - 272.48$	0.92	MAE = 68.9 RMSE = 83.2		14
LAN-E20	(Doxaran et al., 2006)	Gironde Estuary, France	10–2000	$TSS = 29.022 \times \exp(0.0335x)$ $x = R_{rs}(ETM4) / R_{rs}(ETM2)(\%)$	0.88	SD = 21%		132
LAN-E21	(Wang et al., 2006)	Lake Reelfoot, USA	11.5–33.5	$TSS = 22.74 + 156.202\rho(TM2) - 147.62\rho(TM3) - 45.66\rho(TM4)$	0.52	-		18
LAN-E22	(Zhou et al., 2006)	Lake Taihu, China	48.32–120.80	$TSS = -122.4 + 304.1 \left(\frac{\rho(TM4)}{\rho(TM1)} \right) + 10.37$	0.74	MPE = 65.40%		
LAN-A1	(Dorji et al., 2016)	Onslow, Western Australia	2.4–69.6	$TSS = \frac{25.34 \left(\frac{x(B1)}{1-x(B1)} \right)}{1 - 0.69 \left(\frac{x(B1)}{1-x(B1)} \right)}$ $x(B1) = \frac{-g1 + \sqrt{(g1)^2 + 4g2r_{rs}(B1)}}{2g2}$	0.85	MARE = 33.36%		48

$$g1 = 0.084, g2 = 0.17, \text{ and } r_{rs}(B1) = Rrs(B1) / (0.52 + 1.7Rrs(B1))$$

LAN-A2	(Han et al., 2016)	Europe, French Guiana, Vietnam, North Canada, and China	0.154–2627	$TSS = \frac{W_L \cdot TSS_L + W_H \cdot TSS_H}{W_L + W_H}$ $W_L = \begin{cases} 1, & \text{if } Rrs(B1) \leq 0.03 sr^{-1} \\ 0, & \text{if } Rrs(B1) \geq 0.04 sr^{-1} \\ \log_{10}(0.04) - \log_{10}(Rrs(B1)), & \text{otherwise} \end{cases}$ $W_H = \begin{cases} 0 & \text{if } Rrs(B1) \leq 0.03 sr^{-1} \\ 1, & \text{if } Rrs(B1) \geq 0.04 sr^{-1} \\ \log_{10}(Rrs(B1)) - \log_{10}(0.03), & \text{otherwise} \end{cases}$ $TSS_L = \frac{346.353 \rho_w(OLI4)}{1 - \rho_w(OLI4)/0.5}$ $TSS_H = \frac{1221.390 \rho_w(OLI4)}{1 - \rho_w(OLI4)/0.3329}$	-	MRAD = 51.9%–59%	TSS _L = 366 TSS _H = 38
LAN-A3	Zhang et al. (2016b)	Xinánjiang Reservoir, China	0.67–5.66	$TSS = 38.08 \times [0.42 \times ((Rrs(OLI2) + Rrs(OLI3))^{-1} - (Rrs(OLI3) + Rrs(OLI4))^{-1}) \times (Rrs(OLI4) + 0.24)] - 3.39$	>0.8	MRE = 24.3%	45
LAN-A4	Kong et al. (2015a)	Gulf of Bohai Sea	2.1–208.7	$TSS = 8.602 + 1805.26 Rrs(TM4) + 900713.14 Rrs(TM4)^2$	0.844	RMSE = 4.53	70
LAN-A5	Vanhellemont and Ruddick (2014)	Southern North Sea, UK	0.5–100	$TSS = \frac{289.29 \rho_w(OLI4)}{1 - \rho_w(OLI4)/0.1686}$ $\rho_w(OLI4) = 0.529 \times \pi \times r_{rs}(OLI4)$	-	-	-

MRE = Mean Relative Error, MARE = Mean Absolute Relative Error, MAE = Mean Absolute Error, MPE = Mean Percentage Error, SD = Standard Deviation, MRAD = Mean Relative Absolute Difference, RMSE = Root Mean Square Error, SE = Standard Error, ARE = Absolute Relative Error, RPD = Relative Percentage Difference, APD = Absolute Percentage Difference, RRMSE = Relative Root Mean Square Error

Appendix D

Table D.1: Mean of Total Point and Final Scores of MODIS TSS models across different water classes as derived from different sediment types, backscattering ratios and Solar Zenith Angles. The top five and bottom five scores from each water types and the final scores are in bold (top) and bold italics (bottom)

MODEL	Mean Total Score from Sediment					Mean Total Score from Backscattering Ratio (b_b/b)					Mean Total Score from Solar Zenith Angles					Final Score	Error Final Score	
	I	II	III	IV	V	I	II	III	IV	V	I	II	III	IV	V		Lower bound	Upper Bound
MOD-E6	1.69	1.61	1.66	1.61	1.63	2.00	1.72	1.98	1.75	1.72	1.71	1.60	1.67	1.53	1.59	1.70	1.64	1.76
MOD-A1	1.46	1.53	1.50	1.56	1.46	1.54	1.71	1.57	1.82	1.67	1.54	1.67	1.55	1.73	1.65	1.60	1.55	1.63
MOD-E28	1.53	1.51	1.53	1.51	1.51	1.71	1.71	1.71	1.74	1.71	1.52	1.55	1.52	1.51	1.56	1.59	1.56	1.63
MOD-A4	1.47	1.55	1.48	1.42	1.43	1.57	1.71	1.57	1.59	1.51	1.61	1.62	1.60	1.54	1.57	1.55	1.51	1.60
MOD-E10	1.54	1.54	1.54	1.54	1.54	1.57	1.57	1.57	1.57	1.57	1.59	1.50	1.55	1.47	1.50	1.54	1.54	1.56
MOD-E42	1.48	1.49	1.46	1.42	1.47	1.57	1.16	1.57	1.76	1.57	1.61	1.17	1.60	1.51	1.62	1.50	1.40	1.63
MOD-E21	1.57	1.50	1.58	1.49	1.50	1.73	1.46	1.76	1.51	1.53	1.68	1.24	1.37	1.20	1.29	1.49	1.40	1.60
MOD-E31	1.45	1.46	1.43	1.42	1.42	1.55	1.60	1.52	1.46	1.46	1.55	1.51	1.51	1.48	1.55	1.49	1.38	1.58
MOD-A6	1.47	1.46	1.49	1.42	1.40	1.43	1.57	1.43	1.57	1.43	1.47	1.54	1.49	1.50	1.47	1.48	1.44	1.53
MOD-A7	1.50	1.47	1.54	1.47	1.44	1.44	1.53	1.57	1.55	1.43	1.53	1.31	1.59	1.28	1.25	1.46	1.39	1.51
MOD-E44	1.32	1.30	1.31	1.26	1.30	1.57	1.56	1.57	1.51	1.55	1.58	1.47	1.57	1.44	1.56	1.46	1.39	1.49
MOD-E27	1.38	1.42	1.37	1.41	1.41	1.46	1.57	1.47	1.57	1.54	1.49	1.33	1.49	1.27	1.35	1.44	1.38	1.50
MOD-E4	1.47	1.41	1.47	1.40	1.42	1.57	1.43	1.57	1.43	1.45	1.49	1.36	1.47	1.32	1.39	1.44	1.41	1.49
MOD-E34	1.43	1.43	1.43	1.43	1.43	1.43	1.43	1.43	1.45	1.43	1.49	1.43	1.50	1.44	1.43	1.44	1.43	1.46
MOD-E41	1.41	1.40	1.41	1.40	1.41	1.43	1.43	1.43	1.43	1.43	1.46	1.34	1.45	1.32	1.46	1.41	1.41	1.43
MOD-E20	1.36	1.40	1.33	1.46	1.46	1.33	1.47	1.30	1.57	1.52	1.37	1.30	1.33	1.43	1.53	1.41	1.34	1.49
MOD-E35	1.15	1.52	1.15	1.56	1.23	1.29	1.58	1.29	1.68	1.39	1.29	1.53	1.28	1.56	1.40	1.39	1.33	1.51
MOD-E39	1.31	1.31	1.31	1.31	1.31	1.28	1.29	1.29	1.29	1.29	1.31	1.26	1.30	1.25	1.31	1.29	1.29	1.30
MOD-E25	1.15	1.19	1.14	1.32	1.20	1.31	1.40	1.24	1.15	1.34	1.39	1.36	1.31	1.32	1.39	1.28	1.10	1.49
MOD-E3	0.99	1.21	0.83	1.25	1.10	1.39	1.75	1.09	1.67	1.53	1.29	1.33	1.03	1.23	1.53	1.28	1.09	1.48
MOD-E19	1.39	1.22	1.42	1.26	1.24	1.30	1.12	1.40	1.36	1.14	1.38	0.90	1.43	0.98	1.22	1.25	1.05	1.36
MOD-E40	1.14	1.20	1.14	1.23	1.20	1.14	1.29	1.14	1.29	1.29	1.16	1.25	1.15	1.29	1.24	1.21	1.20	1.22
MOD-E11	1.15	1.19	1.12	1.21	1.18	1.23	1.26	1.16	1.18	1.26	1.26	1.19	1.15	1.18	1.25	1.20	1.11	1.28
MOD-E37	1.13	1.09	1.13	1.09	1.10	1.24	1.22	1.25	1.27	1.23	1.14	1.11	1.14	1.11	1.14	1.16	1.08	1.23

MOD-E36	1.18	1.17	1.19	1.17	1.16	1.14	1.14	1.14	1.14	1.14	1.16	1.11	1.15	1.10	1.11	1.15	1.12	1.17
MOD-A5	1.14	1.12	1.14	1.12	1.13	1.14	1.14	1.14	1.14	1.14	1.14	1.14	1.13	1.14	1.14	1.14	1.13	1.14
MOD-E5	1.30	1.16	1.32	1.18	1.19	1.19	0.90	1.20	1.08	0.96	1.33	0.94	1.22	1.01	0.97	1.13	1.02	1.26
MOD-E30	1.12	1.09	1.12	1.08	1.09	1.14	1.14	1.14	1.14	1.14	1.16	1.14	1.16	1.13	1.14	1.13	1.10	1.16
MOD-E17	1.22	1.06	1.24	1.06	1.07	1.27	1.00	1.29	1.00	1.00	1.30	0.81	1.31	0.75	1.10	1.10	1.07	1.12
MOD-E18	1.23	1.12	1.08	1.05	1.11	1.32	1.16	1.12	0.84	0.92	1.47	1.01	1.28	0.71	0.88	1.09	0.88	1.30
MOD-E7	1.17	1.13	1.19	1.15	1.15	0.98	1.04	1.01	1.13	1.02	0.99	1.05	0.99	1.09	1.05	1.08	0.93	1.19
MOD-E14	1.18	1.03	1.21	1.03	1.03	1.16	1.00	1.22	1.00	1.00	1.20	0.80	1.24	0.75	1.07	1.06	1.02	1.11
MOD-E13	0.85	1.02	0.82	1.08	1.03	0.84	1.25	0.81	1.41	1.28	0.97	1.11	0.93	1.17	1.16	1.05	0.87	1.22
MOD-E16	1.11	1.04	1.06	1.16	1.12	1.00	1.00	1.00	1.14	1.05	1.04	0.80	1.05	0.85	1.15	1.04	1.01	1.07
MOD-E12	1.00	1.14	1.04	1.14	1.13	0.88	1.00	0.89	1.07	1.09	0.99	0.97	0.99	1.01	0.96	1.02	0.88	1.16
MOD-E33	0.94	1.03	0.91	1.07	1.03	0.90	1.10	0.82	1.14	1.12	0.93	1.02	0.88	1.03	1.07	1.00	0.90	1.09
MOD-E29	1.00	0.91	1.03	0.87	0.92	1.14	1.00	1.14	1.00	1.00	1.10	0.81	1.10	0.78	0.94	0.98	0.92	1.03
MOD-E45	0.94	1.09	0.94	1.09	0.93	0.87	1.13	0.87	1.22	0.93	0.82	0.98	0.80	0.98	0.86	0.96	0.88	1.08
MOD-E1	0.91	0.85	0.92	0.84	0.86	0.76	0.72	0.78	0.72	0.72	0.82	0.82	0.85	0.83	0.86	0.82	0.77	0.93
MOD-E26	0.85	0.79	0.86	0.83	0.78	0.62	0.50	0.64	0.72	0.55	0.80	0.65	0.82	0.80	0.76	0.73	0.55	0.92
MOD-E15	0.45	0.86	<i>0.44</i>	0.85	0.58	0.35	0.96	0.35	0.98	0.67	0.49	0.85	0.49	0.82	0.77	0.66	0.52	0.88
MOD-E9	0.60	0.71	0.59	0.75	0.73	0.48	0.49	0.47	0.58	0.56	0.68	0.57	0.68	0.67	0.60	0.61	0.49	0.80
MOD-E38	0.45	0.52	0.42	0.61	0.56	0.50	0.64	0.50	0.75	0.63	0.62	0.62	0.58	0.73	0.66	0.59	0.47	0.89
MOD-E23	0.75	0.44	0.79	0.44	0.44	0.75	0.30	0.80	0.53	0.30	0.80	0.27	0.86	0.34	0.57	0.56	0.43	0.69
<i>MOD-E8</i>	0.51	0.41	0.51	0.35	0.48	0.62	0.60	0.59	0.24	0.55	0.60	0.44	0.56	0.24	0.40	0.47	0.18	0.67
<i>MOD-E2</i>	0.51	0.42	0.51	0.34	0.48	0.63	0.59	0.60	0.23	0.54	0.61	0.45	0.56	0.24	0.40	0.47	0.17	0.67
<i>MOD-E24</i>	0.46	0.45	0.45	0.48	0.46	0.44	0.44	0.43	0.55	0.47	0.45	0.49	0.44	0.57	0.51	0.47	0.43	0.58
<i>MOD-E22</i>	0.44	0.23	0.54	0.32	0.24	0.31	0.11	0.42	0.37	0.16	0.46	0.09	0.58	0.25	0.40	0.33	0.17	0.52
<i>MOD-E32</i>	0.38	0.31	0.49	0.42	0.32	0.04	0.14	0.36	0.45	0.18	0.29	0.15	0.53	0.40	0.39	0.32	0.18	0.57

Table D.2: Mean of Total Point and Final Scores of Landsat TSS models across different water classes as derived from different sediment types, backscattering ratios and Solar Zenith Angles. The top five and bottom five scores from each water types and the final scores are in bold and bold italics.

MODEL	Mean Total Score from Sediment					Mean Total Score from Backscattering Ratio (b_b/b)					Mean Total Score from Solar Zenith Angles					Final Score	Error	
	I	II	III	IV	V	I	II	III	IV	V	I	II	III	IV	V		Lower bound	Upper bound
LAN-E3	1.66	1.69	1.67	1.69	1.70	1.85	1.81	1.86	1.82	1.84	1.79	1.61	1.74	1.61	1.64	1.73	1.60	1.77
LAN-A4	1.54	1.63	1.54	1.63	1.64	1.62	1.69	1.64	1.71	1.67	1.59	1.50	1.56	1.48	1.50	1.60	1.46	1.69
LAN-E9	1.28	1.38	1.24	1.36	1.39	1.74	1.94	1.65	1.97	1.98	1.47	1.54	1.39	1.55	1.62	1.57	1.47	1.64
LAN-A5	1.38	1.51	1.39	1.52	1.43	1.52	1.60	1.53	1.59	1.49	1.52	1.54	1.52	1.52	1.52	1.51	1.44	1.59
LAN-A1	1.33	1.53	1.34	1.58	1.45	1.54	1.69	1.46	1.80	1.63	1.52	1.27	1.48	1.33	1.59	1.50	1.43	1.56
LAN-E14	1.47	1.32	1.46	1.33	1.45	1.76	1.37	1.78	1.42	1.56	1.75	1.09	1.74	1.12	1.56	1.48	1.35	1.60
LAN-E20	1.56	1.57	1.53	1.61	1.60	1.52	1.45	1.52	1.48	1.48	1.54	1.17	1.51	1.16	1.49	1.48	1.37	1.59
LAN-E4	1.53	1.42	1.42	1.33	1.58	1.41	1.54	1.46	0.91	1.45	1.51	1.21	1.46	0.68	1.50	1.36	1.23	1.48
LAN-E1	1.36	1.36	1.36	1.36	1.36	1.37	1.34	1.36	1.35	1.35	1.29	1.33	1.29	1.32	1.30	1.34	1.28	1.40
LAN-E8	1.31	1.35	1.32	1.35	1.35	1.35	1.36	1.36	1.41	1.36	1.29	1.26	1.27	1.28	1.28	1.33	1.18	1.42
LAN-E13	1.36	1.39	1.38	1.35	1.37	1.30	1.28	1.35	1.27	1.30	1.35	1.20	1.35	1.12	1.35	1.31	1.28	1.37
LAN-E2	1.33	1.33	1.32	1.34	1.33	1.34	1.30	1.33	1.32	1.30	1.16	1.26	1.21	1.26	1.23	1.29	1.27	1.35
LAN-A2	1.18	1.08	1.19	1.11	1.12	1.38	1.04	1.43	1.20	1.23	1.42	1.08	1.41	1.16	1.26	1.22	1.13	1.38
LAN-E21	1.16	1.11	1.20	1.10	1.11	1.28	1.13	1.43	1.01	1.08	1.25	1.16	1.40	1.05	1.15	1.17	1.07	1.24
LAN-E7	1.11	0.93	1.09	0.93	0.85	1.38	1.04	1.39	1.09	0.89	1.47	0.79	1.46	0.74	0.91	1.07	0.83	1.31
LAN-E17	1.09	1.04	1.10	1.08	1.09	1.00	0.99	1.01	1.02	1.00	0.89	0.97	0.89	0.97	0.94	1.01	0.98	1.03
LAN-E12	1.13	1.02	0.96	1.12	1.24	1.09	0.74	1.11	0.61	1.05	1.25	0.71	1.19	0.50	0.75	0.96	0.73	1.20
LAN-E15	0.98	0.91	0.97	0.99	0.97	1.04	0.92	1.02	0.97	0.99	1.06	0.71	1.09	0.69	0.99	0.95	0.83	1.04
LAN-E5	0.97	0.95	0.95	0.99	0.99	0.94	0.88	0.90	0.89	0.96	0.97	0.70	0.94	0.72	1.03	0.92	0.76	1.05
LAN-A3	0.93	0.93	0.90	0.93	0.89	0.92	0.85	0.88	0.66	0.61	0.92	0.91	0.90	0.72	0.69	0.84	0.68	1.02
LAN-E19	0.66	0.67	0.67	0.69	0.64	0.64	0.73	0.80	0.87	0.76	0.60	0.65	0.66	0.70	0.67	0.69	0.45	1.07
LAN-E6	0.59	0.68	0.57	0.73	0.66	0.61	0.61	0.56	0.76	0.63	0.68	0.58	0.62	0.69	0.65	0.64	0.53	0.81
LAN-E10	0.42	0.45	0.39	0.45	0.45	0.65	0.59	0.61	0.65	0.48	0.66	0.44	0.60	0.44	0.36	0.51	0.28	0.78
LAN-E11	0.40	0.46	0.40	0.48	0.41	0.45	0.37	0.46	0.52	0.38	0.42	0.30	0.40	0.36	0.27	0.41	0.23	0.67
LAN-E22	0.99	0.84	1.02	0.67	0.75	0.56	0.00	0.19	0.00	0.00	0.47	0.05	0.34	0.00	0.00	0.39	0.31	0.51
LAN-E16	0.29	0.20	0.30	0.30	0.31	0.43	0.30	0.43	0.42	0.45	0.36	0.27	0.41	0.32	0.44	0.35	0.16	0.62
LAN-E18	0.00	0.00	0.00	0.00	0.00	0.00	0.00	0.00	0.00	0.00	0.00	0.00	0.00	0.00	0.00	0.00	0.00	0.00

Appendix E

The statistical measures used in assessing the accuracy of the results between modeled and the true value are as follow:

$$\text{MARE} = \frac{\sum_{i=1}^n |(x_i - y_i) / y_i|}{n} \times 100\% \quad (\text{E1})$$

where n is the total number of samples, x_i is the predicted value and y_i is the true value.

The Absolute Relative Error that was used to gauge the tolerance of each TSS model is defined as follows:

$$\text{ARE} = \frac{|x - y|}{x} \times 100\% \quad (\text{E2})$$

where x is the TSS MARE results from the HydroLight validation and y is the MARE result from the TSS distribution generated from the 1000 data points in the Gaussian distribution of errors for 10%, 20% and 50% R_{rs} uncertainty.

Appendix F

This Supplementary contains materials related to MODIS and Landsat TSS models for Chapter 4

MODIS TSS models:

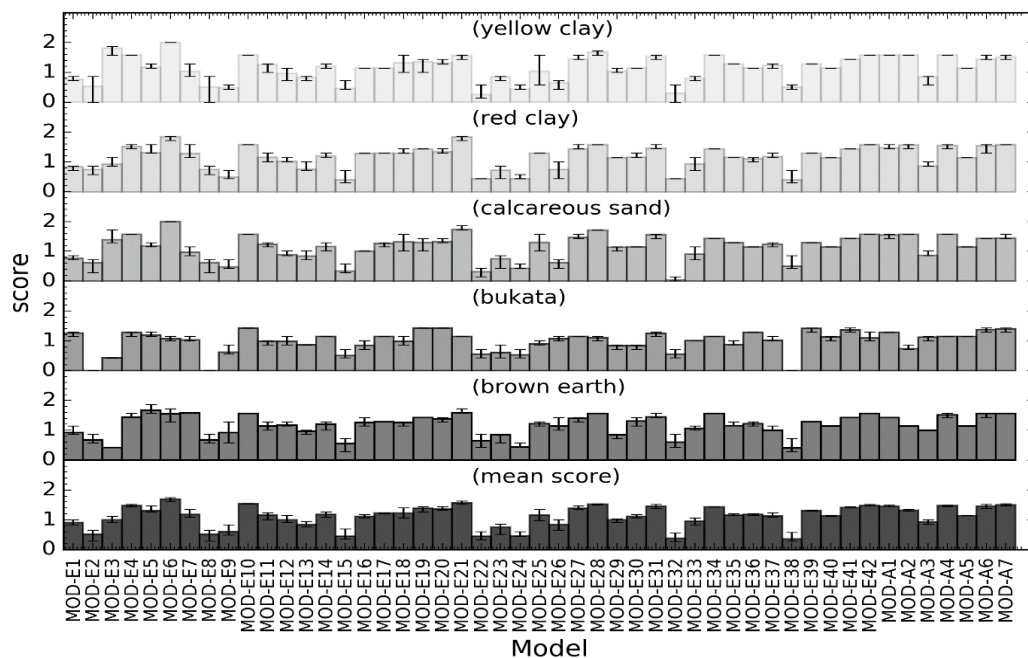


Figure F.1: Total scores for different sediments and the average scores across all five sediments in CLASS-I.

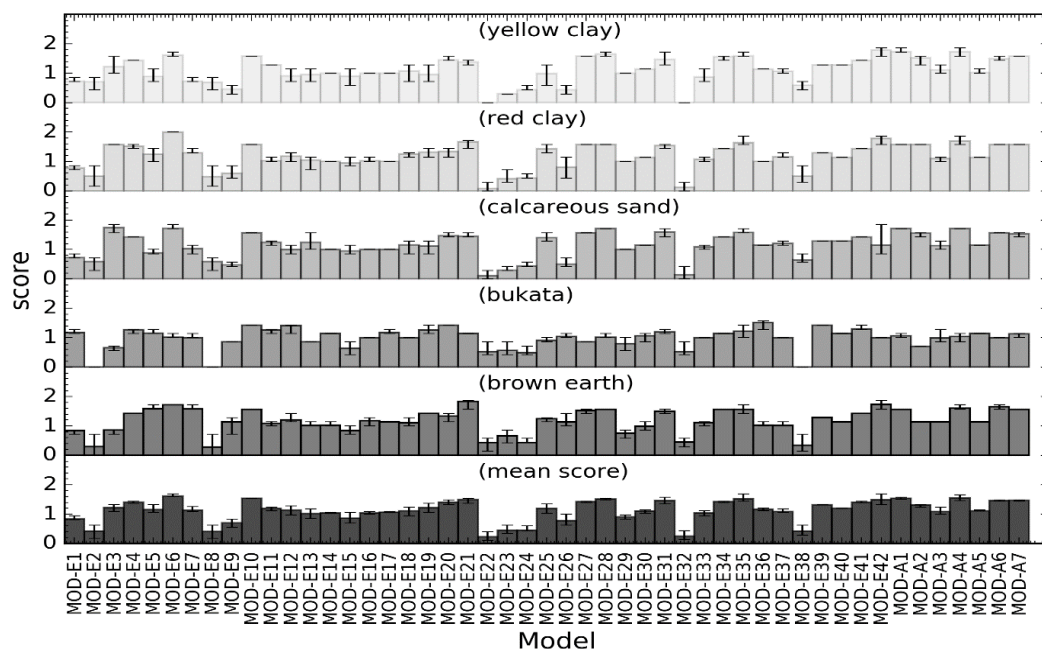


Figure F.2: Total scores for different sediments and the average scores across all five sediments in CLASS-II water.

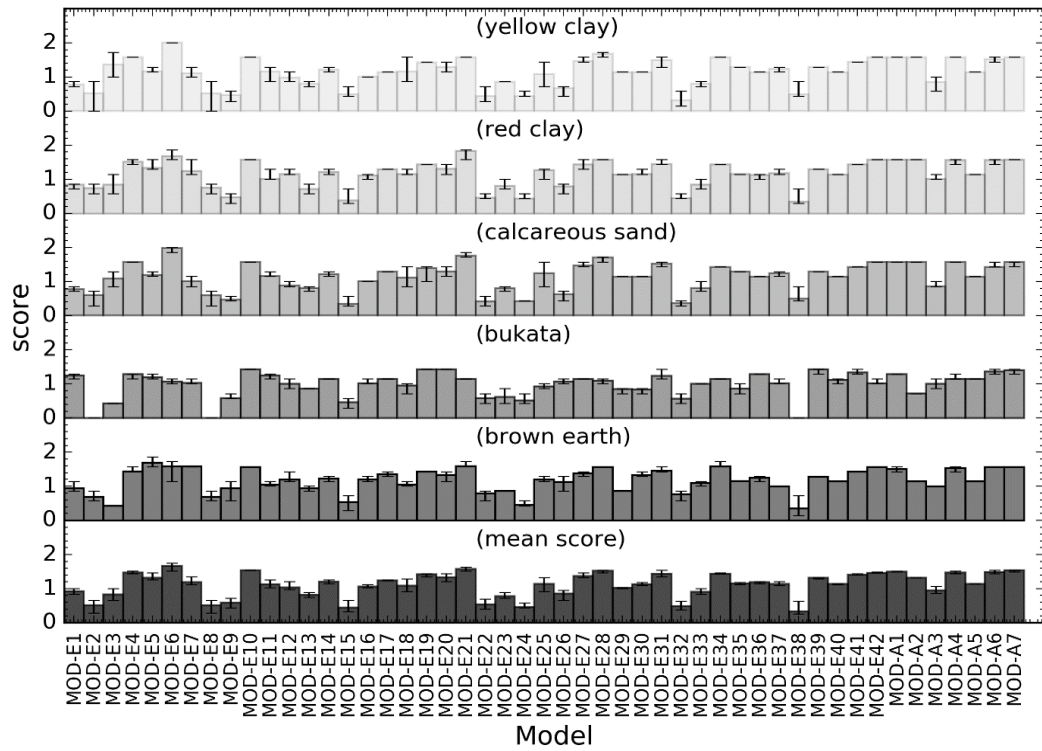


Figure F.3: Total scores for different sediments and the average scores across all five sediments in CLASS-III water.

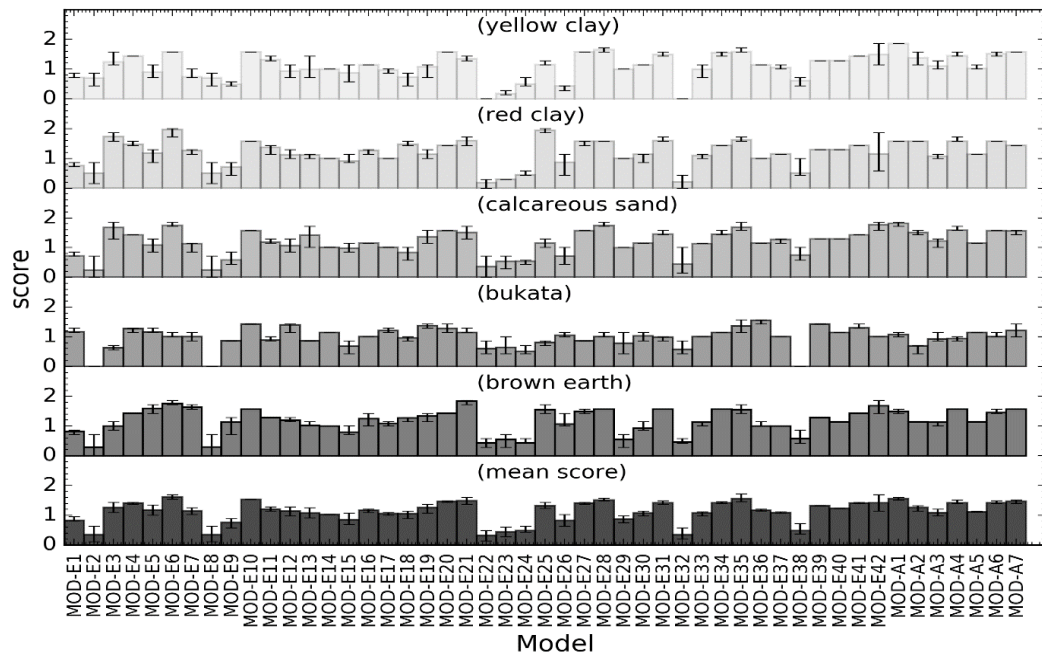


Figure F.4: Total scores for different sediments and the average scores across all five sediments in CLASS-IV water.

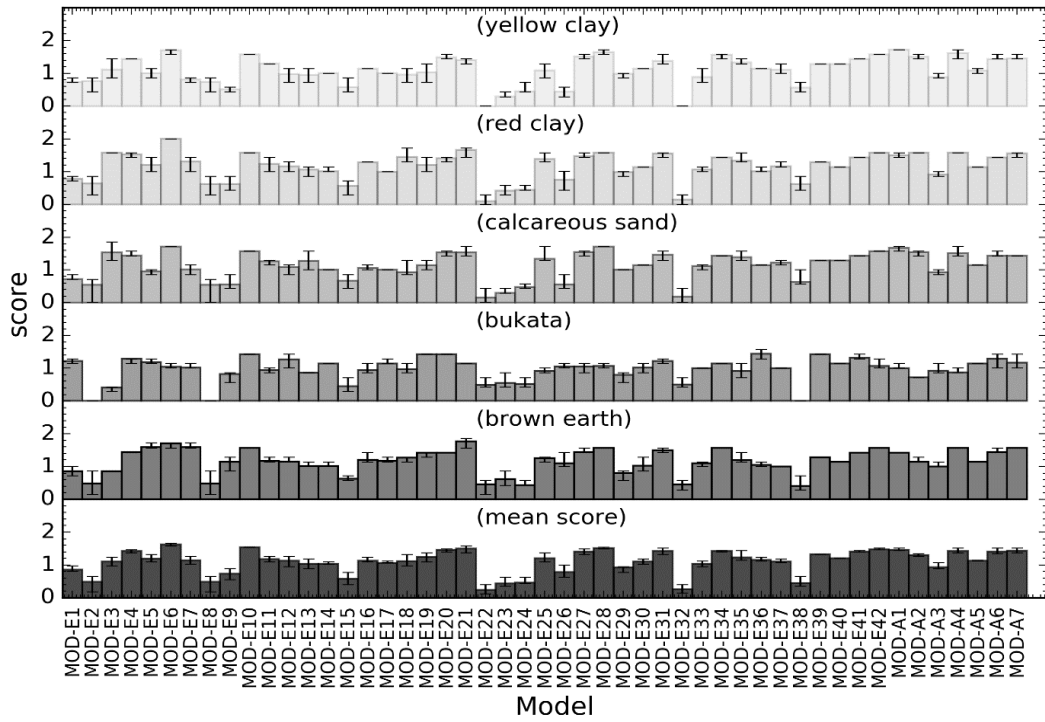


Figure F.5: Total scores for different sediments and the average scores across all five sediments in CLASS-V water.

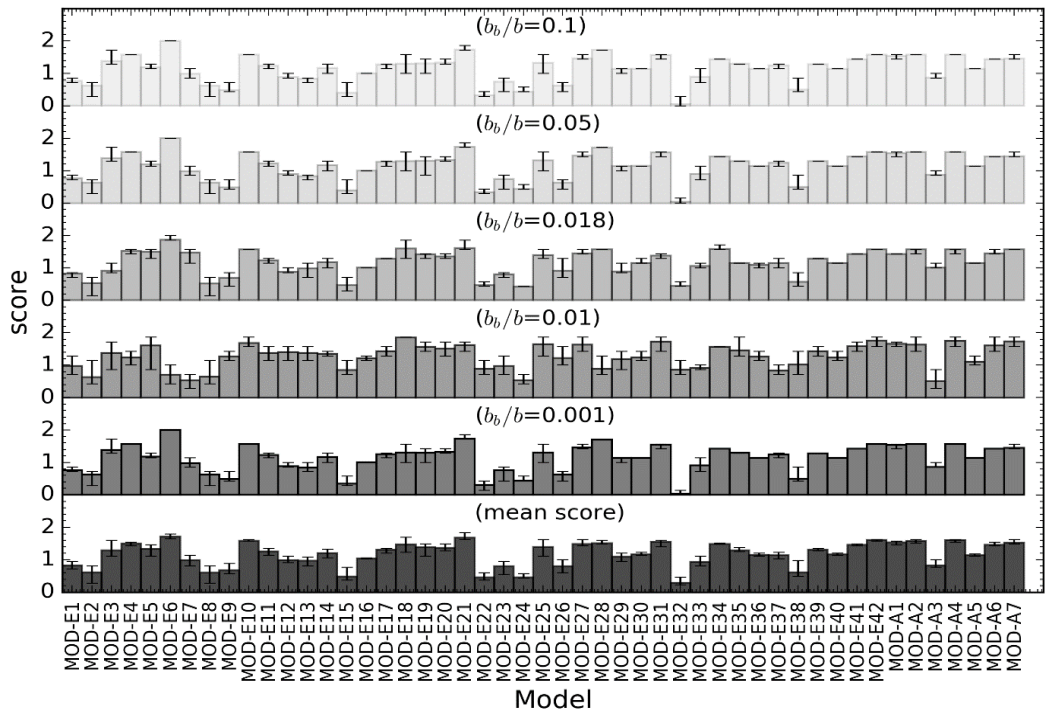


Figure F.6: Total scores for different backscattering ratios and the average scores across all backscattering ratios in CLASS-I water for Calcareous sand.

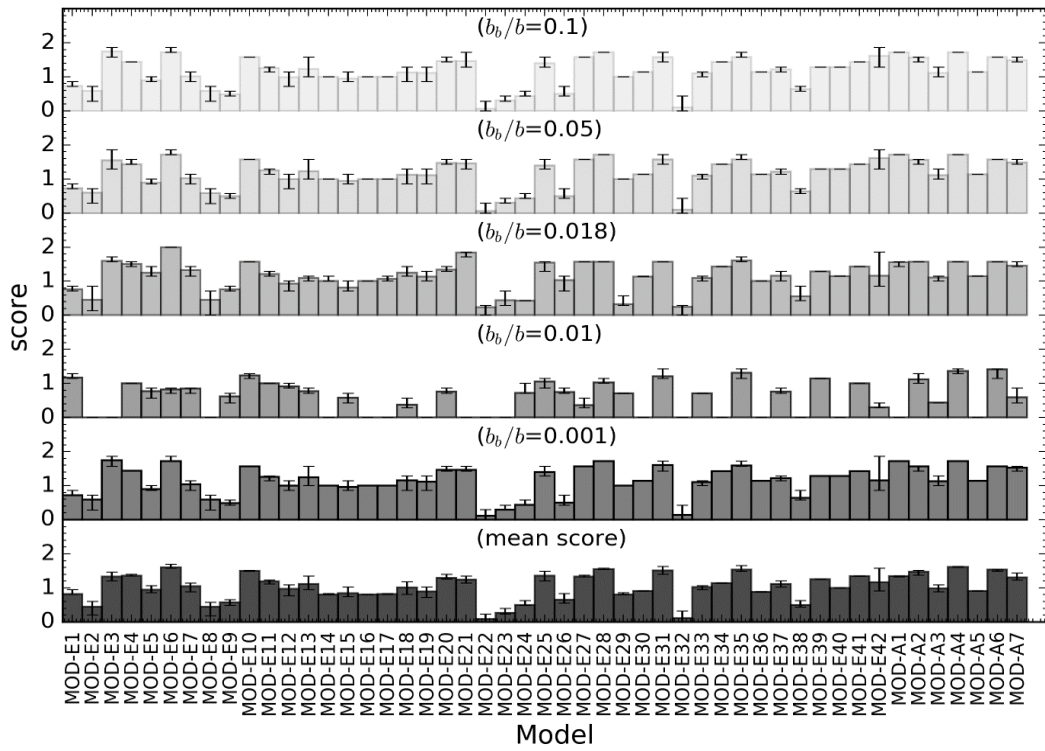


Figure F.7: Total scores for different backscattering ratios and the average scores across all backscattering ratios in CLASS-II water for Calcareous sand.

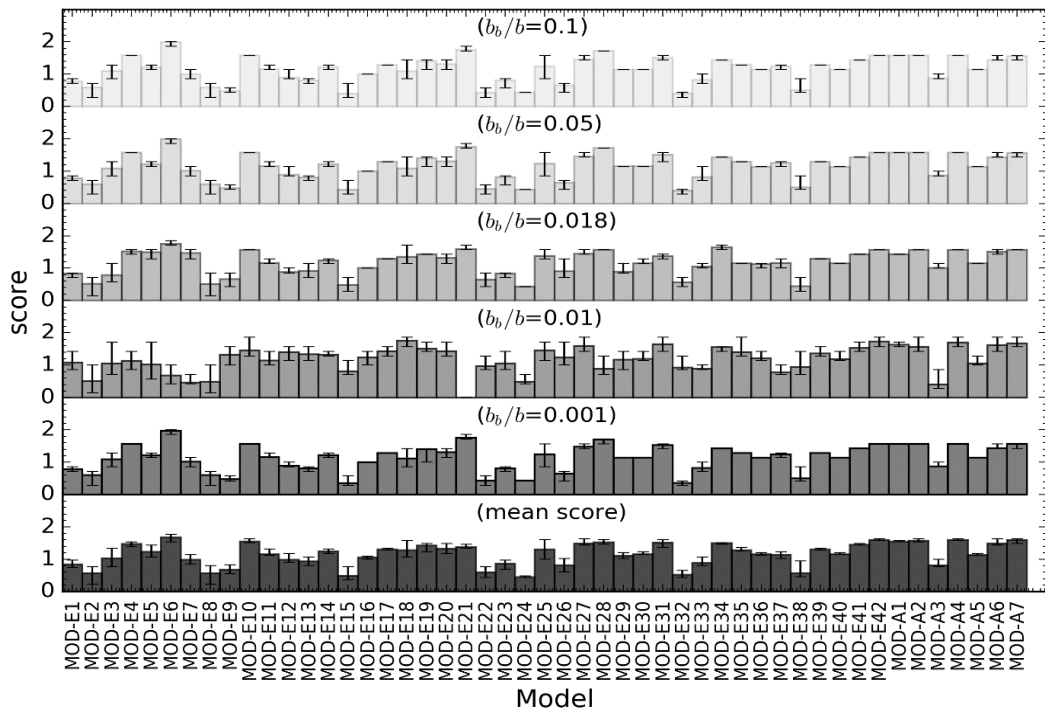


Figure F.8: Total scores for different backscattering ratios and the average scores across all backscattering ratios in CLASS-III water for Calcareous sand.

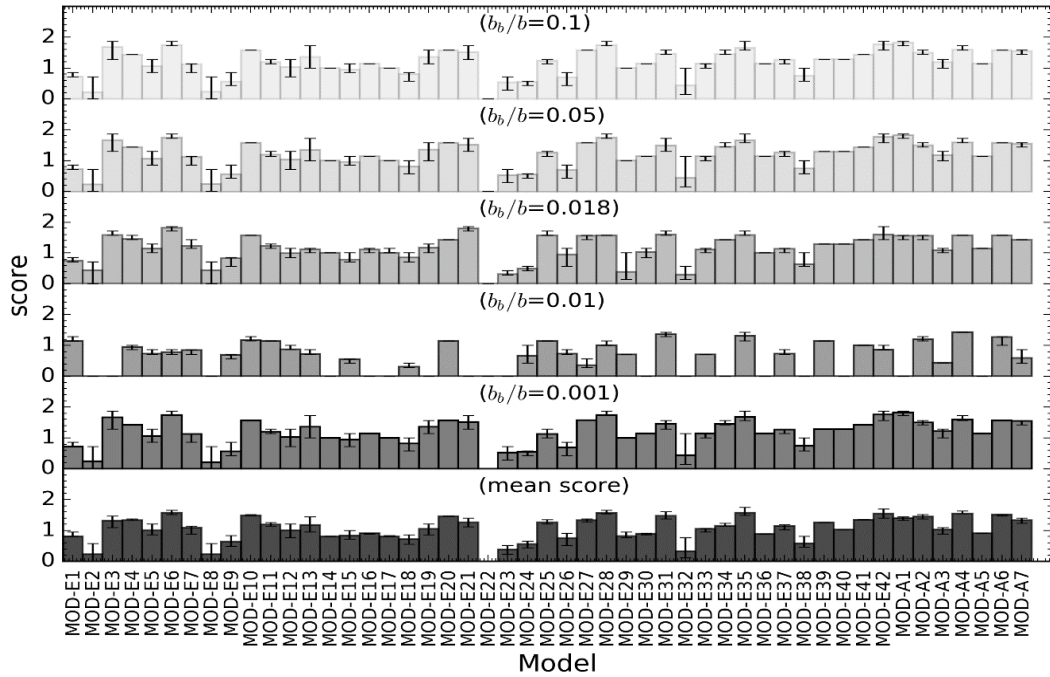


Figure F.9: Total scores for different backscattering ratios and the average scores across all backscattering ratios in CLASS-IV water for Calcareous sand.

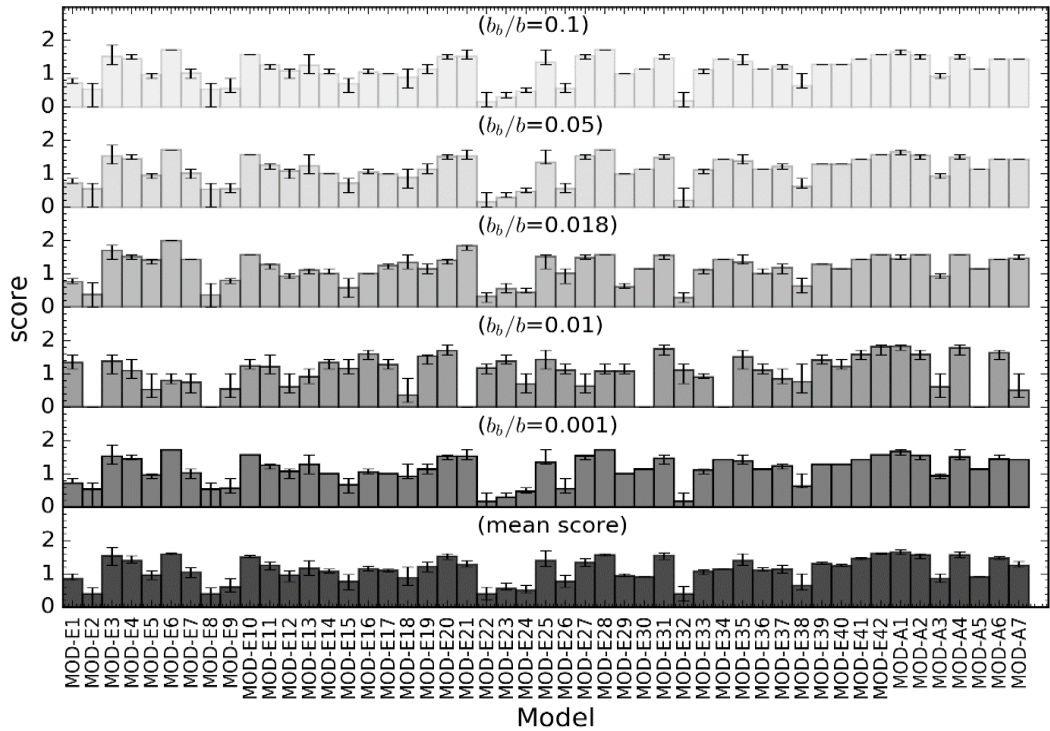


Figure F.10: Total scores for different backscattering ratios and the average scores across all backscattering ratios in CLASS-V water for Calcareous sand.

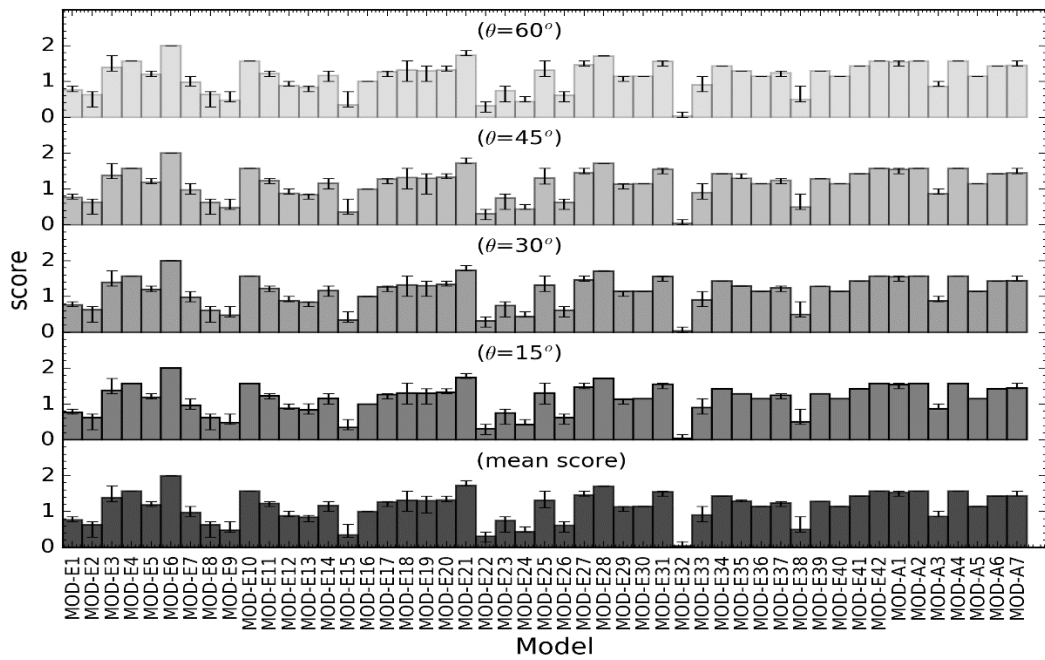


Figure F.11: Total scores for different solar zenith angles and the average scores across all solar zenith angles in CLASS-I water for Calcareous sand.

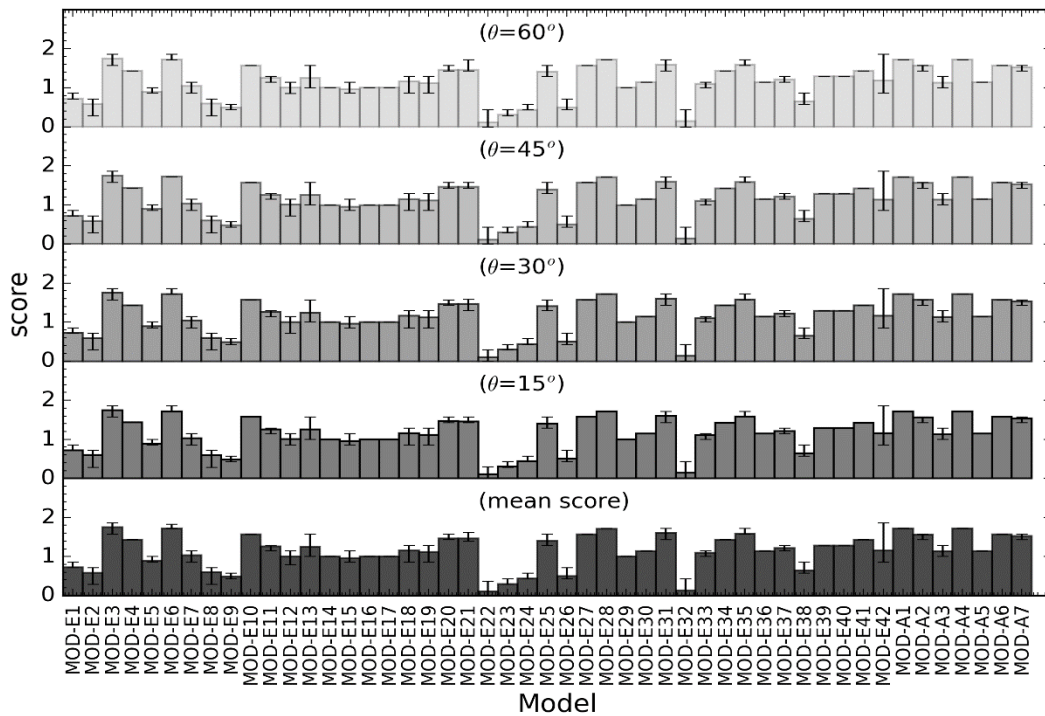


Figure F.12: Total scores for different solar zenith angles and the average scores across all solar zenith angles in CLASS-II water for Calcareous sand.

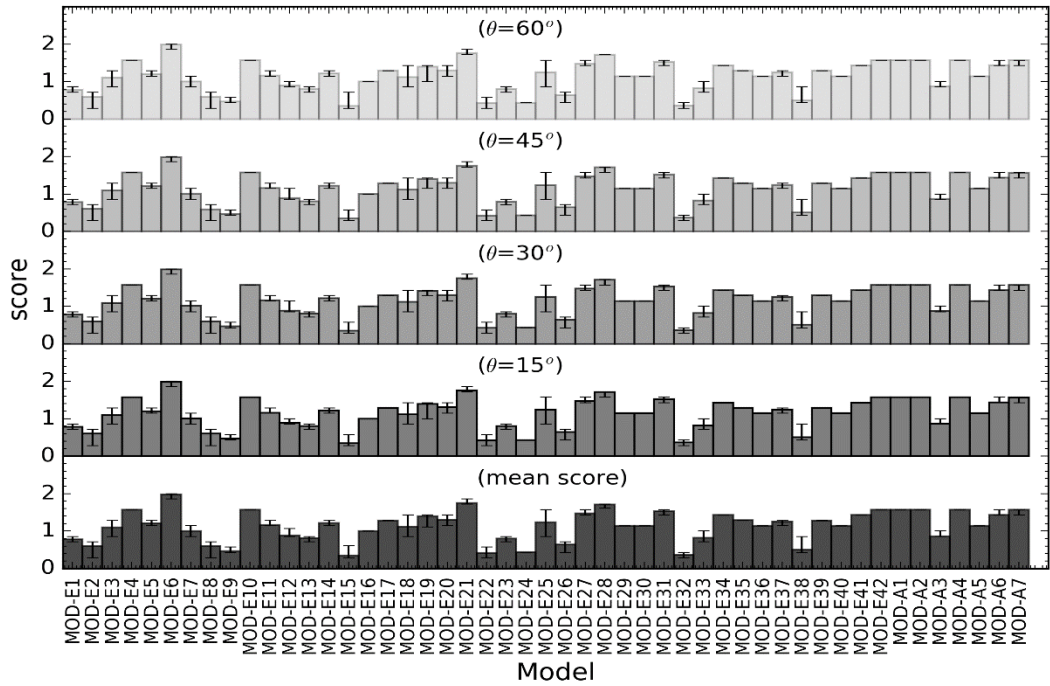


Figure F.13: Total scores for different solar zenith angles and the average scores across all solar zenith angles in CLASS-III water for Calcareous sand.

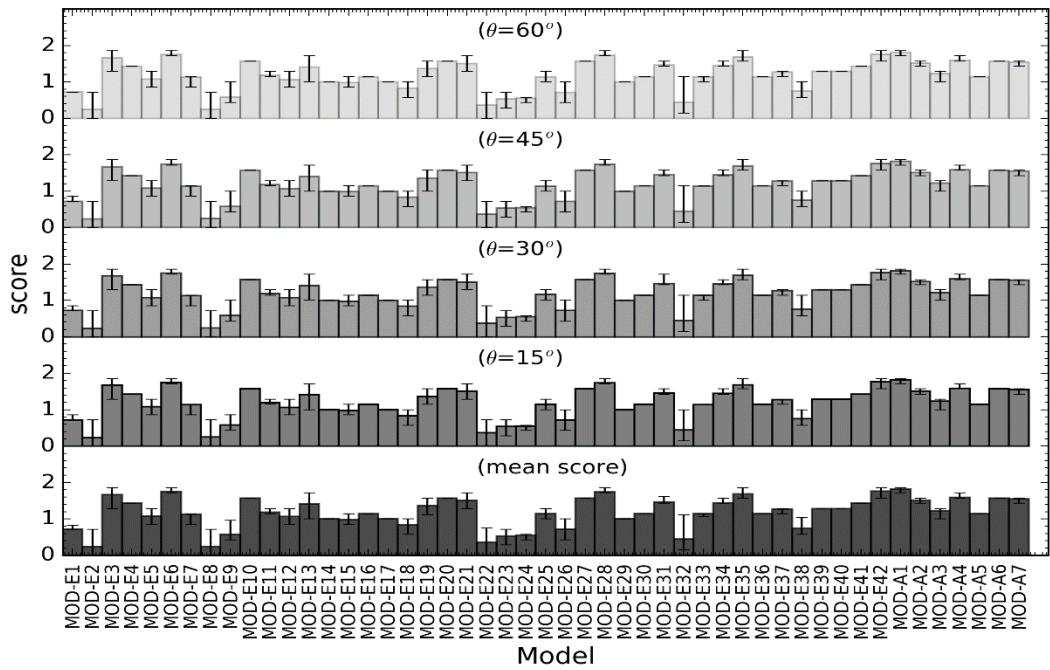


Figure F.14: Total scores for different solar zenith angles and the average scores across all solar zenith angles in CLASS-IV water for Calcareous sand.

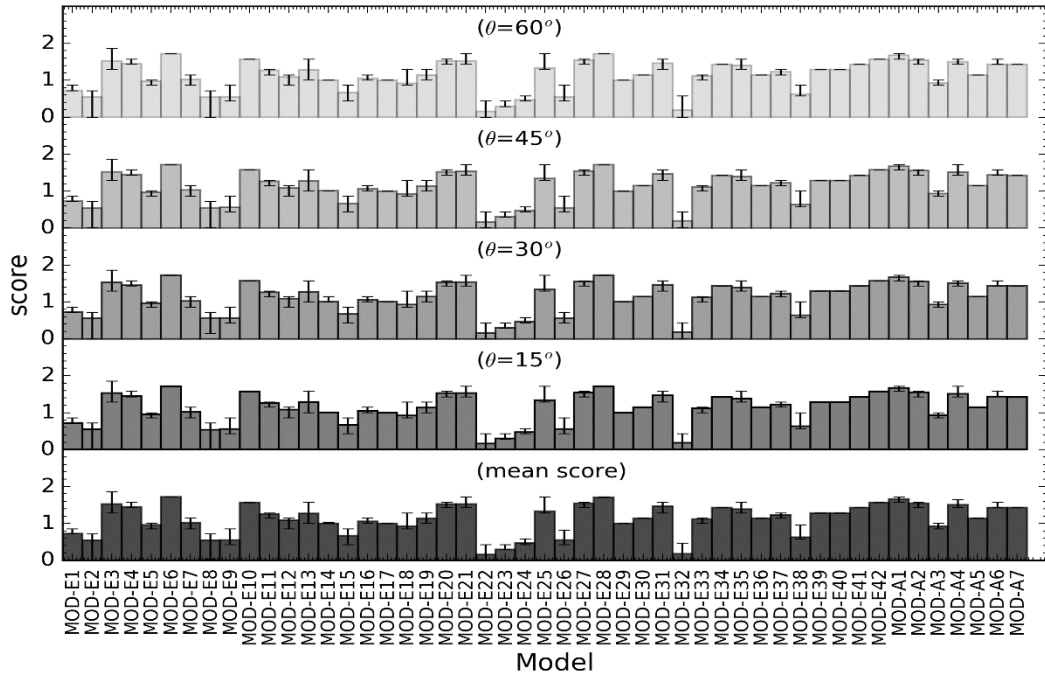


Figure F.15: Total scores for different solar zenith angles and the average scores across all solar zenith angles in CLASS-V water for Calcareous sand.

Landsat TSS Models:

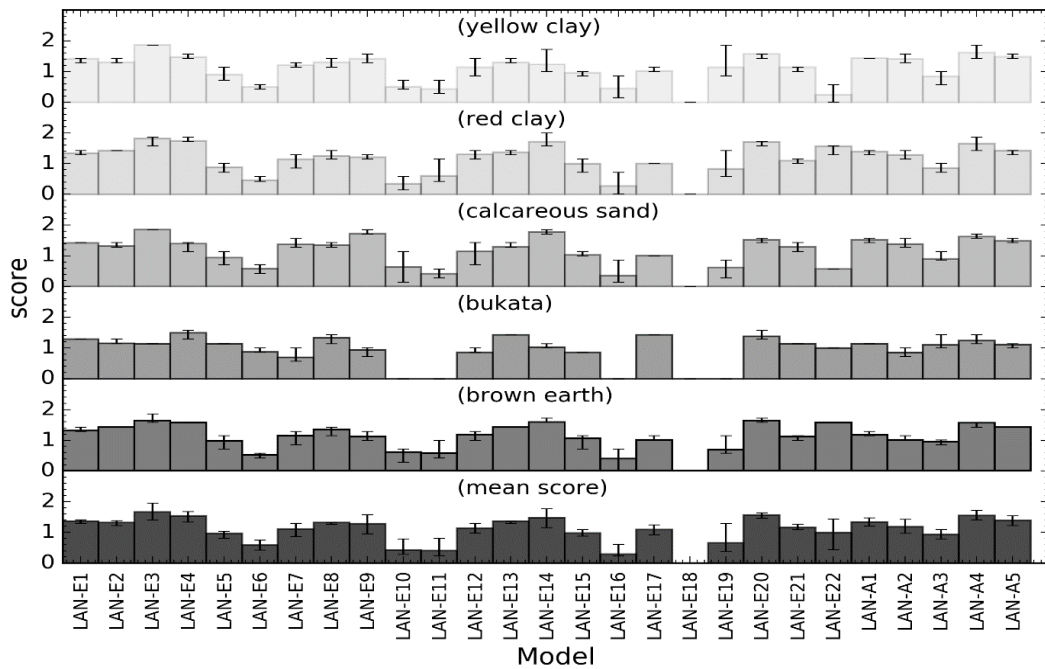


Figure F.16: Total scores for different sediments and the average scores across all five sediments in CLASS-I water.

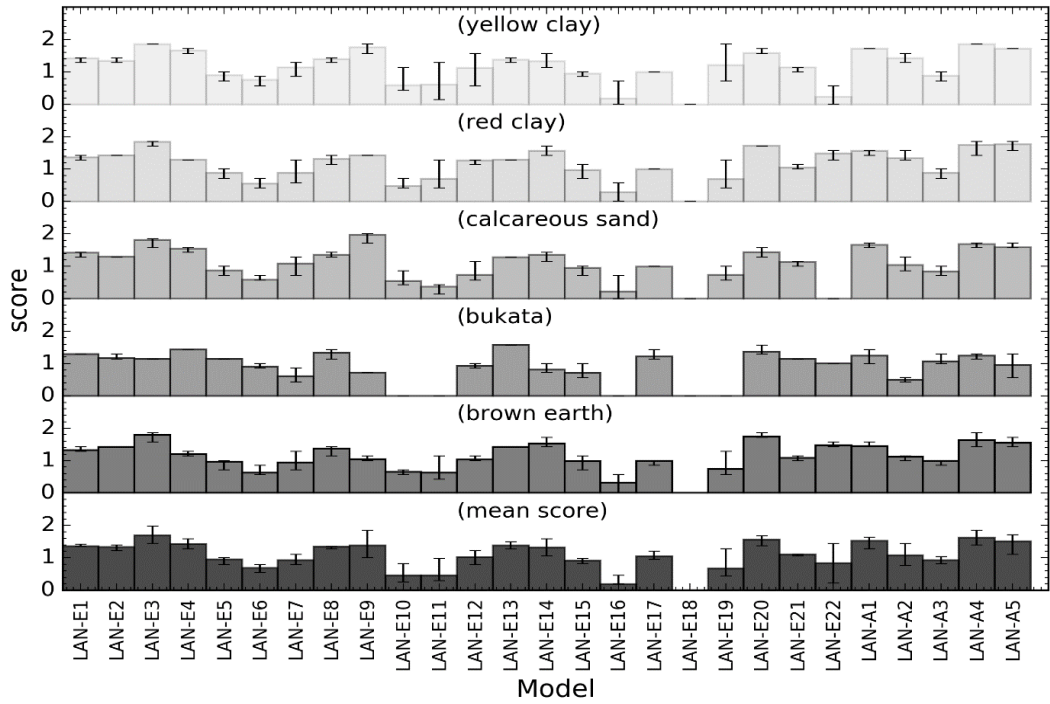


Figure F.17: Total scores for different sediments and the average scores across all five sediments in CLASS-II water.

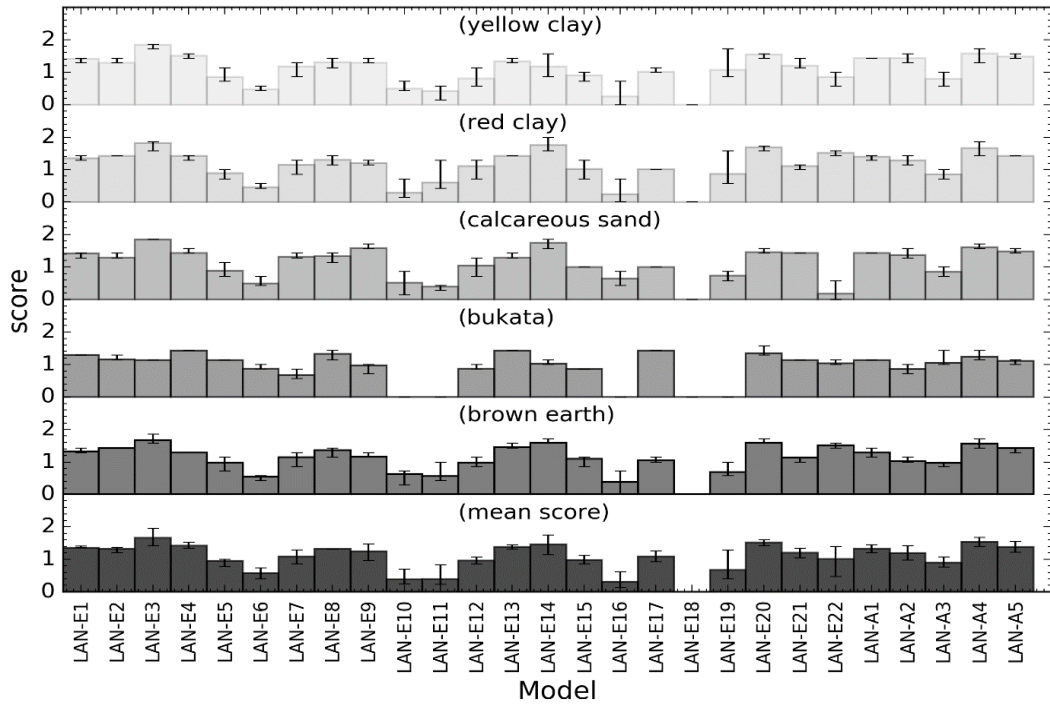


Figure F.18: Total scores for different sediments and the average scores across all five sediments in CLASS-III water.

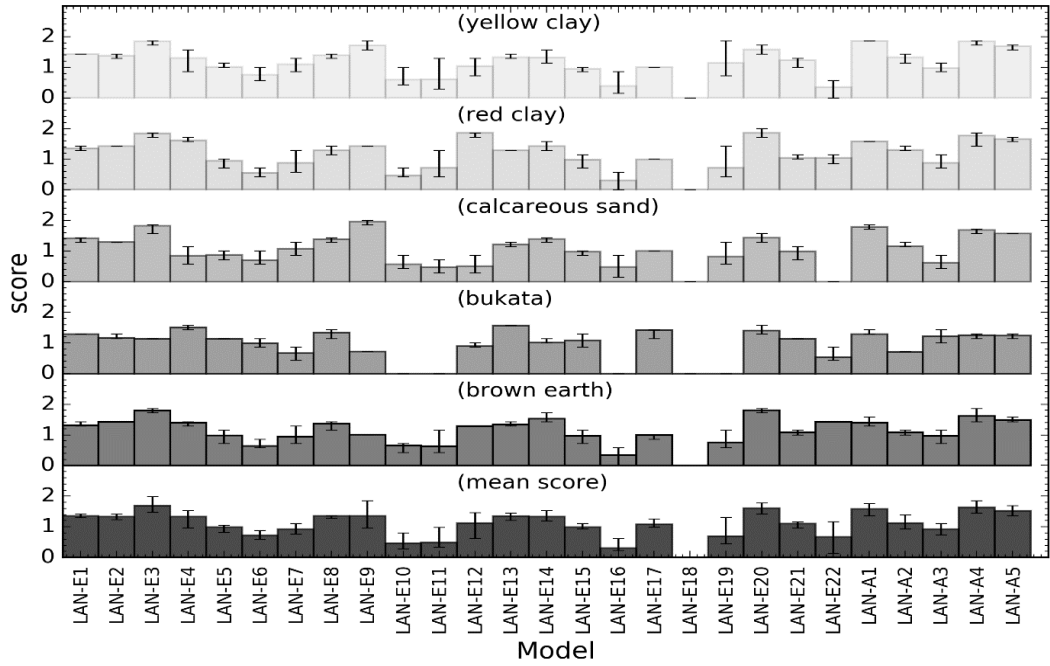


Figure F.19: Total scores for different sediments and the average scores across all five sediments in CLASS-IV water.

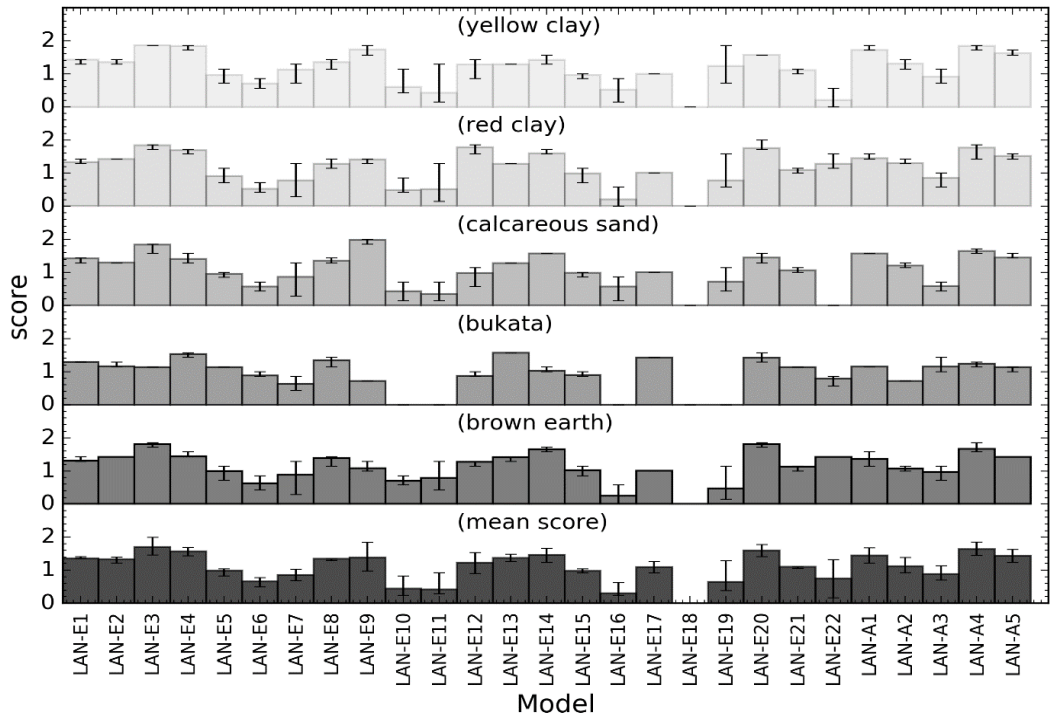


Figure F.20: Total scores for different sediments and the average scores across all five sediments in CLASS-V water.

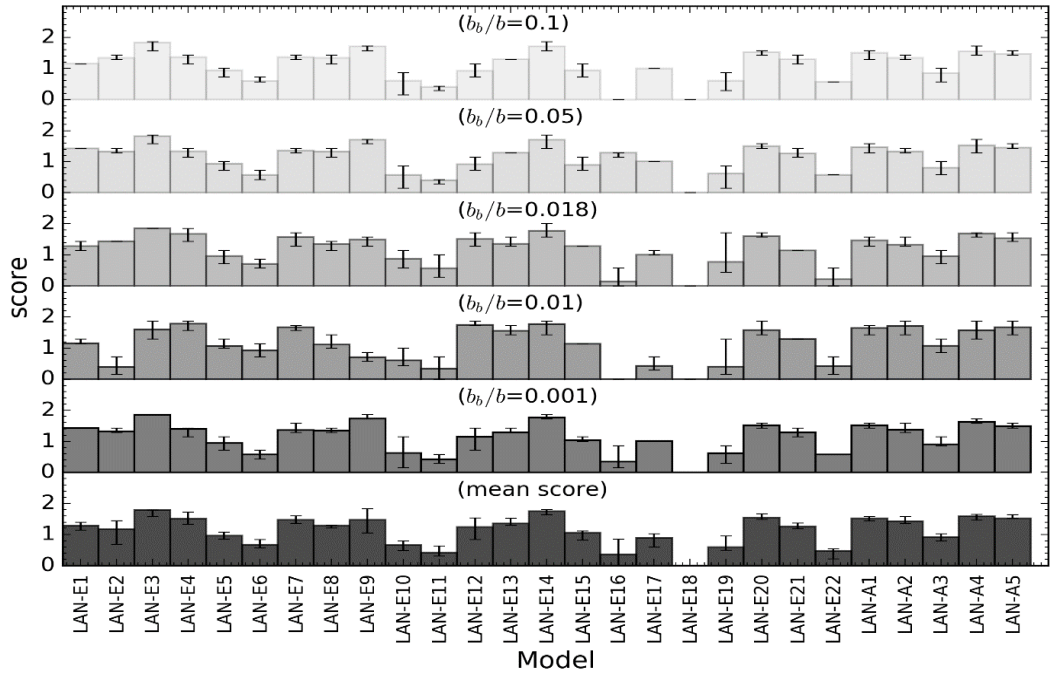


Figure F.21: Total scores for different backscattering ratios and the average scores across all backscattering ratios in CLASS-I water for Calcareous sand.

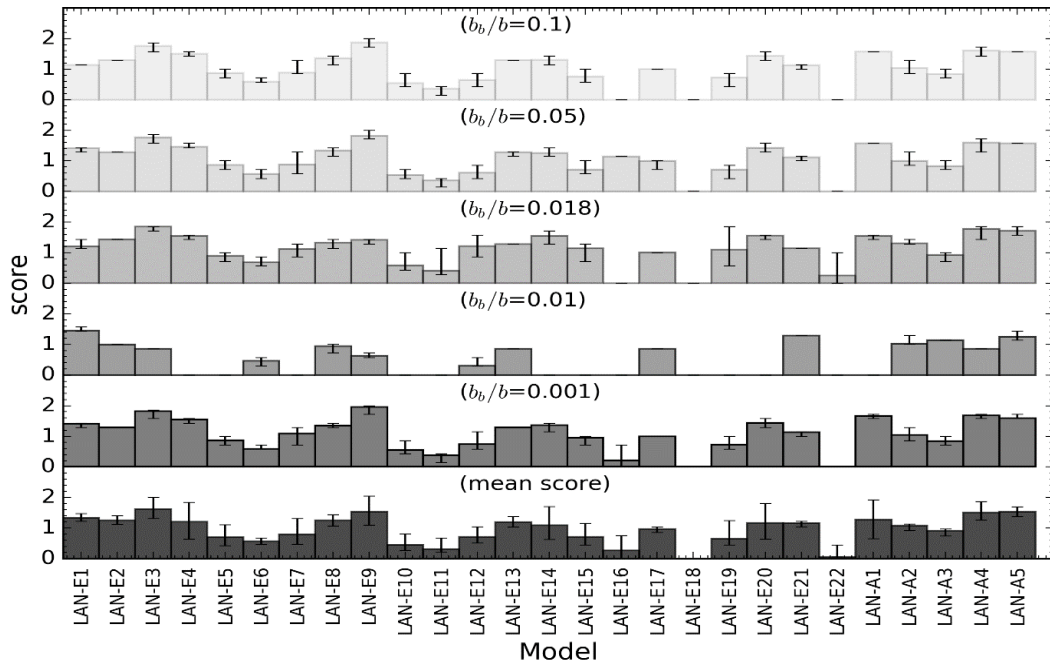


Figure F.22: Total scores for different backscattering ratios and the average scores across all backscattering ratios in CLASS-II water for Calcareous sand.

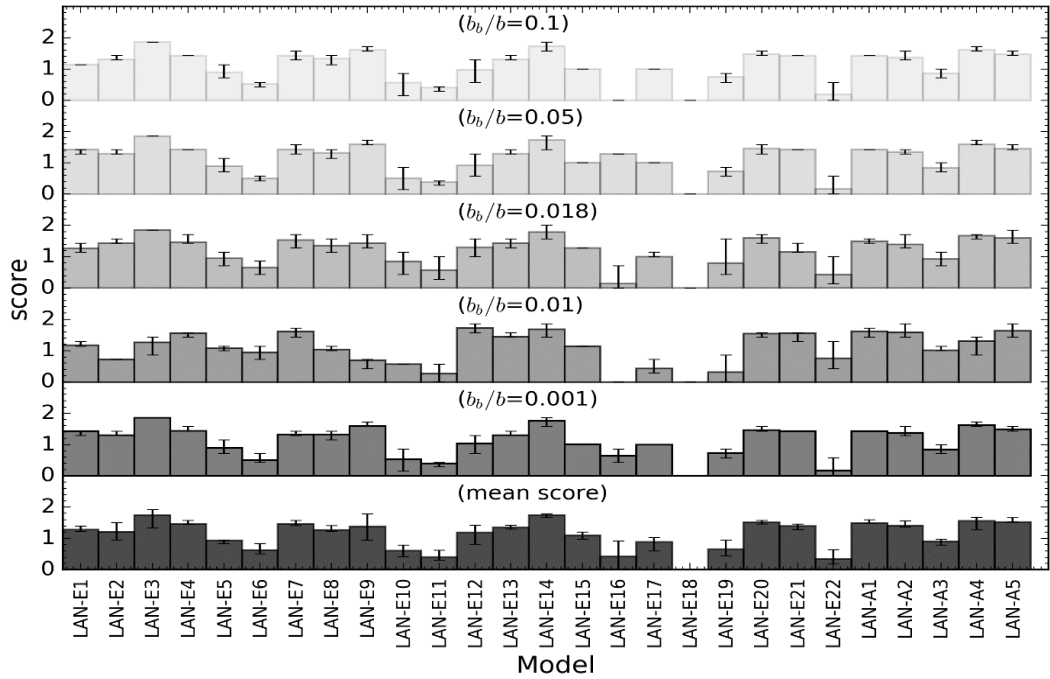


Figure F.23: Total scores for different backscattering ratios and the average scores across all backscattering ratios in CLASS-III water for Calcareous sand.

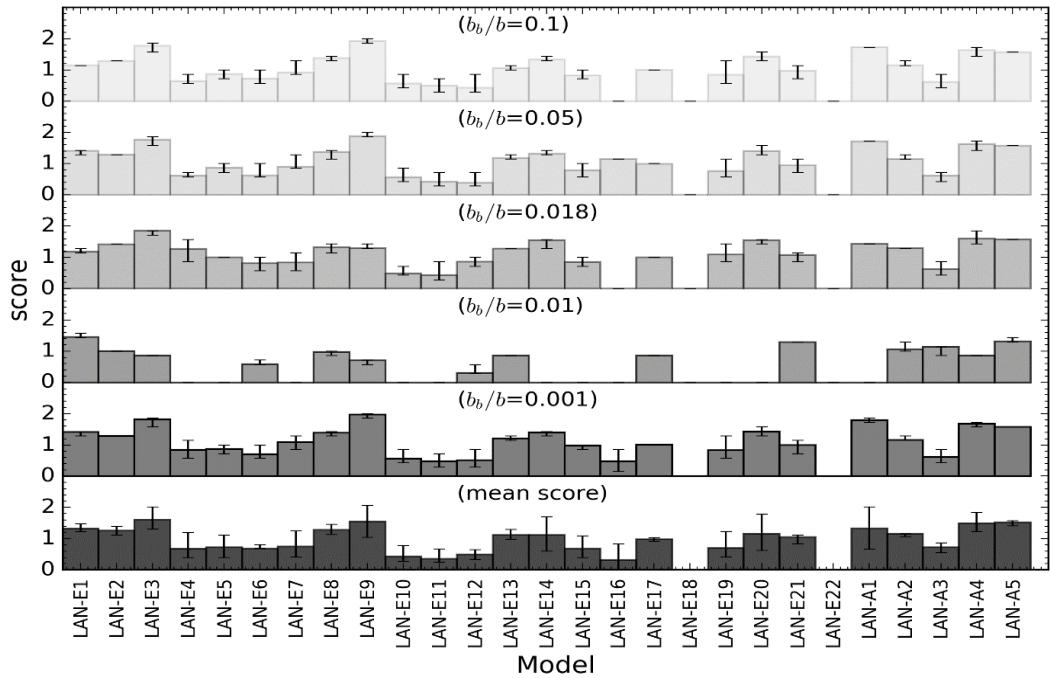


Figure F.24: Total scores for different backscattering ratios and the average scores across all backscattering ratios in CLASS-IV water for Calcareous sand.

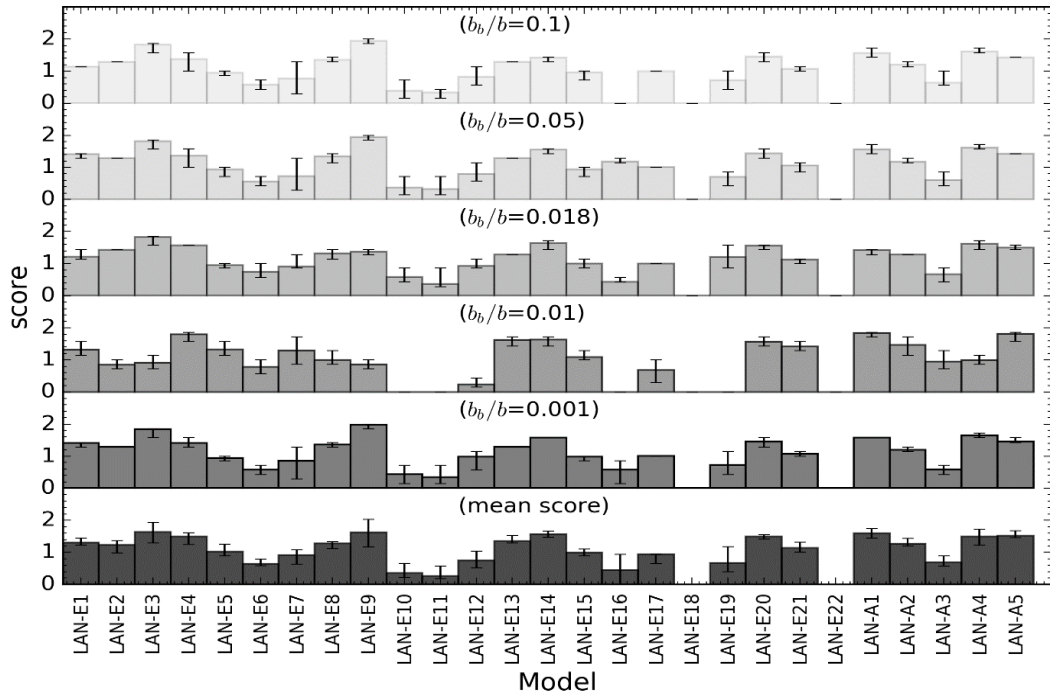


Figure F.25: Total scores for different backscattering ratios and the average scores across all backscattering ratios in CLASS-V water for Calcareous sand.

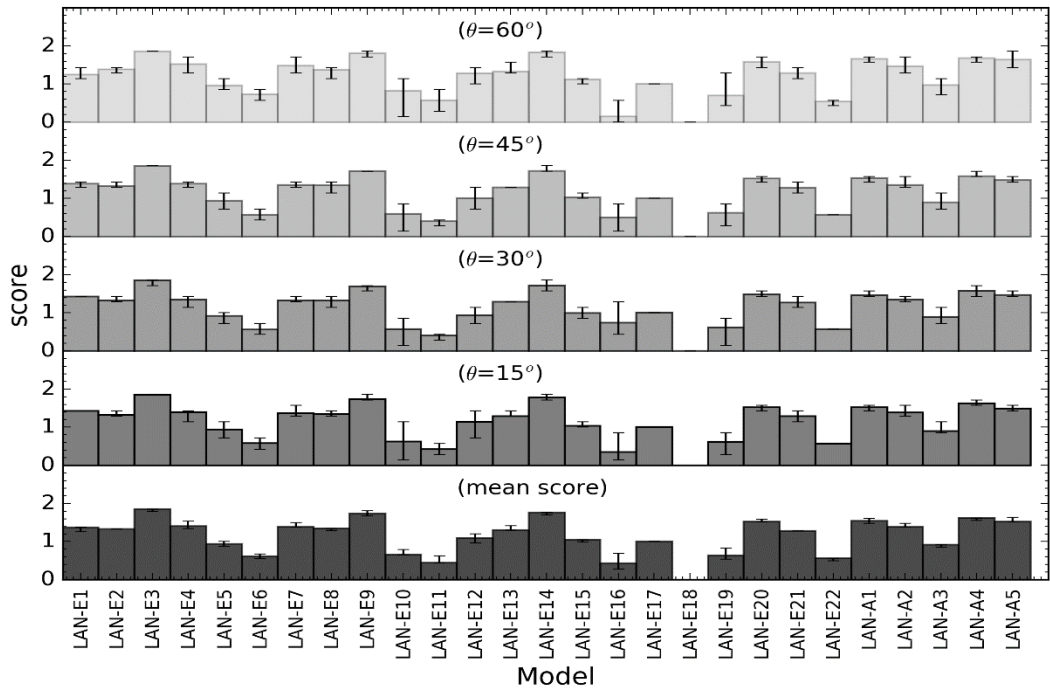


Figure F.26: Total scores for different solar zenith angles and the average scores across all solar zenith angles in CLASS-I water for Calcareous sand.

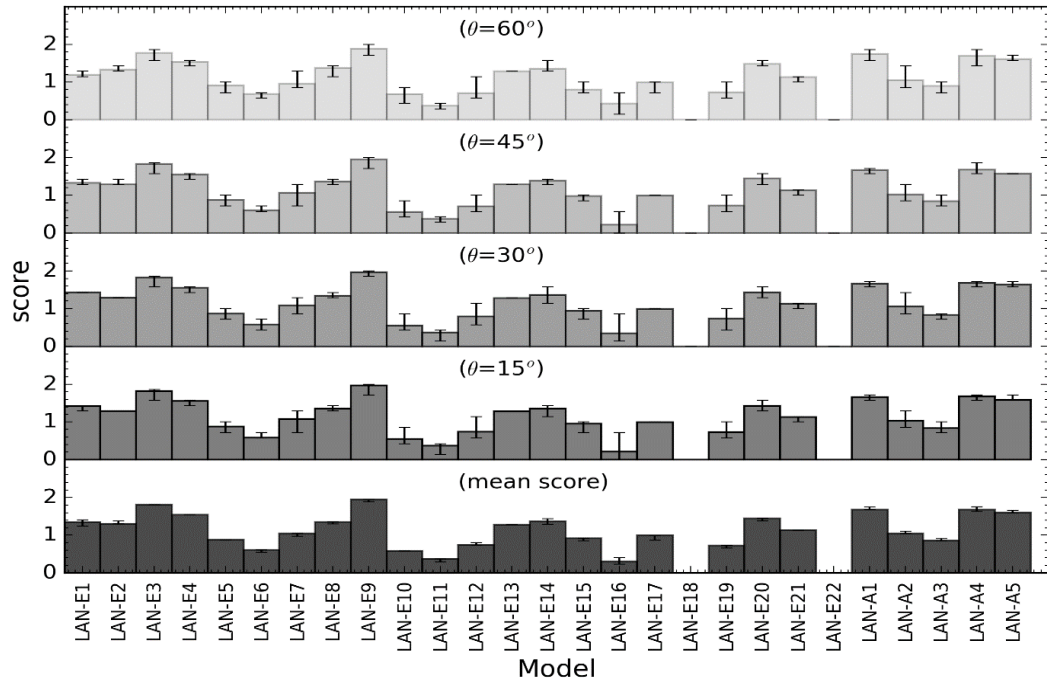


Figure F.27: Total scores for different solar zenith angles and the average scores across all solar zenith angles in CLASS-II water for Calcareous sand.

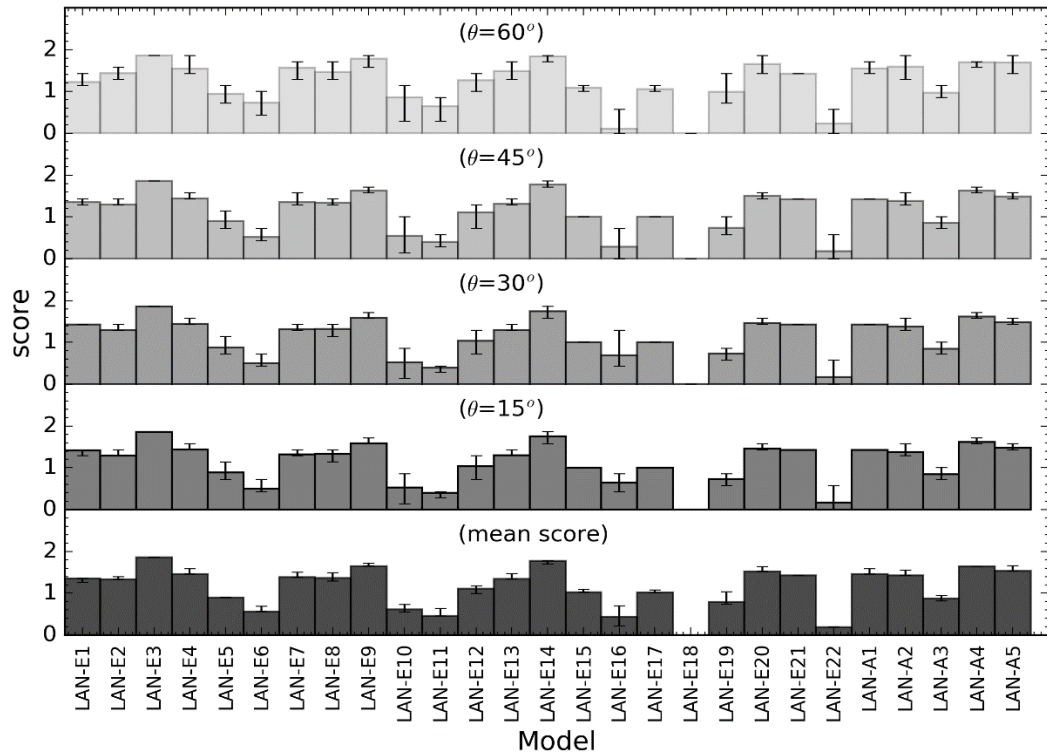


Figure F.28: Total scores for different solar zenith angles and the average scores across all solar zenith angles in CLASS-III water for Calcareous sand.

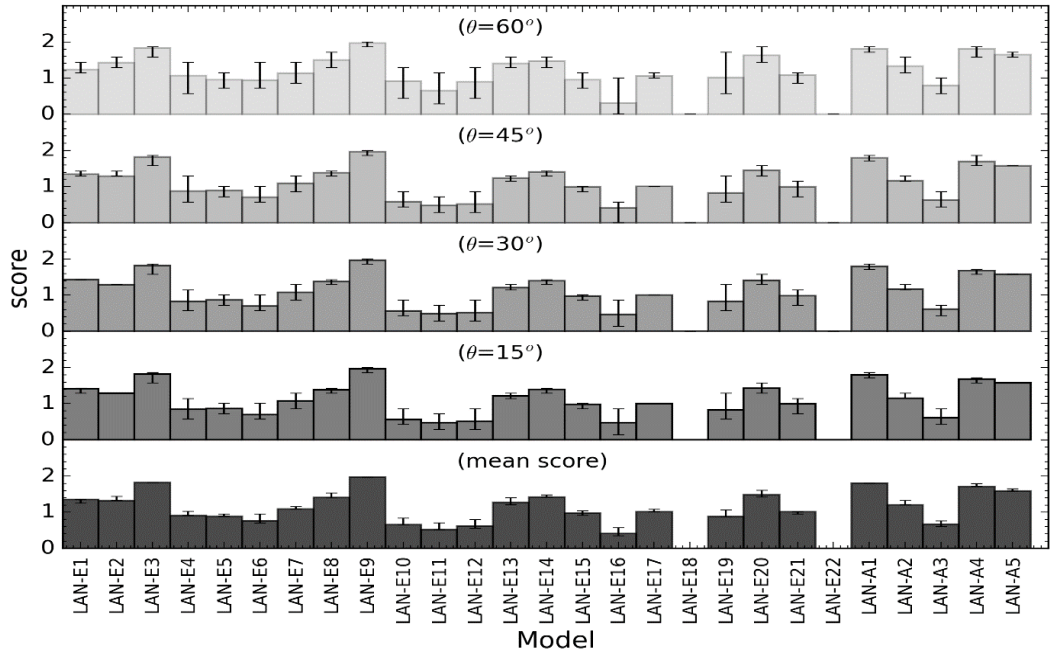


Figure F.29: Total scores for different solar zenith angles and the average scores across all solar zenith angles in CLASS-IV water for Calcareous sand.

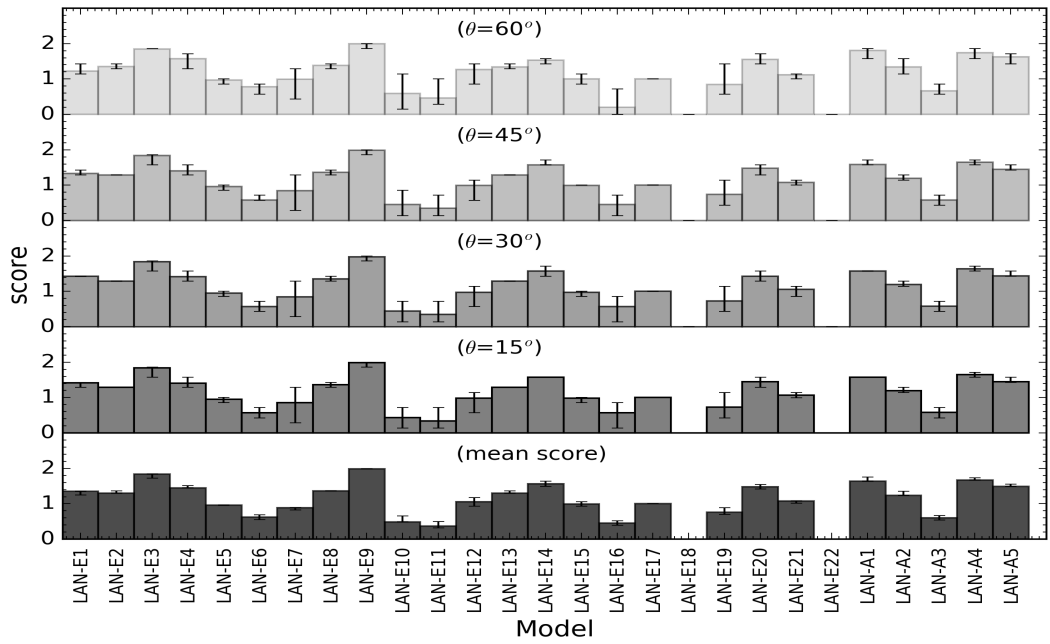
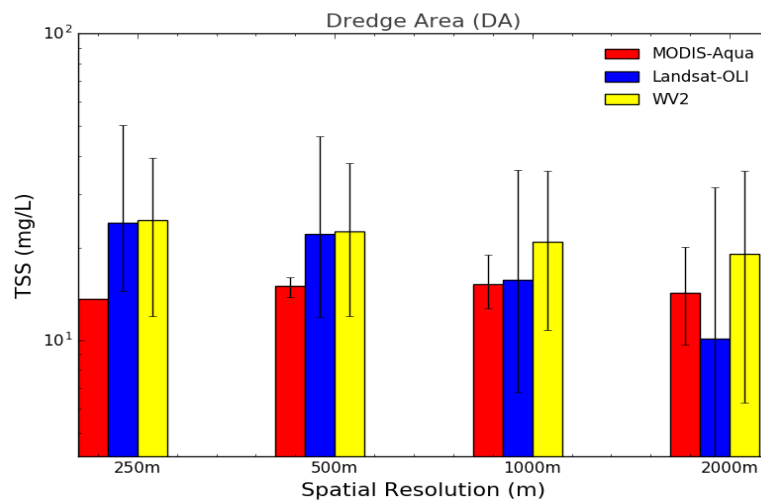


Figure F.30: Total scores for different solar zenith angles and the average scores across all solar zenith angles in CLASS-V water for Calcareous sand.

Appendix G

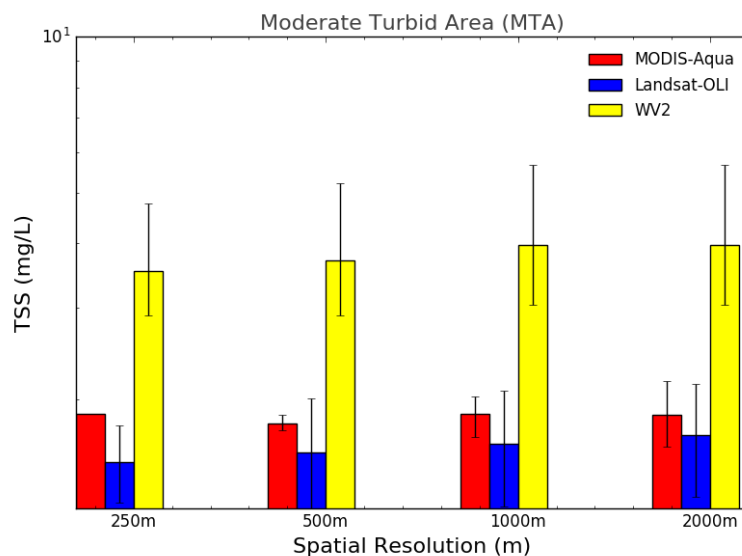
G.1 Inter-Sensor TSS Variability in Dredge, Moderate Turbid, and Clear Area

Figures G1-G3 shows the variability in TSS concentration at 250 m, 500 m, 1000 m, and 2000 m spatial resolutions for MODIS-Aqua, WV2 and Landsat-8 OLI in the DA, MTA and CA respectively. From Figures G1 – G3, we observe that in the MTA and CA (see Figures G2 and G3), TSS concentrations derived by each individual sensor remained similar across different spatial resolutions. In the DA (Figure G1) the MODIS-Aqua derived TSS concentration at 250 m spatial resolution is lower than the Landsat-8 OLI and WV2 sensor, but as the spatial resolution gets coarser all sensors' derived TSS concentrations are similar within the respective error bars. In the turbid region (Figure G1) the MODIS-Aqua sensors displayed little variability as the resolutions were decreased and the spatial extent was increased, but Landsat-OLI and WV2 both displayed a decrease in the mean TSS values. However, Figures G2 and G3 shows that the TSS concentrations derived by the individual sensors were similar across different spatial resolutions, but overall the WV2-derived TSS concentration remained high and Landsat-8 OLI-derived TSS concentration remained low across all spatial resolutions.



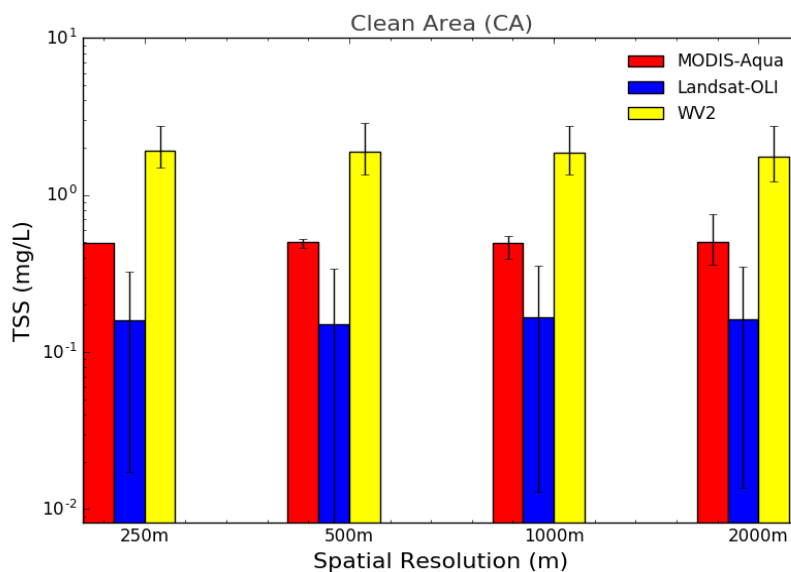
(a)

Figure G.1: TSS concentration variability at different spatial resolutions derived from MODIS-Aqua, WV2 and Landsat-8 OLI for Moderate Turbid Area (MTA).



(b)

Figure G.2: TSS concentration variability at different spatial resolutions derived from MODIS-Aqua, WV2 and Landsat-8 OLI for Moderate Turbid Area (MTA).



(c)

Figure G.3: TSS concentration variability at different spatial resolutions derived from MODIS-Aqua, WV2 and Landsat-8 OLI for Clean Area (CA).

In Figures G1-G3, across different spatial resolution grids (250 m – 2000 m), the DA, MTA and CA region of the study site was quantified to have mean TSS concentration of 12.67 ± 2.15 mg/L, 1.89 ± 0.04 mg/L, and 0.51 ± 0.02 mg/L respectively for MODIS-Aqua sensor. Likewise, for Landsat-8 OLI and WV2 sensors mean TSS concentration in DA, MTA and CA

regions were quantified to be 11.34 ± 6.13 mg/L, 1.61 ± 0.07 mg/L, and 0.16 ± 0.02 mg/L and be $22.04.34 \pm 2.65$ mg/L, 3.85 ± 0.19 mg/L, and 1.84 ± 0.06 mg/L respectively. Further, the range of TSS concentration observed were in CA were 0.70 mg/L to 4.02 mg/L, 0.05 mg/L to 3.2 mg/L, and 0.35 mg/L to 1.9 mg/L for WV2, Landsat-8 OLI and MODIS-Aqua sensors respectively. Likewise, in the turbid regions (DA, SG and RP) the TSS concentrations varied in the ranges of 19.12 mg/L to 41.02 mg/L, 4.06 mg/L to 29.16 mg/L, and 3.77 mg/L to 16.09 mg/L based on WV2, Landsat-8 OLI and MODIS-Aqua sensors respectively. In terms of relative error, MODIS-Aqua, Landsat-8 OLI and WV2 in DA, CA and MTA were 16.96%, 54.09%, and 12.05%, 3.1%, 10.39% and 2.99%, and 2.3%, 4.54% and 4.82% respectively.

Appendix H

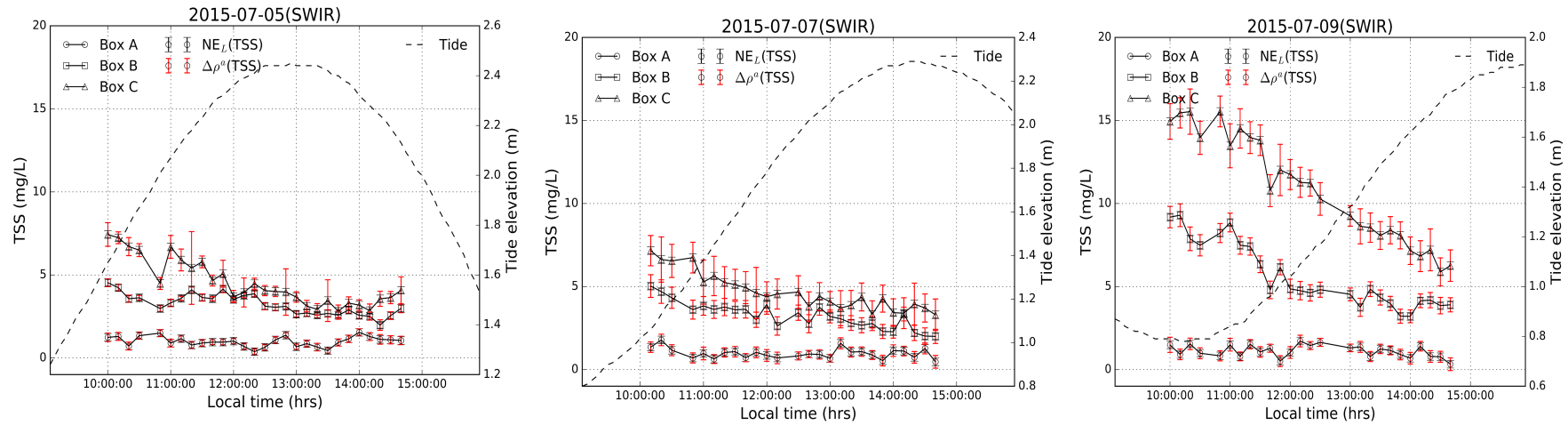


Figure H.1: Daily TSS concentration variability from 10:00 hrs – 15:00 hrs at location, Box A, B and C derived using SWIR atmospheric correction method (Left) July 5th 2015, (Middle) July 7th 2015, and (Right) July 9th 2015. NE_L (TSS) and $\Delta\rho_a$ (TSS) are error derived from AHI sensor noise and aerosol estimation.

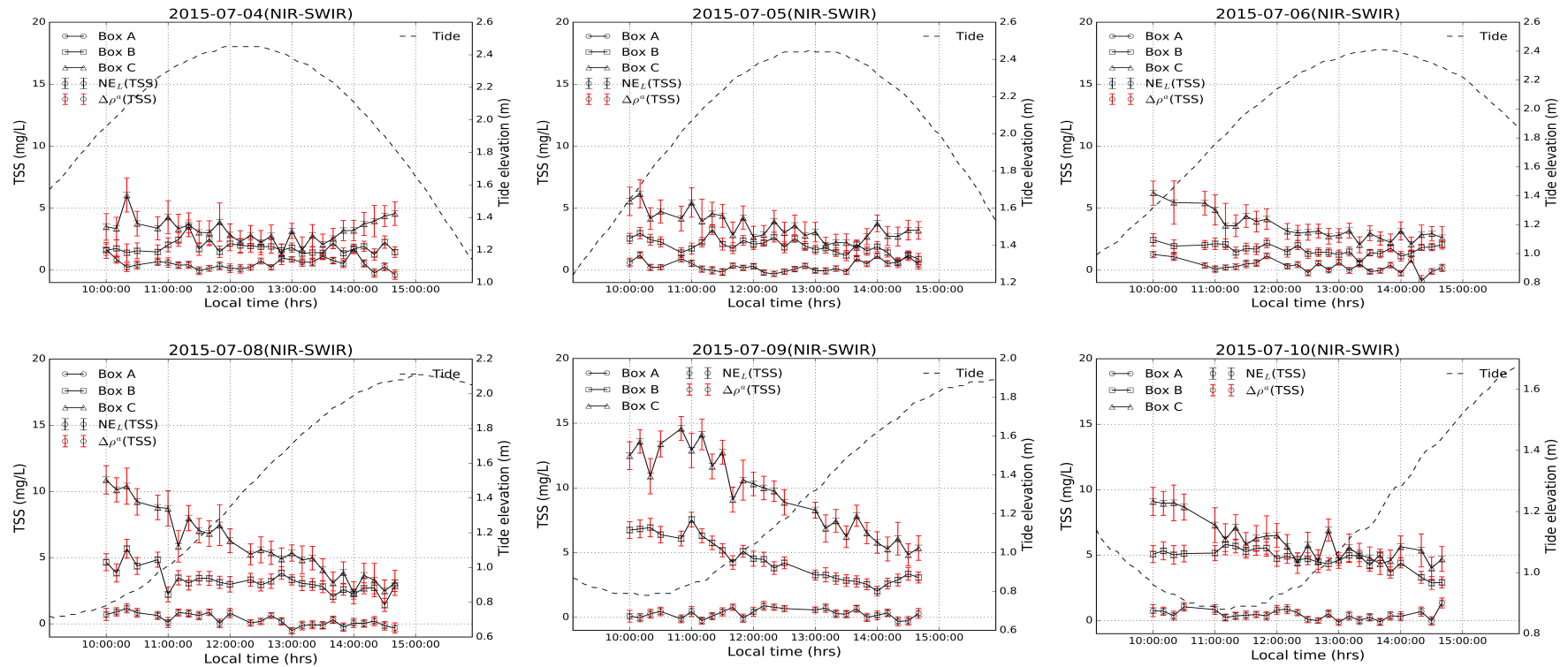


Figure H.2: Daily TSS concentration variability from 10:00 hrs – 15:00 hrs at location, Box A, B and C derived using NIR-SWIR atmospheric correction method (Top Left) July 4th 2015, (Top Middle) July 5th 2015, and (Top Right) July 6th 2015, (Bottom Left) July 8th 2015, (Bottom Middle) July 9th 2015 and (Bottom Right) July 10th 2015. NE_L (TSS) and $\Delta\rho_a$ (TSS) are error derived from AHI sensor noise and aerosol estimation.

Appendix I

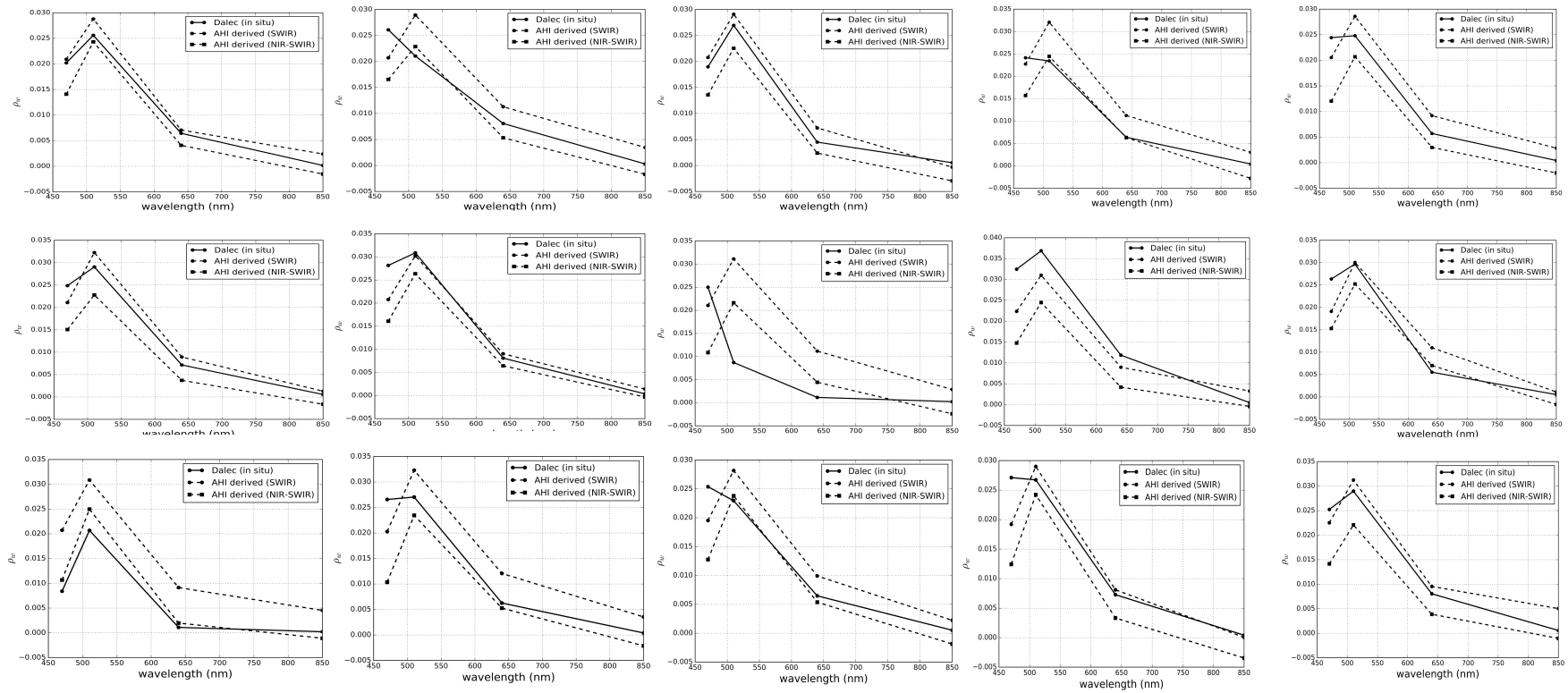


Figure I: Spectral plot of in situ ρ_w of validation data points (Plot from the top-left the every 10th random validation data points).

Appendix J

This Appendix documents the ownership and the author's role in each of the submitted papers together with signed agreement by the co-authors.

I warrant that I have obtained, where necessary, permission from the copyright owners to use any third-party copyright material reproduced in the thesis, or to use any of my own published work in which the copyright is held by another party.

Signed:  Passang Dorji (Candidate)

Signed:  Dr. Peter Rhoderick Fearn (Supervisor)

Statement of Contribution of Others for Chapter 3: “A Semi-Analytic Model for Estimating Total Suspended Sediment Concentration in Turbid Coastal Waters of Northern Western Australia Using MODIS-Aqua 250 m Data”.

31st March 2017

To Whom It May Concern

I, **Dr. Fearn**s, provided an overall project supervision and contributed to the manuscript editing to the publication entitled:

Dorji, P., Fearn, P., & Broomhall, M. (2016). A Semi-Analytic Model for Estimating Total Suspended Sediment Concentration in Turbid Coastal Waters of Northern Western Australia Using MODIS-Aqua 250 m Data. *Remote Sensing*, 8(7), 556.



(Signature of Co-Author)

Dr. Peter Fearns



(Signature of First Author)

Passang Dorji

Statement of Contribution of Others for Chapter 3: "A Semi-Analytic Model for Estimating Total Suspended Sediment Concentration in Turbid Coastal Waters of Northern Western Australia Using MODIS-Aqua 250 m Data".

31st March 2017

To Whom It May Concern

I, **Dr. Broomhall**, helped in *in situ* data collection and contributed to the manuscript editing to the publication entitled:

Dorji, P., Fearn, P., & Broomhall, M. (2016). A Semi-Analytic Model for Estimating Total Suspended Sediment Concentration in Turbid Coastal Waters of Northern Western Australia Using MODIS-Aqua 250 m Data. *Remote Sensing*, 8(7), 556

(Signature of Co-Author)

Dr. Mark Broomhall



(Signature of First Author)

Passang Dorji

Statement of Contribution of Others for Chapter 4: “A Quantitative Comparison of Total Suspended Sediment Algorithms: A Case Study of the Last Decade for MODIS and Landsat-Based Sensors”.

31st March 2017

To Whom It May Concern

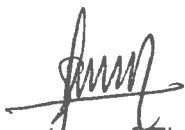
I, **Dr. Fearn**s, provided an overall project supervision and contributed to the manuscript editing to the publication entitled:

Dorji, P., & Fearns, P. (2016). A Quantitative Comparison of Total Suspended Sediment Algorithms: A Case Study of the Last Decade for MODIS and Landsat-Based Sensors. *Remote Sensing*, 8(10), 810.



(Signature of Co-Author)

Dr. Peter Fearns



(Signature of First Author)

Passang Dorji

Statement of Contribution of Others for Chapter 5: "Impact of the Spatial Resolution of Satellite Remote Sensing Sensors in the Quantification of Total Suspended Sediment Concentration".

31st March 2017

To Whom It May Concern

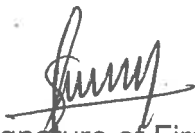
I, **Dr. Fearn**s, provided an overall project supervision and contributed to the manuscript editing to the publication entitled:

Dorji, P., & Fearn, P. (2017). Impact of the Spatial Resolution of Satellite Remote Sensing Sensors in the Quantification of Total Suspended Sediment Concentration: A Case Study in Turbid Waters of northern Western Australia, *PLOS ONE*, 12(4), e0175042.



(Signature of Co-Author)

Dr. Peter Fearns



(Signature of First Author)

Passang Dorji

Statement of Contribution of Others for Chapter 6: “Mapping Total Suspended Sediment in Near Real Time: A Preliminary Assessment of Geostationary Satellite (Himawari-8) in Coastal Waters of Western Australia”.

31st March 2017

To Whom It May Concern

I, **Dr. Fearn**s, provided an overall project supervision and contributed to the manuscript editing to the publication entitled:

Dorji, P., & Fearns, P. (2017). Mapping Total Suspended Sediment in Near Real Time: A Preliminary Assessment of Geostationary Satellite (Himawari-8) in Coastal Waters of Western Australia. *Remote Sensing of Environment, (Submitted)*.



(Signature of Co-Author)

Dr. Peter Fearns



(Signature of First Author)

Passang Dorji

References

- Acker, J. G., Harding, L. W., Leptoukh, G., Zhu, T., & Shen, S. (2005). Remotely-sensed chl a at the Chesapeake Bay mouth is correlated with annual freshwater flow to Chesapeake Bay. *Geophysical Research Letters*, 32(5), L05601.
- Aggarwal, S. (2004). Principles of remote sensing. In M. V. K. Sivakumarn, P. S. Roy, K. Harmsen & S. K. Saha (Eds.), *Satellite remote sensing and GIS applications in agricultural meteorology* (ed., pp. 23-28). Geneva: World Meteorological Organization.
- Alashloo, M. M., Lim, H.-S., Asadpour, R., & Safarpour, S. (2013). Total Suspended Sediments Mapping by Using ALOS Imagery Over the Coastal Waters of Langkawi Island, Malaysia. *Journal of the Indian Society of Remote Sensing*, 41(3), 663-673.
- Albert, A., & Mobley, C. D. (2003). An analytical model for subsurface irradiance and remote sensing reflectance in deep and shallow case-2 waters. *Optics Express*, 11(22), 2873-2890.
- Alikas, K., & Reinart, A. (2008). Validation of the MERIS products on large European lakes: Peipsi, Vänern and Vättern. *Hydrobiologia*, 599(1), 161-168.
- Alparslan, E., Aydoğan, C., Tufekci, V., & Tufekci, H. (2007). Water quality assessment at Ömerli Dam using remote sensing techniques. *Environmental Monitoring and Assessment*, 135(1-3), 391-398.
- Arrigo, K. R., & McClain, C. R. (1994). Spring Phytoplankton Production in Western Ross Sea. *Science*, 266, 261-263.
- Arst, H. (2003). *Optical properties and remote sensing of multicomponental water bodies* Chichester, UK: Praxis Publishing Ltd.
- Asadpour, R., Lim, H. S., Alashoo, M. M., & Mousavi, S. Y. (2012). A statistical model for mapping spatial distribution of total suspended solid from THEOS satellite imagery over Penang Island, Malaysia. *Journal of Applied Sciences Research*, 8(1), 271-276.
- Australia, P. (2014). *Dredging and Australian Ports: Subtropical and Tropical Ports*. Sydney: P. Australia. Retrieved from <http://www.portsaustralia.com.au/assets/Publications/Dredge-Report-Low-Res.pdf>
- Ayana, E. K., Worqlul, A. W., & Steenhuis, T. S. (2015). Evaluation of stream water quality data generated from MODIS images in modeling total

suspended solid emission to a freshwater lake. *Science of The Total Environment*, 523, 170-177.

- Babin, M., Morel, A., Fournier-Sicre, V., Fell, F., & Stramski, D. (2003a). Light scattering properties of marine particles in coastal and open ocean waters as related to the particle mass concentration. *Limnology and Oceanography*, 48(2), 843-859.
- Babin, M., Stramski, D., Giovanni M, F., Claustre, H., Bricaud, A., Obolensky, G., & Hoepffner, N. (2003b). Variations in the light absorption coefficient of phytoplankton, nonalgal particles, and dissolved organic matter in coastal waters around Europe. *Journal of Geophysical Research*, 108(C7), 3211.
- Bartram, J., & Ballance, R. (1996). *Water Quality Water Quality Monitoring-A Practical Guide to the Design and Implementation of Freshwater Quality Studies and Monitoring Programmes* (pp. 22): United Nations Environment Programme and the World Health Organization.
- Binding, C. E., Bowers, D. G., & Mitchelson-Jacob, E. G. (2003). An algorithm for the retrieval of suspended sediment concentrations in the Irish Sea from SeaWiFS ocean colour satellite imagery. *International Journal of Remote Sensing*, 24(19), 3791-3806.
- Binding, C. E., Bowers, D. G., & Mitchelson-Jacob, E. G. (2005). Estimating suspended sediment concentrations from ocean colour measurements in moderately turbid waters; the impact of variable particle scattering properties. *Remote Sensing of Environment*, 94(3), 373-383.
- Bissett, W. P., Patch, J. S., Carder, K. L., & Lee, Z. P. (1997). Pigment packaging and Chl a-specific absorption in high-light oceanic waters. *Limnology and Oceanography*, 42(5), 961-968.
- Boss, E., Pegau, W. S., Zaneveld, J. R. V., & Barnard, A. H. (2001). Spatial and temporal variability of absorption by dissolved material at a continental shelf. *Journal of Geophysical Research: Oceans*, 106(C5), 9499-9507.
- Bowker, D. E., Fleischer, P., Gosink, T. A., Hanna, W. J., & Ludwich, J. (1973). Correlation of ERTS multispectral imagery with suspended matter and chlorophyll in lower Chesapeake Bay. *Significant Results Obtained from ERTS-1, held in Greenbelt, Maryland, March 5-9: NASA Goddard S.F.C.*

- Brando, V., Lovell, J., King, E., Boadle, D., Scott, R., & Schroeder, T. (2016). The Potential of Autonomous Ship-Borne Hyperspectral Radiometers for the Validation of Ocean Color Radiometry Data. *Remote Sensing*, 8(2), 150.
- Brando, V. E., & Dekker, A. G. (2003). Satellite hyperspectral remote sensing for estimating estuarine and coastal water quality. *Geoscience and Remote Sensing, IEEE Transactions on*, 41(6), 1378-1387.
- Brewin, R. J. W., Sathyendranath, S., Müller, D., Brockmann, C., Deschamps, P.-Y., Devred, E., . . . White luj, G. N. (2015). The Ocean Colour Climate Change Initiative: III. A round-robin comparison on in-water bio-optical algorithms. *Remote Sensing of Environment*, 162, 271-294.
- Brezonik, P., Menken, K. D., & Bauer, M. (2005). Landsat-based Remote Sensing of Lake Water Quality Characteristics, Including Chlorophyll and Colored Dissolved Organic Matter (CDOM). *Lake and Reservoir Management*, 21(4), 373-382.
- Bricaud, A., Morel, A., & Prieur, L. (1981). Absorption by dissolved organic matter of the sea (yellow substance) in the UV and visible domains1. *Limnology and Oceanography*, 26(1), 43-53.
- Bukata, R. P. (2005). Applications of water quality products to environmental monitoring *Satellite Monitoring of Inland and Coastal Water Quality*: CRC Press. <http://dx.doi.org/10.1201/9781420037616.ch4>
- Bureau of Meteorology. (2015a). Climate Statistics for Australian Location. Retrieved from http://www.bom.gov.au/climate/averages/tables/cw_005094.shtml
- Bureau of Meteorology. (2015b). Daily Rainfall *Onslow Airport*. Retrieved from http://www.bom.gov.au/jsp/ncc/cdio/weatherData/av?p_nccObsCode=136&p_display_type=dailyDataFile&p_startYear=2013&p_c=-5258470&p_stn_num=005017
- Bureau of Meteorology. (2015c). Severe Tropical Cyclone Rusty. Retrieved from <http://www.bom.gov.au/announcements/sevwx/wa/watc20130222.shtml>

- Burenko, V. I., Ershova, S. V., kopelevich, O. V., Sheberstov, S. V., & Shevchenko, V. P. (2001). An estimate of the distribution of suspended matter in Barents Sea waters on the basis of the SeaWiFS satellite ocean color scanner. *Oceanology*, 41, 622-628.
- Cai, L., Tang, D., Levy, G., & Liu, D. (2015a). Remote sensing of the impacts of construction in coastal waters on suspended particulate matter concentration – the case of the Yangtze River delta, China. *International Journal of Remote Sensing*, 1-16.
- Cai, L., Tang, D., & Li, C. (2015b). An investigation of spatial variation of suspended sediment concentration induced by a bay bridge based on Landsat TM and OLI data. *Advances in Space Research*, 56(2), 293-303.
- Carder, K. L., Hawes, S. K., Baker, K. A., Smith, R. C., Steward, R. G., & Mitchell, B. G. (1991). Reflectance model for quantifying chlorophyll a in the presence of productivity degradation products. *Journal of Geophysical Research: Oceans*, 96(C11), 20599-20611.
- CARSOCRO, & National Research Council. (2011). *Assessing Requirements for Sustained Ocean Color Research and Operations*: National Academies Press.
- Chang, N.-B., Imen, S., & Vannah, B. (2015). Remote Sensing for Monitoring Surface Water Quality Status and Ecosystem State in Relation to the Nutrient Cycle: A 40-Year Perspective. *Critical Reviews in Environmental Science and Technology*, 45(2), 101-166.
- Chavez, F. P., Buck, K. R., Bidigare, R. R., Karl, D. M., Hebel, D., Latasa, M., . . . Newton, J. (1995). On the chlorophyll a retention properties of glass-fiber GF/F filters. *Limnology and Oceanography*, 40(2), 428-433.
- Chen, J., Cui, T., Qiu, Z., & Lin, C. (2014a). A three-band semi-analytical model for deriving total suspended sediment concentration from HJ-1A/CCD data in turbid coastal waters. *ISPRS Journal of Photogrammetry and Remote Sensing*, 93(0), 1-13.
- Chen, J., Cui, T., Tang, J., & Song, Q. (2014b). Remote sensing of diffuse attenuation coefficient using MODIS imagery of turbid coastal waters: A case study in Bohai Sea. *Remote Sensing of Environment*, 140(0), 78-93.
- Chen, J., Cui, T. W., Qiu, Z. F., & Lin, C. S. (2013a). A semi-analytical total suspended sediment retrieval model in turbid coastal waters: A case

- study in Changjiang River Estuary. *Optics Express*, 21(11), 13018-13031.
- Chen, J., D'Sa, E., Cui, T., & Zhang, X. (2013b). A semi-analytical total suspended sediment retrieval model in turbid coastal waters: A case study in Changjiang River Estuary. *Optics Express*, 21(11), 13018-13031.
- Chen, J., Lee, Z., Hu, C., & Wei, J. (2016). Improving satellite data products for open oceans with a scheme to correct the residual errors in remote sensing reflectance. *Journal of Geophysical Research: Oceans*, 121(6), 3866-3886.
- Chen, J., Tingwei, C., Zhongfeng, Q., & Changsong, L. (2014c). A Split-Window Model for Deriving Total Suspended Sediment Matter From MODIS Data in the Bohai Sea. *Selected Topics in Applied Earth Observations and Remote Sensing, IEEE Journal of*, 7(6), 2611-2618.
- Chen, J., Zhang, M., Cui, T., & Wen, Z. (2013c). A Review of Some Important Technical Problems in Respect of Satellite Remote Sensing of Chlorophyll-a Concentration in Coastal Waters. *IEEE Journal of Selected Topics in Applied Earth Observations and Remote Sensing*, 6(5), 2275-2289.
- Chen, S., Han, L., Chen, X., Li, D., Sun, L., & Li, Y. (2015a). Estimating wide range Total Suspended Solids concentrations from MODIS 250-m imageries: An improved method. *ISPRS Journal of Photogrammetry and Remote Sensing*, 99, 58-69.
- Chen, S., Huang, W., Chen, W., & Chen, X. (2011a). An enhanced MODIS remote sensing model for detecting rainfall effects on sediment plume in the coastal waters of Apalachicola Bay. *Marine Environmental Research*, 72(5), 265-272.
- Chen, S., Huang, W., Chen, W., & Wang, H. (2011b). Remote sensing analysis of rainstorm effects on sediment concentrations in Apalachicola Bay, USA. *Ecological Informatics*, 6(2), 147-155.
- Chen, S., Huang, W., Wang, H., & Li, D. (2009). Remote sensing assessment of sediment re-suspension during Hurricane Frances in Apalachicola Bay, USA. *Remote Sensing of Environment*, 113(12), 2670-2681.
- Chen, X., Han, X., & Feng, L. (2015b). Towards a practical remote-sensing model of suspended sediment concentrations in turbid waters using

- MERIS measurements. *International Journal of Remote Sensing*, 36(15), 3875-3889.
- Chen, X., Lu, J., Cui, T., Jiang, W., Tian, L., Chen, L., & Zhao, W. (2010). Coupling remote sensing retrieval with numerical simulation for SPM study—Taking Bohai Sea in China as a case. *International Journal of Applied Earth Observation and Geoinformation*, 12, Supplement 2, S203-S211.
- Chen, Z., Hu, C., & Muller-Karger, F. (2007). Monitoring turbidity in Tampa Bay using MODIS/Aqua 250-m imagery. *Remote Sensing of Environment*, 109(2), 207-220.
- Chevron. (2014). *Dredging and dredge spil placement environmental monitoring and management plan* (WSO-000-HES-RPT-CVX-000-00086-000). C. A. P. Ld.
- Choi, J.-K., Park, Y. J., Lee, B. R., Eom, J., Moon, J.-E., & Ryu, J.-H. (2014). Application of the Geostationary Ocean Color Imager (GOCI) to mapping the temporal dynamics of coastal water turbidity. *Remote Sensing of Environment*, 146, 24-35.
- Chu, V. W., Smith, L. C., Rennermalm, A. K., Forster, R. R., Box, J. E., & Reeh, N. (2009). Sediment plume response to surface melting and supraglacial lake drainages on the Greenland ice sheet. *Journal of Glaciology*, 55(194), 1072-1082.
- Constantin, S., Doxaran, D., & Constantinescu, Ș. (2016). Estimation of water turbidity and analysis of its spatio-temporal variability in the Danube River plume (Black Sea) using MODIS satellite data. *Continental Shelf Research*, 112, 14-30.
- Cui, L., Qiu, Y., Fei, T., Liu, Y., & Wu, G. (2013). Using remotely sensed suspended sediment concentration variation to improve management of Poyang Lake, China. *Lake and Reservoir Management*, 29(1), 47-60.
- Curran, P. J., & Novo, E. M. M. (1988). The Relationship Between Suspended Sediment Concentration and Remotely Sensed Spectral Radiance: A Review. *Journal of Coastal Research*, 4(3), 351-368.
- Dekker, A. G., Vos, R. J., & Peters, S. W. M. (2001). Comparison of remote sensing data, model results and in situ data for total suspended matter (TSM) in the southern Frisian lakes. *Science of The Total Environment*, 268(1-3), 197-214.

- Dekker, A. G., Vos, R. J., & Peters, S. W. M. (2002). Analytical algorithms for lake water TSM estimation for retrospective analyses of TM and SPOT sensor data. *International Journal of Remote Sensing*, 23(1), 15-35.
- Department of Environment, W., Heritage and the Arts,. (2007). *A Characterisation of Marine Environment of the North-west Marine Region, In Reports of A summary of an expert workshop convened in Perth, Western Australia, 5-6 September 2007*. Retrieved from <https://www.environment.gov.au/system/files/resources/b1760d66-98f5-414f-9abf-3a9b05edc5ed/files/nw-characterisation.pdf>
- DigitalGlobe. (2017). Resources: Satellite Information. Retrieved from <https://www.digitalglobe.com/resources/satellite-information>
- Dorji, P., & Fearn, P. (2016). A Quantitative Comparison of Total Suspended Sediment Algorithms: A Case Study of the Last Decade for MODIS and Landsat-Based Sensors. *Remote Sensing*, 8(10), 810.
- Dorji, P., & Fearn, P. (2017). Impact of the spatial resolution of satellite remote sensing sensors in the quantification of total suspended sediment concentration: A case study in turbid waters of Northern Western Australia. *PLoS One*, 12(4), e0175042.
- Dorji, P., Fearn, P., & Broomhall, M. (2016). A Semi-Analytic Model for Estimating Total Suspended Sediment Concentration in Turbid Coastal Waters of Northern Western Australia Using MODIS-Aqua 250 m Data. *Remote Sensing*, 8(7), 556.
- Doxaran, D., Castaing, P., & Lavender, S. J. (2006). Monitoring the maximum turbidity zone and detecting fine-scale turbidity features in the Gironde estuary using high spatial resolution satellite sensor (SPOT HRV, Landsat ETM+) data. *International Journal of Remote Sensing*, 27(11), 2303-2321.
- Doxaran, D., Froidefond, J.-M., & Castaing, P. (2003). Remote-sensing reflectance of turbid sediment-dominated waters. Reduction of sediment type variations and changing illumination conditions effects by use of reflectance ratios. *Applied Optics*, 42(15), 2623-2634.
- Doxaran, D., Froidefond, J.-M., Castaing, P., & Babin, M. (2009). Dynamics of the turbidity maximum zone in a macrotidal estuary (the Gironde, France): Observations from field and MODIS satellite data. *Estuarine, Coastal and Shelf Science*, 81(3), 321-332.

- Doxaran, D., Froidefond, J.-M., Lavender, S., & Castaing, P. (2002). Spectral signature of highly turbid waters: Application with SPOT data to quantify suspended particulate matter concentrations. *Remote Sensing of Environment*, 81(1), 149-161.
- Doxaran, D., Lamquin, N., Park, Y.-J., Mazeran, C., Ryu, J.-H., Wang, M., & Poteau, A. (2014). Retrieval of the seawater reflectance for suspended solids monitoring in the East China Sea using MODIS, MERIS and GOCI satellite data. *Remote Sensing of Environment*, 146, 36-48.
- Du, K., Lee, Z., & Carder, K. L. (2006, 13/11/2006). *Closure between remote sensing reflectance and inherent optical properties*. Paper presented at the Remote Sensing of the Marine Environment, Goa, India Retrieved from <http://dx.doi.org/10.1117/12.693696>
- Duan, H., Ma, R., Zhang, Y., & Zhang, B. (2009). Remote-sensing assessment of regional inland lake water clarity in northeast China. *Limnology*, 10(2), 135-141.
- Durrieu, S., & Nelson, R. F. (2013). Earth observation from space – The issue of environmental sustainability. *Space Policy*, 29(4), 238-250.
- Efron, B. (1979). Bootstrap Methods: Another Look at the Jackknife. *The Annals of Statistics*, 7(1), 1-26.
- Ekercin, S. (2007). Water Quality Retrievals from High Resolution Ikonos Multispectral Imagery: A Case Study in Istanbul, Turkey. *Water, Air and Soil Pollution*, 183(1-4), 239-251.
- Erftemeijer, P. L. A., Riegl, B., Hoeksema, B. W., & Todd, P. A. (2012). Environmental impacts of dredging and other sediment disturbances on corals: A review. *Marine Pollution Bulletin*, 64(9), 1737-1765.
- Espinoza Villar, R., Martinez, J.-M., Le Texier, M., Guyot, J.-L., Fraizy, P., Meneses, P. R., & Oliveira, E. d. (2013). A study of sediment transport in the Madeira River, Brazil, using MODIS remote-sensing images. *Journal of South American Earth Sciences*, 44, 45-54.
- Etcheber, H., Schmidt, S., Sottolichio, A., Maneux, E., Chabaux, G., Escalier, J. M., . . . Castaing, P. (2011). Monitoring water quality in estuarine environments: lessons from the MAGEST monitoring program in the Gironde fluvial-estuarine system. *Hydrology and Earth System Sciences*, 15(3), 831.

- Eugenio, F., Martin, J., Marcello, J., & Bermejo, J. A. (2013, 9-13 Sept. 2013). *Worldview-2 high resolution remote sensing image processing for the monitoring of coastal areas*. Paper presented at the 21st European Signal Processing Conference (EUSIPCO 2013)
- EUMETSAT. (2017). Sentinel-3 is a dedicated Copernicus satellite delivering a variety of high-quality ocean measurements. Retrieved from <http://www.eumetsat.int/website/home/Satellites/CurrentSatellites/Sentinel3/index.html>
- Evans, R., Murray, K. L., Field, S., Moore, J. A. Y., Shedrawi, G., Huntley, B. G., . . . Marrable, D. (2012). Digitise This! A Quick and Easy Remote Sensing Method to Monitor the Daily Extent of Dredge Plumes. *PLoS One*, 7(12), 10.
- Feldman, G. C., & McClain, C. R. (2010). I2gen, Ocean Color SeaDAS. Retrieved from <http://seadas.gsfc.nasa.gov/doc/I2gen/I2gen.html>
- Feng, L., Hu, C., Chen, X., & Song, Q. (2014). Influence of the Three Gorges Dam on total suspended matters in the Yangtze Estuary and its adjacent coastal waters: Observations from MODIS. *Remote Sensing of Environment*, 140, 779-788.
- Fettweis, M., Nechad, B., & Van den Eynde, D. (2007). An estimate of the suspended particulate matter (SPM) transport in the southern North Sea using SeaWiFS images, in situ measurements and numerical model results. *Continental Shelf Research*, 27(10–11), 1568-1583.
- Forkuor, G., Hounkpatin, O. K. L., Welp, G., & Thiel, M. (2017). High Resolution Mapping of Soil Properties Using Remote Sensing Variables in South-Western Burkina Faso: A Comparison of Machine Learning and Multiple Linear Regression Models. *PLoS One*, 12(1), e0170478.
- Franz, B. A., Nechad, B., Meister, G., Kwiatkowska, E. J., Bailey, S. W., Ahmad, Z., & McClain, C. R. (2006, 9-13 October, 2006). *MODIS Land Bands for Ocean Remote Sensing Applications*. Paper presented at the Ocean Optics XVIII, Montreal, Canada Retrieved from https://oceancolor.gsfc.nasa.gov/staff/franz/papers/franz_et_al_2006_oo.pdf
- Gernez, P., Lafon, V., Lerouxel, A., Curti, C., Lubac, B., Cerisier, S., & Barillé, L. (2015). Toward Sentinel-2 High Resolution Remote Sensing

of Suspended Particulate Matter in Very Turbid Waters: SPOT4 (Take5) Experiment in the Loire and Gironde Estuaries. *Remote Sensing*, 7(8), 9507.

Gholizadeh, M. H., Melesse, A. M., & Reddi, L. (2016). A Comprehensive Review on Water Quality Parameters Estimation Using Remote Sensing Techniques. *Sensors (Basel, Switzerland)*, 16(8), 1298.

Giardino, C., Brando, V. E., Dekker, A. G., Strömbeck, N., & Candiani, G. (2007). Assessment of water quality in Lake Garda (Italy) using Hyperion. *Remote Sensing of Environment*, 109(2), 183-195.

Giardino, C., Bresciani, M., Cazzaniga, I., Schenk, K., Rieger, P., Braga, F., . . . Brando, V. (2014). Evaluation of Multi-Resolution Satellite Sensors for Assessing Water Quality and Bottom Depth of Lake Garda. *Sensors*, 14(12), 24116.

Glover, D. M., Jenkins, W. J., & Doney, S. C. (2011). *Modeling methods for marine science*. Cambridge: Cambridge University Press.

Gordon, H. R., Brown, O. B., Evans, R. H., Brown, J. W., Smith, R. C., Baker, K. S., & Clark, D. K. (1988). A semianalytic radiance model of ocean color. *Journal of Geophysical Research*, 93(D9), 10909-10924.

Gordon, H. R., & Castaño, D. J. (1989). Aerosol analysis with the Coastal Zone Color Scanner: a simple method for including multiple scattering effects. *Applied Optics*, 28(7), 1320-1326.

Gordon, H. R., & Morel, A. Y. (1983). Remote assessment of ocean color for interpretation of satellite visible imagery: a review *Lecture notes on coastal and estuarine studies* (Vol. 4, pp. 114): New York: Springer-Verlag.

Gordon, H. R., & Wang, M. (1994a). Influence of oceanic whitecaps on atmospheric correction of ocean-color sensors. *Applied Optics*, 33(33), 7754-7763.

Gordon, H. R., & Wang, M. (1994b). Retrieval of water-leaving radiance and aerosol optical thickness over the oceans with SeaWiFS: a preliminary algorithm. *Applied Optics*, 33(3), 443-452.

Guan, X., Li, J., & Booty, W. G. (2011). Monitoring Lake Simcoe Water Clarity Using Landsat-5 TM Images. *Water Resources Management*, 25(8), 2015-2033.

- Gurlin, D., Gitelson, A. A., & Moses, W. J. (2011). Remote estimation of chl-a concentration in turbid productive waters — Return to a simple two-band NIR-red model? *Remote Sensing of Environment*, 115(12), 3479-3490.
- Han, B., Loisel, H., Vantrepotte, V., Mériaux, X., Bryère, P., Ouillon, S., . . . Zhu, J. (2016). Development of a Semi-Analytical Algorithm for the Retrieval of Suspended Particulate Matter from Remote Sensing over Clear to Very Turbid Waters. *Remote Sensing*, 8(3), 211.
- Hanley, J. R. (2011). Environment monitoring programs on recent capital dredging projects in the Pilbarra (2003-10): a review. *APPEA Journal*, 273-293.
- Härmä, P., Vepsäläinen, J., Hannonen, T., Pyhälähti, T., Kämäri, J., Kallio, K., . . . Koponen, S. (2001). Detection of water quality using simulated satellite data and semi-empirical algorithms in Finland. *Science of The Total Environment*, 268(1–3), 107-121.
- Havens, K. E., Beaver, J. R., Casamatta, D. A., East, T. L., James, R. T., McCormick, P., . . . Rodusky, A. J. (2011). Hurricane effects on the planktonic food web of a large subtropical lake. *Journal of Plankton Research*, 33(7), 1081-1094.
- He, X., Bai, Y., Pan, D., Huang, N., Dong, X., Chen, J., . . . Cui, Q. (2013). Using geostationary satellite ocean color data to map the diurnal dynamics of suspended particulate matter in coastal waters. *Remote Sensing of Environment*, 133, 225-239.
- Hicks, B. J., Stichbury, G. A., Brabyn, L. K., Allan, M. G., & Ashraf, S. (2013). Hindcasting water clarity from Landsat satellite images of unmonitored shallow lakes in the Waikato region, New Zealand. *Environmental Monitoring and Assessment*, 185(9), 7245-7261.
- Hu, C., Chen, Z., Clayton, T. D., Swarzenski, P., Brock, J. C., & Muller-Karger, F. E. (2004). Assessment of estuarine water-quality indicators using MODIS medium-resolution bands: Initial results from Tampa Bay, FL. *Remote Sensing of Environment*, 93(3), 423-441.
- Hu, C., Feng, L., Lee, Z., Davis, C. O., Mannino, A., McClain, C. R., & Franz, B. A. (2012). Dynamic range and sensitivity requirements of satellite ocean color sensors: learning from the past. *Applied Optics*, 51(25), 6045-6062.
- Huang, C., Yang, H., Zhu, A. X., Zhang, M., Lü, H., Huang, T., . . . Li, Y. (2015). Evaluation of the Geostationary Ocean Color Imager (GOCI)

to monitor the dynamic characteristics of suspension sediment in Taihu Lake. *International Journal of Remote Sensing*, 36(15), 3859-3874.

Hubert, L., Lubac, B., Dessailly, D., Duforet-Gaurier, L., & Vantrepotte, V. (2010). Effect of inherent optical properties variability on the chlorophyll retrieval from ocean color remote sensing: an in situ approach. *Optics Express*, 18(20), 20949-20959.

Hudson, B., Overeem, I., McGrath, D., Syvitski, J. P. M., Mikkelsen, A., & Hasholt, B. (2014). MODIS observed increase in duration and spatial extent of sediment plumes in Greenland fjords. *The Cryosphere*, 8(4), 1161-1176.

In-Young, Y., Lang, M., & Vermote, E. (2014). Improved Understanding of Suspended Sediment Transport Process Using Multi-Temporal Landsat Data: A Case Study From the Old Woman Creek Estuary (Ohio). *Selected Topics in Applied Earth Observations and Remote Sensing, IEEE Journal of*, 7(2), 636-647.

IOCCG. (1998). *Minimum Requirements for an Operational Ocean-Colour Sensor for the Open Ocean*. In *Reports of the International Ocean-Colour Coordinating Group, No. 1*. Dartmouth, Canada: IOCCG. Retrieved from <http://ioccg.org/wp-content/uploads/2015/10/ioccg-report-01.pdf>

IOCCG. (2000). *Remote sensing of ocean color in coastal, and other optically-complex, waters*. In *Reports of the International Ocean-Colour Coordinating Group, No. 3*. Dartmouth, Canada: IOCCG. Retrieved from <http://ioccg.org/wp-content/uploads/2015/10/ioccg-report-03.pdf>

IOCCG. (2006). *Remote Sensing of Inherent Optical Properties: Fundamentals, Tests of Algorithms, and Applications*. In *Reports of the International Ocean-Colour Coordinating Group, No. 5*. Dartmouth, Canada: IOCCG. Retrieved from <http://ioccg.org/wp-content/uploads/2015/10/ioccg-report-05.pdf>

IOCCG. (2012). *Ocean -Color Observations from a Geostationary Orbit*. In *Reports of the International Ocean-Colour Coordinating Group, No. 12*. Dartmouth, Canada: IOCCG. Retrieved from <http://ioccg.org/wp-content/uploads/2015/10/ioccg-report-12.pdf>

Irons, J. R., Dwyer, J. L., & Barsi, J. A. (2012). The next Landsat satellite: The Landsat Data Continuity Mission. *Remote Sensing of Environment*, 122, 11-21.

- Islam, M. A., Lan-Wei, W., Smith, C. J., Reddy, S., Lewis, A., & Smith, A. (2007). Evaluation of satellite remote sensing for operational monitoring of sediment plumes produced by dredging at Hay Point, Queensland, Australia. *Journal of Applied Remote Sensing*, 1(1), 011506-011506-011515.
- Islam, M. R., Yamaguchi, Y., & Ogawa, K. (2001). Suspended sediment in the Ganges and Brahmaputra Rivers in Bangladesh: observation from TM and AVHRR data. *Hydrological Processes*, 15(3), 493-509.
- Japan Meteorological Agency. (2015). *Himawari-8/9 Himawari Standard Data User's Guide*. Tokyo, Japan: J. M. Agency.
- Jiang, X., Tang, J., Zhang, M., Ma, R., & Ding, J. (2009). Application of MODIS data in monitoring suspended sediment of Taihu Lake, China. *Chinese Journal of Oceanology and Limnology*, 27(3), 614-620.
- Jutla, A. S., Akanda, A. S., & Islam, S. (2012). Satellite remote sensing of space–time plankton variability in the Bay of Bengal: Connections to cholera outbreaks. *Remote Sensing of Environment*, 123(0), 196-206.
- Kaba, E., Philpot, W., & Steenhuis, T. (2014). Evaluating suitability of MODIS-Terra images for reproducing historic sediment concentrations in water bodies: Lake Tana, Ethiopia. *International Journal of Applied Earth Observation and Geoinformation*, 26, 286-297.
- Kallio, K., Attila, J., Härmä, P., Koponen, S., Pulliainen, J., Hyytiäinen, U.-M., & Pyhälähti, T. (2008a). Landsat ETM+ Images in the Estimation of Seasonal Lake Water Quality in Boreal River Basins. *Environmental Management*, 42(3), 511-522.
- Kallio, K., Attila, J., Harma, P., Koponen, S., Pulliainen, J., Hyytianinen, U. M., & Pyhalahiti, T. (2008b). Landsat ETM+ Images in the estimation of seasonal lake water quality in boreal river basins. *Environmental Management*,(42), 511-522.
- Katlane, R., Nechad, B., Ruddick, K., & Zargouni, F. (2013). Optical remote sensing of turbidity and total suspended matter in the Gulf of Gabes. *Arabian Journal of Geosciences*, 6(5), 1527-1535.
- Kazemzadeh, M. B., Ayyoubzadeh, S. A., & Moridnezhad, A. (2013). Remote Sensing of Temporal and Spatial Variations of Suspended Sediment Concentration in Bahmanshir Estuary, Iran. *Indian Journal of Science and Technology*, 6(8), 5036-5045.

- Keith, D., Lunetta, R., & Schaeffer, B. (2016). Optical Models for Remote Sensing of Colored Dissolved Organic Matter Absorption and Salinity in New England, Middle Atlantic and Gulf Coast Estuaries USA. *Remote Sensing*, 8(4), 283.
- Kim, S. T. (1980). *A QUANTITATIVE EVALUATION OF LANDSAT FOR MONITORING SUSPENDED SEDIMENTS IN A FLUVIAL CHANNEL*. 8021752 (Ph.D.). Louisiana State University and Agricultural & Mechanical College, Ann Arbor.
- Kjelland, M. E., Woodley, C. M., Swannack, T. M., & Smith, D. L. (2015). A review of the potential effects of suspended sediment on fishes: potential dredging-related physiological, behavioral, and transgenerational implications. *Environment Systems and Decisions*, 35(3), 334-350.
- Klemas, V., Borchardt, J. F., & Treasure, W. M. (1973). Suspended sediment observations from ERTS-1. *Remote Sensing of Environment*, 2, 205-221.
- Kloiber, S. M., Brezonik, P. L., Olmanson, L. G., & Bauer, M. E. (2002). A procedure for regional lake water clarity assessment using Landsat multispectral data. *Remote Sensing of Environment*, 82(1), 38-47.
- Kong, J.-L., Sun, X.-M., Wong, D., Chen, Y., Yang, J., Yan, Y., & Wang, L.-X. (2015a). A Semi-Analytical Model for Remote Sensing Retrieval of Suspended Sediment Concentration in the Gulf of Bohai, China. *Remote Sensing*, 7(5), 5373.
- Kong, J., Sun, X., Wang, W., Du, D., Chen, Y., & Yang, J. (2015b). An optimal model for estimating suspended sediment concentration from Landsat TM images in the Caofeidian coastal waters. *International Journal of Remote Sensing*, 36(19-20), 5257-5272.
- Koponen, S., Attila, J., Pulliainen, J., Kallio, K., Pyhälähti, T., Lindfors, A., . . . Hallikainen, M. (2007). A case study of airborne and satellite remote sensing of a spring bloom event in the Gulf of Finland. *Continental Shelf Research*, 27(2), 228-244.
- Koponen, S., Pulliainen, J., Kallio, K., & Hallikainen, M. (2002). Lake water quality classification with airborne hyperspectral spectrometer and simulated MERIS data. *Remote Sensing of Environment*, 79(1), 51-59.
- Kotchenova, S. Y., Vermote, E. F., Matarrese, R., & Klemm, J. F. J. (2006). Validation of a vector version of the 6S radiative transfer code for

atmospheric correction of satellite data. Part I: Path radiance. *Applied Optics*, 45(26), 6762-6774.

- Kratzer, S., Brockmann, C., & Moore, G. (2008). Using MERIS full resolution data to monitor coastal waters — A case study from Himmerfjärden, a fjord-like bay in the northwestern Baltic Sea. *Remote Sensing of Environment*, 112(5), 2284-2300.
- Kumar, A., Equeenuddin, S. M., Mishra, D. R., & Acharya, B. C. (2016). Remote monitoring of sediment dynamics in a coastal lagoon: Long-term spatio-temporal variability of suspended sediment in Chilika. *Estuarine, Coastal and Shelf Science*, 170, 155-172.
- Kutser, T., Metsamaa, L., Vahtmae, E., & Aps, R. (2007). Operative monitoring of the Extent of dredging plumes in coastal ecosystems using MODIS satellite imagery. *J. Coast. Res*, 50(special issue), 180-184.
- Kutser, T., Pierson, D. C., Tranvik, L., Reinart, A., Sobek, S., & Kallio, K. (2005). Using Satellite Remote Sensing to Estimate the Colored Dissolved Organic Matter Absorption Coefficient in Lakes. *Ecosystems*, 8(6), 709-720.
- Kwiatkowska, E. J., & Bonekamp, H. G. (2016). Ocean colour opportunities from Meteosat Second and Third Generation geostationary platforms. *Ocean Science*, 12(3), 703-713.
- L, M. R., & Mckae, B. A. (2004). Using MODIS Terra 250m imagery to map concentrations of total suspended matter in coastal waters. *Remote Sensing of Environment*, 93(1-2), 259-266.
- Lee, Z., Carder, K. L., & Arnone, R. A. (2002). Deriving inherent optical properties from water color: a multiband quasi-analytical algorithm for optically deep waters. *Applied Optics*, 41(27), 5755-5772.
- Lee, Z. P., Carder, K. L., Mobley, C. D., Steward, R. G., & Patch, J. S. (1999). Hyperspectral remote sensing for shallow waters: 2. Deriving bottom depths and water properties by optimization. . *Applied Optics*, 38.
- Li, J., Gao, S., & Wang, Y. (2010). Delineating suspended sediment concentration patterns in surface waters of the Changjiang Estuary by remote sensing analysis. *Acta Oceanologica Sinica*, 29(4), 38-47.

- Lim, H. S., Mat Jafri, M. Z., Abdullah, K., & Abu Bakar, M. N. (2010). Water quality mapping using digital camera images. *International Journal of Remote Sensing*, 31(19), 5275-5295.
- Lim, H. S., MatJafri, M. Z., Abdullah, K., & Asadpour, R. (2013). A Two-Band Algorithm for Total Suspended Solid Concentration Mapping Using THEOS Data. *Journal of Coastal Research*, 29(3), 624-630.
- Lim, J., & Choi, M. (2015). Assessment of water quality based on Landsat 8 operational land imager associated with human activities in Korea. *Environmental Monitoring and Assessment*, 187(384), 17.
- Liu, C.-d., He, B.-y., Li, M.-t., & Ren, X.-y. (2006). Quantitative modeling of suspended sediment in middle Changjiang River from modis. *Chinese Geographical Science*, 16(1), 79-82.
- Loisel, H., & Morel, A. (1998). Light scattering and chlorophyll concentration in case 1 waters: A reexamination. *Limnology and Oceanography*, 43(5), 847-858.
- Loisel, H., Vantrepotte, V., Dessailly, D., & Mériaux, X. (2014a). Assessment of the colored dissolved organic matter in coastal waters from ocean color remote sensing. *Optics Express*, 22(11), 13109-13124.
- Loisel, H., Vantrepotte, V., Dessailly, D., & MÈriaux, X. (2014b). Assessment of the colored dissolved organic matter in coastal waters from ocean color remote sensing. *Optics Express*, 22(11), 13109-13124.
- Lu, J., Chen, X., Tian, L., & Zhang, W. (2014). Numerical simulation-aided MODIS capture of sediment transport for the Bohai Sea in China. *International Journal of Remote Sensing*, 35(11-12), 4225-4238.
- Mabwoga, S. O., Chawla, A., & Thukral, A. K. (2010). Assessment of water quality parameters of the Harike wetland in India, a Ramsar site, using IRS LISS IV satellite data. *Environmental Monitoring and Assessment*, 170(1-4), 117-128.
- Macdonald, R. K., Ridd, P. V., Whinney, J. C., Larcombe, P., & Neil, D. T. (2013). Towards environmental management of water turbidity within open coastal waters of the Great Barrier Reef. *Marine Pollution Bulletin*, 74(1), 82-94.
- Martin, J., Eugenio, F., Marcello, J., & Medina, A. (2016). Automatic Sun Glint Removal of Multispectral High-Resolution Worldview-2 Imagery for Retrieving Coastal Shallow Water Parameters. *Remote Sensing*, 8(1), 37.

- Martinez, J. M., Guyot, J. L., Filizola, N., & Sondag, F. (2009). Increase in suspended sediment discharge of the Amazon River assessed by monitoring network and satellite data. *CATENA*, 79(3), 257-264.
- Matthews, W. M. (2011). A current review of empirical procedures of remote sensing in inland and near-coastal transitional waters. *International Journal of Remote Sensing*, 32(21), 6855-6899.
- McKim, H. L., Marlar, T. L., & Anderson, D. M. (1972). *The Use of ERTS-1 Imagery in the National Programs for Inspection of Dams (Special Report 183)*. US Army Corps of Engineers, Cold Regions Research and Engineering Laboratory, Hanover, New Hampshire, USA:
- Miller, R. L., Liu, C.-C., Buonassissi, C. J., & Wu, A.-M. (2011). A Multi-Sensor Approach to Examining the Distribution of Total Suspended Matter (TSM) in the Albemarle-Pamlico Estuarine System, NC, USA. *Remote Sensing*, 3(5), 962.
- Miller, R. L., & McKee, B. A. (2004). Using MODIS Terra 250 m imagery to map concentrations of total suspended matter in coastal waters. *Remote Sensing of Environment*, 93(1-2), 259-266.
- Min, J.-E., Ryu, J.-H., Lee, S., & Son, S. (2012). Monitoring of suspended sediment variation using Landsat and MODIS in the Saemangeum coastal area of Korea. *Marine Pollution Bulletin*, 64(2), 382-390.
- Mishra, D. R., Narumalani, S., Rundquist, D., & Lawson, M. (2005). Characterizing the vertical diffuse attenuation coefficient for downwelling irradiance in coastal waters: Implications for water penetration by high resolution satellite data. *ISPRS Journal of Photogrammetry and Remote Sensing*, 60(1), 48-64.
- Mobley, C., Stramski, D., Bissett, W. P., & E, B. (2004). Optical modelling of ocean waters: Is the Case 1 - Case 2 classification still useful? *Oceanography*, 17(2), 60-67.
- Mobley, C. D. (1994). *Light and Water: Radiative Transfer in Natural Waters*. San Diego, CA: Academic
- Mobley, C. D. (1999). Estimation of the remote-sensing reflectance from above-surface measurements. *Applied Optics*, 38(36), 7442-7455.
- Mobley, C. D. (2001). Radiative transfer in the ocean.

- Mobley, C. D., Gentili, B., Gordon, H. R., Jin, Z., Kattawar, G. W., Morel, A., . . . Stavn, R. H. (1993). Comparison of numerical models for computing underwater light fields. *Appl Opt*, 32(36), 7484-7504.
- Mobley, C. D., & Sundman, L. K. (2001). *Hydrolight 4.2 Technical Documentation*. Redmond, WA: Sequoia Scientific, Inc. . (pp. 75).
- MODIS Web. (2017). MODIS Design. Retrieved from <https://modis.gsfc.nasa.gov/about/design.php>
- Moore li, T. S., Matear, R. J., Marra, J., & Clementson, L. (2007). Phytoplankton variability off the Western Australian Coast: Mesoscale eddies and their role in cross-shelf exchange. *Deep Sea Research Part II: Topical Studies in Oceanography*, 54(8–10), 943-960.
- Moses, W. J., Ackleson, S. G., Hair, J. W., Hostetler, C. A., & Miller, W. D. Spatial scales of optical variability in the coastal ocean: Implications for remote sensing and in situ sampling. *Journal of Geophysical Research: Oceans*, n/a-n/a.
- Mostafa, Y. E. S. (2012). Environmental impacts of dredging and land reclamation at Abu Qir Bay, Egypt. *Ain Shams Engineering Journal*, 3(1), 1-15.
- Murakami, H. (2016, 04/04/2016). *Ocean color estimation by Himawari-8/AHI*. Paper presented at the Remote Sensing of the Oceans and Inland Waters: Techniques, Applications, and Challenges. <http://dx.doi.org/doi:/10.1117/12.2225422>
- Myint, S. W., & Walker, N. D. (2002). Quantification of surface suspended sediments along a river dominated coast with NOAA AVHRR and SeaWiFS measurements: Louisiana, USA. *International Journal of Remote Sensing*, 23(16), 3229-3249.
- Nebbioso, A., & Piccolo, A. (2013). Molecular characterization of dissolved organic matter (DOM): a critical review. *Analytical and Bioanalytical Chemistry*, 405(1), 109-124.
- Nechad, B., Ruddick, K. G., & Park, Y. (2010). Calibration and validation of a generic multisensor algorithm for mapping of total suspended matter in turbid waters. *Remote Sensing of Environment*, 114(4), 854-866.
- Neukermans, G., Ruddick, K., Bernard, E., Ramon, D., Nechad, B., & Deschamps, P.-Y. (2009). Mapping total suspended matter from

geostationary satellites: a feasibility study with SEVIRI in the Southern North Sea. *Optics Express*, 17(16), 14029-14052.

Neukermans, G., Ruddick, K. G., & Greenwood, N. (2012). Diurnal variability of turbidity and light attenuation in the southern North Sea from the SEVIRI geostationary sensor. *Remote Sensing of Environment*, 124, 564-580.

Odermatt, D., Heege, T., Nieke, T., Kneubuhler, M., & Itten, K. I. (2008). Water quality monitoring for Lake Constance with a physically based algorithm for MERIS data. *Sensors*, 8(8), 4582-4599.

Ody, A., Doxaran, D., Vanhellemont, Q., Nechad, B., Novoa, S., Many, G., . . . Gentili, B. (2016). Potential of High Spatial and Temporal Ocean Color Satellite Data to Study the Dynamics of Suspended Particles in a Micro-Tidal River Plume. *Remote Sensing*, 8(3), 245.

Olmanson, L. G., Bauer, M. E., & Brezonik, P. L. (2008). A 20-year Landsat water clarity census of Minnesota's 10,000 lakes. *Remote Sensing of Environment*, 112(11), 4086-4097.

Onderka, M., & Pekárová, P. (2008). Retrieval of suspended particulate matter concentrations in the Danube River from Landsat ETM data. *Science of The Total Environment*, 397(1-3), 238-243.

Ondrusek, M., Stengel, E., Kinkade, C. S., Vogel, R. L., Keegstra, P., Hunter, C., & Kim, C. (2012). The development of a new optical total suspended matter algorithm for the Chesapeake Bay. *Remote Sensing of Environment*, 119, 243-254.

Östlund, C., Flink, P., Strömbeck, N., Pierson, D., & Lindell, T. (2001). Mapping of the water quality of Lake Erken, Sweden, from Imaging Spectrometry and Landsat Thematic Mapper. *Science of The Total Environment*, 268(1-3), 139-154.

Ouillon, S., Douillet, P., Petrenko, A., Neveux, J., Dupouy, C., Froidefond, J.-M., . . . Muñoz-Caravaca, A. (2008). Optical Algorithms at Satellite Wavelengths for Total Suspended Matter in Tropical Coastal Waters. *Sensors*, 8(7), 4165-4185.

Ouillon, S., & Petrenko, A. (2005). Above-water measurements of reflectance and chlorophyll-a algorithms in the Gulf of Lions, NW Mediterranean Sea. *Optics Express*, 13(7), 2531-2548.

- Park, E., & Latrubesse, E. M. (2014). Modeling suspended sediment distribution patterns of the Amazon River using MODIS data. *Remote Sensing of Environment*, 147, 232-242.
- Passang, D., Peter, F., & Mark, B. (2016). *A Semi-Analytic Model for Estimating Total Suspended Sediment Concentration in Turbid Coastal Waters of Northern Western Australia using MODIS-Aqua 250m data*. Remote Sensing and Satellite Research Group. Curtin University of Technology.
- Peta, G. S. (2001). The Application of Satellite Remote Sensing to Coastal Management in Singapore. *Ambio*, 30(1), 43-48.
- Petus, C., Chust, G., Gohin, F., Doxaran, D., Froidefond, J.-M., & Sagarminaga, Y. (2010). Estimating turbidity and total suspended matter in the Adour River plume (South Bay of Biscay) using MODIS 250-m imagery. *Continental Shelf Research*, 30(5), 379-392.
- Petus, C., Marieu, V., Novoa, S., Chust, G., Bruneau, N., & Froidefond, J.-M. (2014). Monitoring spatio-temporal variability of the Adour River turbid plume (Bay of Biscay, France) with MODIS 250-m imagery. *Continental Shelf Research*, 74, 35-49.
- Pope, R. M., & Fry, E. S. (1997). Absorption spectrum (380–700 nm) of pure water. II. Integrating cavity measurements. *Applied Optics*, 36(33), 8710-8723.
- Prieur, L., & Sathyendranath, S. (1981). An optical classification of coastal and oceanic waters based on the specific spectral absorption curves of phytoplankton pigments, dissolved organic matter, and other particulate materials¹. *Limnology and Oceanography*, 26(4), 671-689.
- Proud, S. R., Fensholt, R., Rasmussen, M. O., & Sandholt, I. (2010). A comparison of the effectiveness of 6S and SMAC in correcting for atmospheric interference of Meteosat Second Generation images. *Journal of Geophysical Research: Atmospheres*, 115(D17), n/a-n/a.
- Qing, S., Zhang, J., Cui, T., & Bao, Y. (2014). Remote sensing retrieval of inorganic suspended particle size in the Bohai Sea. *Continental Shelf Research*, 73, 64-71.
- Qiu, Z. (2013). A simple optical model to estimate suspended particulate matter in Yellow River Estuary. *Optics Express*, 21(23), 27891-27904.
- Raag, L., Uiboupin, R., & Sipelgas, L. (2013). *Analysis of historical MERIS and MODIS data to evaluate the impact of dredging to monthly mean*

surface TSM concentration. Retrieved from <http://dx.doi.org/10.1117/12.2032327>

- Ruddick, K., Neukermans, G., Vanhellemont, Q., & Jolivet, D. (2014). Challenges and opportunities for geostationary ocean colour remote sensing of regional seas: A review of recent results. *Remote Sensing of Environment*, 146, 63-76.
- Ruddick, K. G., Ovidio, F., & Rijkeboer, M. (2000). Atmospheric correction of SeaWiFS imagery for turbid coastal and inland waters. *Applied Optics*, 39(6), 897-912.
- Salama, M. S., & Shen, F. (2010). Simultaneous atmospheric correction and quantification of suspended particulate matters from orbital and geostationary earth observation sensors. *Estuarine, Coastal and Shelf Science*, 86(3), 499-511.
- Sawaya, K. E., Olmanson, L. G., Heinert, N. J., Brezonik, P. L., & Bauer, M. E. (2003). Extending satellite remote sensing to local scales: land and water resource monitoring using high-resolution imagery. *Remote Sensing of Environment*, 88(1-2), 144-156.
- Shen, F., Verhoef, W., Zhou, Y., Salama, M. S., & Liu, X. (2010). Satellite Estimates of Wide-Range Suspended Sediment Concentrations in Changjiang (Yangtze) Estuary Using MERIS Data. *Estuaries and Coasts*, 33(6), 1420-1429.
- Shen, F., Zhou, Y., Peng, X., & Chen, Y. (2014). Satellite multi-sensor mapping of suspended particulate matter in turbid estuarine and coastal ocean, China. *International Journal of Remote Sensing*, 35(11-12), 4173-4192.
- Shi, K., Zhang, Y., Liu, X., Wang, M., & Qin, B. (2014). Remote sensing of diffuse attenuation coefficient of photosynthetically active radiation in Lake Taihu using MERIS data. *Remote Sensing of Environment*, 140, 365-377.
- Shi, K., Zhang, Y., Zhou, Y., Liu, X., Zhu, G., Qin, B., & Gao, G. (2017). Long-term MODIS observations of cyanobacterial dynamics in Lake Taihu: Responses to nutrient enrichment and meteorological factors. *Scientific Reports*, 7, 40326.
- Shi, K., Zhang, Y., Zhu, G., Liu, X., Zhou, Y., Xu, H., . . . Li, Y. (2015). Long-term remote monitoring of total suspended matter concentration in Lake Taihu using 250 m MODIS-Aqua data. *Remote Sensing of Environment*, 164, 43-56.

- Sipelgas, L., Raudsepp, U., & Kõuts, T. (2006). Operational monitoring of suspended matter distribution using MODIS images and numerical modelling. *Advances in Space Research*, 38(10), 2182-2188.
- Siswanto, E., Tang, J., Yamaguchi, H., Ahn, Y.-h., Ishizaka, J., Yoo, S., . . . Kawamura, H. (2011). Empirical ocean-color algorithms to retrieve chlorophyll-a, total suspended matter, and colored dissolved organic matter absorption coefficient in the Yellow and East China Seas. *Journal of Oceanography*, 67(5), 627-650.
- SKM. (2013). *Improved Dredge Material Management for the Great Barrier Reef Region; Appendix B*. Townsville G. B. R. M. P. Authority.
- Slonecker, E. T., Jones, D. K., & Pellerin, B. A. (2016). The new Landsat 8 potential for remote sensing of colored dissolved organic matter (CDOM). *Marine Pollution Bulletin*, 107(2), 518-527.
- Smith, R. C., & Baker, K. S. (1981). Optical properties of the clearest natural waters (200–800 nm). *Applied Optics*, 20(2), 177-184.
- Sokoletsky, L., Yang, X., & Shen, F. (2014). *MODIS-based retrieval of suspended sediment concentration and diffuse attenuation coefficient in Chinese estuarine and coastal waters*. Retrieved from <http://dx.doi.org/10.1117/12.2069205>
- Son, S., & Wang, M. (2012). Water properties in Chesapeake Bay from MODIS-Aqua measurements. *Remote Sensing of Environment*, 123, 163-174.
- Steven, A. D. K., Pantus, F., Brooks, D., & Trott, L. (1998). *Long-term chlorophyll monitoring the Great Barrier Reef lagoon: Status report 1, 1993-1995*. G. B. R. M. P. Authority.
- Stone, M. (1974). Cross-Validatory Choice and Assessment of Statistical Predictions. *Journal of the Royal Statistical Society. Series B (Methodological)*, 36(2), 111-147.
- Stul, T., Gozzard, J., Eliot, I., & Eliot, M. (2014). *Coastal Sediment Cells for the Pilbara Region between Giralia and Beedingarra Creek, Western Australia*. In Report prepared by Seashore Engineering Pty Ltd and Geological Survey of Western Australia for the Western Department of Transport, Freemantle. D. o. Transport.
- Sullivan, C. W., Arrigo, K. R., McClain, C. R., Comiso, J. C., & Firestone, J. (1993). Distribution of Phytoplankton Blooms in the Southern Ocean. *Science*, 262, 1832-1837.

- Sun, D., Li, Y., Wang, Q., Gao, J., Le, C., Huang, C., & Gong, S. (2013). Hyperspectral Remote Sensing of the Pigment C-Phycocyanin in Turbid Inland Waters, Based on Optical Classification. *IEEE Transactions on Geoscience and Remote Sensing*, 51(7), 3871-3884.
- Tang, S., Larouche, P., Niemi, A., & Michel, C. (2013). Regional algorithms for remote-sensing estimates of total suspended matter in the Beaufort Sea. *International Journal of Remote Sensing*, 34(19), 6562-6576.
- Tarrant, P. E., Amacher, J. A., & Neuer, S. (2010). Assessing the potential of Medium-Resolution Imaging Spectrometer (MERIS) and Moderate-Resolution Imaging Spectroradiometer (MODIS) data for monitoring total suspended matter in small and intermediate sized lakes and reservoirs. *Water Resources Research*, 46(9).
- Teodoro, A. C., Veloso-Gomes, F., & Gonçalves, H. (2008). Statistical Techniques for Correlating Total Suspended Matter Concentration with Seawater Reflectance Using Multispectral Satellite Data. *Journal of Coastal Research*, 24(4C), 40-49.
- Thompson, C. E. L., Couceiro, F., Fones, G. R., Helsby, R., Amos, C. L., Black, K., . . . Kelly-Gerreyn, B. A. (2011). In situ flume measurements of resuspension in the North Sea. *Estuarine, Coastal and Shelf Science*, 94(1), 77-88.
- Tilstone, G. H., Lotliker, A. A., Miller, P. I., Ashraf, P. M., Kumar, T. S., Suresh, T., . . . Menon, H. B. (2013). Assessment of MODIS-Aqua chlorophyll-a algorithms in coastal and shelf waters of the eastern Arabian Sea. *Continental Shelf Research*, 65, 14-26.
- Tiwari, S. P., & Shanmugam, P. (2011). An optical model for the remote sensing of coloured dissolved organic matter in coastal/ocean waters. *Estuarine, Coastal and Shelf Science*, 93(4), 396-402.
- Tiwari, S. P., & Shanmugam, P. (2013). An optical model for deriving the spectral particulate backscattering coefficients in oceanic waters. *Ocean Sci.*, 9(6), 987-1001.
- Tyler, A. N., Svab, E., Preston, T., Présing, M., & Kovács, W. A. (2006). Remote sensing of the water quality of shallow lakes: A mixture modelling approach to quantifying phytoplankton in water characterized by high-suspended sediment. *International Journal of Remote Sensing*, 27(8), 1521-1537.

- Tzortziou, M., Herman, J. R., Gallegos, C. L., Neale, P. J., Subramaniam, A., Harding Jr, L. W., & Ahmad, Z. (2006). Bio-optics of the Chesapeake Bay from measurements and radiative transfer closure. *Estuarine, Coastal and Shelf Science*, 68(1–2), 348-362.
- URS. (2014). *Onslow Water Infrastructure Upgrade Project*. Perth:
- Van Raaphorst, W., Malschaert, H., & Van Haren, H. (1998). Tidal resuspension and deposition of particulate matter in the Oyster Grounds, North Sea. *Journal of Marine Research*, 56(1), 257-291.
- Vanhellemont, Q., Neukermans, G., & Ruddick, K. (2014). Synergy between polar-orbiting and geostationary sensors: Remote sensing of the ocean at high spatial and high temporal resolution. *Remote Sensing of Environment*, 146, 49-62.
- Vanhellemont, Q., & Ruddick, K. (2014). Turbid wakes associated with offshore wind turbines observed with Landsat 8. *Remote Sensing of Environment*, 145, 105-115.
- Vanhellemont, Q., & Ruddick, K. (2015). Advantages of high quality SWIR bands for ocean colour processing: Examples from Landsat-8. *Remote Sensing of Environment*, 161, 89-106.
- Vantrepotte, V., Brunet, C., Mériaux, X., Lécuyer, E., Vellucci, V., & Santer, R. (2007). Bio-optical properties of coastal waters in the Eastern English Channel. *Estuarine, Coastal and Shelf Science*, 72(1–2), 201-212.
- Vermote, E. F., Tanre, D., Deuze, J. L., Herman, M., & Morcette, J. J. (1997). Second Simulation of the Satellite Signal in the Solar Spectrum, 6S: an overview. *IEEE Transactions on Geoscience and Remote Sensing*, 35(3), 675-686.
- Viollier, M., & Sturm, B. (1984). CZCS data analysis in turbid coastal water. *Journal of Geophysical Research: Atmospheres*, 89(D4), 4977-4985.
- Volpe, V., Silvestri, S., & Marani, M. (2011). Remote sensing retrieval of suspended sediment concentration in shallow waters. *Remote Sensing of Environment*, 115(1), 44-54.
- Vos, R. J., Hakvoort, J. H. M., Jordans, R. W. J., & Ibelings, B. W. (2003). Multiplatform optical monitoring of eutrophication in temporally and spatially variable lakes. *Science of The Total Environment*, 312(1–3), 221-243.

- WA EPA. (2011). *Environmental Assessment Guideline for Marine Dredging Proposals* Western Australia Environmental Protection Authority, Perth:
- WAMSI. (2014). Dredging Science Node. Retrieved from <http://www.wamsi.org.au/dredging-science-node-0>
- Wang, F., Han, L., Kung, H. T., & Van Arsdale, R. B. (2006). Applications of Landsat-5 TM imagery in assessing and mapping water quality in Reelfoot Lake, Tennessee. *International Journal of Remote Sensing*, 27(23), 5269-5283.
- Wang, F., Zhou, B., Liu, X., Zhou, G., & Zhao, K. (2012). Remote-sensing inversion model of surface water suspended sediment concentration based on in situ measured spectrum in Hangzhou Bay, China. *Environmental Earth Sciences*, 67(6), 1669-1677.
- Wang, F., Zhou, B., Xu, J., Song, L., & Wang, X. (2008). Application of neural network and MODIS 250m imagery for estimating suspended sediments concentration in Hangzhou Bay, China. *Environmental Geology*, 56(6), 1093-1101.
- Wang, F., Zhou, B., Xu, J., Song, L., & Wang, X. (2009a). Application of neural network and MODIS 250 m imagery for estimating suspended sediments concentration in Hangzhou Bay, China. *Environmental Geology*, 56(6), 1093-1101.
- Wang, H., Hladik, C. M., Huang, W., Milla, K., Edmiston, L., Harwell, M. A., & Schalles, J. F. (2010a). Detecting the spatial and temporal variability of chlorophyll-a concentration and total suspended solids in Apalachicola Bay, Florida using MODIS imagery. *International Journal of Remote Sensing*, 31(2), 439-453.
- Wang, J.-J., Lu, X. X., Liew, S. C., & Zhou, Y. (2009b). Retrieval of suspended sediment concentrations in large turbid rivers using Landsat ETM+: an example from the Yangtze River, China. *Earth Surface Processes and Landforms*, 34(8), 1082-1092.
- Wang, J.-J., Lu, X. X., Liew, S. C., & Zhou, Y. (2010b). Remote sensing of suspended sediment concentrations of large rivers using multi-temporal MODIS images: an example in the Middle and Lower Yangtze River, China. *International Journal of Remote Sensing*, 31(4), 1103-1111.

- Wang, J., Lu, X., & Zhou, Y. (2007). Retrieval of suspended sediment concentrations in the turbid water of the Upper Yangtze River using Landsat ETM+. *Chinese Science Bulletin*, 52(2), 273-280.
- Wang, J. J., & Lu, X. X. (2010). Estimation of suspended sediment concentrations using Terra MODIS: An example from the Lower Yangtze River, China. *Science of The Total Environment*, 408(5), 1131-1138.
- Wang, M. (2007). Remote sensing of the ocean contributions from ultraviolet to near-infrared using the shortwave infrared bands: simulations. *Applied Optics*, 46(9), 1535-1547.
- Wang, M., Ahn, J.-H., Jiang, L., Shi, W., Son, S., Park, Y.-J., & Ryu, J.-H. (2013). Ocean color products from the Korean Geostationary Ocean Color Imager (GOCI). *Optics Express*, 21(3), 3835-3849.
- Wang, M., & Shi, W. (2006). Cloud Masking for Ocean Color Data Processing in the Coastal Regions. *IEEE Transactions on Geoscience and Remote Sensing*, 44(11), 3196-3105.
- Wang, M., Son, S., & Shi, W. (2009c). Evaluation of MODIS SWIR and NIR-SWIR atmospheric correction algorithms using SeaBASS data. *Remote Sensing of Environment*, 113(3), 635-644.
- Wang, P., Boss, E. S., & Roesler, C. (2005). Uncertainties of inherent optical properties obtained from semianalytical inversions of ocean color. *Applied Optics*, 44(19), 4074-4085.
- Wang, X. J., & Ma, T. (2001). Application of Remote Sensing Techniques in Monitoring and Assessing the Water Quality of Taihu Lake. *Bulletin of Environmental Contamination and Toxicology*, 67(6), 863-870.
- WAPC. (2011). *Onslow regional hotspot land supply update*. Perth WA: W. A. P. Commission. Retrieved from [www.planning.wa.gov.au/dop_pub_pdf/Onslow Regional Hotspots 2011 report.pdf](http://www.planning.wa.gov.au/dop_pub_pdf/Onslow_Regional_Hotspots_2011_report.pdf)
- Wu, G., Cui, L., Liu, L., Chen, F., Fei, T., & Liu, Y. (2015). Statistical model development and estimation of suspended particulate matter concentrations with Landsat 8 OLI images of Dongting Lake, China. *International Journal of Remote Sensing*, 36(1), 343-360.
- Wu, G., De Leeuw, J., Skidmore, A. K., Prins, H. H. T., & Liu, Y. (2008). Comparison of MODIS and Landsat TM5 images for mapping tempo-spatial dynamics of Secchi disk depths in Poyang Lake National

Nature Reserve, China. *International Journal of Remote Sensing*, 29(8), 2183-2198.

- Wu, M., Zhang, W., Wang, X., & Luo, D. (2009). Application of MODIS satellite data in monitoring water quality parameters of Chaohu Lake in China. *Environmental Monitoring and Assessment*, 148(1-4), 255-264.
- Wulder, M. A., Masek, J. G., Cohen, W. B., Loveland, T. R., & Woodcock, C. E. (2012). Opening the archive: How free data has enabled the science and monitoring promise of Landsat. *Remote Sensing of Environment*, 122, 2-10.
- Xie, Y., Sha, Z., & Yu, M. (2008). Remote sensing imagery in vegetation mapping: a review. *Journal of Plant Ecology*, 1(1), 9-23.
- Xing, X., Claustre, H., Uitz, J., Mignot, A., Poteau, A., & Wang, H. (2014). Seasonal variations of bio-optical properties and their interrelationships observed by Bio-Argo floats in the subpolar North Atlantic. *Journal of Geophysical Research: Oceans*, 119(10), 7372-7388.
- Yang, W., Matsushita, B., Chen, J., & Fukushima, T. (2011). Estimating constituent concentrations in case II waters from MERIS satellite data by semi-analytical model optimizing and look-up tables. *Remote Sensing of Environment*, 115(5), 1247-1259.
- Zhang, M., Dong, Q., Cui, T., Xue, C., & Zhang, S. (2014). Suspended sediment monitoring and assessment for Yellow River estuary from Landsat TM and ETM + imagery. *Remote Sensing of Environment*, 146, 136-147.
- Zhang, M., Tang, J., Dong, Q., Song, Q., & Ding, J. (2010). Retrieval of total suspended matter concentration in the Yellow and East China Seas from MODIS imagery. *Remote Sensing of Environment*, 114(2), 392-403.
- Zhang, Y., Shi, K., Zhou, Y., Liu, X., & Qin, B. (2016a). Monitoring the river plume induced by heavy rainfall events in large, shallow, Lake Taihu using MODIS 250 m imagery. *Remote Sensing of Environment*, 173, 109-121.
- Zhang, Y., Zhang, Y., Shi, K., Zha, Y., Zhou, Y., & Liu, M. (2016b). A Landsat 8 OLI-Based, Semianalytical Model for Estimating the Total Suspended Matter Concentration in the Slightly Turbid Xin'anjiang Reservoir (China). *IEEE Journal of Selected*

Topics in Applied Earth Observations and Remote Sensing, 9(1), 398-413.

Zhao, H., Chen, Q., Walker, N. D., Zheng, Q., & MacIntyre, H. L. (2011). A study of sediment transport in a shallow estuary using MODIS imagery and particle tracking simulation. *International Journal of Remote Sensing*, 32(21), 6653-6671.

Zhao, W., Tamura, M., & Takahashi, H. (2001). Atmospheric and spectral corrections for estimating surface albedo from satellite data using 6S code. *Remote Sensing of Environment*, 76(2), 202-212.

Zheng, Z., Li, Y., Guo, Y., Xu, Y., Liu, G., & Du, C. (2015). Landsat-Based Long-Term Monitoring of Total Suspended Matter Concentration Pattern Change in the Wet Season for Dongting Lake, China. *Remote Sensing*, 7(10), 13975.

Zhou, W., Wang, S., Zhou, Y., & Troy, A. (2006). Mapping the concentrations of total suspended matter in Lake Taihu, China, using Landsat-5 TM data. *International Journal of Remote Sensing*, 27(6), 1177-1191.

Every reasonable effort has been made to acknowledge the owners of copyright material. I would be pleased to hear from any copyright owner who has been omitted or incorrectly acknowledged.